Investigating the Potential of Industrial Waste Stream Ammonia as a Fuel for Low Carbon, Gas Turbine Power Generation.

By

Sally Hewlett

A thesis submitted for the degree of Doctor of Philosophy in Engineering

School of Engineering

Cardiff University

November 2021

Summary

Ammonia (NH_3) is found in many industrial waste streams, including as a component of a concentrated aqueous vapour stream, arising from the cleansing of coke oven gas (COG) on integrated steelworks sites. Anhydrous ammonia (AA) can be recovered from the vapour via the Phosam process. Ammonia has recently gained significant research interest as a carbon-free fuel for use in gas turbines. Major challenges are its comparatively low reactivity and a propensity for high NO_x emissions.

Numerical simulations in Chemkin-Pro and experimental investigations in a premixed, representative gas turbine combustor (~500 K inlet, ~0.1 MPa) were used to identify the optimal blend of ammonia (both AA and humidified ammonia of 30%$_{vol}$ H_2O) with a locally available support fuel, to maximise reactivity whilst minimising pollutant emissions. The findings enabled the development of novel anhydrous and humidified ammonia thermodynamic cycles in Aspen Plus, scaled to 10 tonnes per day NH_3, i.e. from a 2 Mt p.a. steelworks.

Optimal fuel support was found with 15%$_{vol}$ COG for both AA and humidified ammonia (HA). The AA blend outperformed the HA blend for emissions, achieving a minimum 172, 5 and 1 ppm for NO_x, NH_3 and CO respectively, for staged combustion (fuel-rich then lean) at 0.11 MPa. Modest experimental pressure elevations of 17% (0.13 MPa) produced ~25% NO_x reductions, with kinetic modelling predicting ~70% reduction for typical gas turbine operating pressures, suggesting regulatory compliance is possible. Partial secondary air substitution with nitrogen produced ~10% reductions in NO_x. Delaying the second stage (10 cm further downstream) reduced NO_x at 0.11 MPa but not 0.13 MPa. Inlet temperature elevations of just 30 K above 500 K significantly increased overall NO_x emissions.

The Brayton/Rankine cycle with recuperator modelled in Aspen Plus achieved >48% cycle efficiency and generated ~1.2 MW_e net power, with >80% greenhouse gas reductions versus natural gas.

Table of Contents

Index of Figures

Index of Tables

Nomenclature

0-D	-	Zero-Dimensional (time independent)
1-D	-	One-Dimensional (time constrained)
AA	-	Anhydrous Ammonia
ADJ-WFLO	-	Calculator for maximising steam mass flow to minimise Q-RESID
AEGL	-	Acute Exposure Guideline Level
AFR	-	Air to Fuel Ratio
AFT	-	Adiabatic Flame Temperature
AIRCOMP	-	Air Compressor
AIRSPLIT	-	Splits AIRCOMP outlet for premix combustion and cooling flows
AV	-	Ammonia Vapour
BF	-	Blast Furnace
BF-BOF	-	Blast Furnace to Basic Oxygen Furnace
BFG	-	Blast Furnace Gas
BOF	-	Basic Oxygen Furnace
BOILER	-	Boiler side of the heat recovery steam generator (HRSG)
CH_4	-	Methane
C_2H_2	-	Ethyne (or acetylene)
C_2H_4	-	Ethene
C_2H_6	-	Ethane
C_3H_8	-	Propane
CHP	-	Combined heat and power
CFD	-	Computational Fluid Dynamics
CO	-	Carbon Monoxide
CO_2	-	Carbon Dioxide
COG	-	Coke Oven Gas
COGCOMP	-	COG Compressor
COMBAIR	-	Primary combustion air
COMBPROD	-	Combustor exhaust gases before the gas turbine
COOLAIR	-	Portion of compressor air entering secondary combustion zone
COOLMIX	-	Fuel/air premix before recuperator - at combustor pressure
COND-2	-	Condensate exiting the steam cycle condenser
CONDNSAT	-	Condensate entering the steam cycle pump
CONDNSR	-	Steam cycle condenser
CRZ	-	Central Recirculation Zone
C_p	-	Specific Heat Capacity
DDF	-	Dry Dilution Factor
EAF	-	Electric Arc Furnace
EF	-	Emissions Factor

EOS	-	Equation of state
EU	-	European Union
EX-SPLIT	-	Splits G-TURB exhaust for recuperator and Rankine cycle feeds
FAR	-	Fuel to Air Ratio
FLUE-1	-	Post-recuperator exhaust gases
FLUE-2	-	Post heat recovery steam generator exhaust gases
FTIR	-	Fourier-Transform Infra-Red
FUELHEAT	-	Recuperator for preheating reactant stream
FUELMIX	-	Fuel blend of NH_3 and COG streams only, at combustor pressure
FUELMIXR	-	Combines fuel streams
FWHM	-	Full Width Half Maximum
G	-	Gibbs Free Energy
GHG	-	Greenhouse Gas
GT-EXIT	-	Combustor exhaust gases exiting the gas turbine
GTRC	-	Gas Turbine Research Centre (Cardiff University)
G-TURB	-	Gas Turbine
H_2	-	Molecular Hydrogen
H_2O	-	Water (or Steam)
H_2S	-	Hydrogen Sulphide
H_2SO_4	-	Sulphuric Acid
HA	-	Humidified Ammonia
H-B	-	Haber-Bosch
HCN	-	Hydrogen cyanide
HHV	-	Higher Heating Value
HNO	-	Nitroxyl
HOTMIX	-	Fuel/air premix after recuperator - at combustor pressure
HP-AIR	-	Total cycle air after the air compressor - at combustor pressure
HP-COG	-	COG only stream, after its compressor - at combustor pressure
HP-NH3	-	Liquid NH_3 inlet to cycle - supply pressure 20 bara
HP-STEAM	-	High pressure steam leaving the steam cycle boiler
HP-WATER	-	High pressure water (condensate) leaving the steam cycle pump
HRSG	-	Heat Recovery Steam Generator
IEA	-	International Energy Agency
LEANZONE	-	Secondary combustion stage (i.e. fuel lean)
LHV	-	Lower Heating Value
LP-AIR	-	Total air supply inlet to cycle - at ambient pressure
LP-COG	-	COG supply inlet to cycle - at ambient pressure
LP-NH3	-	Liquid NH_3 supply after letdown valve - combustor pressure
LP-STEAM	-	Low pressure steam leaving the steam turbine
MCP	-	Medium Combustion Plant

MFC	-	Mass Flow Controller
MGA	-	Multi Gas Analyser
MIE	-	Minimum Ignition Energy
n	-	Number of Moles
N_2	-	Molecular Nitrogen
N_2O	-	Nitrous Oxide
NASA	-	National Aeronautics and Space Administration
NH_3	-	Ammonia
NH3-HEAT	-	Recuperator when used to preheat NH_3 only stream
NH3-VALV	-	Pressure letdown valve for NH3
NH3-VAP	-	Post recuperator NH_3 only stream - partially or fully vapourised
NH_4^+	-	Ammonium Ion
$(NH_4)_2SO_4$	-	Ammonium Sulphate
NO	-	Nitric Oxide
NO_2	-	Nitrogen Dioxide
NO_2^- & NO_3^-	-	Nitrite and Nitrate Ions
NO_x	-	Nitrogen Oxides (NO and NO_2)
O_2	-	Molecular Oxygen
OH	-	Hydroxyl radical
ORZ	-	Outer Recirculation Zone
Φ (PHI)	-	Equivalence Ratio
Φ_{opt}	-	Optimal Primary Stage Equivalence Ratio for minimal combined NO_x and NH_3 concentrations. Also known as Φ specific (or Φ_{sp})
Φ_{prim}	-	Primary Combustion Stage Equivalence Ratio
Φ_t	-	Target Primary Stage Equivalence Ratio range for minimal combined NO_x and CO concentrations.
P	-	Pressure
PFR	-	Plug-Flow Reactor
PMT	-	Photomultiplier Tube
PR	-	Peng-Robinson equation of state
PR-BM	-	Peng-Robinson equation of state with Boston-Mathias modification
PREMIX	-	Combines primary air and fuel streams
PSR	-	Perfectly-Stirred Reactor
PUMP	-	Steam cycle condensate (water) pump
Q-BOILER	-	Heat leaving Brayton cycle via the HRSG
Q-CONDSR	-	Heat leaving the condenser
Q-RESID	-	Residual heat (minimised) when heating water with Q-BOILER
R	-	Ideal Gas Constant
RICHPROD	-	Combustion products exiting the primary (fuel rich) stage
RICHZONE	-	Primary combustion stage (fuel rich)

RMM	-	Relative Molecular Mass
S_2	-	Molecular (elemental) Sulphur
S_g	-	Geometric Swirl Number
S_L	-	Laminar Flame Speed
S_N	-	Swirl Number
S(N)CR	-	Selective (Non) Catalytic Reduction (i.e. of NO_x)
SET-P	-	Makes S-TURB discharge pressure = CONDNSAT vapour pressure
SO_2	-	Sulphur Dioxide
S-TURB	-	Steam Turbine
T	-	Temperature
TET	-	Turbine entry temperature
THC	-	Total (unburned) Hydrocarbon
TO-HRSG	-	Portion of gas turbine exhaust going to the HRSG
TO-HX	-	Portion of gas turbine exhaust going to the recuperator
V	-	Volume
W-COMP	-	Work done (power consumed) by the air compressor
WDF	-	Wet Dilution Factor
W-FCOMP	-	Work done (power consumed) by the COG (fuel) compressor
W-G-TURB	-	Work done (power generated) by the gas turbine
W-PUMP	-	Work done (power consumed) by the steam cycle water pump
W-STURB	-	Work done (power generated) by the steam turbine

Acknowledgements

First, I would like to thank my supervisors, Dr Agustin Valera-Medina for his positivity and enthusiasm, Dr Daniel Pugh for helping me find order in the chaos and Dr Alberto Roldan-Martinez for his attention to detail.

I would next like to thank Mr Steve Morris and Mr Jack Thomas for, amongst many things, helping me shape my ideas into something feasible and then safely bringing them into the real world, via several builds and Jack's CAD skills.

The experiments were a real team effort. Sincere thanks go to Dr Burak Goktepe for capturing excellent emissions data under extremely challenging circumstances and Dr Jon Runyon for setting up and capturing the chemiluminescence and fuel flow data. Also, Dr Anthony Giles for being such a combustion guru that he can just step into any role as needed, and does.

Personal thanks go to Gina, who took a research team and created a community and to Malcolm, who, although not involved in this work, supported me on other projects in Cardiff during the last 4 years. I am also deeply grateful to all my fellow PhD friends who made this the enjoyable and memorable time it has been. In particular, I would like to thank my dear friends Julian, Odi and Ogb for the laughs and Seif for mailing me the Excel graphing tip (boy did that save me some time).

This thesis would not have happened without the support of my amazing husband Paul, who is now an unwitting expert on ammonia for power. I'm also very grateful to my daughters for their support and personal resolve. Harmony for being a model daughter, despite having to put her own young life on hold during the pandemic lockdown and Grace for remaining positive despite not being able to see the rest of us for months on end. Jay, thanks for keeping Grace happy!

I would also like to acknowledge the financial support I have received from the Engineering and Physical Sciences Research Council.

Preface

Thesis Publications:

Hewlett S.G., Pugh D.G., Valera-Medina A., Giles A., Runyon J., Goktepe B. & Bowen P.J., (2021) Industrial wastewater as an enabler of green ammonia to power via gas turbine technology. *ASME Turbomachinery Technical Conference & Exposition*, Virtual, 21-25 September 2020 (DOI: 10.1115/GT2020-14581)

Hewlett S.G., Valera-Medina A., Pugh D.G., Bowen P.J. (2019) Gas turbine co-firing of steelworks ammonia with coke oven gas or methane: A fundamental and cycle analysis. *ASME Turbomachinery Technical Conference & Exposition*, Phoenix, Arizona, USA, 17-21 June 2019. (DOI: 10.1115/GT2019-91404)

Chapter 1 Introduction

1.1 Anthropogenic Climate Change

1.1.1 Fossil Fuels, Greenhouse Gases and Climate Change

To date, human activities are responsible for an estimated 1°C increase in global climate warming above pre-industrial levels. It is believed that anthropogenic emissions of greenhouse gases (GHGs) up to the present day are unlikely to result in an additional global temperature rise of more than 0.5°C. However, due to the current and future predicted levels of release, temperature increase is accelerating and is likely to reach 1.5°C between 2030 and 2052 [1]. Many other climate change markers are also increasing, including a rise in sea levels of approximately 0.2 m in the last century [2] and a 30% increase in ocean acidification since the beginning of the industrial revolution [3].

As Figure 1.1 shows, of all the persistent GHGs (i.e. excluding water vapour) carbon dioxide (CO_2) is the largest contributor to global warming, accounting for over 66% of the effect [4]. The average atmospheric concentration in August 2021 was 414 ppm [5].

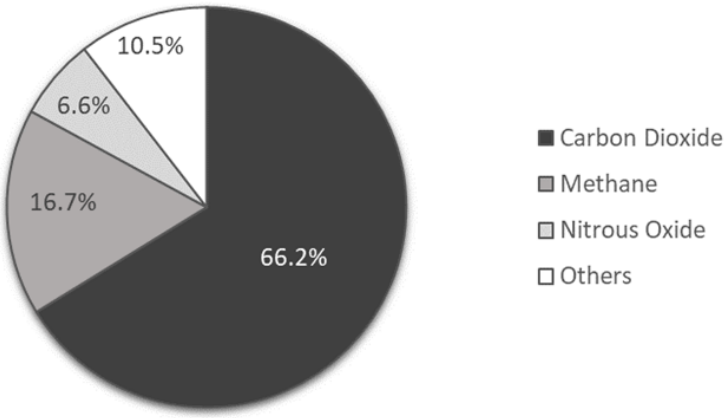

Figure 1.1 The percentage contribution of persistent greenhouse gases to global warming (2017 values)[4].

While risks to health, livelihoods, food security, water supply, human security and economic growth are predicted to increase with a warming of 1.5°C, these risks are believed to be significantly lower than for a 2°C or greater increase. To stay below an approximate 1.5°C increase, requires that global net anthropogenic CO_2 emissions

decline approximately 45% from 2010 levels by 2030 and reach net-zero in around 2050 [1]. Thus, the urgent need for wide-ranging and substantial action cannot be overstated.

In 2018, fossil fuels represented an 81% share of global primary energy demand [6] (in the UK in 2019, the share was 78.3% [7]). Therefore, the world's energy requirements are primarily being met by CO_2 generating fuels. Fossil fuel consumption not only increases atmospheric CO_2 concentrations, but also those of the other main GHGs; methane (CH_4) as fugitive natural gas during fossil fuel extraction, storage, etc. and nitrous oxide (N_2O) formed during the combustion process. Although the atmospheric concentrations of CH_4 and N_2O are much lower than for CO_2, their global warming potentials (on a mass basis) measured over a 100-year period, are 28 CO_2e (i.e. CO_2 equivalent) and 265 CO_2e respectively [8]. Thus, tonne for tonne, their global warming effects are considerably more potent than that of CO_2. Proposed climate change solutions must therefore take proper account of the production of all GHGs, while meeting the challenge to reduce CO_2.

Unsurprisingly, the threat GHGs pose to global climatic conditions and ocean health has prompted many national and international policies on GHG reduction.

1.1.2 International Climate Change Policy Commitments

In December 2015, 195 nations met in Paris agreeing an aim to keep the global temperature rise this century well below 2°C and to drive efforts to limit the temperature increase even further, to 1.5°C above pre-industrial levels [9].

The 2015 Paris Agreement was one of a succession of international agreements developed under the United Nations Framework Convention on Climate Change, which was ratified in 1994. The objective of the Convention is to stabilise greenhouse gas concentrations *"at a level that would prevent dangerous anthropogenic (human induced) interference with the climate system"*. Those countries responsible for the greatest contribution to past GHG emissions are expected to do the most to reduce emissions going forward [10].

As the birthplace of the industrial revolution, the UK has a significant legacy of contributing to GHG emissions. In 2008, the Climate Change Act established legally

binding targets for UK GHG emissions (including CO_2, N_2O and CH_4) to be reduced by 80% of 1990 levels by the year 2050. 'The Carbon Plan', published in 2011, set out a path for GHG reductions in each sector, to meet the 80% reduction target. Many publications, including a range of industry specific 'Industrial Decarbonisation and Energy Efficiency Roadmaps to 2050' followed, including one in March 2015 for the steel industry [11]. In May 2019, in response to a request from UK Government to reassess the UK's long-term emissions targets, The Committee on Climate Change published its report 'Net Zero – The UK's contribution to stopping global warming' [12]. The Climate Change Act was subsequently amended in June 2019 to commit the UK to a 100% reduction in GHG emissions, or net-zero contribution, by 2050 [13], the World's first such commitment. On 30th September 2021 the UK government announced that, henceforth, all companies bidding for UK government contracts worth more than £5,000,000 per year, will be required to demonstrate their commitment to zero carbon emissions by 2050 at the latest, accounting for all direct and indirect carbon emissions (e.g. waste management and employee commuting) [14]. Another global first in carbon policy making. Thus, industries wishing to bid for UK government contracts, will now need to establish their own net-zero by 2050 carbon roadmaps. Consequently, Tata Steel UK is requesting a revised roadmap from the UK Government, with specific details on how government can partner the industry in developing the necessary infrastructures (e.g. hydrogen and carbon capture) for the production of low carbon emissions steel [15].

1.1.3 Iron and Steel Industry Carbon Emissions

There are two primary methods for the production of crude steel, the blast furnace to basic oxygen furnace (BF-BOF) route and the electric arc furnace (EAF) route. The BF-BOF route is the most widely used process, accounting for approximately 75% of the 1,860 Mt of world crude steel production in 2020 [16].

Typically, coal, imported electricity and natural gas account for 89%, 7% and 3% of the energy needs of an integrated BF-BOF site respectively (1% from other gases and sources) [17]. At approximately 1.2 Gt or 15% of global coal use [18] it is unsurprising that the iron and steel industry accounts for approximately 10% of global energy systems' CO_2 emissions (when including emissions from the combustion of fossil fuels,

industrial process emissions, indirect emissions from the power sector and the combustion of steel off-gases) [19]. Coal processing to coke, for use in the blast furnace, generates an ammonia waste stream introduced later in Section 1.3. For sustainable development aligned with the Paris Agreement, the International Energy Agency (IEA) has recommended that the average direct CO_2 emission intensity of steel production must decline by 60% by 2050 [19]. One specified IEA measure towards sustainable development targets is to approximately halve global crude steel manufacture by the BF-BOF route by 2050, in favour of the less energy intensive EAF route and also through the development of innovative technologies which use molecular hydrogen (H_2) as the reductant [19]. However, by 2050, global steel production is expected to increase by approximately 1.5 times that of 2018 levels [20]. Therefore, although there is intended movement towards the EAF and H_2 based processes, it appears the BF-BOF process will contribute significantly to global crude steel production in the medium to long term.

Direct GHG emissions from industry accounted for 21% (104 $MtCO_2e$) of UK emissions in 2018, 61% of which came from manufacturing [21]. In addition, indirect emissions from the consumption of a third of UK grid electricity increases industrial GHG emissions by 5%, to around 26% of UK emissions [22]. However, industrial emissions and production are not evenly spread. In Wales, industry accounts for more than one third of the country's GHG emissions, nearly half of which are generated by the Port Talbot steelworks, the largest producer of crude steel in the UK [22].

In Wales, the UK Government recommendation of net-zero by 2050 was instead set at 95% reduction from 1990 levels. This derogation from net-zero was not made in light of the comparatively large contribution of Wales' steel industry, but in response to limited opportunities for CO_2 storage in the region (via forestation), coupled with relatively high agricultural emissions, which are difficult to reduce [12].

Therefore, while there is likely to be considerable medium term global demand for steel produced via the BF-BOF process, significant effort is required to reduce GHG emissions in the steel industry, if it is to survive in those regions of the globe with the most aspirational climate change commitments.

1.2 Ammonia for Low Carbon Energy

1.2.1 Ammonia's Potential as a Hydrogen Vector and Fuel

Ammonia (NH_3), is a carbon-free molecule. It can be synthetically produced from atmospheric nitrogen (N_2) (using an air separation unit) and H_2. It was first manufactured on an industrial scale in 1913 [23], thanks to the work of Fritz Haber and Carl Bosch. In 2018, NH_3 produced via the Haber-Bosch (H-B) process amounted to a global trade in the region of 150 Mt (nitrogen equivalent) [24] with approximately 80% of this NH_3 used in fertiliser production [25]. Consequently, NH_3 has large scale, established transport and handling networks throughout the world.

Anhydrous (without water) NH_3 has a boiling point of 240 K and a vapour pressure of approximately 1 MPa at room temperature [26, 27]. Consequently, anhydrous NH_3 is easily stored as a liquid, under similar conditions to those of propane. This is in stark contrast to the conditions required for the storage of H_2, widely regarded as the primary carbon-free fuel. The comparative H_2 densities of H_2 and NH_3 under a variety of storage conditions are shown in Figure 1.2.

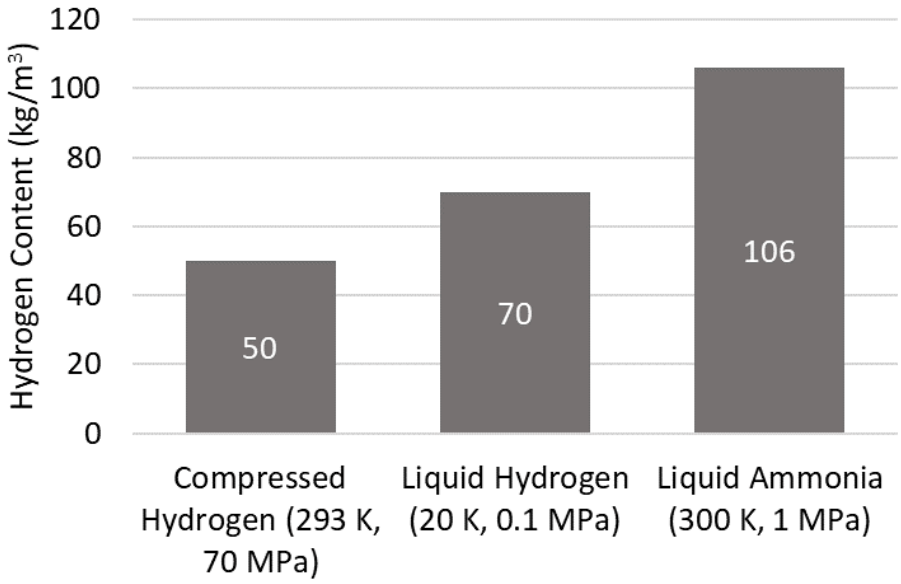

Figure 1.2 The comparative hydrogen densities of hydrogen and ammonia under varying storage conditions [26].

Liquefying H_2 requires a temperature of 20 K at atmospheric pressure [26]. The extreme conditions required to liquefy H_2 consume 30% of the energy content of H_2 and there

are further losses during storage [28]. In addition, due to the diatomic nature of H_2, the hydrogen density of liquid H_2 is considerably lower than that of liquid NH_3. Milder storage conditions and higher hydrogen density, mean storing NH_3 over a six month period costs less than 4% that for the equivalent amount of hydrogen stored as pure H_2 [29]. In addition to higher storage costs, H_2 has no existing distribution network to compare with that of NH_3. Another significant benefit in the transportation and storage of NH_3 over H_2 concerns its very low comparative flammability. This is discussed further in Section 1.2.2.

For over 60 years, many have been voicing their concerns regarding the contribution fossil fuels make to increasing atmospheric CO_2 levels. In his 2012 paper titled "The Dual-Fuel Strategy: An Energy Transition Plan", W. Ahlgren [30] reminds us that L. Green [31] had identified NH_3 as a carbon-free fuel, and therefore a potential solution to climate change, in his 1967 paper "Energy needs versus environmental pollution: a reconciliation?".

The simplified chemical equation, given in Equation 1.1, shows the products for the reaction of NH_3 with oxygen (O_2) to be essentially N_2 and water vapour.

$$4NH_3 + 3O_2 \rightarrow 2N_2 + 6H_2O \qquad \textit{Equation 1.1}$$

It is notable that the 7 moles of reactants produces 8 moles of products. In gas turbines, this increase in moles increases product volumes beyond those achieved by temperature increases alone.

Although the combustion of NH_3 itself is carbon-free, over 95% of global H_2 is currently produced from fossil fuels with CO_2 as a by-product, with approximately half of this H_2 used in the manufacture of NH_3 via the H-B process [32]. In addition to this CO_2 by-product from H_2 sourcing, the H-B process is energy intensive and even under best practice, using natural gas as a H_2 source, 7.8 MWh of energy is required per tonne of NH_3 product, leading to further CO_2 emissions [28]. Consequently, NH_3 production is responsible for over 1% of global CO_2 emissions [32]. Ammonia produced in the manner outlined in L. Green's quote, whereby the CO_2 from fossil fuel consumption could be captured during the synthesis of NH_3, is termed blue NH_3. While not yet commercialised,

blue NH_3 is considered by some as a potential step towards transition to a wholly carbon-free route to NH_3 production, as described next [33].

H_2 can also be produced via the electrolysis of water using renewable electricity. This is not a new technology. Until the 1960s, most fertilizer sold in Europe came from Norway, via hydropower-based electrolysis of water, providing the H_2 for NH_3 production [32]. When renewable electricity is used to power the electrolyser, the low-carbon H_2 evolved is termed green H_2. If utilised as a fuel for power generation, green H_2, as chemical storage of renewable electricity, has the potential to overcome the intermittency problems of renewables generation. This conversion of electrical energy to chemical energy and then back to electrical energy is known as a power-to-gas-to-power cycle. Naturally, the conversion of green H_2 to green NH_3, not only leads to a lower storage and distribution cost alternative for green H_2, but can also produce a 'green' fertiliser feedstock. Additionally, green NH_3 is being considered as a carbon-free fuel for direct use in energy systems [34–36].

The lower heating value (LHV) of NH_3 is 18.6 MJ/kg, so in comparison with other liquid fuels, it is similar to that of methanol and half that of diesel. While this energy density could (with appropriate system modifications) make NH_3 suitable for applications serving 95% of the world's energy needs, its toxicity and corrosiveness (limiting it to professional end-use) would likely restrict its potential use to 80% of global requirements [30].

As shown in Equation 1.2, the conversion, or cracking, of NH_3 to H_2 and N_2, for use as a fuel (including for power generation) is an endothermic reaction requiring 45.7 kJ/mol of NH_3 at 298 K [37].

$$2NH_3 \rightarrow N_2 + 3H_2 \qquad (\Delta H^{\ominus} = +45.7 \text{ kJ/mol}) \qquad \textit{Equation 1.2}$$

This energy input for cracking represents approximately 15% of the LHV of NH_3 (or 2.7 MJ/kg). Using NH_3 directly for heat and/or power generation instead, would not only reduce the complexity of the combustion system, dispensing with the need for an upstream fuel cracker, but also avoid the substantial energy requirements required by the converter. Technologies proposed for the direct use of NH_3 for low-carbon power

(and potentially heat) are solid oxide fuel cells, reciprocating engines and gas turbines [37–40].

1.2.2 Ammonia use in Gas Turbines

In the same year that L. Green was making his observations concerning the potential of NH_3 as a fuel [31], a significant work by Verkamp et al. [41] investigated the direct use of NH_3 in gas turbines, sized for hydrocarbon fuels. The motivation on this occasion was to overcome the logistical issues of supplying fuels for remote military operations. A fuel that can be synthesised from environmental materials (i.e. air and water) made NH_3 the prime candidate. The same reasoning naturally makes the case for NH_3 use in other off-grid applications, especially where its use as fertiliser could also be useful.

One of the two main challenges of using pure NH_3 as a fuel is its low reactivity. Low reactivity manifests itself across a number of combustion characteristics (e.g. high ignition energy and low laminar burning velocity). Some of these characteristics were explored at depth in the Verkamp et al. study. Several fuel additives, to support combustion, were investigated including acetylene (C_2H_2), carbon monoxide (CO) and nitric oxide (NO). One important contribution of the paper was the finding that NH_3 dissociation to 28%$_{vol}$ H_2 (simulated by $N_2/H_2/NH_3$ mixtures) improved reactivity sufficiently to enable its use in existing engines. Also in 1967, D. Pratt was investigating NH_3 fuelled gas turbines and experiencing the same issues of low reactivity [42]. Pratt noted that NH_3's very low burning velocity necessitated reduced reactant flows to prevent flame extinction, which in turn led to poor mixing and low combustion efficiency. This study concluded that 'new and unique techniques may be required to achieve this mixing'. As a consequence of its low reactivity, the employment of NH_3 as a fuel was generally abandoned at this time.

With the renewed emphasis on the need for low-carbon fuels, the challenge of NH_3's low reactivity in gas turbines is being addressed in several ways:

- The use of support fuels either through addition (e.g. CH_4 and H_2) or partial cracking to H_2.
- Pre-heating reactants to increase flame speed and aid ignition.

- Flame stabilisation techniques to enable increased mixing and hence more efficient fuel consumption.

The other major challenge in NH_3 combustion, is its propensity for pollutant nitrogen oxide (NO_x) emissions. Nitric oxide (NO), and to a lesser extent nitrogen dioxide (NO_2) and the GHG N_2O, form in combustion systems. Post combustion, NO reacts with atmospheric O_2 to become NO_2. Hence, it is conventional in industry for NO and NO_2 emissions to be considered together, under the single banner of NO_x. While this term can also include N_2O emissions in the academic field, this thesis limits the use of the term NO_X to NO and NO_2 only, to reflect industrial emissions measurement conventions which are a feature of this study.

Nitrogen dioxide is a precursor to acid rain and a contributor to photochemical smog, with its deleterious health effects. Consequently, the chemical reactions of nitrogen compounds, when occurring in combustion processes, have been studied intensively for over eighty years [43].

Conventional gas turbine fuels do not contain nitrogen. The formation of NO occurs when sufficiently high combustion temperatures provide enough thermal energy to enable the oxidation of atmospheric N_2. The overall reaction is expressed as:

$$\frac{1}{2}N_2 + \frac{1}{2}O_2 \rightleftharpoons NO \qquad \textit{Equation 1.3}$$

The reaction as shown in Equation 1.3 is highly endothermic and so would progress too slowly to account for significant amounts of NO. Rather, free oxygen atoms, present in flames at high temperatures, attack the N_2 triple bond (see Equation 1.4) [44].

$$O^{\cdot} + N_2 \rightleftharpoons NO + N^{\cdot} \qquad \textit{Equation 1.4}$$

$$N^{\cdot} + O_2 \rightleftharpoons NO + O^{\cdot} \qquad \textit{Equation 1.5}$$

This initiates a chain reaction whereby liberated ‘N’ atoms react with O_2 to generate NO plus more oxygen radicals in the second reaction (see Equation 1.5), which in turn feeds the first reaction. This pair of reactions, first postulated by Zel’dovich et al. in 1946 [45], explains the basis of thermal NO production via the fixation of atmospheric nitrogen.

The first reaction is highly endothermic and therefore the slower of the two reactions (i.e. the rate limiting step). Thus, lowering peak combustion temperatures and limiting incidences of the first reaction step, is effective in minimising thermal NO_x production in conventional systems. Excess air, facilitating considerable cooling of the flame, is a practical method widely employed in natural gas fired gas turbines, as is staged combustion, with intervening quenching, to limit maximum temperatures.

As NH_3 is a nitrogen containing molecule, combustion reactions involving fuel bound nitrogen are unavoidable. Reaction pathways naturally include NO_x formation. Therefore, not only can NH_3 produce thermal NO_x (when achieving sufficiently high combustion temperatures), but also fuel derived NO_x, termed fuel NO_x. Indeed, for fuels with a considerable nitrogen component, oxidation of fuel-bound nitrogen constitutes the dominant source of NO_x emissions [46]. Coal and biomass are also nitrogen containing fuels, so the study of fuel NO_x goes beyond and predates interest in straight NH_3 combustion. Therefore, despite not having been generally considered a fuel in its own right until very recently, NH_3 has for many decades been employed as a vehicle for investigating fuel NO_x formation in conventional fuels.

The NH_3 oxidation reaction pathways as described in the 2018 paper by Glarborg et al. [46] are reproduced in Figure 1.3.

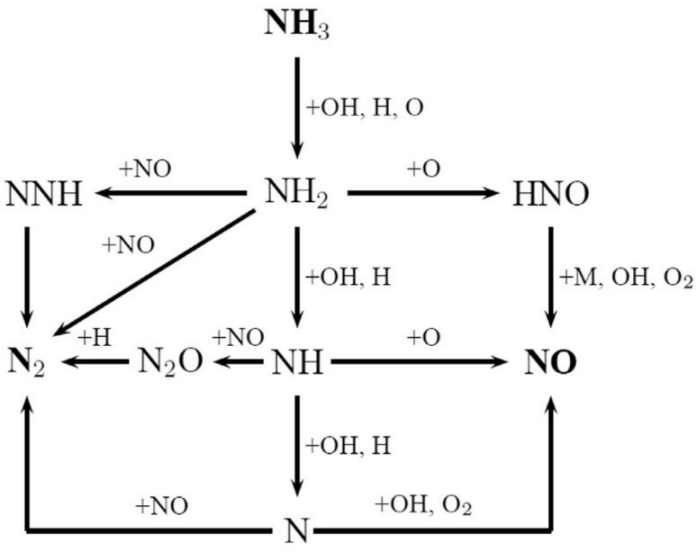

Figure 1.3 Reaction pathways for the oxidation of ammonia [46].

It can be seen that the pool of oxygen and hydrogen (O/H) radicals present in the flame (i.e. hydroxyl (OH), H and O), abstract hydrogen to initially convert NH_3 to the amine radical NH_2 and then potentially other amine radicals (i.e. NH and N) in turn. Whether amine radicals react with NO to form N_2 or instead with O/H radicals (and O_2 in the case of the N radical and the nitroxyl (HNO) intermediate) to form NO, will depend in part on the relative concentrations of the radicals and NO. Therefore, under fuel-lean conditions, where there is a high concentration of 'O' radicals and O_2 present, NO production is high. Fuel-rich conditions are thus favoured in NH_3 combustion, in contrast to the thermal NO_x mitigation measures (i.e. excess air) as used in conventional systems.

Fuel-rich combustion conditions naturally result in unburned fuel and the need for a subsequent combustion stage for burnout. A staged approach is more easily achieved in the combustor of a gas turbine than in a reciprocating engine, so gas turbine technology is selected for use in this study.

A third type of NO formation, prompt NO_x, is formed due to the attack of CH_n radicals on atmospheric N_2 [47]. It is an important source of NO in conventional combustion systems where fuel/air mixing takes place solely in the combustion chamber, i.e. for diffusion flames [46]. While not relevant to pure NH_3 or H_2 combustion, prompt NO_x can become relevant in NH_3 systems through the use of certain support fuels (e.g. CH_4).

With ever more stringent limits on NO_x emissions, conventional systems are increasingly required to do more than is achievable using primary measures (i.e. within combustion chambers alone). In a narrow temperature range of around 1100-1400 K and in the presence of O_2, NH_3 (anhydrous, aqueous or as urea) is commonly used in conventional systems as a post combustion additive in the exhaust gases, lowering NO by 30-75% [48]. This process of selective non-catalytic NO_x reduction (SNCR), also known as thermal de-NO_x, takes advantage of the NO consuming reaction pathway from NH_2 to N_2, either directly or via NNH, as shown in Figure 1.3. This process is an alternative to the more effective (60-85%) de-NO_x process called selective catalytic reduction (SCR), in situations where catalyst poisoning needs to be avoided (e.g. from contaminants such as sulphur oxides) [48]. As with SNCR, SCR also uses NH_3 based reductants.

1.3 Industrial Waste Stream Ammonia

1.3.1 Nitrogen and Sulphur in Industrial Waste Streams

Nitrogen and sulphur are components of proteins, which are present in all living things. As proteins degrade anaerobically, nitrogen and sulphur are converted to NH_3, ammonium ions (NH_4^+) and hydrogen sulphide (H_2S). Therefore, it is unsurprising that all industries handling material of organic origin, will have NH_3 and H_2S in their material flows. Once in the atmosphere NH_3 can rapidly return to ground as NH_3 (dry deposition) or react with acid gases to form NH_4^+, a fine inorganic aerosol which can persist across international boundaries. This aerosol contributes to PM 2.5 (particulate matter < 2.5 µm diameter) concentrations, with negative consequences for respiratory health. Like NH_3, the aerosol also eventually returns to ground via precipitation (wet deposition). Once returned to ground (as NH_3 or NH_4^+), it can cause eutrophication in water bodies, threatening aquatic life and impacting biodiversity [49]. In the UK, around 63% of sensitive habitats are believed to be suffering deposition in excess of critical loads for eutrophication [50]. Deposited NH_3 (and NH_4^+) is transformed by microbes to a range of other compounds including NO, N_2O and molecular nitrogen, dependant on soil conditions [51].

UK agriculture was estimated to have released 234,000 tonnes of NH_3 to the atmosphere in 2014 [52]. Other European countries have shown it is possible to reduce agricultural NH_3 emissions by around 50% through improvements in waste stream management [50]. This suggests that if these measures were implemented in the UK, approximately 100,000 tonnes of NH_3 resource could be diverted each year from agriculture alone.

Ammonia in sewage treatment (as in natural environments) is normally destroyed biologically, via the nitrogen cycle, whereby nitrifying bacteria convert the NH_4^+, first to nitrite ions (NO_2^-), then to nitrate ions (NO_3^-). Denitrifying bacteria then convert the NO_3^- to N_2 for release to the atmosphere. This process route requires significant amounts of aeration, consuming anywhere between 50% and 75% of the total energy consumption from large to small plants respectively [53].

Fossil fuels are also organic in origin, so coal processing and oil refining have significant waste streams containing NH_3 and H_2S. Ammonia dissolves readily in water, forming an

aqueous solution. Hence, water is commonly used for the removal of NH_3 from process gases in fossil fuel processing industries. Aqueous NH_3 is capable of dissolving molar amounts of H_2S, equivalent to that of the NH_3, into solution [54]. The resulting toxic solution of water, NH_3 and H_2S is termed sour water and requires further processing before release of the water component into the environment. In contrast to agriculture and sewage treatment, steelworks have a long history of managing NH_3 by producing waste streams of increasing NH_3 concentration, rather than dispersing it into the environment (agriculture) or destroying it via the nitrogen cycle (sewage). For this reason, the steel industry is the focus for this study. However, these other industries (agriculture and sewage) may be seeking to change practice in response to climate change and environmental policies and demonstrated benefits arising from contemporary NH_3 research.

1.3.2 Ammonia Handling in the Steel Industry

A modern blast furnace requires 450 to 480 kg of coke [55] (i.e. ~780 kg of coal [18]) for every tonne of iron produced. Coke acts as both a reductant and fuel for the iron smelting process and, due to the considerable amounts of coke required, steelworks commonly have coke ovens, for the conversion of coal to coke, situated on site.

During the pyrolysis (i.e. oxygen-free, high temperature decomposition) of coal into coke, a gaseous fraction of moisture and volatiles is evolved. This fraction, termed raw coke oven gas (COG), is laden with contaminants with the potential to foul and corrode pipework. These contaminants include tar, NH_3 and H_2S. Once recovered, many of these contaminants are considered valuable by-products [56]. COG is comprised of approximately 60%$_{vol}$ H_2 and 25%$_{vol}$ CH_4. For practical comparison (i.e. in volumetric terms) COG has a typical lower heating value (LHV) of between 17 and 20 MJ/*Nm^3 [56, 57], approximately half that of CH_4 (i.e. ~36 MJ/m^3 at 1 atm and 273 K). Therefore, once cleansed, integrated steelworks (i.e. those with on-site coke ovens) utilise COG around plant for the provision of heat and power.

Under typical coke oven processing conditions of ≥ 1200 K, NH_3 in COG constitutes around 10-15% of all the nitrogen originally present in the coal [58]. Consequently, coal carbonisation produces a particularly concentrated NH_3 waste stream of approximately

3 kg per tonne of coke [56], equivalent to approximately 1.4 kg of NH_3 per tonne of steel (in a modern blast furnace). Hence, a modest sized integrated steelworks (e.g. 2.7 Mt steel per annum) will produce approximately of 3,800 tonnes of NH_3 from its coke ovens each year (assuming no imports of coke), equivalent to approximately 10 tonnes of NH_3 per day. It is this significant flow of NH_3 that serves to explain the considerable body of literature concerning the management of by-product NH_3 from coking (dating back over a century), and why the steel industry, unlike other industries, has to first concentrate and then recover or destroy the NH_3.

Given that in 2020, 75% of global crude steel production was via the BF-BOF route, this equates to annual production of ~1,400 Mt of steel. Hence, waste stream NH_3 in the global steel industry would be greater than 1.9 Mt per year (given that not all blast furnaces are modern). This amount of NH_3 is equivalent to approximately 1% of current synthetic NH_3 production. In contrast, before the advent of synthetically produced NH_3, COG was the only source of fixed NH_3 (i.e. ammonium salts), making it a once valuable by-product of the steel industry [58].

* The units Nm^3 refer to a 'normal' volume in m^3 at standard temperature and pressure, where the standard used is not defined in the literature. The standard commonly (though not certainly) refers to 1 atm and 273 K.

1.3.3 Steel Industry By-product Ammonia Treatments

The most significant NH_3 treatments to have been used in the steel industry include methods for the production of ammonium sulphate ($(NH_4)_2SO_4$) fertiliser, the recovery of NH_3 as anhydrous NH_3 and the catalytic or oxidative destruction (i.e. combustion) of the NH_3. Reacting NH_3 with sulphuric acid (H_2SO_4) to produce $(NH_4)_2SO_4$ for use as fertiliser was usual practice for most of the 20th century.

Competition from large scale, synthetic NH_3, manufactured using natural gas as a H_2 source, has grown over recent decades. In 2018, it represented in the region of 72% of global NH_3 production [28]. The decreasing price of US natural gas to an average of $3.90 per thousand cubic feet in 2019, down from a peak of $9.65 a decade earlier (in 2008) [59], has greatly reduced the costs of fertiliser production in recent years. Although Covid-19 has been responsible for recent peaks ($9.33 in February 2021) and troughs ($2.57 in July 2020) in US natural gas prices, they have since returned to <$5 [59]. Although high gas prices caused temporary interruptions to NH_3 production in Europe in 2021, global fertiliser company Yara increased imports of NH_3 to Europe from countries such as the US, to meet the challenge [60]. Thus, it is unlikely that localised escalation of production costs can significantly impact the competitiveness of synthetic NH_3 versus steelworks by-product NH_3. Naturally, these market conditions could change if CO_2 emissions from the use of natural gas (~1.6 tonnes/tonne NH_3 [28]) were costed to significantly impair the economics of producing synthetic NH_3 from natural gas.

Further issues have negatively impacted the marketability of steelworks $(NH_4)_2SO_4$ fertiliser over time. The price of H_2SO_4 feed can exceed the value of the $(NH_4)_2SO_4$ product [61] and $(NH_4)_2SO_4$ fertiliser is not best suited to European soils, so European product would normally need to be exported [62]. In 1965, in response to this poor economic situation, Firma Carl Still developed a process to catalytically destroy rather than recover the NH_3 [62]. Catalytic destruction avoids the high concentrations of NO_x emissions associated with NH_3 incineration.

Another alternative, the process for the recovery of anhydrous NH_3 from COG, called the Phosam process, was first commercialised in 1968. This process, as described by A. Kohl and R. Nielsen [58], uses phosphoric acid, which binds with NH_3 to form the

intermediate monoammonium phosphate ($(NH_4)H_2PO_4$), a non-volatile compound. This compound temporarily binds with a second NH_3 molecule (i.e. an absorption process) to form diammonium phosphate ($(NH_4)_2HPO_4$), which is thermally unstable. Downstream from the absorption process, the diammonium phosphate solution is heated in the presence of steam, which strips NH_3, thus regenerating the intermediate as described in Equation 1.6.

$$NH_3 + (NH_4)H_2PO_4 = (NH_4)_2HPO_4 \qquad \textit{Equation 1.6}$$

The steam and recovered NH_3 blend is then condensed and fed to a fractionator where an anhydrous NH_3 product of over 99.5% purity (0.2-0.5% water) can be produced from the overhead vapour stream [58]. By 1990, large Phosam plants were the only process capable of generating a profit from the sale of by-product NH_3, albeit a small profit [62].

There is a dearth of contemporary literature, detailing the relative prevalence of the many by-product NH_3 treatments as currently practiced on steelworks sites. A European Union (EU) commissioned 1992 report [63] is the most recent in-depth review of the methods used in COG cleansing. With 25 responses to their survey of 52 European sites (no responses from the UK), their assessment was that systems for COG cleansing are extremely varied, essentially 'tailor-made' to each individual site and it is therefore not relevant to make comparisons of data between sites or to use the reported data to predict the practices of those sites failing to respond.

The processing of by-product NH_3 is primarily dictated by the chosen method for the management of the significant H_2S in the waste stream (approximately 2.5 kg per tonne of coke [56]). Therefore, while all coking plants have, in theory, the opportunity to recover NH_3 for use as fuel, the considerable variety of by-product plant arrangements mean that the material flows often preclude this.

The author does not believe a discussion of the many alternative H_2S and interdependent NH_3 processing routes would serve a useful purpose in this thesis. As indicated by the findings of the EU 1992 report, the degree of relevance of any given process arrangement to the *status quo* cannot be known and any such discussion would be necessarily lengthy, highly detailed and take the focus of the study into chemical engineering processes, rather than the potential of by-product NH_3 as fuel.

Crucially, there are COG by-product plants which produce a concentrated NH_3/water vapour stream, where the relative concentration of H_2S and other acid gases has been greatly reduced upstream. An example of such an arrangement is given in the following chapter. The composition of the concentrated NH_3 vapour is variable, depending on processing conditions, but is normally between 20 to 40%$_{vol}$ NH_3, several percent by volume of roughly equal amounts of CO_2, H_2S and hydrogen cyanide (HCN) with the balance as water vapour. As mentioned earlier, there is also a proven method for the recovery of high purity anhydrous NH_3 (i.e. the Phosam process). Hence, with appropriate modifications, similar arrangements could, in theory, be an option for all COG by-product installations.

The two remaining BF-BOF steelworks in the UK, are situated in Port Talbot, South Wales and Scunthorpe, North-East England. The Port Talbot site incinerates its by-product NH_3 [64]. The Scunthorpe site produces ammonium sulphate, as confirmed in personal communication. Historic under-investment and sustained threat of closure, may serve to explain why their by-product plants are still adopting these practices, decades after more environmentally friendly or economically sound processes were first proposed. Clearly, an opportunity exists for the adoption of better arrangements, should funding be available, or if more stringent environmental regulations are enforced.

Currently, energy recovery from the destruction of NH_3 is not a requirement, however, catalytic cracking followed by combustion of the H_2 can lead to the raising of steam in boilers [62]. The use of NH_3 ovens in China in the 1990s is the only example found in the literature where NH_3 has been used directly as fuel for energy recovery (raising steam) at steelworks sites [65]. There is no evidence in the literature of steelworks installations utilising by-product NH_3 for power generation, using any technology, either in its aqueous vapour form or as recovered anhydrous NH_3. This is unsurprising given that power from NH_3 is such an immature field.

The revival of research concerning the conversion of NH_3 to power using gas turbines essentially dates back only several years, spurred on by the interest in green NH_3. Although immature, it is a rapidly expanding field offering novel solutions to the challenges of low reactivity and NO_x minimisation. As a readily available, often destroyed

and contaminated resource, by-product NH_3 for power research offers the potential to offset industrial carbon emissions while simultaneously advancing NH_3 in gas turbine research.

1.4 Thesis Aims and Structure

1.4.1 Thesis Aims

The thesis aims to address the following research questions:

- Does by-product NH_3 from coke oven gas have the potential to be utilised in gas turbine technology for power generation?
- If so, how can this best be achieved whilst simultaneously minimising pollutant emissions and maximising power?

1.4.2 Thesis Structure

The structure of this thesis reflects a systematic approach to answering the above two questions. The thesis uses several very different methods, in a sequence of studies, where the outcome of each investigation informs the nature of the subsequent one. Therefore, method, results and discussion are contained together within each chapter, where each chapter relates to a separate study. Included chapter summaries highlight the findings of each study. The objectives of each chapter are outlined below:

Chapter 2 – A review of the literature was conducted to provide the necessary background information on the properties of the fuels used in this study (e.g. compositions and combustion characteristics) and to determine appropriate methods for evaluating the safe and efficient use of these fuels in gas turbine technology, for the gathering of industry relevant data.

Chapter 3 – Equilibrium and kinetic (flame speed and reactor) modelling was performed for a wide range of fuel blends to predict their emissions and comparative reactivity. These blends consisted of steelworks NH_3 in either its raw (aqueous) form or as recovered anhydrous NH_3, each blended with support fuels that are readily available on steelworks sites. This enabled selection of two optimal blends (one aqueous and one anhydrous) for progression to experimental investigation. Numerical analysis also established fuel-rich combustion as a strategy for minimising NO_x emissions.

Chapter 4 – A combustor with an industrially relevant configuration (and proven value in relevant publications) was used to experimentally investigate the performance of the selected blends under fuel-rich conditions, representing a primary stage of combustion. Several parameters were varied, including fuel-air ratios and fuel humidity, to verify the earlier numerical findings and to optimise performance for the blends investigated.

Chapter 5 – The experimental results of Chapter 4 were used to improve the reactor model, as originally used in Chapter 3. The improved model was then used to predict emissions (for the optimised primary stage) under industrially relevant pressures, make emissions predictions for those species not able to be measured experimentally and to inform the design of a new combustion chamber to include secondary air staging, for use in the subsequent work of Chapter 6.

Chapter 6 – Two new combustors, with secondary air-staging at different locations, were used to investigate relative emissions concentrations and effects on flame structure during complete combustion of the two fuel blends previously selected. This was conducted at optimised, primary stage fuel-air ratios as first estimated in Chapter 4 and reappraised using the new confinements (at revised inlet temperatures and with greater resolution of fuel-air ratios). Some modest pressure elevation was performed to enable comparison of experimental results with modelled predictions for emissions.

Chapter 7 – The Aspen Plus software program was used for cycle analysis, when using the selected blends under industrially relevant conditions, for the prediction of a wide range of performance criteria including net power and efficiency. A Brayton/Rankine cycle with use of a recuperator (to facilitate preheating of the fuel/air premix) was employed. This modelling enabled comparison of this novel cycle with conventional CCGT systems (e.g. for greenhouse gas emissions).

Chapter 8 – Thesis conclusions, where the thesis findings are discussed in line with the original thesis aims.

Chapter 9 – Suggested further work.

Chapter 2 Literature Review and Background

2.1 Characterising Ammonia as a Fuel

An appreciation of the physical, chemical, thermodynamic and combustion characteristics of NH_3, and how they differ from those of other conventional fuels, is important when considering how NH_3 might be used in existing infrastructure and where adaptation may be necessary. The mild conditions required for liquefying NH_3 make it essentially a liquid fuel for storage and distribution purposes. However, NH_3 fuel delivery into reciprocating and gas turbine engines may occur in either the gaseous or liquid phase. The following sections explore important parameters requiring consideration when using NH_3 as a fuel and compares these with those for conventional and alternative fuels in both the liquid and gaseous phases, as appropriate.

2.1.1 Physical and Chemical Characteristics of Ammonia

The relative molecular mass of NH_3 is 17.031, similar to CH_4 (i.e. 16.043). The NH_3 molecule has a trigonal pyramid geometry, created by the negative charge of a lone pair of electrons on the nitrogen atom, repelling the electrons involved in the bonding of the three hydrogen atoms, as shown in Figure 2.1.

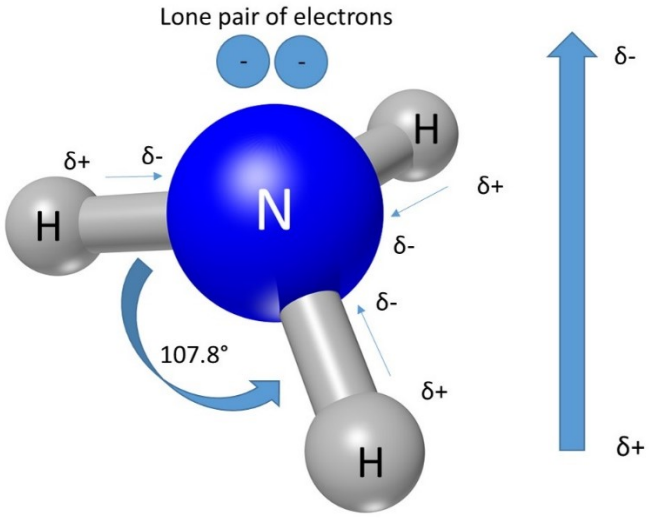

Figure 2.1 The shape and polarity of the ammonia molecule.

Nitrogen is more electronegative than hydrogen, so the electrons in the N-H bond are attracted toward the N atom from the H atoms. This creates a distribution of charge

across the molecule, polarising it and leading to intermolecular hydrogen bonding. This intermolecular hydrogen bonding accounts for the relatively high boiling point of NH_3 and its storage advantages over H_2, as discussed in Chapter 1. Like NH_3, small alcohols also manifest strong intermolecular hydrogen bonding, accounting for the relatively high boiling point of methanol (338 K at 1 atm) when compared with CH_4 (112 K at 1 atm) [66]. Hydrogen (H_2) and hydrocarbons do not form intermolecular hydrogen bonds, so intermolecular attraction increases primarily in relation to molecular size (i.e. attraction is limited to Van der Waals forces only).

Water is also a highly polar molecule (more so than NH_3), therefore, opposite charges on the NH_3 and water molecules attract each other, resulting in the high solubility of NH_3 in water (termed aqueous NH_3) of ~30%$_{vol}$ at room temperature and 1 atm [58], decreasing with increasing temperature. While small alcohols are highly soluble in water, solubility decreases with increasing chain length. Not possessing intermolecular hydrogen bonding, conventional hydrocarbon fuels and hydrogen are essentially insoluble in water.

The partial dissociation of water in a NH_3/water solution produces NH_4^+ and OH^- ions, and so an alkaline solution that is highly corrosive. Whether in its anhydrous or aqueous form NH_3 is especially corrosive towards copper and zinc, necessitating careful materials selection [67]. For metals selection, both stainless steel (type 304), cast iron and aluminium have excellent corrosion resistance, although aluminium's rating is restricted to < 22 °C [68]. For seals etc., EPDM (ethylene propylene diene monomer) rubber and PTFE (Polytetrafluoroethylene) are also rated as excellent, but both natural and fluorocarbon rubber (i.e. FKM, commonly known as Viton) perform poorly, so must be avoided [68].

Ammonia is produced during the natural breakdown of organic matter, so low level exposure from the environment is inevitable, but at high enough concentrations and prolonged exposure, the corrosive and toxic nature of NH_3 makes it dangerous to life. Although a colourless gas (and liquid), it has a strong pungent odour that is detectable by humans at concentrations between 5 and 53 ppm (depending on the individual), helping to mitigate for dangerous exposure levels [69]. Table 2.1 outlines the acute

exposure guideline levels (AEGLs) for a variety of concentrations and durations, with their respective consequences to health. Ammonia is hygroscopic, reacting exothermically with moisture to produce a caustic solution on moist areas of the body such as eyes, nose, throat, and skin, resulting in severe chemical burns at high concentrations. Workplace exposure limits in the UK are 25 ppm and 35 ppm of NH_3 for 8 hours and 15 minutes respectively [70]. De-NO_x processes can lead to unreacted NH_3 entering the atmosphere, known as NH_3 slip. The best practice limit for NH_3 slip in the iron and steel industry is 5 mg/m^3 or 7 ppm [56].

Table 2.1 NH_3 acute exposure guideline levels - effects on health [69]

Classification	Description of effect	Duration of exposure and concentration (ppm)				
		10 min	30 min	1 hr	4 hr	8 hr
AEGL-1	Mild irritation (non-disabling)	30	30	30	30	30
AEGL-2	Irritation of eyes and throat, urge to cough (disabling)	220	220	160	110	110
AEGL-3	Lethal	2,700	1,600	1,100	550	390

2.1.2 Thermodynamic Properties of Ammonia

For comparison, Table 2.2 lists the boiling points, densities and lower heating values (LHV) of NH_3 and a range of conventional and alternative fuels in both the liquid (l) and gaseous (g) phases [with references].

The high volumetric energy densities and mild storage conditions of the fossil fuels is a major obstacle to overcome when aiming to replace them. This is especially true when replacing with H_2, having a volumetric energy density 0.03% that of diesel at 288 K and 1 atm.

For mobile applications, it is the energy density of liquid NH_3, compared with fuels such as gasoline and diesel, which is most relevant. The natural variability in composition of gasoline and diesel is accounted for in the ranges given in Table 2.2, where a mid-range

value has been used to calculate an approximate energy density. Liquid NH_3 has energy densities of ~42% and ~37% those of these liquid fuels, in mass and volumetric terms respectively, and consequently more on-board storage (~3 times the volume and > twice the mass) is required for the same power output. This is especially challenging for aeronautical applications.

Methanol, which can be renewably produced, has similar energy densities to liquid NH_3, with the advantage of a much higher boiling point, but with the obvious disadvantage of CO_2 release to the atmosphere (without the aid of carbon capture technology).

Table 2.2 Boiling points and energy densities for ammonia, conventional and alternative fuels at varying temperatures and atmospheric pressure.

Fuel	Molar Mass (g/mol)	Boiling point (K) @ 1 atm	Density (kg/m^3) at 1 atm	Temp (K) at specified density	Lower Heating Value (MJ/kg)	Energy Density by Volume (MJ/m^3 - LHV)
Ammonia (l)	17.03	239.82 [66]	682 [66]	239.8	18.6 [40]	12,685
Ammonia (g)			0.729 [66]	288		13.6
Diesel (l) (C12-C20)	150-250 [71]	633 (>95%$_{vol}$) [72]	820 – 845 [72, 73]	288	43.4 [74]	~36,000
Gasoline (l) (C4-C12)	60-150 [71]	423 (>75%$_{vol}$) [72]	720 – 775 [73]	288	44.8 [74]	~33,500
Methanol (l)	32.04	337.63 [66]	796 [66]	288	19.9 [75]	15,840
Methane (l)	16.04	111.7 [66]	423.3 [66]	111	50.0 [40]	21,165
Methane (g)			0.68 [66]	288		34.0
Hydrogen (l)	2.02	20.37 [66]	71.28 [66]	20	120 [40]	8,554
Hydrogen (g)			0.085 [66]	288		10.2

For stationary power systems delivering fuels in the vapour phase, natural gas power stations for example, it is the energy density of NH_3 in the vapour phase which is of more interest. These are shown in Table 2.2 for fuels which are gases at 288 K, 1 atm. For example, with a volumetric energy density 40% that of CH_4, gaseous NH_3 lines would need cross-sections 2.5 times larger than those designed for natural gas, to flow fuel of equivalent power (at the same pressure). The values for CH_4 can be considered

applicable to those for natural gas as CH_4 constitutes 85 to 100%$_{vol}$ of the composition of natural gas [76]. Hence, energy densities in this thesis are quoted interchangeably in either a mass or volumetric basis as required.

Ammonia's relatively strong intermolecular forces can lead to practically significant non-ideal gas behaviour, which is at its maximum effect at temperatures just above boiling and under high pressures. In keeping with the first law of thermodynamics, when a gas expands adiabatically and without the production of work (e.g. through an orifice), the temperature of the gas will fall, as work must be done to overcome these attractive forces. This phenomenon is termed the Joule-Thomson effect or a throttling process. All real gases exhibit this cooling effect, however, for helium and hydrogen the temperatures at which this effect occurs is significantly lower than for other non-ideal gases, due to very weak intermolecular attraction [77]. Pressure and temperature fluctuations along pipework and through valves, due to the Joule-Thomson effect, in combination with variation in ambient conditions along pipework, can result in the condensation of NH_3 vapour within the pipework, making effective purging of fuel lines challenging. Electric heating of the pipelines has been reported as an effective method for the prevention of NH_3 condensation in fuel lines [78].

Although the density of NH_3 vapour is approximately half that of air (under ambient conditions), in the event of spillage, dispersal of the toxic gas is hindered by its high heat of vapourisation. As the liquid evaporates it has a tendency to 'hug the ground', so its dispersal is not as rapid as its gaseous density would suggest. The heat of vapourisation for NH_3 is 1370 kJ/kg, over 7% of its LHV [75, 79], compared with 510 kJ/kg for CH_4 at 1% of LHV [75]. This high heat of vapourisation, coupled with a boiling point below that required in the majority of refrigeration applications, makes NH_3 a useful industrial refrigerant. However, these characteristics present a significant operational challenge when using NH_3 vapour as a fuel. At ambient temperature, partially filled fuel cylinders contain NH_3 in both the liquid and vapour phases. As vapour is withdrawn (from the top of the container), the drop in vapour pressure above the liquid surface leads to rapid evaporation of the liquid NH_3, with a significant cooling effect. This cooling, unless compensated for, will in turn reduce the subsequent rate of NH_3 evaporation, limiting

the possible rate of vapour withdrawal from the cylinder. For example, the vapour pressure at 278 K (0.5 MPa) is half that at 298 K (1 MPa). The gradual chilling of the vapour upstream of restrictions naturally exacerbates the issues of condensation related to the Joule-Thomson effect. Reported methods for overcoming this challenge include having more than one liquid NH_3 tank [80] to enable alternation, withdrawing from the cylinder as liquid that is then vapourised in an electrically heated water bath [78] or, with sufficient ambient conditions (i.e. summer temperatures), spraying the cylinder with water [78].

2.1.3 Combustion Characteristics of Ammonia and Ammonia Blends

Once in the combustion chamber, NH_3 exhibits notable deviations from conventional and other alternative fuels, for a number of important combustion characteristics. A pure NH_3 flame is intensely orange, the colour being induced not only by the NH_2 ammonia α-band spectra, but also by the superheated water vapour spectra [81]. Fuels containing carbon can also exhibit an orange colour, but this is due to the formation of soot where oxidant supply is inadequate for efficient combustion, and so is unrelated. In contrast, pure CH_4 and H_2 flames are blue and invisible, respectively.

Table 2.3 Combustion characteristic of NH_3 and other gaseous fuels (inlet 298 K, 1 atm)

Combustion characteristic	Fuel			
	NH_3	CH_4	H_2	C_3H_8
Stoichiometric air to fuel ratio (AFR) - molar basis	3.58	9.55	2.39	23.87
Flammability range (%$_{vol}$ fuel in air)	15 - 29 [75, 82, 83]	5 – 15 [75, 82]	4 – 75 [75]	2 – 9.5 [75, 82]
Minimum ignition energy (MIE) (mJ)	8 [41]	0.28 [84]	0.011 [84]	0.4 [85]
Minimum auto ignition temperature (K)	923 [40]	793 [40]	903 [40]	723 [40]
Peak laminar flame speed (S_L) (cm/s)	7 [86]	37 [40, 87]	291 [40]	43 [40, 87]
Adiabatic flame temperature (AFT) (K)	2074 [88]	2226 [88]	2383 [88]	2268 [88]
Mass of CO_2 per MJ fuel input (g)	0	49.4	0	59.5*

**derived from the heating value of propane, as sourced from* [75]

Some other important NH_3 combustion characteristics are summarised in Table 2.3, alongside those of H_2, CH_4 and propane (C_3H_8). These three fuels are currently used or proposed for use in gas turbine combustion and are (like NH_3) in the gas phase under ambient conditions (298 K, 1 atm). Many of the characteristics listed in Table 2.3, and discussed in this section, relate to the reactivity of these fuels (the importance of which was introduced in Section 1.2.2). While NO_x formation is also an important combustion characteristic of NH_3, strategies for minimising NO_x emissions are complex and so are discussed separately in Section 2.3.

Equation 2.1 is for the complete, stoichiometric combustion of 1 mole of NH_3 in air (i.e. no excess air), assuming air to be 79%$_{vol}$ N_2 and 21%$_{vol}$ O_2 for simplicity (i.e. the ratio of N_2 to O_2 is 3.76). It can be seen that, aside from small amounts of NO_x gases, the products of NH_3 combustion are essentially water (H_2O) and N_2.

$$NH_3 + 0.75\,(O_2 + 3.76N_2) \rightarrow 1.5\,H_2O + 3.32\,N_2 \qquad \textit{Equation 2.1}$$

The air to fuel ratios (AFRs) as stated in Table 2.3 are calculated using the stoichiometric equations for each of the fuels, enhanced to account for a more precise air composition of 78.09%$_{vol}$ N_2, 20.95%$_{vol}$ O_2 and 0.96%$_{vol}$ argon. This air composition is sourced from Gaseq, an equilibrium modelling program described later in Chapter 3 [88]. The AFR of NH_3 on a mass basis is 6.09 (with a relative molecular mass of air of 28.96). A quantity known as the equivalence ratio, denoted as 'Φ' (i.e. phi), has been used throughout this study. It represents the ratio between the stoichiometric air requirement of the fuel and the actual air used, according to Equation 2.2.

$$Equivalence\ Ratio\ (\Phi) = \frac{AFR_{stoich}}{AFR_{actual}} \qquad \textit{Equation 2.2}$$

Alternatively, the fuel to air ratio (FAR) can be used instead of the AFR, in which case Φ is calculated as FAR_{actual} divided by FAR_{stoich}. In either case, Φ > 1 refers to a fuel-rich reactant mixture, Φ < 1 a fuel-lean mixture (i.e. excess air) and Φ = 1 a perfectly stoichiometric mixture of reactants.

For a stoichiometric blend, using air as the oxidant, NH_3 represents 21.8%$_{vol}$ of the blend, which is marginally lower than the midpoint of the reported flammability limits. The flammability limits of 15 and 29%$_{vol}$ fuel in air (see Table 2.3) are equivalent to an Φ range of 0.63 to 1.46.

As for H_2, complete combustion of NH_3 requires only a fraction of the oxidant required by organic fuels, due to the lesser oxygen requirements of hydrogen compared with carbon. Therefore, although the LHV of NH_3 is much lower than those of the organic fuels listed in Table 2.2, stoichiometric fuel/air blends have comparable energy density. For example, Gill et al. (2012) reported that the energy content per unit mass of a stoichiometric NH_3/air mixture is only 7% lower than that of a comparable diesel/air mixture [37]. Similarly, with 2.5 moles of NH_3 needed to match the LHV of one mole of CH_4 (see Table 2.2), stoichiometric molar flows for the same power are only 8.5% higher for an NH_3/air mix than a CH_4/air mix. When one considers that inlet flows are generally fuel-lean for natural gas combustion and proposed as fuel-rich for the initial stages of NH_3 combustion (as introduced in Section 1.2.2), the primary combustion inlet flows become even more aligned, suggesting minimal adaptation of existing infrastructure with regard to specifications such as combustor sizing.

Minimum ignition energy (MIE) is determined empirically by measuring the minimum spark energy required to initiate a sustained flame, across a range of air to fuel ratios, for a given temperature and pressure. The chosen percentage probability of ignition is also a factor (e.g. whether 5% or 50% of ignition attempts being successful is sufficient to claim ignition of a blend for the specified conditions). Even for a fuel as widely utilised and well understood as propane, values used over the last half century have ranged from 0.25 to 0.46 mJ and in recent years was found to be between 0.4 and 0.45 mJ [85]. Therefore, comparisons of MIE between fuels could be considered most meaningful when made using the same equipment, method and conditions. Verkamp et al. (1967) compared the MIEs of propane and NH_3 in air at 1 atmosphere and at ambient temperature (the precise temperature was not supplied) [41]. Several NH_3/H_2 blends in air were also tested to simulate partial cracking of the NH_3. The MIEs reported by Verkamp et al. are given in Table 2.4.

Table 2.4 Minimum ignition energies for propane, NH_3 and NH_3/H_2 blends (ambient conditions) [41]

Fuel	C_3H_8	NH_3	NH_3 : 5.6%$_{vol}$ H_2	NH_3 : 14.1%$_{vol}$ H_2	NH_3 : 28%$_{vol}$ H_2
Minimum Ignition Energy (mJ)	0.37	8	3	0.7	0.2

Given the reported value for propane in Table 2.4 (0.37 mJ) is in reasonable agreement with more recent findings (i.e. 0.4 mJ), the values reported by Verkamp et al. for NH_3 could also be considered reasonably accurate. The low reactivity of NH_3 is clearly evident when comparing the MIE value of pure NH_3 (8 mJ) against the other fuels in Table 2.3 (e.g. 0.011 mJ for H_2). However, Table 2.4 shows that with 28%$_{vol}$ H_2 addition, the MIE decreases from approximately 30 times that of natural gas, to a very similar value (0.2 mJ for NH_3 versus 0.28 mJ for CH_4). Thus, H_2 blending is seen as an effective strategy for addressing poor NH_3 ignition, bringing it more in line with conventional fuels.

In addition to its high MIE, Table 2.3 also shows that NH_3 has the highest minimum auto-ignition temperature (e.g. 130 K > than CH_4) and the highest fuel to air requirement for ignition to occur (i.e. 15%$_{vol}$ for NH_3 versus 2-5%$_{vol}$ for the others), thus risk of unintended NH_3 ignition is considerably lower than for the other fuels. Although beneficial for transport and storage, such low flammability becomes an obvious drawback at the point of combustion and it is then that these other fuels, with their superior reactivity, can be used to support and promote the reactivity of NH_3.

Both H_2 and CH_4 have, in recent years, been experimentally and numerically evaluated as potential support fuels for gas turbine NH_3 combustion in the vapour phase, for premixed and diffusion flames [89–98]. Looking to a low-carbon future, both fuels can be sourced renewably (e.g. bio-methane). Only one study, from late 2020, has investigated NH_3 injection into the gas turbine combustor in the liquid phase, delivered both as pure NH_3 and alternatively with gaseous CH_4 support [79]. Although stable combustion was achieved for liquid NH_3 injection, liquid phase research is currently at an embryonic stage.

Laminar flame speed (S_L) is an idealised value for the velocity of a one-dimensional (1-D) adiabatic flame propagating through a perfectly premixed fuel/oxidant blend, at a specified temperature and pressure. In almost all cases, the maximum value occurs at an Φ of between 1.05 and 1.10. Notable exceptions to this general rule are H_2 and carbon monoxide with velocities reaching a maximum at an Φ of around 2.0 [99]. Laminar flame speeds are derived experimentally, and being a significant parameter in turbulent flame structures and flame stability, are used in the numerical modelling of turbulent flows to validate the efficacy of models.

The lower flammability limit of ~5%$_{vol}$ CH_4 in air (see Table 2.3) suggests a theoretical fuel-lean Φ limit of 0.53 (at 298 K, 1 atm). With inlet temperatures and pressures above ambient (increasing reactivity), this can be lower still. In real-world gas turbine applications it is reported that very fuel-lean natural gas combustion is conducted at an Φ of between 0.5 and 0.7 [99]. Under equivalent conditions of temperature, pressure and volumetric flow rate, the S_L value for CH_4 combustion at Φ ~0.5 could serve to approximate a minimum S_L for majority NH_3 fuel blends intended for use in existing natural gas, gas turbine combustors.

As was introduced in Section 1.2.2, NH_3's low peak burning velocity (~7cm/s) necessitates strategies to prevent flame extinction, the detachment of the flame from the reactant feed (i.e. flame blow-off). In contrast, H_2 has a very high diffusion rate and extremely rapid peak burning rate of ~300 cm/s (see Table 2.3). Hence, blending H_2 with NH_3 can help to mitigate for the low S_L of NH_3. However, for combustors utilising a fuel/air blend premixed upstream of the combustor inlet, blending with H_2 risks the flame advancing too rapidly though the incoming reactants and retreating into the burner and causing damage, with the risk increasing at higher H_2 percentages. This phenomenon is termed 'flashback'. The issue of flashback is exacerbated by the relatively low air requirements of NH_3 combustion, resulting in relatively low bulk flows into the combustor. As found by Valera-Medina et al. (2019), flashback practically limits the molar contribution of H_2 to ~30%$_{vol}$ of the fuel blend [90].

The peak laminar flame speeds of CH_4 and C_3H_8 are a more modest ~5 to 6 times that of NH_3 (at a similar Φ of ~1.05 and under ambient conditions), increasing with carbon chain

length. Adding these organic fuels to NH_3 instead of H_2 offers a potential boost in reactivity but with lower flashback risk and lower peak temperatures (reducing thermal NO_x). The accidental ignition risk of CH_4 and C_3H_8 is also lower than H_2, due to the very low MIE and wide flammability limits of H_2. However, significant substitution of NH_3 with organic fuels naturally raises CO_2 product concentrations, so is unattractive in the bid for net-zero carbon emissions.

The comparatively lower adiabatic flame temperature (AFT) of NH_3 (see Table 2.3), if observed in isolation, could be considered to indicate a relatively lower potential for power generation, lower temperatures being related to less expansion of the product gases in the combustion chamber. However, according to Equation 2.2, for the stoichiometric combustion of NH_3 in air, the product moles are 5.5% higher than the reactant moles. For stoichiometric CH_4 combustion in air, reactant and product moles are equivalent and for H_2 in air, combustion product moles are 15% lower than reactant moles. Fewer product moles naturally means higher temperatures in the combustor and vice-versa, so it is unsurprising that H_2 has the highest AFT listed, ~300 K higher than NH_3 and ~150 K higher than CH_4. Equally, the lower temperature of NH_3 is indicative of its increase in moles from reactants to products, leading to a ~5% increase in product volume unrelated to temperature increase, and thus helping to compensate for the lower AFT. Hence, AFT in isolation is not an appropriate indicator of NH_3's power generation potential relative to other fuels.

This section has discussed the comparatively low reactivity of NH_3 and how the recruitment of other more reactive fuels can help to overcome some of the combustion challenges. However, either due to performance issues (i.e. H_2 flashback) or environmental issues (i.e. CH_4 carbon emissions) there are limits to the contribution these fuels can make. Fortunately, the use of support fuels is not the only method for addressing the challenge of NH_3's low reactivity, with other strategies, such as generating swirling flows in the combustor and fuel preheating, available for adoption.

2.2 Swirling Flows for Flame Stabilisation in Premixed Flames

The primary purpose of introducing swirling flows in the combustor is to increase turbulence and recycle flow. Turbulence serves to promote the mixing of reacting

species and to redirect the heat generated from the combustion reactions to the reactant inflows. Hence turbulent flames consume reactants at a far greater rate than laminar flames.

In gas turbines, premixed inlet streams have an average velocity far greater than the S_L of the fuel/air premix, allowing them to achieve high power densities. To achieve this, it is necessary to create a region in the flow field that has velocities no greater than the burning velocity of the reactant mixture, enabling continuous ignition at a particular point in the flow.

Swirling flows are flows that simultaneously experience both axial and tangential vortex motion as shown in Figure 2.2.

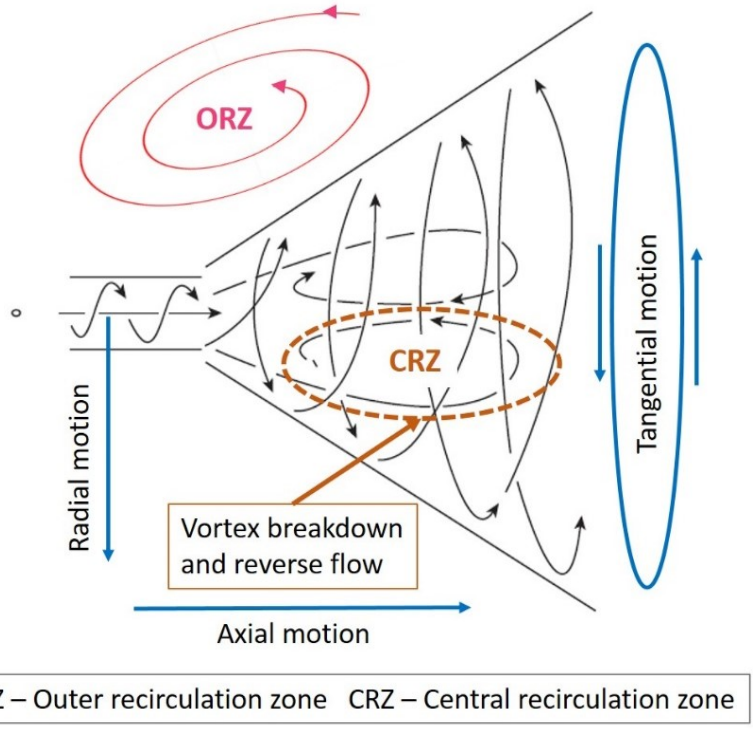

Figure 2.2 Swirling flows and vortex breakdown – adapted from [100]

When the degree of rotation imparted to the reactant flows upstream of the combustor is sufficiently high, vortex breakdown occurs. This well-known phenomenon causes flow reversal and large recirculation eddies along the central axis, increasing the residence time of the reacting flows. The axi-symmetric region of recirculation, termed the central recirculation zone (CRZ), directs heat and active chemical species to the root of the

flame, enabling flame stabilisation and flame establishment to occur in regions of relatively low velocity [101]. In addition to the CRZ, the rapid expansion of the reacting flows in the combustion chamber creates an outer recirculation zone (ORZ) [40]. The use of swirl-stabilised combustion is wide-spread, including in power station burners, gas turbine combustors, internal combustion engines, refinery and process burners [100]. Swirl burners have been successfully used to achieve stable flames in many recent experimental NH_3 combustion studies, with [89–94] and without [94, 95, 102, 103] support fuels (other than for ignition support in some cases).

An important parameter of the swirling flow is the swirl number (S_N). This parameter characterises the amount of rotation imparted to the inlet flow by comparing the levels of axial and tangential momentum in the flow. For $S_N < 0.4$, no flow recirculation is obtained, and the swirl is described as weak, so most swirlers of practical interest, operate under conditions of strong swirl ($S_N > 0.6$) [99].

2.2.1 Swirl Burners

Swirl burners essentially come in two configurations, equipped with either an axial or a radial swirler. Axial swirlers have vanes with flat or twisted blades, whereas radial swirlers use inlets that are perpendicular to the central axis of the burner, as shown in Figure 2.3.

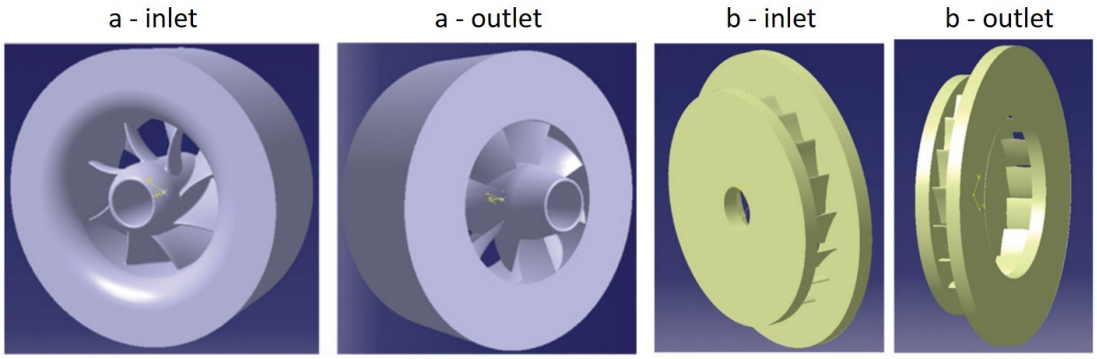

Figure 2.3 The two main swirler types, axial (a) and radial (b) [104]

In a radial burner, the S_N can be derived from the geometry of the swirl burner and the reactant flowrates. A S_N derived this way is termed the geometric swirl number (S_g) and can be calculated according to Equation 2.3 [105].

$$S_g = \frac{A_{noz}.r_{tan}}{A_{tan}.r_{noz}} \left(\frac{Q_{tan}}{Q_{tot}}\right)^2 \qquad \textit{Equation 2.3}$$

Where A_{noz} is the exit area of the burner exit nozzle, A_{tan} is the area of the tangential inlet, r_{tan} is the effective radius of the tangential inlet, r_{noz} is the radius of the burner exit nozzle, Q_{tan} is the tangential flow rate, and Q_{tot} is the total flow rate.

An equivalent equation for calculating the S_N for axial swirlers (see Equation 2.4), uses only the inner and outer diameters of the swirler (D_i and D_o) and the vane angle (α) [95, 106].

$$S_N = \frac{2}{3}\left[\frac{1-\left(\frac{D_i}{D_o}\right)^3}{1-\left(\frac{D_i}{D_o}\right)^2}\right] tan\,\alpha \qquad \textit{Equation 2.4}$$

2.2.2 Achieving Swirl Stabilised NH_3 Flames

The use of swirlers for the successful stabilisation of NH_3 flames is a very recent field of study. An early published work using swirling flows for experimentally investigating premixed NH_3/air combustion was conducted by Valera-Medina et al. (2015) [89]. This study, and a series of subsequent studies by the same group [91, 92], found that stable flames could be achieved with low emissions, using a radial swirler to produce strong swirling flows (S_g = 1.05) for both CH_4/NH_3 (20 and 33%$_{vol}$ CH_4) and H_2/NH_3 (50%$_{vol}$ H_2) premixed blends, albeit limited to a narrow range of Φ (<< 1.0) with flashback presenting significant issues. Despite efforts, the stable combustion of pure NH_3/air remained elusive. The observation was made that a medium S_N (i.e. ~1) can be detrimental to the stability of the flame when using NH_3, mainly due to the low bulk flows entering the combustor, and it was therefore suggested that a lower S_N be assessed to improve burning characteristics, while ensuring that vortex breakdown phenomena could be achieved for flame anchoring purposes.

Around the same time, Kurata et al. (2017) [95] used an axial air swirler (vane angle 60° and S_N 1.6) to surround and successfully stabilise a diffusion flame of pure NH_3 vapour in a 50 kW class micro gas turbine combustor. Ignition was achieved through the initial

use of kerosene liquid fuel injection. A maximum combustion efficiency of 96% was achieved with the highest inlet temperature ~500 °C (773 K), associated with the maximum inlet power investigated (41.8 kW). The high inlet temperatures were made possible through the use of a heat regenerative cycle (i.e. recuperator). Efficiency was greatly improved with the addition of CH_4 support. With NH_3 and CH_4 stated as providing equivalent LHV (i.e. an inferred 30%$_{vol}$ CH_4 support), the blend achieved ~100% efficiency at the highest inlet power. Highest powers were associated with highest inlet temperatures, with stable combustion of the CH_4/NH_3 blend capable at combustor inlet temperatures much lower than that for pure NH_3, leading to the conclusion that CH_4 enhances the flame stability in the combustor.

The same year, premixed NH_3/air flames were successfully stabilised by Hayakawa et al. (2017) [102], at atmospheric pressure and with a 298 K inlet. Two axial swirlers of S_N 0.74 and 1.27 were investigated. It was observed that the flame stability limits broadened when the lower swirl number was employed (to a maximum Φ range of 0.63 to 1.4), supporting the findings of Valera-Medina et al. [89, 91, 92]. Inlet velocities were low, so flame structures were not generally the classic vortex 'V' shape as utilised in natural gas fired gas turbine combustion and as described in Figure 2.2. In most instances described, the NH_3/air flame included a significant ORZ, anchoring the flame to the plate surrounding the base of the burner. Heat transfer from such an attached flame can cause damage to equipment, so is not appropriate in gas turbines. Only when velocities were increased, and stability limits narrowed, did the flame assume the 'V' structure.

More recently, employing a broad range of flame stabilising techniques (i.e. support fuel, inlet temperature elevation and lower S_N) Valera-Medina et al. (2019) achieved stable combustion of a fuel-rich NH_3/H_2 – air premixed blend (30%$_{vol}$ H_2) up to an Φ of 1.4. A radial swirler, S_g of 0.8 was employed, thus lower than the earlier experiments. As inlet temperature was elevated from inlet 288 to 484 K, a 24% decrease in flame profile was observed, indicating a more reactive and stable flame. Profiles also adopted the classic 'V' shape of CH_4/air flames (for which existing natural gas infrastructure is designed). Using the same swirler, a subsequent investigation by Pugh et al. (2019) also

demonstrated that the same premixed fuel/air blend, with steam of ~10%$_{vol}$, could be stably combusted up to Φ = 1.3, with a combustor inlet temperature of 423 ± 5 K, under atmospheric pressure [93].

In summary, these recent findings have greatly advanced the earlier work of the 1960s, highlighting the effectiveness of adopting relatively low intensity (S_N < 1) swirling flows in the efficient, stable combustion of > 70%$_{vol}$ NH_3 fuel blends. An overview of the recent studies suggests that a S_N of ~0.8 has the potential for efficient combustion of NH_3 (with and without modest humidification) under fuel-rich conditions when supported by ~30%$_{vol}$ H_2 or CH_4, with combustor inlet temperatures of approximately 400 to 800 K (potentially achieved through utilisation of exhaust heat).

2.3 NO_x Mitigation

Aside from health, safety and low reactivity, the other significant challenge for employing NH_3 in combustion systems is its propensity for NO_x emissions, primarily resulting via the NH_3 oxidation pathways (i.e. as fuel NO_x), as outlined in Section 1.2.2. Although there are significant benefits to utilising *post* combustion de-NO_x technologies for NO_x reduction, this is a well understood and established field. In contrast, when utilising NH_3 as a fuel, understanding on how best to optimise *primary* combustion conditions for minimal NO_x is in its infancy. Therefore, this study choses to focus on reduction in NO_x through the effective use of primary combustion measures, as this not only lowers NO_x formation in the first instance, but also facilitates the use of smaller scale de-NO_x installations, reducing the operating and capital costs of the chosen post-combustion treatment.

2.3.1 NO_x Regulations and Measurement

Given the atmospheric conversion of NO to NO_2, regulatory limits for NO_x emissions (i.e. NO and NO_2) are expressed in terms of the mass of NO_2 per cubic meter (i.e. mg/Nm^3) under standard temperature (273.15 K) and pressure (101.3 kPa) [107]. However, the measurement of emissions concentrations is usually conducted in terms of their mole fraction or parts per million (ppm) in the exhaust gases. These conditions of temperature

(T) and pressure (P) can be substituted into the ideal gas equation, Equation 2.5, and rearranged to find the moles of gas (n) in 1 m^3.

$$PV = nRT \qquad \textit{Equation 2.5}$$

V is expressed in litres (or dm^3), so is equal to 1000. R is the ideal gas constant with value 8.314 J/mol.K. Thus, total moles of gas in 1 m^3 (i.e. n) is 44.618 and the volume of 1 mole of NO_2 is therefore 0.0224 m^3 at standard temperature and pressure.

Equation 2.6 is used to convert the concentration of a substance expressed in g/m^3 (Y) to its mole fraction (X). For example, substituting in the volume of one mole of gas (n^{-1}), multiplying this by the actual mass of that same substance Y (in g/m^3) and then dividing by the relative molecular mass (RMM) of the substance (i.e. 46 g for NO_2), 200 mg/Nm^3 is a NO_x mole fraction of 9.7E-05 or 97 ppm.

$$X = \frac{n^{-1} \times Y}{RMM} \qquad \textit{Equation 2.6}$$

In the European Union and the UK, the maximum permissible NO_x concentration for combustion plants depends on the technology used and the total rated thermal input to the combustor in MW. The NH_3 from a modest-sized steelworks (i.e. 10 tonnes/day) would amount to a net thermal input of 2.15 MW. The addition of support fuels and higher NH_3 flows in larger steelworks would naturally increase this figure. A medium combustion plant (MCP) is defined as having a range of rated thermal input equal to or greater than 1 MW and less than 50 MW [107], so the MCP regulations are applicable to the scale of combustion investigated in this study.

For plant in existence prior to December 2018, permitted NO_x emissions from MCP, using gas turbine technology to combust gaseous fuels other than natural gas, are 200 mg/Nm^3 (for over 70% load). For the same category of plant commencing operation after this date, the limit is significantly reduced to 75 mg/Nm^3 [107] . However, the scope of this legislation does not apply to many types of plant that could be considered

functionally similar to the type proposed in this thesis. Some examples of where the regulations do not apply are as follows:

- Post-combustion plants designed to purify the waste gases from industrial processes by combustion, and which are not operated as independent combustion plants.
- Reactors used in the chemical industry.
- Coke battery furnaces.
- Combustion plants firing refinery fuels alone or with other fuels for the production of energy within mineral oil and gas refineries.

The NO_x regulatory values are for dry samples rated against a standardised 15%$_{vol}$ O_2 concentration in the exhaust. However, concentrations of NO_x are experimentally measured with H_2O present in the sample, termed a wet sample (for reasons explained in later chapters). Once the concentration of NO_x is adjusted to account for the removal of the H_2O component, to give a dry concentration, the concentration naturally increases. This increase can be substantial, especially when H_2O concentrations are high (e.g. fuel-rich NH_3 combustion). The NO_x concentrations in the dry sample are normalised for 15%$_{vol}$ O_2 according to Equation 2.7 as taken from ISO 11042-1 (1996), for the measurement and evaluation of gas turbine exhaust gas emissions [108].

$$NO_{x(norm)} = NO_{x(dry)} \times \left(\frac{20.9 - 15}{20.9 - \%O_{2(dry)}} \right) \qquad \textit{Equation 2.7}$$

However, this standard is not applied universally. For example, 16%$_{vol}$ O_2 is used in Japan [109] and 6%$_{vol}$ is used in the NH_3 work of Khateeb et al. (2020) [110, 111]. Replacing the O_2 concentration of 15%$_{vol}$ with 16%$_{vol}$ (in the numerator of Equation 2.7), naturally lowers the normalised NO_x value. In addition, while many research papers report NO_x emissions as dry, many do not (or at least do not make the necessary statement concerning wet or dry sampling). This includes the contemporary NH_3 gas turbine research work from Japan, which constitutes a significant portion of relevant literature. The natural consequence of reporting wet, at 16%$_{vol}$ O_2 is to doubly lower the reported NO_x concentration value when compared with dry, 15%$_{vol}$ O_2, and without reporting the

H_2O product fraction, normalising to the same standard for direct comparison between research papers becomes impossible. Therefore, the reporting of NO_x should be standardised in the research, to allow for meaningful comparisons of NO_x performance to be made globally.

The NO_x standards could be considered to carry a bias in favour of hydrocarbon fuels, calling into question the validity of applying such a standard (dry, 15%$_{vol}$ O_2) to NH_3 combustion. If one further considers Equation 2.1 for the stoichiometric combustion of one mole of NH_3, comparing it with the stoichiometric combustion of CH_4, as shown in Equation 2.8, it is clear that the higher air demand of CH_4 coupled with the CO_2 product leads to many more moles of product gases for CH_4-air combustion (10.52) versus NH_3-air combustion (4.82).

$$CH_4 + 2(O_2 + 3.76\,N_2) \rightarrow 2H_2O + CO_2 + 7.52N_2 \quad \textit{Equation 2.8}$$

Once dehydrated (i.e. without H_2O product), the ratio of product gases per mole of fuel is 8.52 for CH_4 to 3.32 for NH_3 and it is in these moles of product gases that the NO_x concentrations are diluted and measured. With excess air, e.g. leading to 15%$_{vol}$ O_2 in the exhaust, this disparity between fuels would be far less, as the products in Equation 2.1 and Equation 2.8 would represent a minority of the exhaust flow, however, the disparity would still exist. Therefore, it seems unreasonable to compare emissions concentrations of NH_3 combustion using regulations designed for carbon containing fuels (with their higher air demands and the additional CO_2 diluent in the products), because it effectively holds the performance of NH_3 fuel to a higher standard than conventional gas turbine fuels.

However, there is a further consideration which warrants discussion. For equivalent energy flows into the turbine, the number of moles of NH_3 is 2.5 times that of CH_4 (see Section 2.1.3). Thus, moles of product gases per MW of power into the cycle are approximately equivalent (at 8.3 for NH_3). Hence, whether the emissions standards are designed primarily to maintain low concentrations of emissions in exhaust gases or low emissions per MW, is of importance. The standards do not consider system efficiencies (e.g. NO_x emissions per exported unit of power). As the standards are based solely on

exhaust concentrations, the primary purpose of the standard seems to be to control NO_x *concentrations* and not *mass of emissions per MW*. In any event, this standard is the only standard available, so will be used, but the validity of its use for NH_3 combustion is in question, for those reasons given above.

In consideration of all the above points, it is unclear how gas turbine technology fuelled by coke oven by-product NH_3, on a steelworks site, would or should be legislated for. With this in mind, it is believed that a value of 200 mg/Nm^3 (i.e. 97 ppm) is a reasonable NO_x limit to work to, for the purposes of this study.

2.3.2 NO_x and Equivalence Ratio

In Chapter 1, the diagram for the oxidation pathways of NH_3 (Figure 1.3) showed the selectivity for forming NO or N_2 is determined competitively, based on whether the amine radicals (i.e. NH_2, NH or N) react with the O/H radical pool (or O_2) to form NO, or with NO to form N_2 [46].

This paragraph summarises the work of Miller and Bowman (1989) [43], where they describe how Φ dictates which are the dominant chemical pathways in NH_3 oxidation. The amine radical primarily responsible for determining the relative NO/N_2 production/destruction depends on the Φ. For very lean flames, the critical amine radical is NH_2, but as Φ increases, the increase in H atoms shifts the critical species from NH_2 to NH and N. For most conditions, all three NH_i species have a role, although even in moderately rich flames, the N atom dominates. The production and destruction of NO by N atoms occurs via what is known as the extended Zel'dovich mechanism, the three reactions (Equations 2.9 to 2.11) that constitute the bottom layer of the NH_3 oxidation pathways diagram (as was shown in Figure 1.3).

$$N + NO \leftrightarrow N_2 + O \qquad \textit{Equation 2.9}$$

$$N + O_2 \leftrightarrow NO + O \qquad \textit{Equation 2.10}$$

$$N + OH \leftrightarrow NO + H \qquad \textit{Equation 2.11}$$

Concentrations of O/H radicals peak at Φ ~0.9, serving to explain why lean NH_3 flames have peak NO concentrations around this Φ [40, 89, 96, 102]. As the flame becomes

richer, and O/H radical concentrations decrease, the relative concentration of H in the O/H radical pool increases [40]. These H radicals abstract hydrogen from NH_i (i = 1, 2, 3) according to the reactions $NH_i + H \rightarrow NH_{(i-1)} + H_2$, leading to substantial H_2 production.

Typical emissions trends for premixed fuel-rich NH_3 combustion are shown in Figure 2.4, which is reproduced from the computational fluid dynamics (CFD) modelling of Somarathne et al. (2017) [106] for an NH_3-air flame with inlet temperature 500 K. The trends in Figure 2.4 show that, while NO emissions can be very effectively controlled under fuel-rich combustion conditions, there is a trade-off in the relationship between NO and NH_3 emissions, which has implications for overall NO_x concentrations in staged combustion. A paper by Miller and Bowman (1989) [43] claims most of the residual fixed nitrogen (i.e. NH_3 and HCN) leaving the first stage (the fuel-rich primary stage in which the majority of the fuel is consumed) is converted to NO in the second stage (where excess air is introduced for fuel burnout and cooling of products ahead of the turbine inlet).

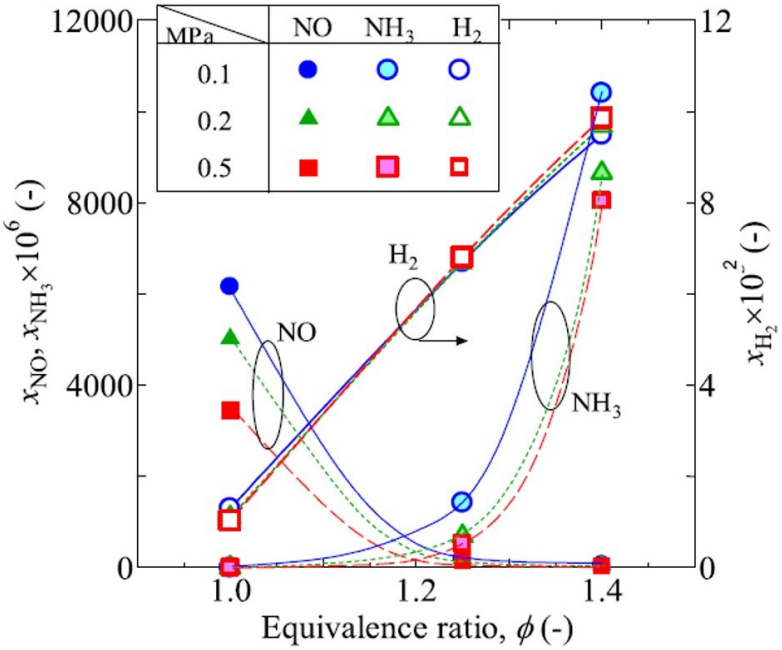

Figure 2.4 Emissions concentrations from premixed NH_3-air flames with changes in Φ and pressure (500 K inlet) reproduced from [106]

Work by Somarathne et al. [106] investigated this using CFD modelling and showed that unburned NH_3 exiting the primary combustion zone, was indeed predicted to pave the way for NO generation in the secondary combustion zone (from 162 to 891 ppm for

primary stage Φ (Φ_{prim}) of 1.2 and 1.4 respectively) and consequently recommended that the Φ_{prim} should simultaneously minimise for both NO and NH_3 emissions by adopting the point of lowest combined NO and NH_3 emissions, often referred to as the optimum or specific Φ (Φ_{opt} or Φ_{sp}).

Pugh et al. (2020) [103] experimentally investigated single-stage emissions performance for NH_3-air flames, in both premixed and diffusion configurations (1 atm, 473 K). The diffusion flame generated much lower combined NO/NH_3 emissions at $\Phi < 1.1$, but at $\Phi \geq 1.1$ the situation reversed with the premixed flame achieving lowest combined emissions overall, at $\Phi = 1.2$. At $\Phi = 1.2$, the low combustion efficiency of the diffusion flame lead to significant NH_3 emissions that, with subsequent air-staging to improve efficiency, generated NO three times greater than the premixed configuration. The NH_3 concentrations from the diffusion flame with highest secondary stage air mass loading also remained far higher at ~1000 ppm compared with practically zero for the premixed flame with the same loading. This work suggests that at sufficiently rich Φ_{prim}, the homogeneity of Φ in premixed flames offers superior combustion efficiency and thus lower combined emissions than diffusion flames, in NH_3-air staged configurations.

A numerical study by Okafor et al. (2021) [79] showed a decrease in Φ_{opt} at lower inlet temperatures. Naturally, the decrease in inlet temperature results in a decrease in the AFT and consequently, a decrease in the rate of production of O/H radicals. This lead Okafor et al. [79] to speculate that, as lower radicals concentrations simultaneously hinders NO production and NH_3 oxidation (for any given Φ), this will shift the Φ_{opt} towards leaner values for lower inlet temperatures. It is reasonable to assume other parameters affecting flame temperature (e.g. support fuel fraction and blend humidification) could also influence Φ_{opt} but as yet, there is no literature comprehensively addressing this issue with existing work tending to focus on NO_x concentrations, rather than combined emissions.

At the Φ_{opt} shown in Figure 2.4 (Φ ~1.2), there are significant H_2 concentrations of ~6%$_{vol}$. This highly reactive H_2 and other hot product gases exiting the primary stage, offer the possibility of a subsequent fuel-lean combustion stage, in which to fully combust the fuel and cool the products upstream of the turbine, without the need for

additional fuel in the second stage. Staged, rather than single stage combustion lowers peak temperatures, and thus thermal NO, by distributing some of the heat release from the fuel consumption into the second stage.

2.3.3 Pressure Elevation for NO_x Reduction

Figure 2.4 shows that pressure elevation is predicted to significantly lower NO concentrations (an approximate halving of emissions when moving from 0.1 to 0.5 MPa in the example). This trend of decreasing NO with increases in pressure (holding inlet temperature steady), has been numerically replicated [81, 93, 112, 113] and experimentally verified [81, 92, 93, 114] albeit not at gas turbine relevant pressures. Fuel flow restriction (discussed later) make ammonia investigations at elevated pressure challenging, so little pressurised work has been published to date. The presumed mechanism for the NO reduction is that the pressure sensitive reaction shown in Equation 2.12 is promoted to the right with increases in pressure. Being a chain terminating reaction this decreases the O/H radical pool, thus reducing NO production [40, 81].

$$H + OH + M \leftrightarrow H_2O + M \qquad \textit{Equation 2.12}$$

The primary consumption step for NH_3 (i.e. its conversion to amine radical NH_2) remains essentially unaltered as pressure increases, despite the pressure induced depletion of the O/H radical pool [40]. Therefore, the relative increase in NH_3 concentrations at richer Φ and a dearth of O/H radicals, leads to a significant increase in NH_2 in the post-flame zone. Owing to the low reactivity of NH_2 towards O_2, the key step in the presence of even small amounts of NO is the fast chain terminating reaction $NH_2 + NO \leftrightarrow H_2O + N_2$ [46]. The chain carrying reaction $NH_2 + NO \leftrightarrow NNH + OH$ also serves to reduce NO [93]. Naturally, pressure induced reduction of absolute NO_x concentrations is most significant at fuel-rich Φ values closer to stoichiometry, as the more fuel-rich flames have far lower NO to begin with.

Xiao et al. (2017) [112] modelled NO_x emissions for changing pressure (1 to 22 atm) with varying inlet temperatures (300 – 700 K) for a NH_3/CH_4 ($39\%_{vol}$ CH_4) blend at a fixed Φ = 1.14, as shown in Figure 2.5. Increases in inlet temperature (and hence O/H radical pool)

are thus shown not only to enhance NO_x production, but also to lessen the beneficial impact of pressure elevation on NO_x reduction. Therefore, while temperature elevation can aid blend reactivity, it should be moderated to only what is necessary to achieve stable flames.

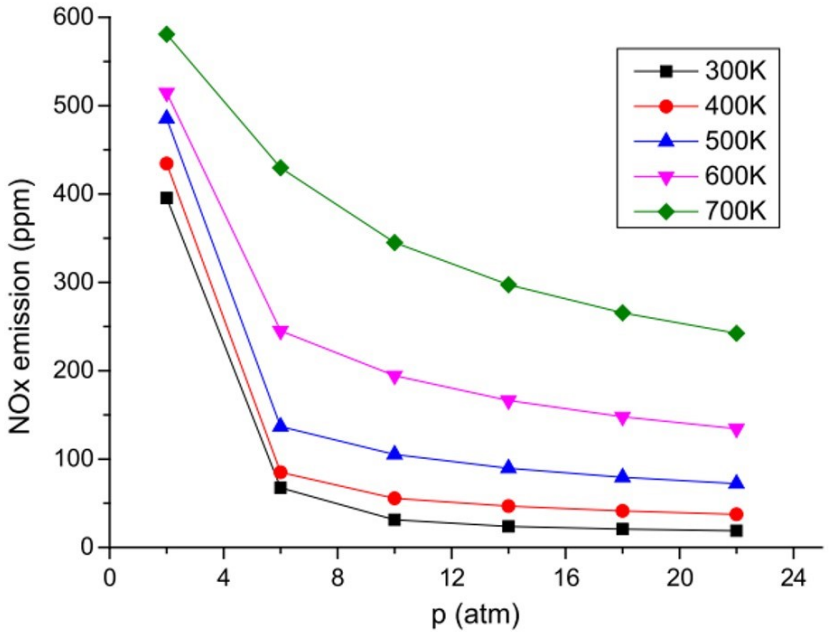

Figure 2.5 Numerically modelled NO_x emissions for changing pressure at varying inlet temperature, NH_3/CH_4 blend reproduced from [112].

2.3.4 Effects on NO_x of Utilising Support Fuels

Wendt and Sternling (1974) [115] showed that CH_4/NH_3-air premixed blends with minority molar volumes of NH_3, although having lower NO_x emissions overall, have higher rates of conversion to NO_x relative to NH_3 blend contribution. For example, at Φ = 1.0, for blends of 1%$_{vol}$ NH_3, approximately 90% of the NH_3 was converted to NO, while for 24%$_{vol}$ NH_3 blends, 30% was converted. These results are shown in Figure 2.6. The reader should also note the rapid decrease in NO_x with increasingly sub-stoichiometric percentages of air (Φ > 1.0). As a result of these findings, the paper recommends that NH_3 should not be diluted with other fuel gases (that reduce its self-inhibitory effect on NO_x) and that a fuel-rich primary stage, followed by a second stage for the addition of the remaining air, is an effective NO_x control measure. This trend of more NO_x with greater fuel support has also been observed in other similar studies [78, 95, 110, 113]. For example, Khateeb et al. (2020) [110] experimentally investigated NH_3/CH_4 blends

ranging from 0 to 100%$_{vol}$ NH_3 (S_g = 1, ambient pressure and temperature), showing that for NH_3 > 60%$_{vol}$ and Φ ≥ 0.85 the exhaust NO concentration consistently decreases with increased ammonia addition (see Figure 2.7).

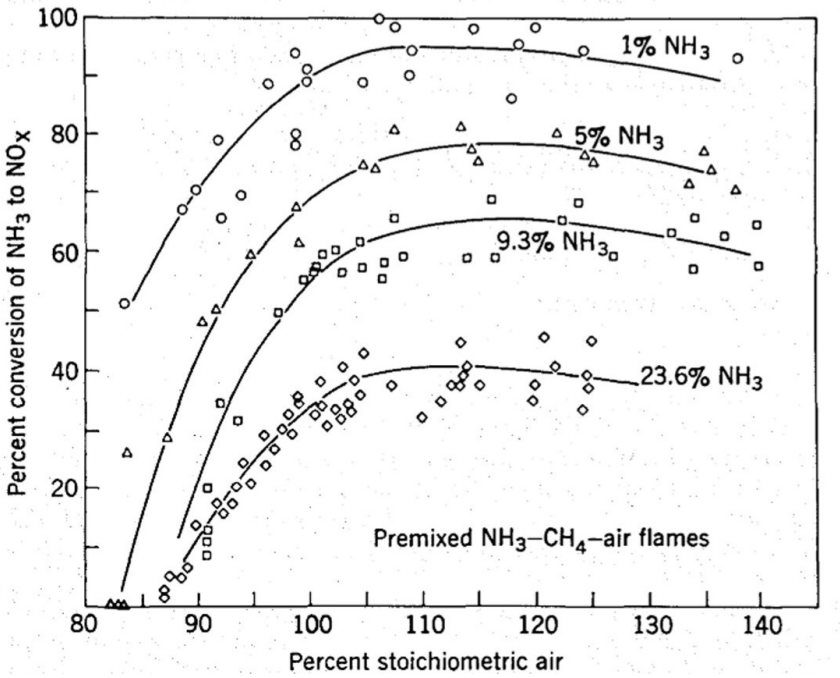

Figure 2.6 Percentage conversion to NO_x by percentage of stoichiometric air reproduced from [115]

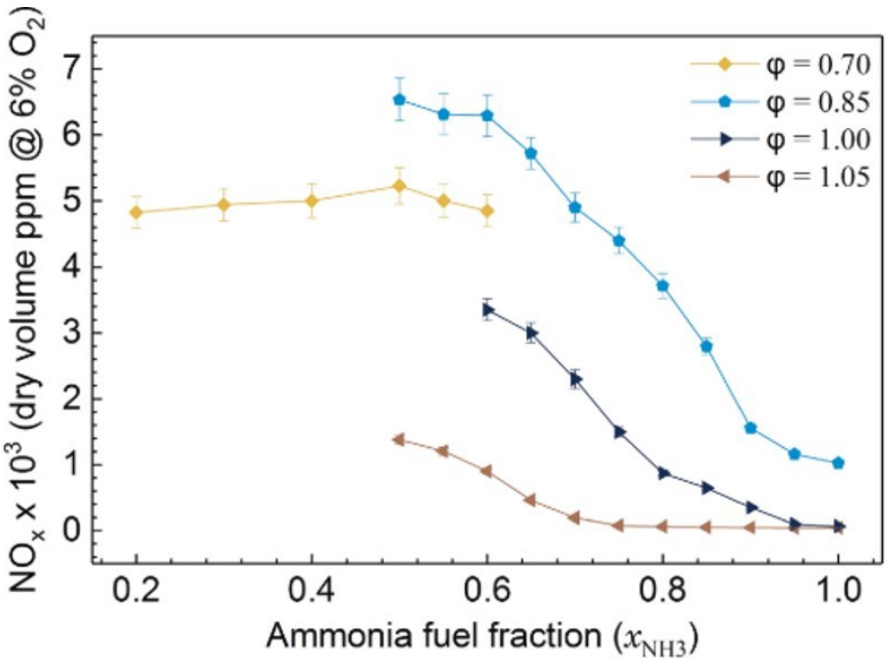

Figure 2.7 NO_x emissions of NH_3/CH_4 fuel blends at Φ 0.7 to 1.05 (1 atm, 293K) reproduced from [110]

For Φ ≥ 0.85, instabilities prevented stable combustion of blends with < 50%$_{vol}$ NH_3. For Φ = 0.7, NO_x concentrations increased slightly between NH_3 of 20 to 50%$_{vol}$ and blow-off (i.e. flame detachment) prevented stable combustion for NH_3 > 60%$_{vol}$. Khateeb et al. (2020) [111] also investigated NH_3/H_2 blends with the same methodology and found, across fuel-rich Φ values, the same trend of lowest NO_x concentrations for pure NH_3. The explanation offered is that the lower AFT of NH_3 leads to lower flame temperatures and, hence, reduced O/H radicals at any given Φ, so the more NH_3 in the fuel blend, the less fuel NO_x is generated [110]. However, neither study [110, 111] quantified the NH_3 emissions entering the burnout stage, which are likely to be higher for pure NH_3 with its lower reactivity, especially at ambient inlet temperature. As was discussed in Section 2.3.2, this can raise overall NO_x in staged configurations. From the two papers [110, 111] it appears that the 80%$_{vol}$ NH_3 blends (with either CH_4 or H_2) achieved similar NO_x results to that of pure NH_3 where Φ > 1.1, suggesting rich combustion can successfully mitigate for NO_x emissions when using fuel support (H_2 or CH_4), to enhance reactivity.

2.3.5 Effects of Steam Addition on NO_x

Lower flame temperatures result in fewer O/H radicals and hence less fuel and thermal NO_x production such that thermal NO formation is usually considered to be unimportant at temperatures below 1800 K [116]. Steam injection can be used to lower flame temperatures, so has been investigated for NH_3/H_2-air and NH_3-air flames [93, 103]. Steam also serves to lower the availability of O radicals via the reaction described in Equation 2.13 [116] thereby reducing the contribution to thermal NO_x formation of the rate-limiting reaction in the Zel'dovich mechanism (see Equation 1.4).

$$O + H_2O \leftrightarrow OH + OH \qquad \textit{Equation 2.13}$$

Pugh et al. (2020) [103] found that, for NH_3-air flames (1 atm, 473 K), H_2O loading was limited to 3%$_{vol}$, due to diminished reactivity and, although a reduction in NO with H_2O increase was observed (for a premixed flame), there was also an increase in exhaust NH_3, which could lead to prohibitive NO production in the burnout stage of a staged combustor. However, Pugh et al. (2019) [93] showed humidification to be an effective mechanism for NO_x reduction in premixed NH_3/H_2-air flames (a 70%$_{vol}$ NH_3 to 30%$_{vol}$ H_2

fuel blend). The NO_x concentrations reduced by an order of magnitude for reactant loadings of ~10%$_{vol}$ H_2O (1 atm, 423 K inlet). With modest humidification and pressure elevation combined (3.5%$_{vol}$ and 0.184 MPa) the same work [93] demonstrated an optimal performance point at a global Φ of 0.98 (Φ_{prim} = 1.25), achieving NO_x and NH_3 concentrations of 32 and ~50 ppm (dry, 15%$_{vol}$ O_2) respectively. A global Φ of 0.98 is significantly higher than is need for cooling combustion products upstream of turbine blades, so the effects on emissions of a more industrially relevant global Φ would be of interest.

2.3.6 Mitigating for N_2O

For NH_3 with or without H_2 support, the mechanism for N_2O formation via NH_3 oxidation is via the NH + NO reaction, where N_2O quickly progresses to N_2 for fuel-rich conditions (i.e. due to the presence of a H radical).

For NH_3 oxidation with hydrocarbon support (e.g. natural gas), there is an additional route for N_2O formation, via the oxidation of hydrogen cyanide (HCN). HCN can form during the oxidation of NH_3/CH_4 blends via the fuel-N route. Additionally, when CH_n radicals attack the triple bond of atmospheric N_2, the NCN radical is formed (and a H radical) and at conditions richer than Φ ~1.2 the NCN radical reacts with H radicals to form HCN (and a N radical) with the concentration of HCN increasing rapidly with increases in Φ [46]. Once formed in the fuel-rich primary zone, HCN can then progress (along with H_2 and NH_3), to a fuel-lean burnout stage. Being a highly toxic gas (one minute exposure ~300 ppm is lethal [117]) efficient combustion in the second stage is imperative.

HCN has a greater capacity for nitrogen oxides (NO, NO_2 and N_2O) production in the burnout stage than NH_3 as it is less prone to decomposition in the primary stage [118]. Under lean conditions, HCN yields nitrogen oxides via a complex reaction scheme [117]. A main decomposition path of HCN in the burnout stage yields NH which, in the presence of NO, leads to N_2O production. However, at temperatures above 1300 K N_2O decomposes rapidly to N_2 [119].

In summary, N_2O can be mitigated for by minimising the fuel hydrocarbon component and by maintaining temperatures above 1300 K in the burnout stage (facilitating N_2O decomposition).

2.3.7 NO_x Mitigation Summary

- NO_x emissions, as reported in the literature, are not comparable, as there is a lack of consistency in measurement method (i.e. $\%_{vol}$ O_2 and wet versus dry concentrations). Carbon-free fuels may require different measurement regulations for fair comparison with hydrocarbon fuels (i.e. due to lower air requirements, higher relative H_2O product mole fraction and the absence of CO_2 diluent for carbon-free fuels).
- Premixed flames have a higher combustion efficiency than diffusion flames. Although a diffusion flame can produce lower combined NO_x and NH_3 emissions than a premixed flame at $\Phi \sim 1.1$, premixed flames offer much lower combined emissions of NO_x and NH_3 overall at richer Φ (~1.2), as described in Section 2.3.2.
- NO_x emissions can easily be minimised with a sufficiently fuel-rich Φ in a primary stage, but with fuel-rich combustion comes the risk of significant NH_3 emissions (and HCN for hydrocarbon addition). Hence simultaneous reporting of the NO and unburned fuel emissions, especially after industrially relevant levels of air-staging, is required for proper evaluation of any such system.
- Blends with $NH_3 > 60\%_{vol}$ have greater stability for fuel-rich Φ values and lower NO_x than NH_3 minority fuels, with pure NH_3 having lowest NO_x, but lowest reactivity.
- Pressure elevation reduces NO_x for any given Φ by reducing the O/H radical pool.
- Inlet temperature elevation aids reactivity (reducing unburned fuel), but reduces the effectiveness of pressure elevation on NO_x emissions.
- Water addition is an effective way to lower NO_x for any given Φ, but reactivity and unburned emissions can limit this as a strategy.
- N_2O production is insignificant for the fuel-rich high temperature primary stage. For lean burnout, N_2O is minimised by limiting hydrocarbon support (i.e. the HCN $\rightarrow$ N_2O path) and maintaining temperatures > 1300K.

2.4 Steelworks NH_3 Removal, Processing and Composition

2.4.1 Steelworks By-Product NH_3 Removal

As was discussed in Section 1.3.3, configurations for COG cleansing are wide-ranging and bespoke to the site and while all coking facilities have the potential to recover by-product NH_3 for use as fuel, many COG cleansing configurations preclude this activity. This section gives a simplified overview of a steelworks COG cleansing process [58, 62] that would result in a concentrated aqueous NH_3 waste stream with minimised H_2S, which, like recovery of anhydrous NH_3 via the Phosam process, makes possible the subsequent use of by-product NH_3 as a fuel. For more detail on this and other gas purification technologies involving NH_3, including the Phosam process, see Kohl and Nielsen (1997) [58].

The moisture and volatiles, from the coking of the coal, first enters a collection main, above the coke oven. A large volume of 'flushing liquor' (described shortly) is sprayed into the collection main, quenching the raw COG to about 75 to 100°C. The raw COG moisture fraction condenses and most of the tar, plus the 'fixed' NH_3 are washed (i.e. flushed) from the COG. 'Fixed' NH_3 (as opposed to 'free' NH_3), refers to the ammonium salts, which typically represent about 30% of the NH_3 originally present in the gas. The flushing liquor then proceeds to a tar decanting facility, before its return to the collection main as the flushing liquor. Thus, the flushing liquor is primarily a weak aqueous NH_3 solution containing some tar. To maintain low concentrations of NH_3 in the flushing liquor and to account for the continued addition of more coal moisture, a portion of the flushing liquor is continuously withdrawn from the cycle.

The COG is further cooled to a temperature of 28 to 30°C in the primary cooler (e.g. using water cooled heat exchangers) and then passes through an electrostatic precipitator to remove fine droplets of tar. After the precipitator, modest compression of the COG occurs (from atmospheric to about 1.15 atm) upstream of the by-product NH_3 removal process.

The absorption of NH_3 into H_2O is quite rapid. The rate of absorption of H_2S into aqueous NH_3 is dependent upon the NH_3 concentration, increasing significantly at higher NH_3 concentrations [58]. This fact accounts for the availability of integrated NH_3/H_2S removal

processes. However, this integrated approach of using NH_3 solutions to remove H_2S from COG is more common in Europe than elsewhere [120]. Therefore, stand-alone NH_3 removal is described here as it has the simpler process flows and demonstrates all the necessary steps relevant to NH_3 removal.

As shown in Figure 2.8, the COG enters a secondary cooler at the base of the NH_3 absorber (i.e. the first tower). The cooler cools and recycles a portion of the absorber's rich solution over the bottom section, to remove the heat gains from the earlier gas compression and to introduce a high liquid flow rate as the COG enters.

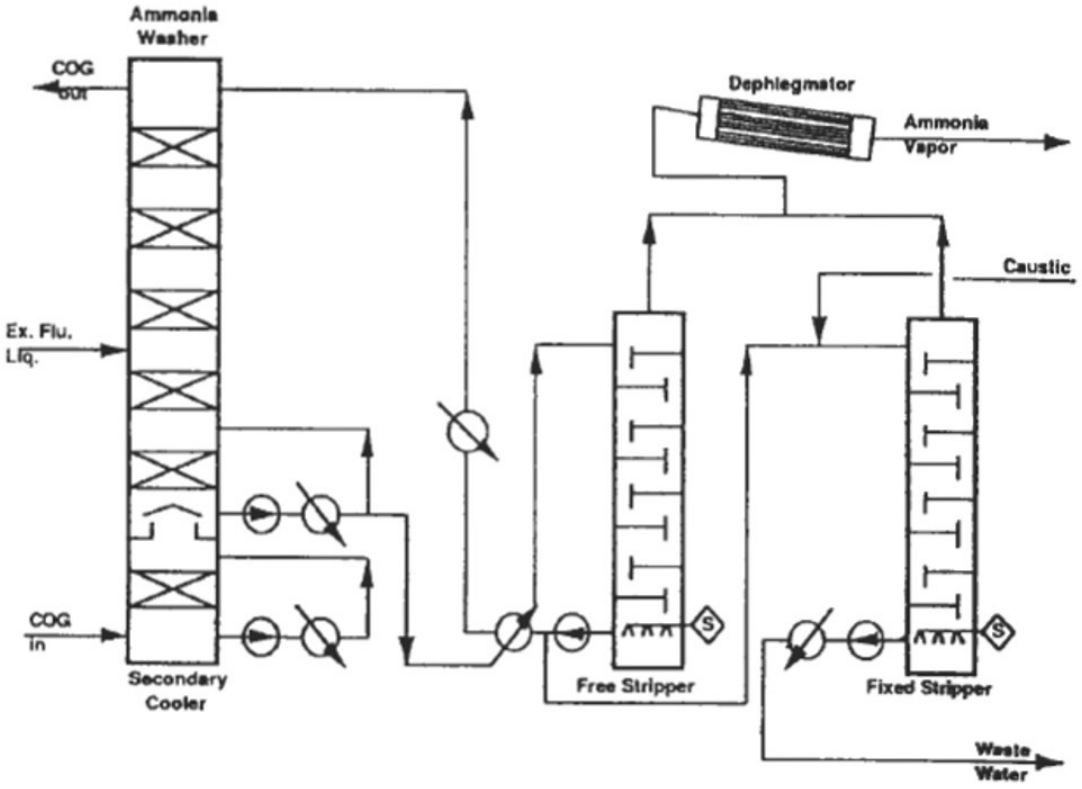

Figure 2.8 Process flow diagram for stand-alone NH_3 removal from COG (reproduced from [62])

On its journey to the top of the absorber, COG first contacts counter-current flows of the withdrawn excess flushing liquor previously mentioned, followed by water stripped of free NH_3, reducing the NH_3 in COG by ~99% [62].

Heat exchange from the waters leaving the base of the free NH_3 stripper, together with steam injection, heats the rich absorber solution as it enters the top of the free NH_3 stripper. This rich solution contains all the removed NH_3 (including entrained fixed NH_3),

plus amounts of co-absorbed H_2S, HCN and CO_2 [62]. NH_3 and some of the co-absorbed vapours leave the top of the free NH_3 stripper and the excess portion of the stripped water not sent to the absorber, and still containing the fixed NH_3, is sent to the fixed NH_3 stripper.

A caustic solution (e.g. sodium hydroxide) raises the pH in the fixed NH_3 stripper to ~10.5, liberating the NH_3, and more steam is used to strip the NH_3 to join the overhead vapours from the free NH_3 stripper [62]. The stripped water leaving the base of the fixed NH_3 stripper is further treated (if necessary).

2.4.2 Steelworks By-Product NH_3 Processing and Composition

The overhead vapours are partially condensed (in the dephlegmator) to reduce the H_2O component. Upstream processing and the degree of condensing (e.g. operating temperature and pressure) affects the composition. Concentrated NH_3 vapour compositions as found in the literature and sourced confidentially are given in Table 2.5 [62, 65].

Table 2.5 Typical compositions for concentrated by-product NH_3 vapour [62, 65].

Component	Compositions ($\%_{vol}$)		
	Ref [62]	Ref [65]	Confidential source (normalised without Phenol)
Ammonia (NH_3)	38.7	26	31.6 (32)
Carbon dioxide (CO_2)	2.5	1	1.7 (1.7)
Hydrogen sulphide (H_2S)	1.7	3.8	0.4 (0.4)
Hydrogen cyanide (HCN)	1.4	5.1	0.3 (0.3)
Water (H_2O)	55.9	64	65 (65.6)
Phenol (C_6H_6O)	-	-	1 (0)
Total	100.2	99.9	100 (100)

Phenol is recoverable in a separate extraction step [58]. It is a valuable by-product, maintaining a spot price of over €1000 per tonne in Europe (from August 2018 to August 2019) [121], and is assumed not to be a typical component of the NH_3 vapour (being absent from two of the three compositions referenced). Also, in the composition where

phenol is present, it represents just 1%$_{vol}$ of the composition (5% by mass). Therefore, in deriving a typical vapour for this investigation, the composition containing phenol is normalised without phenol content, as shown in parentheses.

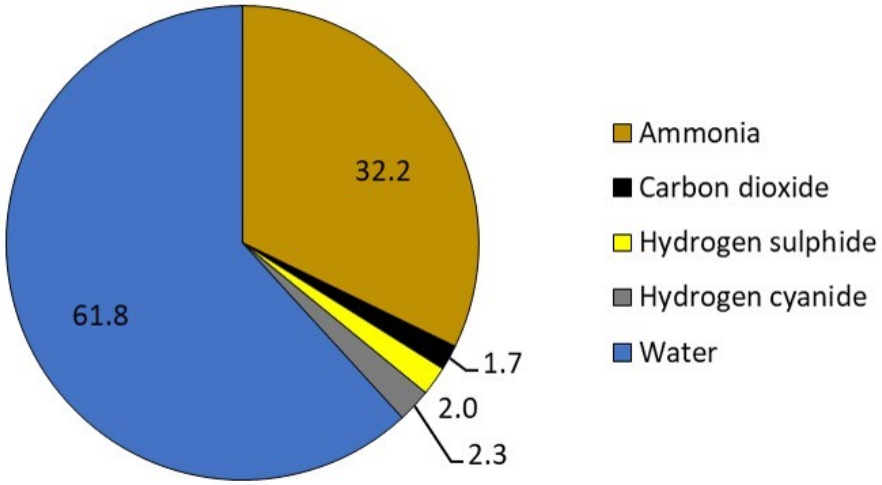

Figure 2.9 Typical ammonia vapour composition as derived from the literature (%$_{vol}$) [62, 65]

The values in Table 2.5 are averaged to give the composition used in this study. Thus, Figure 2.9 shows that NH_3 represents approximately one third of the composition of the representative vapour, with water accounting for ~60%$_{vol}$ and the remaining 6%$_{vol}$ consisting of acid gases. A spreadsheet tool, discussed later in Section 4.3, was used to calculate the heating value of the waste stream composition in Figure 2.9. Higher and lower heating values were calculated as 8.0 and 6.8 MJ/kg (on a mass basis) and 6.1 and 5.2 MJ/Nm^3 (on a volumetric basis) respectively.

The European Union's Industrial Emissions Directive 2010/75/EU, best available techniques reference document for iron and steel [56], provides the only stated value for the mass of NH_3 per tonne of coke available in the literature, i.e. 3 kg. This value appears to have been derived from a table of related data which compounds six reference sources, so as to encompass the full range of values given by all the original sources. For example, the raw COG yields range from 280 to 450 m^3 per tonne of dry coal with NH_3 concentrations of 6 to 8 g/Nm^3. As the NH_3 per tonne of coke is in mass terms, the density of the COG is also stated as ranging from 0.42 to 0.65 kg/Nm^3 across all sources. The mass value of 3 kg appears to have been calculated with the assumption

that typical values would be those in the middle of the compounded data ranges. Using the data from the table and mid-range values generates a value of 3.41 kg NH_3 per tonne of coke, so the 3 kg figure is probably a rounding-down of this value. Given the importance of the value for this study, further research was undertaken. A representative of Worldsteel, a global organisation whose members represent around 85% of global steel production, agreed to circulate a bespoke survey to their members working in steelworks' by-product plants [122]. Unfortunately, only two responses were forthcoming and these failed to provide usable responses (e.g. 'zero NH_3' and 'quantification not readily available'). Hence, direct contact was made with a steelworks producing ammonium sulphate fertiliser. Historical records for annual coke production, along with annual fertiliser sales figures and the mass of NH_3 per unit mass of ammonium sulphate (25.8%$_{mass}$), gave the value 4.04 kg NH_3/tonne coke. Additionally, an online source [61] gives a value of approximately 12 tonnes per day, per million tonnes of coke per year, which equates to 4.4 kg NH_3/tonne coke. Therefore, it appears 4 kg NH_3/tonne coke may be a better estimate, a 33% increase on the reference document value. Thus, global NH_3 liberated annually from coal coking for steel manufacture is probably > 2.5 Mt p.a. (i.e. rather than >1.9 Mt p.a., see Section 1.3.2).

Updating earlier figures from Section 1.3.2, 10 tonnes/day of NH_3 by-product would likely be produced by an integrated crude steel plant of ~2 Mt p.a. of crude steel, down from ~2.7 Mt p.a.. For a UK context, the Port Talbot steelworks in Wales running at full capacity is more than twice this size (~5 Mt p.a.) [123].

As previously discussed, by-product NH_3 from a modest-sized steelworks could provide >2 MW_{th} before combustion support fuels are added (see Section 2.3.1). Gas turbines in the range of 2 to 5 MW_e have typical compression ratios of 7 to 14 respectively [124]. Therefore, a gas turbine relevant to this type of application on a typical steelworks site could be assumed to have a typical operating pressure of ~10 atm.

2.5 Steelworks Process Gases

Several gases are available on a steelworks sites that could potentially serve to support NH_3 combustion. These include indigenous process gases coming from coke ovens

(COG), blast furnaces (BF gas) and from basic oxygen furnaces (BOF gas). As previously mentioned imported natural gas (essentially composed of CH_4 [76]) provides ~3% of the energy needs of an integrated BF-BOF site, so is also available [17].

BF gas is the most abundant of the process gases [125]. A typical molar composition of BF gas is 50% - 55% N_2, 20 - 28% CO, 17 - 25% CO_2 with a balance of 1 - 5% H_2, affording it a heating value of 2.7 – 4.0 MJ/Nm^3 [56]. This is an even lower heating value than by-product NH_3 vapour. It is the most variable and the least calorific process gas and consequently the most unstable to burn, often requiring the addition of supplementary fuel [125]. Hence, it is dismissed as a candidate support fuel.

Hot crude steel is reacted with oxygen to remove a range of impurities from the metal. Carbon, the main impurity, reacts with oxygen to form CO and CO_2, which are collected from above the reacting vessel as the major constituents of BOF gas. This is a batch process with product gas composition varying considerably across the duration of processing. There exist two main approaches for handling the gas, partial/full combustion in the flue duct immediately after the furnace, or alternatively, supressed combustion, to allow for combustion elsewhere. Therefore, it is not possible to generalise about the availability of non-combusted BOF gas in a steelworks except to say that there is a tendency towards suppression as a practice [56]. In the case of suppressed combustion, a large holding tank is utilised to control gas quality for local use. Downstream of the gas holder a typical molar composition of the BOF gas is 72.5% CO, 16.2% CO_2, 8% N_2/argon and 3.3% H_2 with a heating value of ~9.5 MJ/Nm^3 [126]. Although an improvement on BF gas, this is still much lower than the lower heating value of anhydrous NH_3, as stated in Table 2.2 (i.e. ~13.6 MJ/m^3 at 288 K and 1 atm). Also, neither H_2 nor CH_4, which have been shown to promote reactivity, are present in significant amounts. This is in stark contrast with COG, whose composition (~60%$_{vol}$ H_2 and ~25%$_{vol}$ CH_4) and heating value (17 and 20 MJ/Nm^3) were briefly introduced in Section 1.3.2.

2.5.1 Deriving a Typical Composition for COG

COG, as a potential support fuel for by-product NH_3 combustion, has three main strengths. Firstly, even in the case of a steel plant importing some of its coke [64], levels

of COG production can exceed its on-site utilisation, resulting in flaring (for safety) [16, 64, 125]. Secondly, as NH_3 vapour is a by-product of the coking process, COG is guaranteed to be locally available to support by-product NH_3 combustion, even at stand-alone coking sites exporting to steelworks elsewhere. Lastly, the aforementioned high proportions of H_2 and CH_4 components in its composition, which have been shown to support NH_3 combustion as discussed in Sections 2.2.2 and 2.3.4.

Table 2.6 shows typical COG compositions as sourced from the literature. The COG composition for the first case is given with value ranges for four of its components. Interestingly, the range of possible H_2 values for this composition does not include the actual values found for the other two cases, suggesting that the first composition represents values typical of a certain region (i.e. reflecting regional coal composition or processing norms for that region).

Table 2.6 Typical COG compositions (volumetric basis) [57, 65, 125].

Component	Compositions ($\%_{vol}$)		
	Ref [57]	Ref [65]	Ref [125]
Hydrogen (H_2)	55-60	61	62.12
Methane (CH_4)	23-27	24	22.94
Carbon dioxide (CO_2)	<2	2.1	1.63
Carbon monoxide (CO)	5-8	7.5	6.67
Nitrogen (N_2)	3-6	3.2	3.95
Oxygen (O_2)	-	-	0.49
Ethane (C_2H_6)	No specified value	2.2 in total	0.5
Ethene (C_2H_4)			1.7

Mid-range values for the first composition are 57.5%$_{vol}$ H_2, 25%$_{vol}$ CH_4, 6.5%$_{vol}$ CO and 4.5%$_{vol}$ N_2. To formulate a typical COG composition, these four mid-range values and the equivalent values of the other two cases are averaged. The first case CO_2 value is ambiguous, i.e. <2%$_{vol}$, so the value of CO_2 will be calculated as the average of the other two cases, i.e. 1.9%$_{vol}$ CO_2, which also satisfies the requirement of being <2%$_{vol}$. While the reference source of the first case alludes to the presence of small hydrocarbons, no

specified value is given. The ethene/ethane components of the other two cases both total 2.2%$_{vol}$, so the individual ethene/ethane values of the third case are ascribed to all cases. As a consequence of all the above modifications, the components of the first case sum to 97.6%, so the individual component values are normalised to 100%.

Oxygen is only stated as present (in very small amounts) for the third case. Given that the first case consists of ranges (and therefore more than one case) and that oxygen is also absent from the second case, the presence of oxygen in the third case will be considered atypical or insignificant. Therefore, all other components in the third case have been normalised without oxygen.

Averaging the three (normalised) cases, the representative COG composition used in this study is shown in Figure 2.10. The composition of the representative COG can be summarised as ~60%$_{vol}$ H_2, approximately one quarter small hydrocarbons (C_{1-2}), 7%$_{vol}$ CO and ~6%$_{vol}$ inert gases. The spreadsheet tool, discussed later in Section 4.3, was again used to calculate heating values. Higher and lower heating values for the representative COG were calculated as 45.8 and 40.6 MJ/kg (mass basis) and 19.7 and 17.4 MJ/Nm^3 (volumetric basis) respectively, so within expected values [56, 57] and significantly higher than for NH_3 (i.e. LHVs of 18.6 MJ/kg and 13.6 MJ/Nm^3).

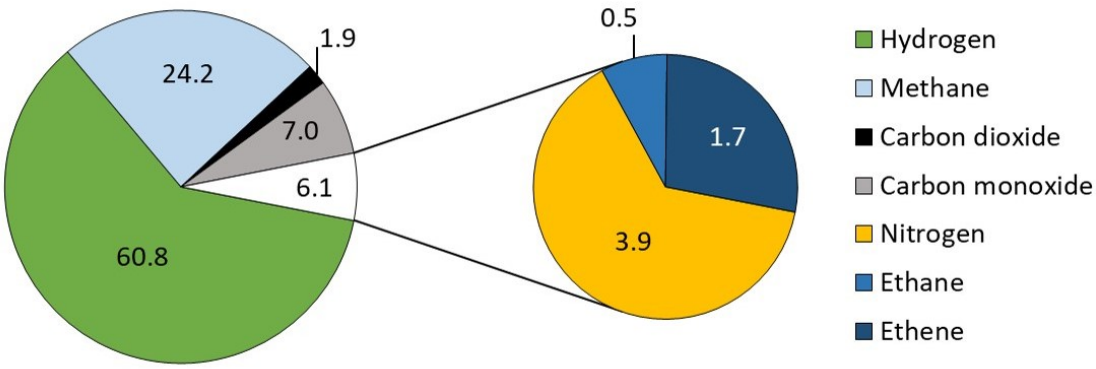

Figure 2.10 Representative COG composition as derived from the literature [57, 65, 125]

Given COG's general availability and superior combustion characteristics, when compared to other process fuels available on a steelwork's site, it is chosen as the indigenous support fuel for further investigation. Methane, as a surrogate for natural

gas (imported to steelworks) and as a demonstrated support fuel from the literature, will also be investigated.

2.5.2 Process Gases for NH_3 Combustion Support in Other Industries

Although this study is focussed on steelworks by-product NH_3, it is important to observe that other industries also identified as having substantial NH_3 waste streams (e.g. biomass gasification, sewage and farming), have renewably derived process gases available with similar characteristics to those of COG and natural gas. These renewably derived process gases could potentially act as support fuels for the recovered NH_3 combustion in these other more sustainable industries. For example, biomass gasification produces a process gas (i.e. syngas) primarily consisting of a CO/H_2 blend and bio-methane can also be sustainably produced from organic wastes. Hence, this study can offer insights for the use of renewably produced by-product NH_3 combustion supported by renewably generated process gases extending its potential reach beyond the use of industrial waste stream NH_3 from BF-BOF steelmaking.

2.5.3 Carbon Monoxide Emissions Considerations

As both chosen support fuels (and industrial process gases more generally) contain carbonaceous components (including CO in the case of COG), the potential for toxic CO emissions exists and requires consideration (i.e. regulatory and safety implications).

Gas-fired combustion plants over $50MW_{th}$, including biomass plants, are limited to 100 mg/Nm^3 (i.e. 80 ppm) of CO [127]. However, combustion plants firing COG or low calorific gases from gasification of refinery residues are exempt from these CO limits [127]. For a perspective relating to regular outdoor exposure levels from combustion sources, the UK's Driver and Vehicle Standard's Authority, set the CO emissions limits on car exhausts at $0.3\%_{vol}$ (i.e. 3,000 ppm) under normal idle conditions [128]. For an industrial health and safety perspective, the 8 hours workplace exposure limit for CO is 30 ppm [70]. Unlike NO_x emissions, CO is not reported in relation to a $\%_{vol}O_2$ and may be released to the atmosphere as wet or dry.

The relative molecular mass of CO is 28, so approximately the same as air (~29). Thus, with adequate dispersal using a stack and for low powered, remote experimental

facilities where emissions exposure is monitored through the use of personal monitors, a CO limit of 10,000 ppm seems reasonable for experimental investigations. Naturally, high CO emissions levels only apply to fuel-rich single stage investigations as CO emissions would be expected to be virtually absent in staged combustion work utilising an efficient secondary burnout stage.

2.5.4 By-Product NH_3 and COG Co-Combustion

Until now, the discussion has focussed on removing NH_3 from COG, to minimise NO_x formation during the combustion of COG. However, there are instances in the literature where cleansed COG has been subsequently reintroduced to by-product NH_3. Figure 2.9 indicated that ~2%$_{vol}$ of by-product NH_3 vapour is H_2S. Several important H_2S oxidation and reduction reactions are shown in Equations 2.14 to 2.17 [62]. Hydrogen sulphide reacting with O_2 forms sulphur dioxide (SO_2) as shown in Equation 2.14. The SO_2 combines with H_2S to form elemental sulphur (S_2) that plugs pipework.

$$H_2S + 1.5O_2 \leftrightarrow SO_2 + 1.5H_2O \qquad \textit{Equation 2.14}$$

$$2H_2S + SO_2 \leftrightarrow 1.5S_2 + 2H_2O \qquad \textit{Equation 2.15}$$

$$SO_2 + 3H_2 \leftrightarrow H_2S + 2H_2O \qquad \textit{Equation 2.16}$$

$$S_2 + 2H_2 \leftrightarrow 2H_2S \qquad \textit{Equation 2.17}$$

COG's high H_2 content makes it useful in by-product NH_3 catalytic destruction, not for its high reactivity or energy content, but because the presence of H_2 both prevents and reverses the formation of elemental sulphur by moving the reactions described by Equations 2.16 and 2.17 completely to the right [62].

In consuming H_2S in a lean second stage, as would be the case for rich-lean staged combustion in a gas turbine, SO_2 formation is inevitable. According to Equations 2.14 to 2.17, the high availability of O_2, H_2O and H_2 at the commencement of a second combustion stage minimises the risk of downstream plugging due to S_2 formation.

COG was also investigated by Teng (1996) as a potential support fuel in the aforementioned Chinese NH_3 ovens (see Section 1.3.3), for the lowering of NO_x [65]. For NH_3 vapour flows of ~2000 Nm^3/h, COG addition of up to ~200 Nm^3/h (i.e. ~10%$_{vol}$)

lowered exhaust concentrations of NO_x by >80%. Teng (1996) attributed this lowering of NO_x to the H_2 and CO in COG promoting several reactions that increase H radical formation and consume OH and O radicals. As COG was increased above 220 Nm^3/h, NO_x began to increase. This was attributed to an increase in operating temperature >1290 °C (1563 K) promoting the formation of O and OH radicals and also decreasing reaction rates for NO consumption (e.g. via amine radicals).

2.6 Equilibrium and Kinetic Modelling of NH_3 Oxidation

Equilibrium modelling calculates product concentrations of species as though reactions take place over infinite time, i.e. zero-dimensional (0-D) [75]. At chemical equilibrium, the rates of formation and destruction become equivalent (a dynamic equilibrium) and therefore species concentrations are unchanging. Chemical equilibrium is usually described by either of two equivalent formulations, equilibrium constants or minimisation of free energy [129]. Equilibrium constants can be used to find equilibrium compositions for simple systems, but this method is not suited to use in complex systems (e.g. combustion). In the late 1960s, researchers at NASA developed a general Gibbs minimisation approach for finding the equilibrium composition of complex systems. The algorithm they developed is so successful that it has been adopted as the basis for most equilibrium codes developed since, including those used in this study.

However, as was described in Section 2.3, NO_x product concentrations from fuel-bound nitrogen are primarily influenced by chemical kinetics (e.g. reaction rate) and not equilibrium [115]. Therefore, NO_x concentrations in NH_3 combustion often reach far higher levels than at equilibrium and can vary greatly depending on parameters such as flame configuration (diffusion versus premixed) or single stage versus multi-staged combustion, despite equivalent global Φ and residence time [103, 115].

As NH_3 combustion in gas turbines is a recent proposition, it is only in recent years that research has begun to evaluate the performance of existing combustion reaction mechanisms relevant to NH_3 combustion, in the high temperature, high pressure environments typical of gas turbines. As both the potential support fuels contain small hydrocarbons, many of the existing NH_3 reaction mechanisms are unsuitable for use in this study because they do not provide for carbon chemistry.

In finding mechanisms suitable for NH_3/CH_4 modelling, Xiao et al. (2017) [112] numerically investigated five chemical mechanisms for their ability to accurately predict the reaction kinetics (ignition delay) and emissions concentrations when compared with experimental results under gas turbine relevant combustor conditions. Being the most reliable mechanism for predicting NO_x emissions for fuel-rich Φ values of 1.03 to 1.26 and joint best for ignition delay predictions, the mechanism developed by Tian et al. (2009) [130] (henceforth referred to as the Tian mechanism) was selected as the most appropriate for further studies of NH_3/CH_4 combustion. The strength of agreement between the Tian mechanism and experimental results held when the pressure was doubled to 2 atm. In a similar NH_3/H_2 numerical study evaluating twelve mechanisms, Xiao et al. (2017) [131] found the Tian mechanism and an NH_3 oxidation mechanism developed by Mathieu and Petersen (2015) [132] to be joint best for predicting ignition delay and NO_x, further validating the Tian mechanism for NH_3 blends. In the same study, the Mathieu and Petersen mechanism was found to be best for predicting flame speeds, however, the absence of carbon chemistry precludes its use in this study. Hayakawa et al. [102], compared experimental S_L results for NH_3-air combustion (Φ of 0.7 to 1.3 and pressure up to 0.5 MPa) with those from five NH_3 relevant mechanisms using the reaction kinetics simulator Chemkin-Pro [133] to simulate flame speeds. GRI Mech 3.0 [134], the established mechanism for CH_4-air modelling, was found to be superior to the others for flame speed predictions. However, GRI Mech 3.0 lacks some important NH_3 oxidation steps and the Tian mechanism was the superior of the remaining four mechanisms investigated.

The Tian mechanism built on an earlier chemical kinetic model by Skreiberg et al. (2004) [135] that, while investigating the combustion of a wide range of product gases from biomass gasification (primarily H_2 and CO), only had NH_3 concentrations of 1000 ppm for a maximum temperature of 1273 K. Therefore, Tian et al. developed the Skreiberg mechanism to produce a more complete set of flame species (84 species) with 703 reactions, focusing primarily on CH_4–NH_3 combustion. Developed experimentally and numerically under low pressure conditions (of 4kPa), molar ratios of NH_3:CH_4 were varied from 0.0 to 1.0 (11 cases) at an Φ of 1.0 in a premixed O_2/argon environment, primarily to ascertain concentrations of product species.

Experimental investigations of NH_3/CH_4-air flames by Okafor et al. (2018) [96] led to the development and validation of a new mechanism (henceforth referred to as the Okafor mechanism) that sought to improve on a measured under-prediction in flame speed by the Tian mechanism. The under-prediction was found to predominate in blends for NH_3 energy content of < 30%. The Okafor mechanism is a blending of the Tian mechanism and GRI Mech 3.0, modelling for 59 species via 356 reactions. The Okafor mechanism was able to simultaneously find agreement with GRI Mech 3.0, with regard to temperature and species profiles in CH_4-air combustion, and find close agreement with the Tian mechanism for NO concentrations for Φ values of 0.8 to 1.3. This agreement was found for the highest concentration of NH_3 used in the study, 30% NH_3 by energy content.

Therefore, the two mechanisms used in this study are the Tian mechanism and the Okafor mechanism. Mechanisms capable of modelling both NH_3 and small hydrocarbon chemistry naturally have more species and reactions than those for NH_3 or NH_3/H_2 blends (due to H_2 being an intermediate species in NH_3 chemistry). The large numbers of species and mechanisms makes these mechanism too cumbersome for CFD modelling (i.e. processing time and hardware costs), hence the widespread practice of simulating flame speed and emissions using the reaction kinetics simulation software Chemkin-Pro (developed by Ansys Inc.) [133].

2.7 Thesis Objectives

The literature review and other background research undertaken in this chapter enables the identification of several objectives, essential for achieving the thesis aims.

- Premixed, preheated, staged combustion (with a fuel-rich primary stage) is recommended. Before experimental investigations for primary stage combustion can proceed, gas phase numerical simulations will be made for the combustion of preheated, premixed by-product NH_3 (i.e. humidified and anhydrous) blended with varying amounts of COG or CH_4. Pressures should be modelled at near ambient, in anticipation of fuel flow restrictions for the subsequent experimental work. The simulations will model the comparative reactivity of the various blends and the product concentrations exiting the

primary stage. Balancing predicted reactivity versus emissions, the results of the numerical studies will enable the selection of two optimal blends (one humidified, one anhydrous) and predict their respective approximate optimal equivalence ratios, for simultaneously minimising both NO_x and NH_3 emissions.

- Gaseous phase experimental fuel flows, representative of the two chosen blends, will need to be formulated and tested in an industrially representative combustor (under the same conditions as previously modelled) using a swirl burner of appropriate geometry. This will require the creation of a bespoke fuel delivery system. A quartz confinement will be used to enable non-intrusive, optical observations of combustion stability and flame structure. A gas analyser system, capable of measuring NO_x and unburned fuel emissions, in line with industrial measurement practices, is required to ensure the results are relevant to the gas turbine industry. Slightly varying the contribution of the support fuel to the chosen blends (~±5%$_{vol}$) will enable trending of reactivity and emissions with changes in support, checking the veracity of the earlier modelled trends and ensuring the chosen blends are, in fact, optimal.
- The experimental results will be used to modify the original numerical model to enable simulations at industrially relevant pressure elevations, indicating the likely effect of pressure elevation on emissions (from primary stage combustion). Additionally, the improved reactor model results for the post flame zone will be used to inform the design of two novel secondary air-staging combustion confinements. These quartz confinements will aim to have staging positions sufficiently different to show how staging location might influence exhaust emissions.
- The novel confinements will be used in the same experimental rig as before, combusting the two optimal blends at their respective optimal primary zone equivalence ratios (as will have been previously identified) to observe the effects of air-staging on flame stability, fame structure and emissions, under complete combustion conditions. Staging holes will be sized to permit staging flows that facilitate sufficient mixing and maintain exhaust temperatures relevant to real systems (resulting in relevant post flame combustion chemistry). Hence,

additional entrainment of air from the surroundings, upstream of gas sampling, should be prevented. Comparisons between the two blends' performance (emissions and flame stability) can then be made. Additionally, a comparison of the effects of the two staging locations can be made. Modest pressure elevation should be investigated to verify the modelling predictions.

- Lastly, the complete combustion of the two optimal fuel blends should be simulated in gas turbine power cycles that model at industrially relevant combustor pressures for a variety of real-world scenarios, using relevant equipment efficiencies. The cycles should be designed to facilitate the elevated fuel/air inlet temperatures investigated in the prior work, via the use of a recuperator. The cycle net power, gas turbine size and cycle efficiencies of each of the two chosen blends can be compared. The global warming potential of the bespoke by-product NH_3 cycles should be compared with that of conventional, natural gas combined cycles.

Chapter 3 Preliminary Numerical Analyses

3.1 Equilibrium Modelling – Method

It is accepted that equilibrium modelling cannot provide representative values for NO_x product concentrations. However, when looking to simply select several of the most promising candidates, from a considerable number of potential fuel blends, it is not the specific values for each blend which were most important, but more how the values of one blend compared with those of another. Equilibrium modelling informed on the relative performance of each blend. Additionally, the time and resources necessary for conducting equilibrium modelling were far less than those employed in kinetic modelling. Therefore, equilibrium modelling offered an opportunity to quickly and easily establish which few blends had the greatest potential to fulfil the specified aims of lowest emissions in conjunction with highest adiabatic flame temperature (AFT). The trends in performance identified during equilibrium modelling were later verified using more complex kinetic modelling (for the several blends ultimately selected during the equilibrium modelling) to ensure those trends identified still held and that the preliminary blend selection remained valid.

Thus, the first phase of the numerical simulations utilised an open source software program called Gaseq, that has previously been used to numerically model NH_3 use in other gas turbine studies [89, 92]. A gas phase 0-D equilibrium program, Gaseq's programming is derived from a method developed by NASA for calculating the products of multiple reacting species of gas through the minimisation of Gibbs free energy [88] according to Equation 3.1. The Gibbs Free Energy (G) of the mixture at pressure P is given by:

$$\frac{G}{RT} = \sum_{i=1}^{nSp} \left(\frac{x_i G_i^0}{RT} + x_i \ln \frac{x_i}{\sum x_i} + x_i \ln P \right) \qquad \textit{Equation 3.1}$$

Where the equilibrium number of moles of species i is x_i (and i = 1 to nSp), G_i^0 is the molar free energy at 1 atmosphere of species i and Σx_i is the total number of moles in the mixture. At equilibrium G/RT is at a minimum. Capable of solving for a variety of

problem types, in this instance it was used to obtain the AFT and product compositions for a variety of NH_3 based blends under constant pressure.

3.1.1 Inlet Temperature

An inlet temperature of 550 K was adopted to balance between the competing factors of maximising reactivity and minimising NO_x. The premixed fuel/air inlet temperature of 550 K was also considered to approximate the maximum achievable combined fuel/air inlet temperature for the subsequent experimental campaign. This is similar to the inlet temperature of 500 K used by Somarathne et al. (2017) in their NH_3/air premixed swirling flame simulations, with NO and unburned NH_3 minimised to 700 ppm (wet basis) at atmospheric pressure (200 ppm at 0.5 MPa) without secondary air injection [106].

Although the elevated pressure effects inherent in gas turbine operation are not being considered at this stage of the thesis, it is worth noting that the isentropic compression of air increases the inlet temperature into the combustor. The compressor outlet temperature (assuming 100% compressor efficiency) can be found from Equation 3.2.

$$T_2 = T_1 \left(\frac{P_2}{P_1}\right)^{\frac{k-1}{k}} \qquad \textit{Equation 3.2}$$

Where T_1 and T_2 are the compressor inlet and outlet temperatures respectively and P_1 and P_2 are the corresponding pressures. The isentropic exponent k, is the ratio of the specific heats (C_p/C_v) which has a value of ~1.4 for air [75]. For example, the compressor outlet temperature for the adiabatic compression of ambient air (e.g. 283 K) to 10 atm (see Section 2.4.2 for relevance of this pressure), is calculated to be 546 K. This inlet temperature (~550 K) is therefore relevant to conventional gas turbine operation. To help overcome the cooling effects of the fuel in the fuel/air premix, which can be considerable for NH_3 combustion, additional heating could be practically achieved via recuperation of heat from the exhaust gases [78] (considered later in Chapter 7) or via harnessing some of the waste heat available on a steelworks sites [136, 137].

3.1.2 Entering Reactants

The Gaseq program has a facility which allows the user to input a gaseous mix of their choice, created from a vast array of available species in its database. The user can then save this composition to file as a named mixture (e.g. COG) for subsequent recall. The composition of air is the only preset named mixture. While modifiable, the preset air composition was accepted for this study and had the molar composition of 78.09% N_2, 20.95% O_2 and 0.96% Argon. The representative COG and representative aqueous ammonia vapour (AV) compositions (as derived in Sections 2.5.1 and 2.4.2 respectively) were input on a molar basis and each saved as named mixtures (i.e. 'genericcog' and 'genericvap'). Methane was used as a surrogate for natural gas.

Two fuel blend matrices were generated. The first matrix blended AV with each of the support fuels, COG or CH_4, in turn. The molar proportions of AV to support fuel were varied in $5\%_{vol}$ increments making a total of thirty-eight AV blends. For example, the AV blends include a $5\%_{vol}$ CH_4 to $95\%_{vol}$ AV blend, a $10\%_{vol}$ CH_4 to $90\%_{vol}$ AV blend and so on. The second matrix blended AA with each of the two support fuels in a similar fashion, for a further thirty-eight blends. Both AA and AV as individual, unsupported fuels were also investigated.

Although this chapter is concerned with optimising the products from a fuel-rich primary stage of combustion, for eventual incorporation into a staged configuration, for completeness and to demonstrate the trends of NO_x production through lean to rich environments, the AV blends were varied from an equivalence ratio (Φ) of 0.75 to 1.4 in increments of 0.05. Therefore, each blend gave results for fourteen different air to fuel ratios. The Φ range used in the parameter study for the AA blends was 1.0 to 1.4, giving nine cases per blend. The total number of cases was therefore ~900 across all blends and stoichiometries. The results were exported to one of two Excel workbooks for analysis (i.e. one each for the AV and AA blends).

Figure 3.1**,** a screenshot of the Gaseq interface, includes the initial and equilibrium conditions, reactant/product compositions and a selection of other calculated variables for a sample case, a blend of 95% AV and 5% COG with air under stoichiometric conditions (molar basis).

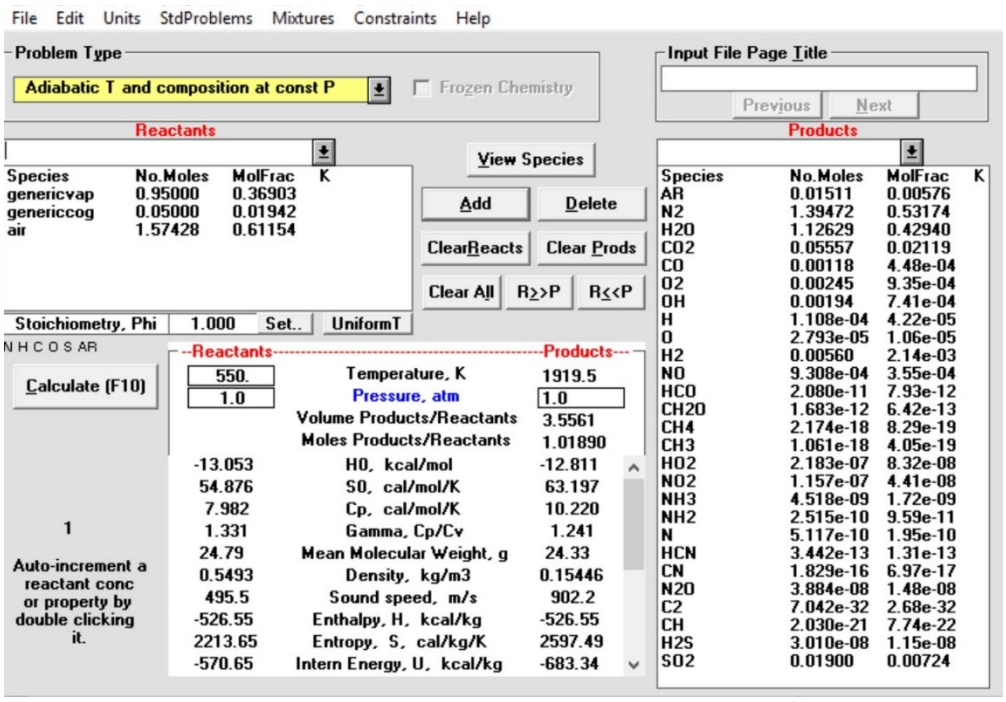

Figure 3.1 Gaseq interface showing inputs and results for a sample case.

The Gaseq program is (in software terms) archaic, having been originally written in Visual Basic 3 on operating system Windows 3.1. While the program can achieve some functionality on a modern system, displaying the results for individual cases on-screen, it was not possible to export the displayed data, or the results data obtained from parameter studies. However, a PC running the operating system Windows Vista and Microsoft Excel 2007 enabled the results to be written to file. Given the difficulties in using the program, the reasons for using it are two-fold. Firstly, the open-source nature of the Gaseq program, whereas the ANSYS program Chemkin (the alternative equilibrium program), was only available on a single departmental license. Lastly (and more importantly), given the complexity of both the AV and COG fuel mixtures and the large number of blend combinations under investigation, there are clear advantages in being able to simply input the molar contribution of each named mixture to each of the investigated blends, e.g. entering 0.95 from AV and 0.05 from COG as shown in Figure 3.1. Without this facility one would have to first calculate, outside of the program itself, the overall molar contribution of each of the dozen or so individual species to each fuel blend and then manually import this data. Unfortunately, this more lengthy procedure is required when using equilibrium modelling in Chemkin, making Gaseq the preferred

choice for the equilibrium modelling of complex fuel mixtures for large numbers of blends, despite the difficulties experienced in using it on a modern system.

To illustrate the similarities in equilibrium results for Gaseq versus Chemkin, for a high temperature, high NO_x example, the AFT for the stoichiometric ($\Phi = 1.0$) combustion of NH_3 in Chemkin was 2220.5 K, so < 3K lower than for Gaseq (at 2223.4 K). Total NO_x using Gaseq was 1,421 ppm compared with 1,341 ppm for Chemkin (i.e. < 6% lower for the same case and conditions). While both programs use the minimisation of Gibbs free energy approach, Chemkin uses the STANJAN library of routines, developed by Stanford University, in its solution method. First published in 1986, STANJAN is an established alternative to the NASA library [138]. The thermal conductivities for diatomic and polyatomic molecules are observed to be generally lower for Gaseq. The reason given is that Gaseq uses a mixture-averaged method rather than the more rigorous multicomponent formulation used for Chemkin [88]. The results modelled here (for stoichiometric NH_3 combustion) are in agreement with this observation. These observed differences are considered inconsequential for the initial blend selection work, especially as those blends initially selected will be interrogated further using kinetic modelling in Chemkin.

3.1.3 Generating and Evaluating Emissions Concentrations

The Gaseq program offers several standard sets of product species from which to choose. The 'extended' list of hydrocarbon, oxygen, nitrogen products was selected. As argon was present in the reactants (for the composition of air), it was necessary to add it to the products list. On inspection over a range of Φ values, it was found that the concentrations of H_2S and SO_2 were by far the two most dominant species for the sulphur chemistry resulting from the presence of H_2S in the AV. The products list was therefore extended to include these two products also (as can be seen in Figure 3.1).

Although NO_x equilibrium values are unrepresentative of values found experimentally and are only being used to compare relative performance, threshold values for emissions were nonetheless required in order to select blends with superior simulated emissions performance. Given the existence of regulations which limit NO_x concentrations, these limits were adopted for blend selection. As was discussed in

Section 2.3.1, it is unclear which NO_x limits would be applicable in this case of industrial waste NH_3 combustion and so a limit of 97 ppm (or 200 mg/Nm^3), was thought to be a reasonable assumption [107]. The NO_x product concentrations in each of the two workbooks were normalised as dry, using the specific mole fraction of H_2O (derived under equilibrium for each case) for the calculations. The dry concentrations were then normalised to 15%$_{vol}$ O_2 as per the regulations, using the relevant equation (see Equation 2.7). The cases were then ranked in order of ascending NO_x concentration in each workbook. Those cases below the threshold NO_x value were forwarded to the next round of selection criteria.

Other than for the case of unsupported AA (i.e. pure NH_3), rich Φ values will necessarily result in CO emissions. An emissions threshold for CO was therefore applied to those cases successful in the first round of selection. As the proposed blends were ultimately to be tested in an experimental rig, the minimisation of CO emissions was a necessary consideration for both safety and measurement purposes. After an initial inspection of the calculated CO concentrations (dry basis), and in the absence of any relevant regulatory limit (see Section 2.5.3), the selection criteria was limited to a maximum of 10,000 ppm, to enable the selection of several potential AV and AA blends. This threshold is ten times the maximum scale of the CO analyser, necessitating significant dilution of the sample for measurement. In a staged combustion system (the ultimate aim of this study and any energy application) the unburned fuel from the first stage would be consumed in the second stage, hence nullifying this as a practical issue.

3.2 Equilibrium Modelling – Results and Discussion

3.2.1 Selection of Potential AV Blends by Emissions Concentrations

The NO_x and CO concentrations for the AV blends able to satisfy the previously specified selection criteria are shown in Figure 3.2 and Figure 3.3 respectively. Figure 3.2 shows that pure AV and five other AV blends (i.e. supported by CH_4 or COG) were modelled as capable of satisfying the NO_x concentration limit of 97 ppm or less at a value of Φ **higher than or between 1.05 and 1.1**, for the stated conditions (the relevance of this Φ range is revealed shortly). The compositions for these fuel blends are detailed in Appendix A.1a. As predicted by the literature, NO_x concentrations for these blends are shown to

climb rapidly under increasingly fuel-lean conditions, reaching values approximately an order of magnitude higher at their peak (Φ ~ 0.8) than for an Φ of 1.05. Thus, all subsequent modelling results focus on fuel-rich combustion conditions.

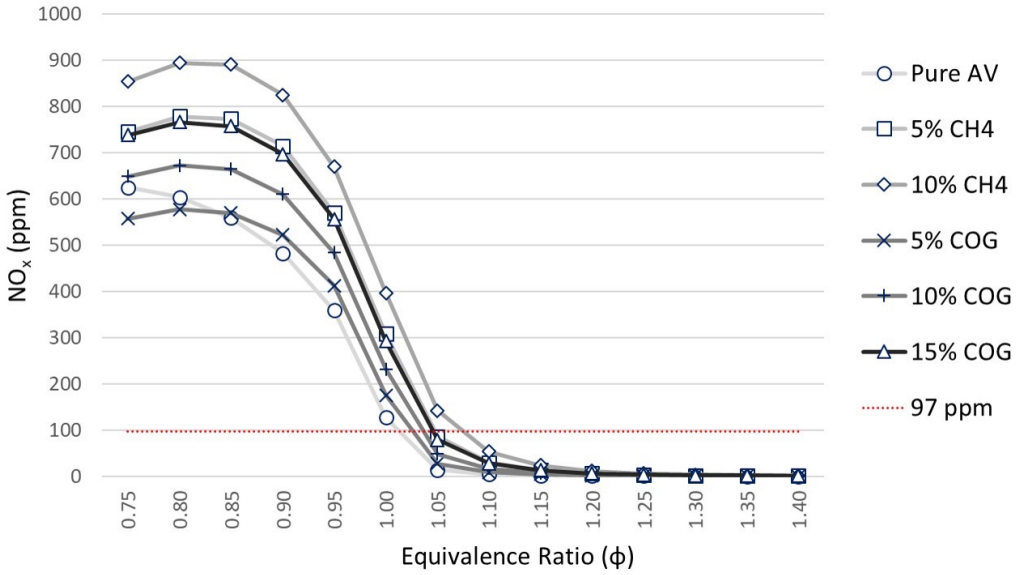

Figure 3.2 NO_x concentration (dry, 15%$_{vol}$ O_2) by Φ for selected AV blends at equilibrium (1 atm, 550 K inlet).

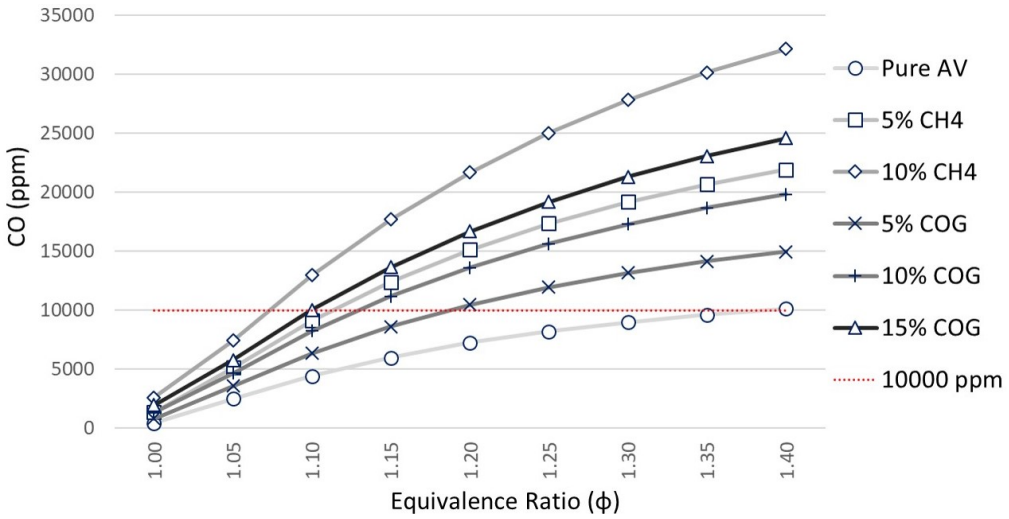

Figure 3.3 CO concentration (dry) by Φ for selected AV blends at equilibrium (1 atm, 550 K inlet).

Figure 3.3 shows that the same six AV blends, under the same equilibrium conditions, satisfy the threshold for CO concentrations of 10,000 ppm or less, for Φ **lower than or between 1.05 and 1.1**. While the CO concentrations for all blends increases with increasing Φ, CO concentrations naturally climb far more rapidly for those blends with

the greatest proportion of carbon in the fuel and is therefore less significant for COG blends (COG being ~65%$_{vol}$ carbon-free) than for the equivalent proportion of support fuel in the natural gas blends.

Although the 10%$_{vol}$ CH_4 with AV blend, is not able to simultaneously satisfy both the NO_x and CO concentration limits for the values of Φ modelled (specifically 1.05 or 1.1), the blend qualifies for further investigation by virtue of having concentrations less than both these limits within the Φ range of 1.05 to 1.10, appearing to satisfy both limits simultaneously at an Φ of approximately 1.075.

3.2.2 Selection of Potential AA Blends by Emissions Concentrations

The same selection criteria was applied to the thirty-nine AA blends. NO_x and CO concentrations for the five selected blends are shown in Figure 3.4 and Figure 3.5 respectively.

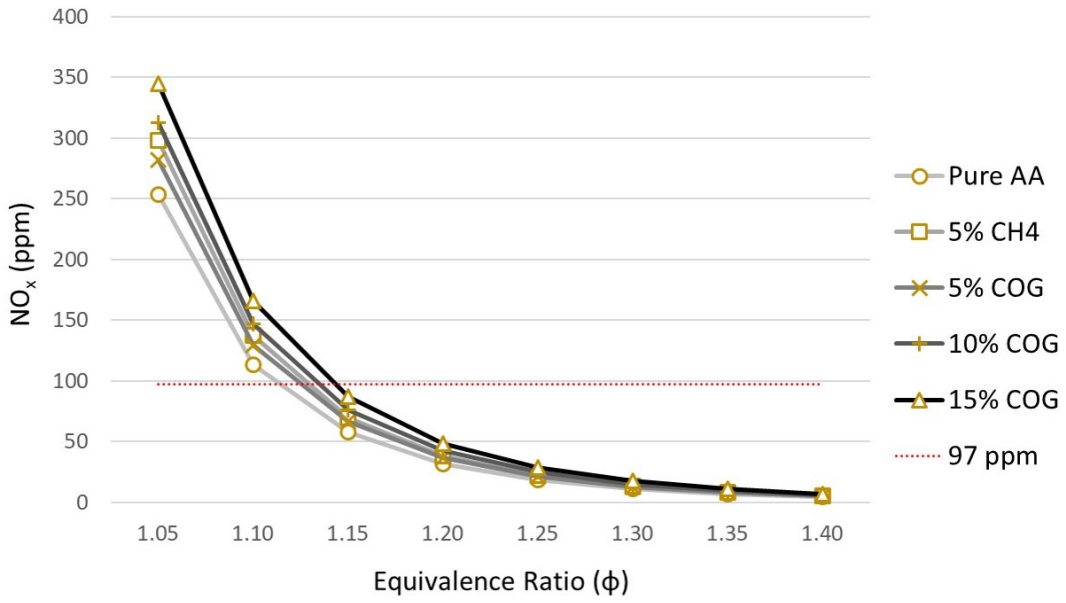

Figure 3.4 NO_x concentration (dry, 15%$_{vol}$ O_2) by Φ for selected AA blends at equilibrium (1 atm, 550 K inlet).

Pure AA and four other blends (i.e. supported by CH_4 or COG) are capable of simultaneously satisfying the NO_x and CO limits in the Φ range 1.15 to 1.25, under the stated conditions. These five blends (the compositions of which are detailed in Appendix A.1b) are composed of similar percentages of support fuel to those selected for AV, minus the 10%$_{vol}$ CH_4 blend, which did not qualify on this occasion.

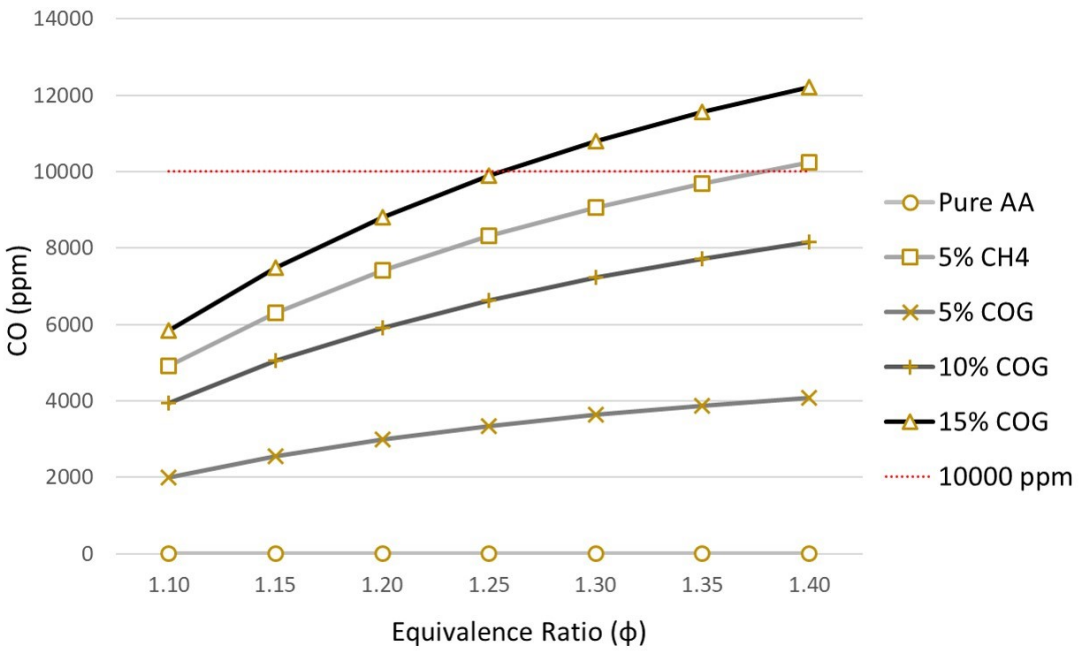

Figure 3.5 CO concentration (dry) by Φ for selected AA blends at equilibrium (1 atm, 550 K inlet).

The qualifying range of Φ values for the AA blends is approximately 0.1 richer than for the equivalent AV blends. This suggests that richer combustion is needed when optimising emissions in AA combustion, when compared with humidified NH_3. The reasons for this are two-fold. Firstly, the comparatively lower NO_x of the AV blends for a given Φ is a consequence of the lower equilibrium temperatures modelled for their products. This is discussed in more detail in the next section. Hence, AV blends are able to satisfy the NO_x limit at leaner Φ values than equivalent AA blends.

Secondly, AV blends have the disadvantage that, at any given value of Φ, they have higher CO than the equivalent AA blend. For example, AV with $5\%_{vol}$ CH_4 breaches CO of 10,000 ppm at an Φ just above 1.1 compared with a concentration of ~5000 ppm for the equivalent AA blend. This is because the carbon content in AV blends comes from both the carbonaceous components in the support fuels and from the contribution of the HCN and CO_2 components in raw AV, making the carbon content of AV blends considerably higher than for equivalent AA blends. Thus, for both these reasons, the optimal Φ for AV blends is shifted leaner than for equivalent AA blends and vice-versa.

Figure 3.6 illustrates this differing carbon content for equivalent AA and AV blends using the $15\%_{vol}$ COG blends as an example. The percentage of the overall carbon content, as

attributable to each fuel component in the AA blend, is shown. Taking the AA blend as representing a standardised 100% carbon content, the AV blend is calculated as containing 60% more carbon than the equivalent AA blend. Figure 3.6 clearly illustrates that, although CO_2 and HCN represent only $4\%_{vol}$ of the composition of AV, their potential additional contribution to CO (and CO_2) emissions is significant because AV contributes $85\%_{vol}$ of the blend.

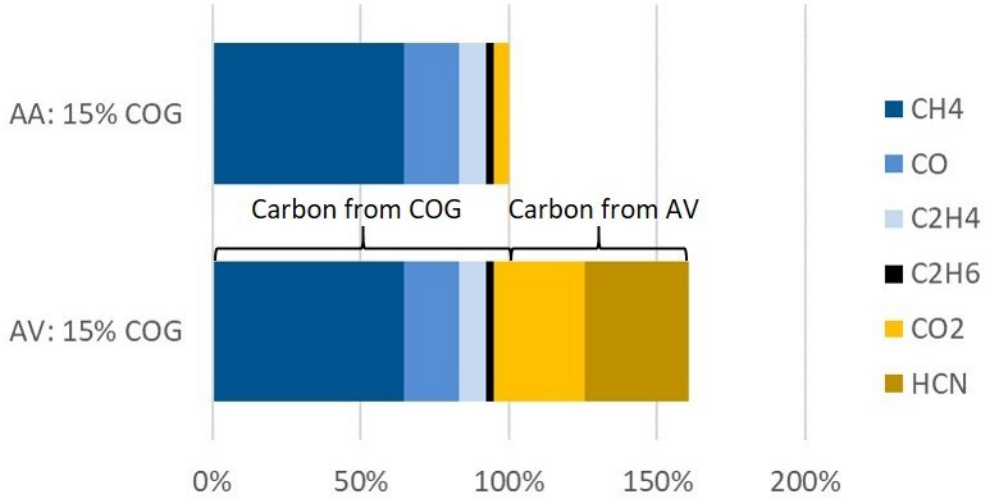

Figure 3.6 Comparative carbon content of AA vs AV fuels – $15\%_{vol}$ COG example

Equilibrium NH_3 product concentrations for the AA and AV blends did not exceed 1 ppm (wet basis), even for the most fuel-rich of cases (at $\Phi = 1.4$). As these NH_3 concentrations are well below workplace exposure limits and do not have other mandatory limits, they did not form part of the blend selection criteria at this stage.

In summary, the equilibrium results indicate that the greater the Φ, the lower the levels of NO_x and the higher the levels of CO. The equilibrium modelling suggests the optimal balance of NO_x versus CO product is centred between Φ 1.05 to 1.1 for the selected AV blends and 1.15 to 1.25 for the AA blends. These target Φ ranges will henceforth be referred to as the target Φ, or Φ_t ranges for conciseness.

3.2.3 Adiabatic Flame Temperatures for the Selected Blends

The equilibrium values of AFT for the selected AV and AA blends are shown in Figure 3.7. AFT naturally decreases with an increase in equivalence ratio. For example, at $\Phi = 1.4$, the AFT for any given blend was around 220 K to 250 K lower than at its peak, for the AV

and AA blends respectively. This rapid decrease in AFT with increasing Φ will negatively impact the blends' reactivity (i.e. chemical reaction rates) when operating under increasingly fuel rich conditions. At Φ = 1.0, the temperature of each AV blend was between 234 K and 364 K lower than for its equivalent AA blend, with the difference between equivalent blends increasing only slightly as Φ increased. At the Φ_t range of the AV blends (i.e. 1.05 to 1.1) the relevant AFT values are at the higher end of the AV blends' temperature range, when minimising emissions. This not so for the richer Φ_t range of the AA blends (i.e. 1.15 to 1.25). Thus, the difference in AFT between equivalent AV and AA blends, within their respective Φ_t ranges, is less than for any fixed Φ value.

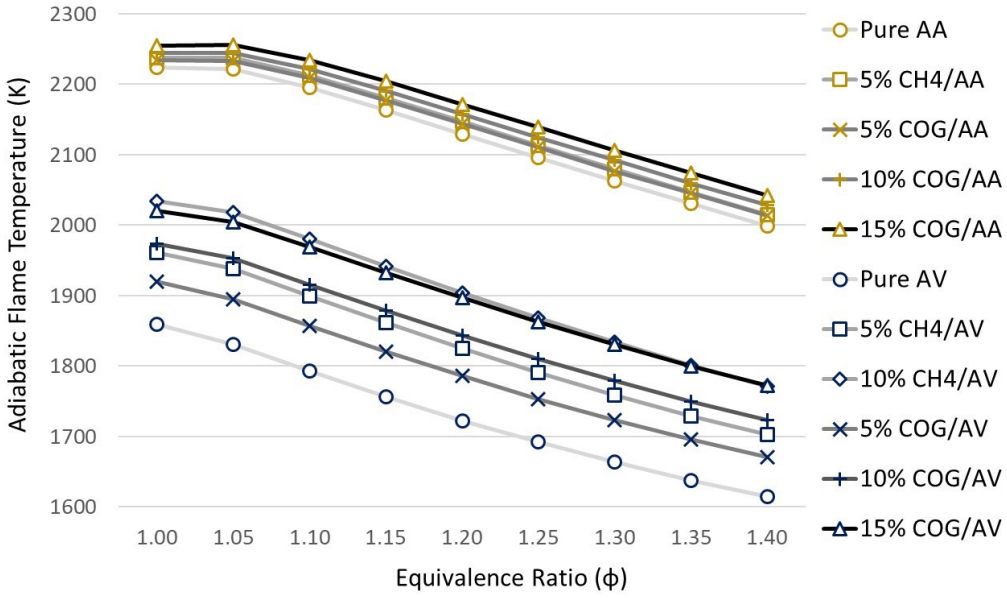

Figure 3.7 Adiabatic flame temperature by Φ for the selected AA and AV blends under equilibrium conditions (1 atm, 550 K inlet).

AFT varied more considerably across the AV blends than across the AA blends. There was a difference of ~175 K between the hottest and coolest AV blends for the Φ_t range (i.e. 1.05 to 1.1) compared with a difference of just 43 K across the AA blends at the mid-point of their Φ_t range (i.e. at Φ = 1.2). The inert water fraction in the AV blends is significant and varies greatly between blends (i.e. 52.5%$_{vol}$ for AV with 15%$_{vol}$ COG and 61.8%$_{vol}$ for pure AV). As water (or steam) has a relatively high specific heat capacity, it lowers AFTs for the least supported AV blends most significantly. At Φ = 1.2 (the AA blends Φ_t mid-point), the lowest AFT for the AA blends (i.e. pure AA) was ~120 K higher than the hottest AV blend within its Φ_t range. This suggests less of a difference in overall

reactivity between the hottest AV blends and the coolest AA blends than across the range of AV blends. Consequently, the differences in reactivity are likely to be smallest across the AA blends, greatest across the AV blends and the difference in reactivity between the coolest AA blends and the hottest AV blends lays somewhere in-between.

3.3 Kinetic Modelling of Laminar Flame Speed – Method

The PREMIX reactor in the ANSYS software program Chemkin-Pro was employed to model 1-D, freely propagating, premixed flames to determine their laminar flame speeds (S_L) over a range of Φ values. Solutions were based on an adaptive grid of 1,000 points, with multi-component transport properties and trace species approximation as derived from the use of the chemical mechanisms developed by Tian et al. [130] and Okafor et al. [96]. As ammonia and carbon containing fuel blends, the rationale for the use of these two mechanisms is explained in Section 2.6. They will henceforth be referred to as the Tian mechanism and the Okafor mechanism or 'T' and 'O' respectively in the plots. The AV blend compositions were normalised without the presence of H_2S as the mechanisms do not include sulphur chemistry. The compositions for the normalised blends are detailed in Appendix A.1c. The parameter studies were conducted over an Φ range of 1.0 to 1.4, using the default oxidiser composition of 79%$_{vol}$ N_2 and 21%$_{vol}$ O_2.

3.4 Kinetic Modelling of Flame Speed – Results and Discussion

The S_L results for ten of the eleven previously selected AV and AA blends are shown in Figure 3.8 and Figure 3.9 respectively, for an inlet temperature 550 K and a pressure of 0.1 MPa.

There is good agreement between the two mechanisms for AV blend S_L values, especially at values in the AV $Φ_t$ range. The Tian mechanism consistently predicts peaks in S_L at Φ 1.1, which is in keeping with the findings of Mei et al. (2020) when they investigated syngas/NH_3/air blends [139] and Hayakawa et al. (2015) for premixed NH_3/air flames [86]. The Okafor mechanism almost as consistently shows S_L peaks at an Φ of 0.05 leaner than those of the Tian mechanism. Unblended AV did not resolve to a solution for any values of Φ, so there were no S_L results for this blend.

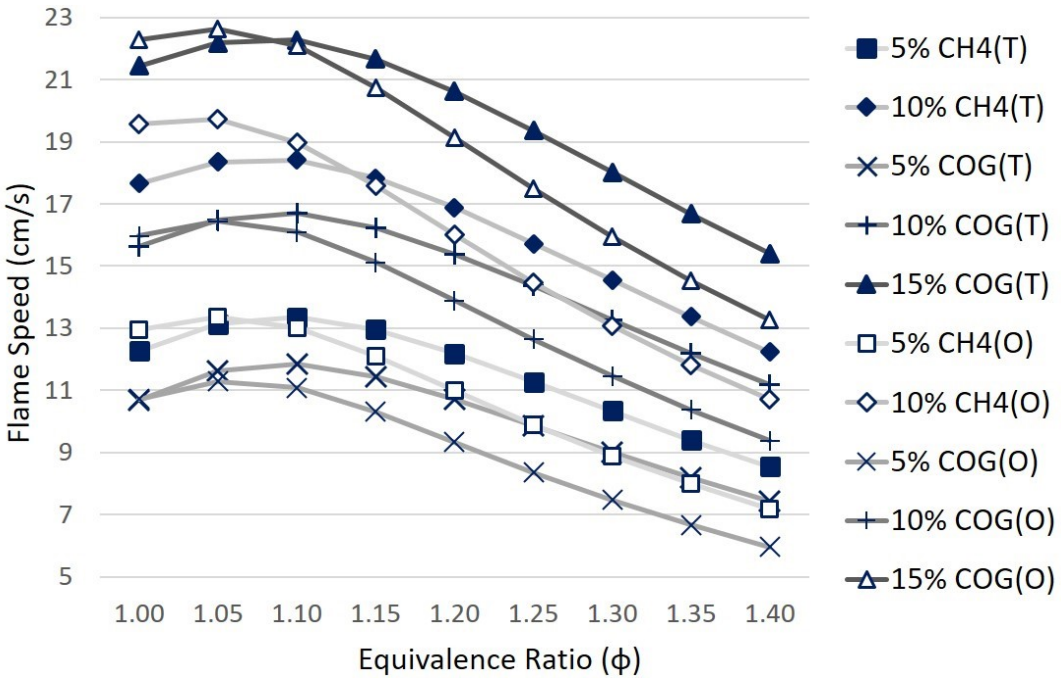

Figure 3.8 Laminar flame speed (S_L) by Φ for the selected AV blends (0.1 MPa, 550 K inlet) Tian (T) and Okafor (O) mechanisms.

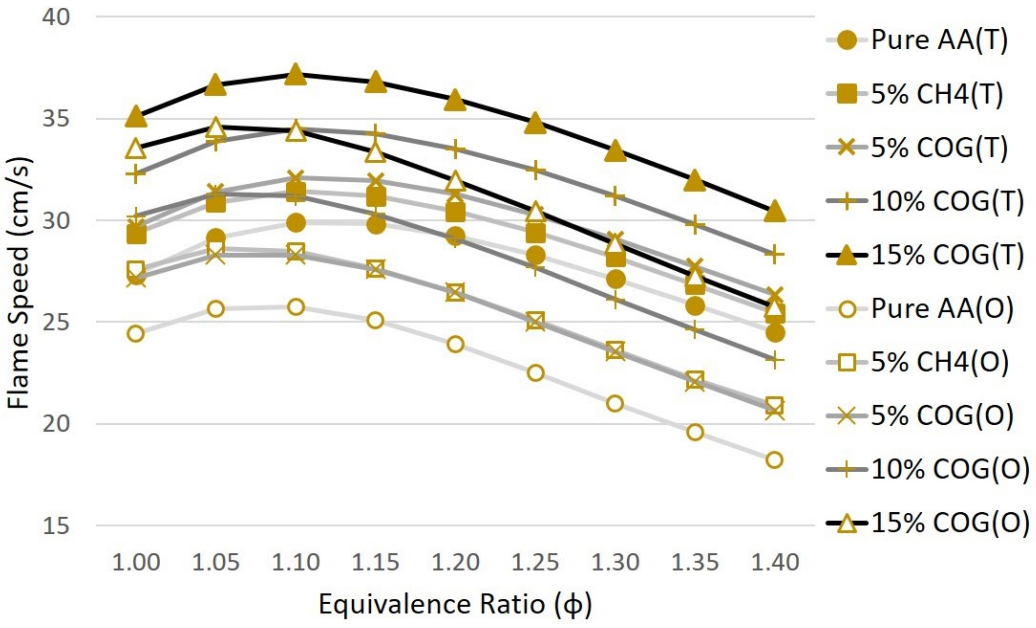

Figure 3.9 Laminar flame speed (S_L) by Φ for the selected AA blends (0.1 MPa, 550 K inlet) Tian and Okafor mechanisms.

There is less agreement between the mechanisms for the S_L predictions of the AA blends (see Figure 3.9). As was discussed in Section 2.6, the Okafor mechanism was developed to address a perceived under-prediction of S_L when using the Tian mechanism. However, the results in Figure 3.9 are that the Tian mechanism predicts higher S_L values than the

Okafor mechanism for all values of Φ. An explanation for the apparent reversal in the predictions of Okafor et al. is offered in a study by Kumar and Meyer [140] during their work on NH_3/H_2 flames. They found that the Tian mechanism can both significantly over and under predict S_L depending on both the degree to which heat losses are considered and the contribution NH_3 makes to the fuel blend's energy content. They suggest that when using the Tian mechanism to model fuels where 80, 50 and 20% of their energy content is derived from NH_3, predictions were more accurate for the 80% case and especially when ignoring heat losses. The selected AA blends derive 80% or more of their energy content from NH_3 and heat losses are not being considered here.

Under the same conditions, H_2 and CH_4 have much higher laminar S_L values than NH_3 [40]. Consequently, the blends with the higher contribution of support fuel, produce the higher S_L values. Pre-heating the reactants also increases S_L. Under the conditions stated (550 K), the S_L of pure AA has more than trebled when compared to the often cited value of ~7 cm/s, at 298 K [78, 86].

With S_L being indicative of the general reactivity of fuel blends, it is of interest to compare the S_L values of the selected blends with those of natural gas flames, to gauge the likely suitability of the blends in existing infrastructure. To this end, the fastest S_L values of the AA and AV blends, those supported by 15%$_{vol}$ COG, are plotted in Figure 3.10 alongside those of CH_4 (as a surrogate for natural gas) and under the same conditions of temperature and pressure, for fair comparison.

The S_L values of CH_4 are simulated employing the prevailing CH_4 reaction mechanism, GRI-Mech 3.0 [134]. The Φ of conventional fuel-lean gas turbine systems ranges from Φ 0.5 to 0.7 [99] (shown as shaded points on the CH_4 plot). The shaded data points of the NH_3 blends indicate the Φ_t ranges where emissions were optimised in the work in Sections 3.2.1 and 3.2.2. It can be seen that the shaded points for the AA 15%$_{vol}$ COG blend are within the S_L range of CH_4 operating at Φ 0.5 to 0.55 (i.e. 29.3 to 39.1 cm/s). Under these conditions, three of the five selected AA blends sit within the same S_L range as for CH_4, indicating that these three NH_3 blends, when optimised for emissions, may be capable of stable flames in combustors designed to burn natural gas.

The AV 15%$_{vol}$ COG blend failed to reach similar simulated speeds with a maximum S_L of ~22.5 cm/s, suggesting that flame stabilisation could be particularly challenging for the AV blends.

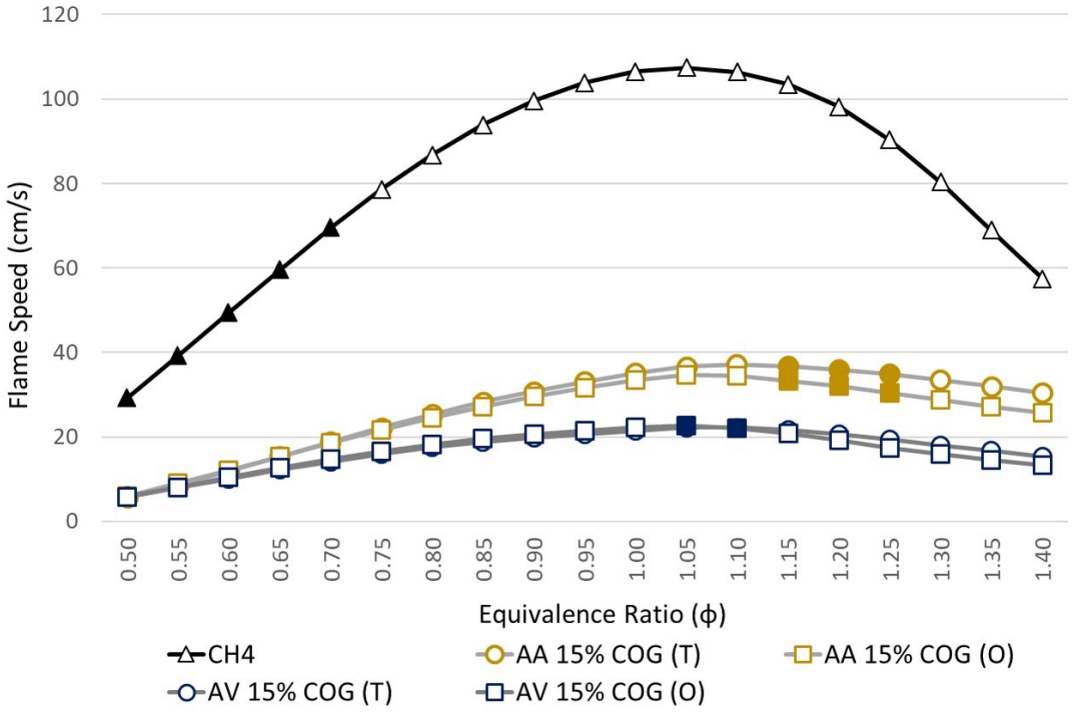

Figure 3.10 Laminar flame speed (S_L) by Φ for AV and AA with 15%$_{vol}$ COG blends (Okafor and Tian mechanisms) vs methane (GRI-mech 3.0) at 0.1 MPa, 550 K inlet.

A large enough reduction of the water fraction, possibly through a combination of AV with AA, could be used to raise the S_L to bring it within the aforementioned CH_4 S_L range, thus improving its reactivity sufficiently to allow for stable combustion. Therefore, a subsequent short study was conducted to simulate S_L for a 50:50$_{vol}$ blend of AV with AA, supported by 15%$_{vol}$ COG, under the same conditions. This blending reduces the H_2O content from ~60%$_{vol}$ (as in the case of pure AV) to ~30%$_{vol}$.

As Figure 3.11 shows the Φ_t range would be ~1.1 to 1.2 (assuming the emissions of the 50:50 blend would be halfway between those of the AA and AV blends). The 50:50 blend slightly exceeded the lower CH_4 S_L (of 29.3 cm/s at Φ 0.5), to achieve 29.4 cm/s at Φ 1.1, using the Okafor mechanism, which is the more conservative predictor of S_L. If the S_L of CH_4 at Φ 0.5 is to be considered indicative of a minimum S_L for stable combustion in combustors designed to burn natural gas, these results suggest a halving of the water

content may be sufficient to enable stable combustion of an aqueous NH_3 blend (~30%$_{vol}$ H_2O) supported by 15%$_{vol}$ COG blend. How a ~30%$_{vol}$ H_2O aqueous NH_3 blend could be practically achieved is in question. A potential solution is presented in the following chapter.

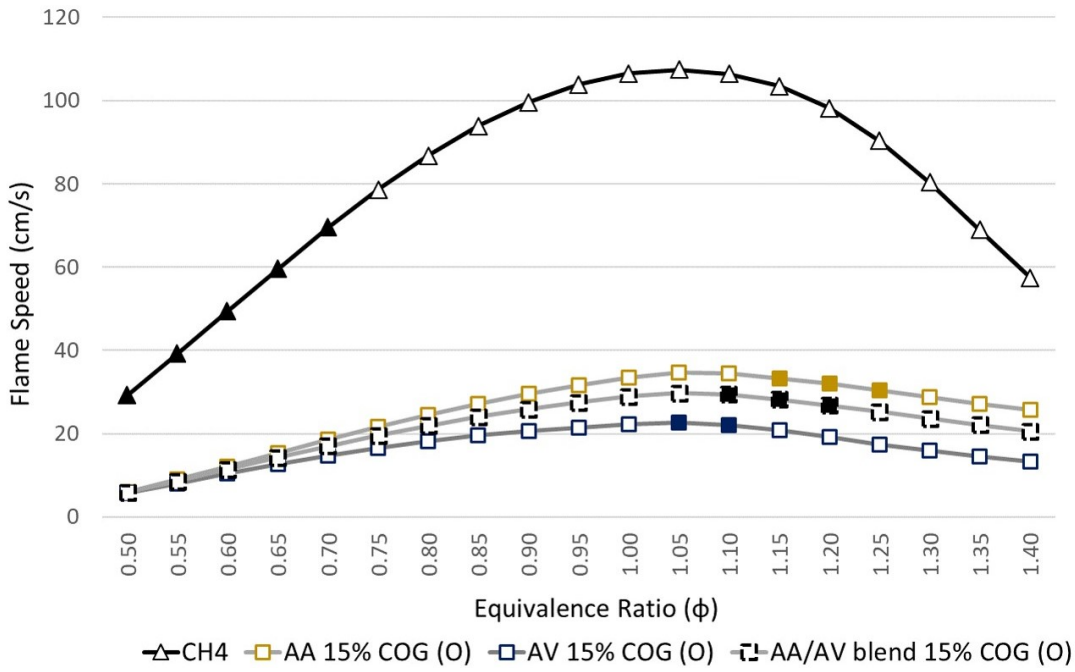

Figure 3.11 Laminar flame speed by Φ for AA, AV and a 50:50 blend, all with 15%$_{vol}$ COG (Okafor mechanism) vs methane (GRI-mech 3.0) at 0.1 MPa, 550 K inlet.

3.5 Kinetics Investigation - Reactor Network Model Method

Using Chemkin and the same two reaction mechanisms, the ten remaining blends were modelled for their behaviour in a hybrid perfectly-stirred reactor/plug-flow reactor network, shown schematically in Figure 3.12. This type of network is commonly used to simulate mixing and flow characteristics in gas turbine combustors [91, 92]. These models would normally be derived from empirical data, but as this modelling precedes the experimental work in this case, the modelling method of similar studies will initially need to be used instead. This configuration is almost identical to the gas turbine model provided in the Chemkin sample library, modified for a premix rather than a diffusion flame. This and similar reactor network models have previously been shown to model representative emissions concentrations from NH_3/H_2 premixed swirling flames [91, 93]. The rig used in those studies is the same one used for the subsequent experimental

investigation in this thesis. The data from the subsequent experimental work in Chapter 4, is used to improve the model later, in Chapter 5.

The preheated, premixed fuel and air is fed into a first cluster (C1) of three perfectly-stirred reactors (PSR1 to PSR3) representing the ignition zone at the burner inlet, the central recirculation zone (CRZ) and the flame zone respectively. The black arrows show where the material flows are generally progressing towards the exhaust, whereas the blue arrows indicate the recirculating flows.

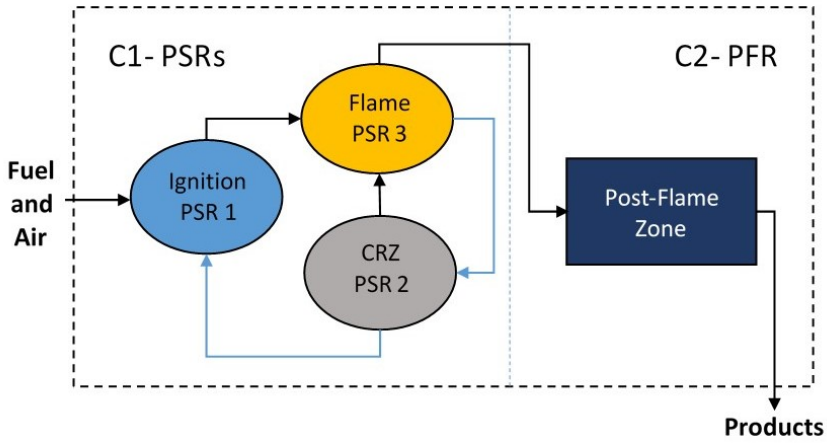

Figure 3.12 Chemkin Reactor Network Schematic.

The second cluster (C2) is a plug-flow reactor (PFR), 40 cm in length with a 10 cm diameter, representing the post flame zone. Inlet air/fuel mass flow and residence times for each of the PSRs 1 to 3 were set to 5 g/s, 0.0005 s, 0.0015 s and 0.0015 s respectively. This total mass flow rate is approximately equivalent to a 15 kW_{th} stoichiometric flame (LHV basis). The recirculated mass fractions from PSR 2 to PSR 1 and PSR 3 to PSR 2, were both assumed to be 20%. These residence times and recirculation rates were the same as those used in previous NH_3/H_2 and NH_3/CH_4 studies using a reactor network [91–93, 112]. As for the equilibrium study, inlet conditions were again 550 K and 1 atm (~0.1 MPa), for an Φ range of 1.0 to 1.4 with 0.05 increments. No heat or pressure losses were included. Consequently, temperatures reached in reality would be lower than those modelled in this study. Omitting heat losses, while affecting simulated values, is unlikely to change the ultimate ranking of blends' performance, so did not influence blend selection for the subsequent experimental work. The AFTs, as obtained during equilibrium modelling, were entered into PSRs 2 and 3 for each blend, for each Φ. This

gave the program a value from which to begin its iterations. Without this input, the program's solutions were irregular.

3.5.1 Adiabatic Flame Temperatures – Results and Discussion

As shown in Figure 3.13, and later in Figure 3.14, both mechanisms were in close agreement for AFT for all cases, with a maximum difference between mechanisms of 14 K for the AV cases and 10 K for the AA cases. Therefore, any substantial differences in reactivity and product concentrations found by the two mechanisms (as is the case later in this chapter), cannot be attributable to differences in modelled temperature.

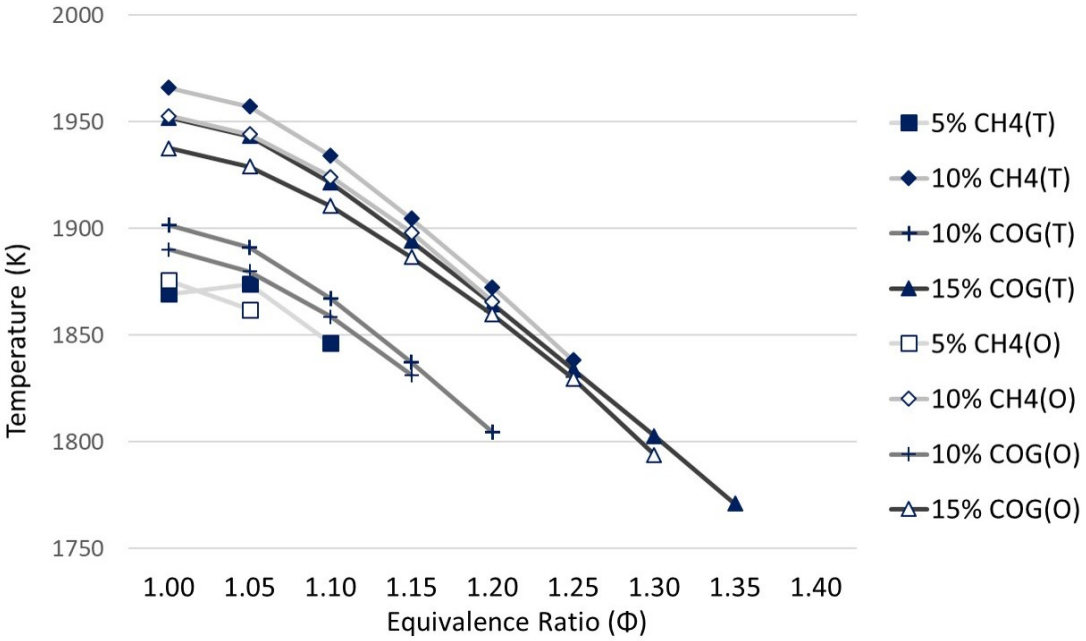

Figure 3.13 Temperature by Φ for AV blends - reactor network (1 atm, 550 K inlet)

As was the case in the S_L simulations, pure AV gave no results. The $5\%_{vol}$ COG with AV blend behaved likewise. Both mechanisms predicted the chemistry of these blends as incapable of reacting under the specified conditions. This finding is consistent with the predicted lower reactivity of these two blends obtained from the equilibrium AFT and kinetic S_L modelling. Consequently, these two blends were discounted from further consideration. For all other AV blends, the Okafor mechanism consistently predicted a failure to react for an Φ of 0.05 less than that predicted by the Tian mechanism. This failure to react is likely due to the lower predicted S_L of the Okafor mechanism in almost all cases. The $5\%_{vol}$ CH_4 with AV blend failed at an Φ > 1.05 and 1.1, for the Okafor and

Tian mechanisms respectively. This poor reactivity, coupled with the general trend of considerably higher NO_x when operating at the lower Φ, favoured the other blends over this one, thus, three AV blends remained for further consideration. Again, the exclusion of this third AV blend agrees with the predictions of next lowest reactivity as found in the S_L and equilibrium AFT modelling, offering additional confidence in the blend selection process.

The kinetic results for AFT were only slightly lower than those for the equilibrium results. The degree of difference varied with blend and stoichiometry. For example, at Φ = 1.1, the $15\%_{vol}$ COG blend had an AFT of 1961 K compared with an average of 1915 K (between mechanisms) in the reactor simulation. The necessary omission of sulphur chemistry in the kinetic modelling would naturally account for some of the difference. For example, when modelling the same case under the same equilibrium conditions in Gaseq and normalising the AV blend minus the H_2S component, the derived AFT falls from 1961 K to 1956 K. Therefore, it is clear that H_2S is only a minor contributor to the difference in AFT between the equilibrium and kinetic modelling and the omission of H_2S would not lead to significant changes in flame temperatures if excluded from experimental work. The remaining difference is due to the difference in the methods used. As previously introduced in Section 2.6, equilibrium approximates product concentrations achieved over infinite time (0-D) by minimising Gibbs free energy, whereas kinetics modelling is time constrained (1-D) via rates of reaction. The number and types of modelled species is also constrained (i.e. different for the two methods) and the library of data for these species may differ. It was discussed in Section 3.1.2 how two equilibrium programs (Gaseq and Chemkin), both modelling for the minimisation of Gibbs free energy can generate different results, thus modest differences between equilibrium and kinetic modelling results are to be expected.

As Figure 3.14 shows, all AA blends gave results for all values of Φ and they were once again very similar to those of the equilibrium modelling, suggesting no obvious errors have been made in the two different simulation methods and that combustion reactions in the PSR cluster are near completion under the simulated conditions. For example, the $15\%_{vol}$ COG blend at Φ = 1.2 had AFT values of 2172 K and 2153 K for equilibrium and

kinetic modelling respectively. As in the equilibrium modelling, there was a maximum difference of just 42 K between the AA blends (at Φ = 1.4), and across the range of Φ, the peak temperature for each blend was approximately 180 K higher than the lowest temperature (it was 175 K for equilibrium modelling). These results suggest that increasing Φ values by > 0.15 would be far more effective in limiting thermal NO_x production than any reduction due to choice of a particular AA blend. The AFT results do not invite the exclusion of any of the six previously selected AA blends.

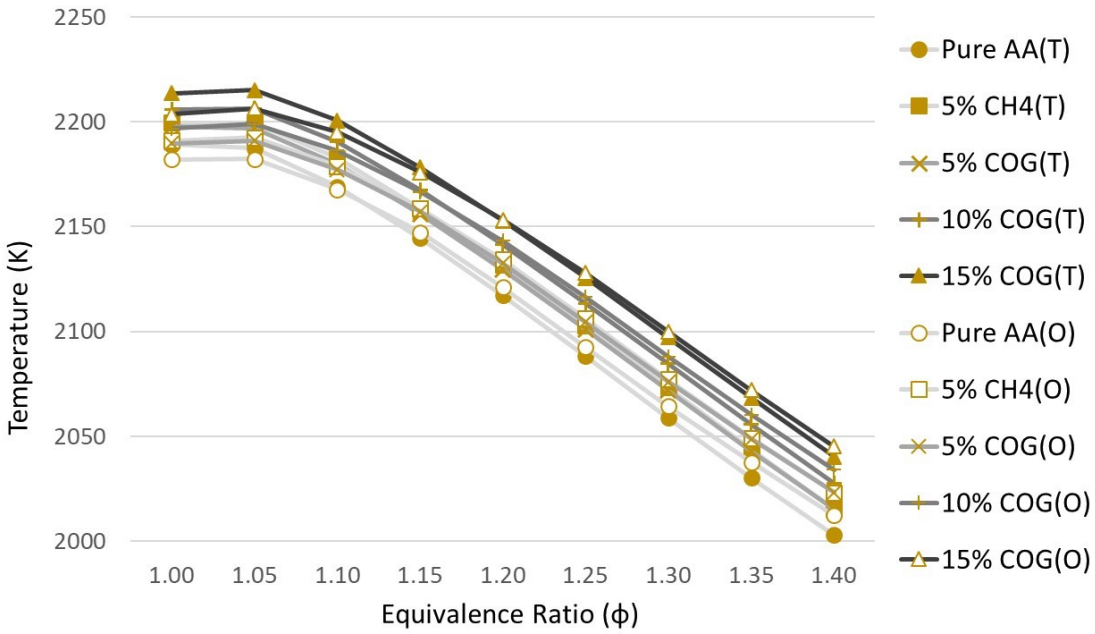

Figure 3.14 Temperature by Φ for AA blends using a reactor network (1 atm, 550 K inlet)

3.5.2 Product Concentrations of the Remaining AV Candidate Blends

It was stated in the equilibrium modelling that NH_3 product concentrations were negligible for all cases, this is not so when the blends are modelled kinetically. Thus, a threshold value of 7 ppm (dry basis) is used for the NH_3 concentrations (as was discussed in Section 2.1.1).

The NO_x, CO and NH_3 product concentrations for the three remaining candidate AV blends are shown in Figure 3.15, Figure 3.16 and Figure 3.17, respectively. Figure 3.15 shows that the two mechanisms are in close agreement for NO_x concentrations for all cases. Where a difference exists, the Okafor mechanism predicts slightly higher NO_x than the Tian mechanism, representing a reversal of the trend for temperature and so this

difference is not explainable in relation to thermal NO_x production, but must be related to calculated differences in the NH_3 oxidation pathways.

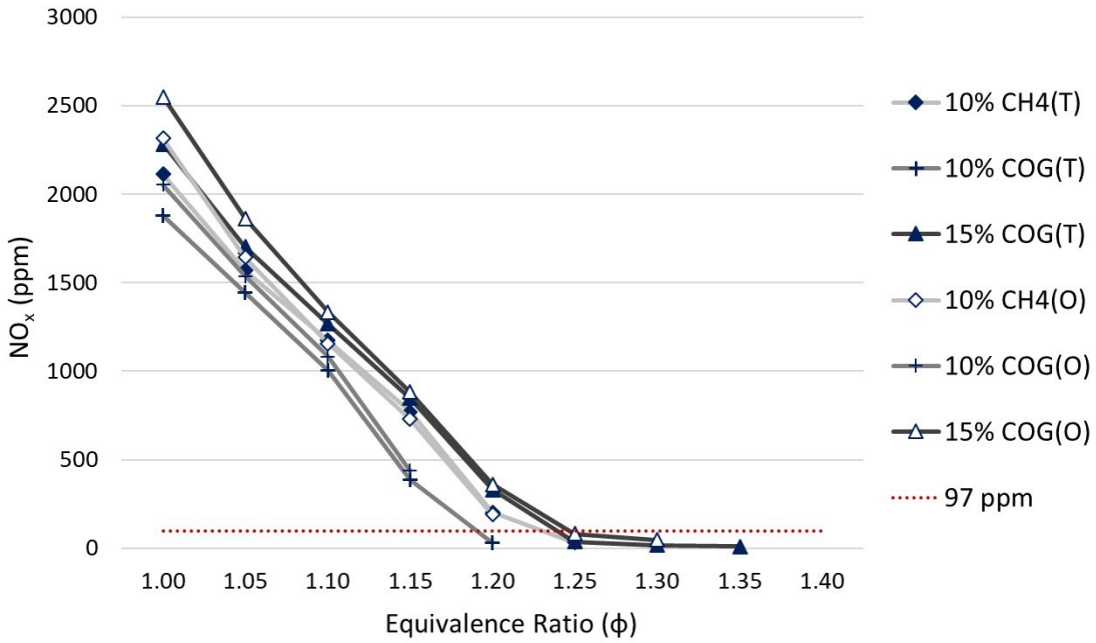

Figure 3.15 NO_x (dry, 15%$_{vol}$ O_2) by Φ, AV blends, reactor network (1 atm, 550 K inlet).

The NO_x results are significantly higher than those predicted by the equilibrium modelling, not going below the 97 ppm threshold until Φ > 1.2, compared with ~1.05 to 1.1 for the equilibrium modelling. However, these kinetically derived results are likely to be higher than for actual gas turbine systems for two main reasons. Firstly, being adiabatically derived, the NO_x values are higher due to a higher contribution from thermal NO_x production via the Zel'dovich mechanism and a greater O/H radical pool for fuel NO_x formation. Secondly, pressures in industrial gas turbines are ~1 MPa (an approximate order of magnitude greater than the modelled pressure) and elevated pressure can significantly reduce NO_x (see Section 2.3.3).

The NO_x concentrations for the 10%$_{vol}$ CH_4 and 15%$_{vol}$ COG blends are sufficiently similar that they overlap between mechanisms (as did their AFT results). The 10%$_{vol}$ COG blend, produced lower NO_x concentrations than the other two blends, for the Φ values for which results were forthcoming. The lower NO_x was likely due to the lower AFTs. Additionally, more favourable kinetics resulting from the higher water content of the 10%$_{vol}$ COG blend could have reduced NO_x further, as discussed in Section 2.3.5 and as observed by Pugh et al. (2019) [93]. The 10%$_{vol}$ COG blend was able to achieve below

threshold concentrations for the Tian mechanism only, having failed to give results for an Φ of 1.2 when using the Okafor mechanism. This failure suggests significant problems with reactivity over the low-NO_x range of Φ for this blend, especially when one considers that these are adiabatic conditions offering higher reactivity than would apply in reality. Essentially, both mechanisms predict significantly lower reactivity for the 10%$_{vol}$ COG blend when compared to the other two AV blends, with failure to react at an Φ = 0.15 less than for the 15%$_{vol}$ COG blend.

The simulated results for CO product, as shown in Figure 3.16, were very closely matched between mechanisms, for all cases, with an almost complete overlay of results.

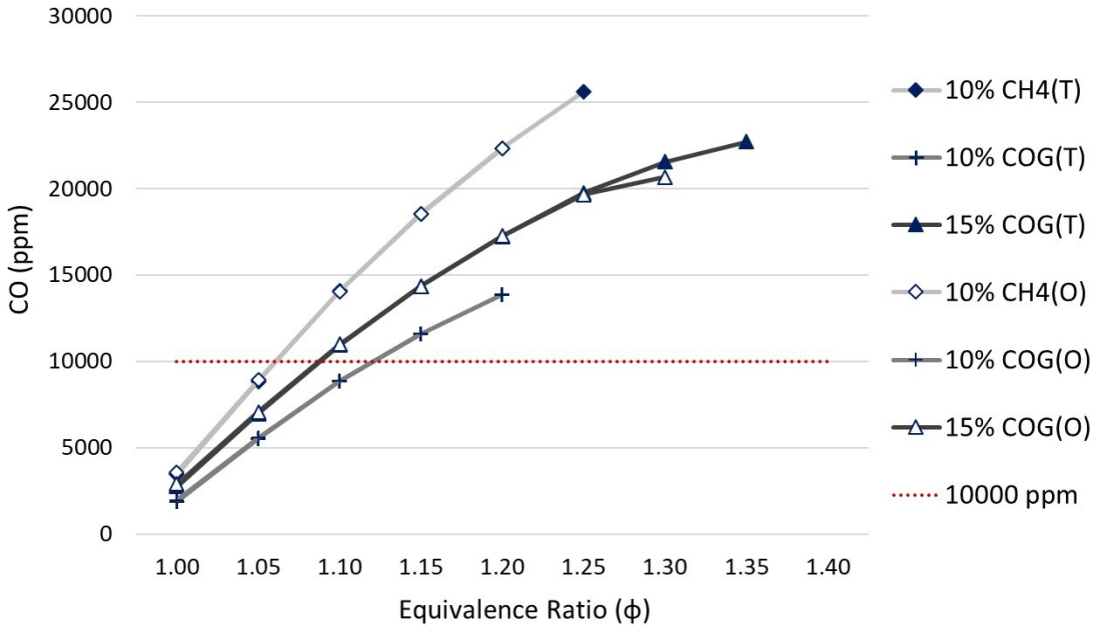

Figure 3.16 CO concentration (dry) by Φ for AV blends – reactor network (1 atm, 550 K inlet)

Both the 10%$_{vol}$ CH_4 and 15%$_{vol}$ COG blends cross the set threshold value between Φ 1.05 and 1.1, while 10%$_{vol}$ COG crossed at Φ > 1.1. As expected, this was the same trend as was found in the equilibrium modelling, with similar CO concentrations (i.e. < 10% higher for kinetic modelling at Φ = 1.1). At Φ = 1.1, CO (and ultimately CO_2) for the 10%$_{vol}$ CH_4 blend is ~30 to ~60% higher than for the 15%$_{vol}$ and 10%$_{vol}$ COG blends, favouring these over the 10%$_{vol}$ CH_4 blend.

As Figure 3.17 shows, all the AV blends experience a rapid increase of NH_3 concentration in the product gases (i.e. NH_3 slip) at varying values of Φ, dependent on blend. The

reader should note that, unlike for other plots, it is necessary to use a logarithmic scale to best represent the rapidity of the increase for the range of Φ investigated. Ammonia slip is experienced at lower Φ for the least reactive blend (i.e. > 1.15) and > 1.2 for the others. With heat losses, the resulting lower reactivity would likely cause the NH_3 slip to occur at lower values of Φ, suggesting that Φ should be limited to ≤ 1.15, to avoid the progression of significant concentrations of NH_3 into a second leaner stage, where it would be a precursor for NO_x. As was the case with NO_x emissions, there is very little difference in the performance of the 10%$_{vol}$ CH_4 and 15%$_{vol}$ COG blends for NH_3 emissions and close agreement between mechanisms.

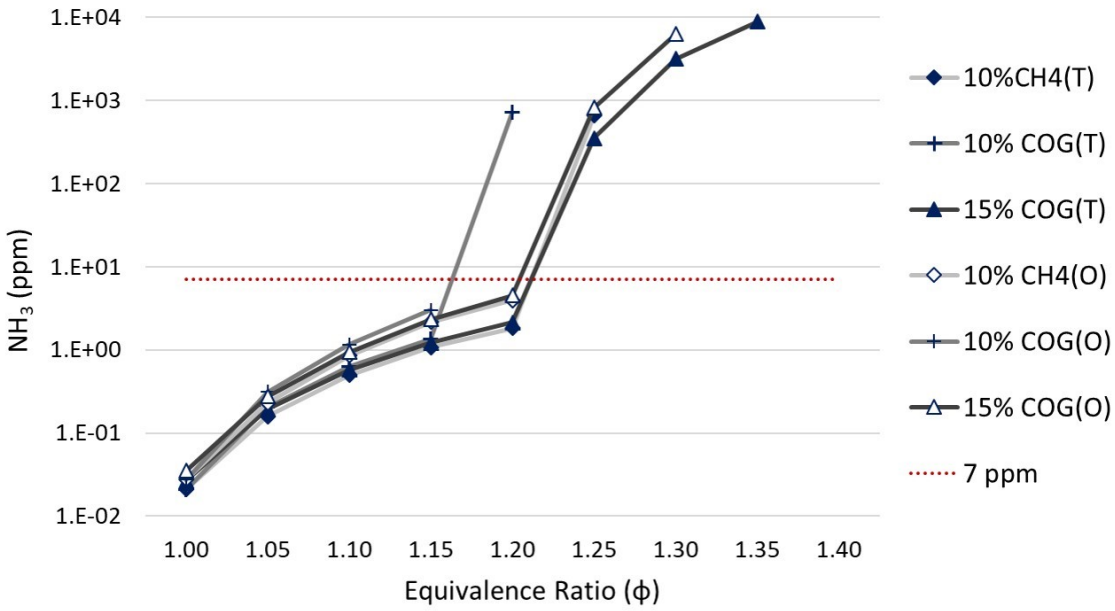

Figure 3.17 NH_3 concentration (dry) by Φ for AV blends – reactor network (1 atm, 550 K inlet)

As has been found in other similar NH_3 studies [102] (see Section 2.3.2), when examining the results of Figure 3.15 and Figure 3.17 together, it is evident that increases in Φ reduced NO_x concentrations, but, once Φ increased above a certain value, it lead to a rapid increase in NH_3 product concentrations. Therefore, there will be an Φ where the concentrations of both NO_x and NH_3 (a NO_x precursor) can be simultaneously minimised at molar concentrations of the same order of magnitude, introduced as Φ_{opt} in Chapter 2. This is not so dissimilar to the Φ_t variable used in this chapter (for simultaneously minimising both NO_x and CO) as both CO and NH_3 product represent unburned fuel.

The lower reactivity of the 10%$_{vol}$ COG blend suggests this blend would either fail to react or would experience unstable combustion at Φ values close to the blend's predicted Φ_{opt}, especially when considering heat losses are not included in this modelling. This finding favours the other two blends over the 10%$_{vol}$ COG blend. When considering the remaining two blends, there is no appreciable difference in the NO_x and NH_3 performance from which to choose a best candidate. The choice is therefore based on the CO product of the blends and the comparison of their S_L values. Not only does higher CO ultimately lead to higher CO_2 product but if the support fuel is sourced from outside the steelworks, as in the case of natural gas, it leads to extra CO_2 to that already produced by the process gases within the plant. As this study aims to mitigate CO_2 from steelworks sites, it is preferable that steelworks use a resource they already have (i.e. COG), as opposed to importing and consuming natural gas. Thus, the 15%$_{vol}$ COG blend is preferred over the 10%$_{vol}$ CH_4 blend. Additionally, the 15%$_{vol}$ COG blend has a higher S_L. For example, at Φ = 1.1, the S_L is ~22 cm/s, compared with ~19 cm/s for the 10%$_{vol}$ CH_4 blend. Hence, the 15%$_{vol}$ COG blend was the AV blend selected for further study. Referring to the results from Figure 3.15 and Figure 3.17, the Φ_{opt} for this blend under experimental conditions was predicted to be ~ 1.15 (considering the potential for NH_3 slip from heat losses). However, with S_L values calculated as significantly lower than those of the leanest CH_4 combustion (i.e. 21 cm/s versus 29 cm/s) it was considered unlikely that stable combustion would be achievable in the subsequent experimental campaign. At Φ = 1.15, the omission of the CO_2 and HCN components from the AV of the 15%$_{vol}$ COG/AV blend would reduce CO by ~38%, making CO emissions ~8,900 ppm.

3.5.3 Product Concentrations of the Selected AA Blends

Figure 3.18 shows NO_x concentrations for the AA blends, focussing on an Φ values of 1.1 to 1.3 for improved resolution of the range of greatest interest. Unlike for the AV blends, it is now the Tian mechanism which consistently predicts the higher NO_x values. This could not be due to any differences in modelled AFT, which have been shown to be very modest. For example, deviation between mechanisms is greatest for the pure AA cases at Φ = 1.2, where the Tian mechanism predicts almost twice the concentration (191 ppm versus 111 ppm). At this Φ, it is the Okafor mechanism that predicts the higher flame temperatures (and hence the more favourable conditions for thermal NO_x).

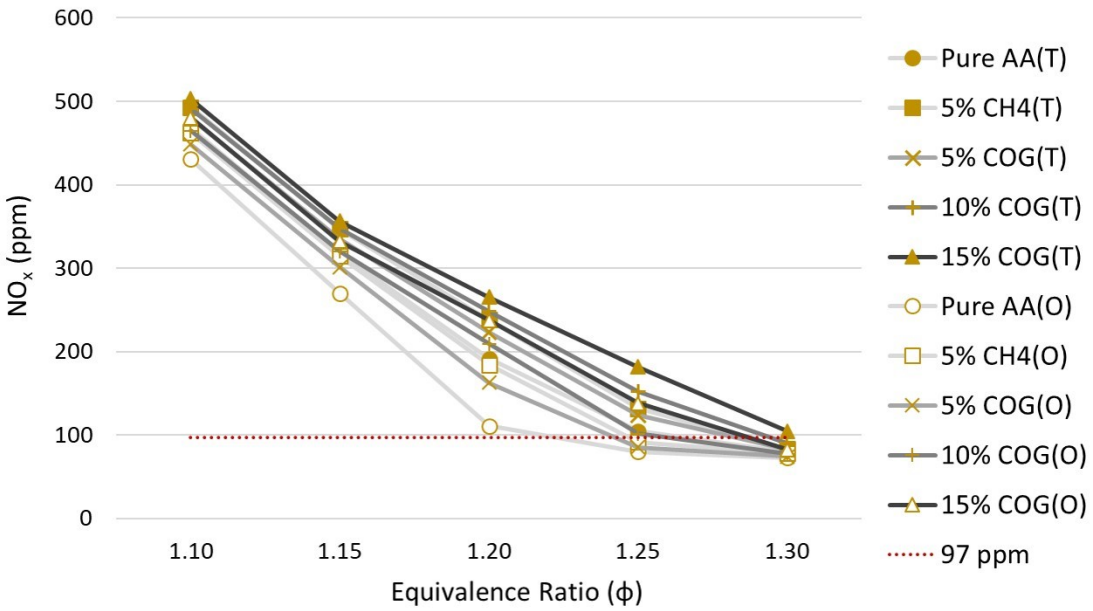

Figure 3.18 NO_x (dry, 15%$_{vol}$ O_2) by Φ for AA blends – reactor network (1 atm, 550 K inlet).

To explain the modelled differences in NO_x, the output files showing the emissions concentrations at the various stages of progress through the reactor network were examined, for both mechanisms for the pure AA case at Φ = 1.2. At the exit from cluster 1 the difference in NO concentrations was 1679 and 1423 ppm for the Tian and Okafor mechanisms respectively. This minor difference (15% less for Okafor) does not account for the more substantial difference (42% less) by the end of the PFR.

Just 0.8 cm into the PFR, the concentrations are 1003 and 532 ppm, with the Tian mechanism now modelling approximately twice the concentrations of Okafor. Therefore, a reaction path analysis was performed for the two mechanisms using pure AA at Φ = 1.2 at 0.8 cm into the PFR, to see the dominant NO formation and consumption paths. Temperatures at this location were almost identical at 2120 K and 2129 K for the Tian and Okafor mechanisms respectively. The most important reaction paths for NO consumption are shown in Figure 3.19. The rate of NO formation (increase in molar fraction) was 7.5 x 10^{-7} and 3.1 x 10^{-7} for the Okafor and Tian mechanisms respectively. The same two reactions, (i.e. HNO+M ↔ NO+H+M and N+OH ↔ NO+H), dominated the NO formation reactions for both mechanisms accounting for over 90% of the NO production. Although the NO formation rate was greater for the Okafor mechanism, rates of NO consumption for this mechanism were even more pronounced, with overall

values of 13.8 x 10^{-7} compared with just 4.6 x 10^{-7} for the Tian mechanism. Thus, the net consumption rate for the Okafor mechanism was found to be 6.3 x 10^{-7}, hence over four times higher than for the Tian mechanism (1.5 x 10^{-7}) at this PFR location. Figure 3.19 shows that this higher net consumption rate is not due to any particular reaction path, but rather that all NO consumption (and formation) paths have markedly higher rates for the Okafor mechanism.

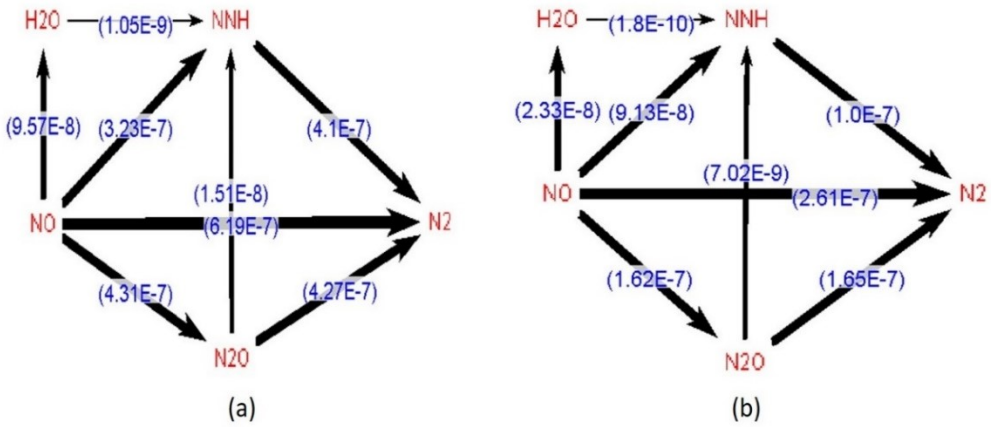

Figure 3.19 Reaction path analysis of NO consumption in the PFR (location 0.8 cm) for the pure NH_3 blend at Φ = 1.2 (inlet 550 K, 1 atm) for the Okafor (a) and Tian (b) mechanisms.

In agreement with the seminal work of Miller et al. (1983) [141] and many since, all these paths to NO consumption are via the combination of an N, NH or NH_2 radical with NO to form either N_2, N_2O or NNH in the first step, with H, O, OH or H_2O co-produced. As the concentration of the NH_3 derived radicals entering the PFR was similar for both mechanisms, only an increased rate of conversion of NH_3 to the N, NH and NH_2 radicals in the PFR would explain the increased rate of NO consumption for the Okafor mechanism. The reaction pathways for NH_3 consumption are shown in Figure 3.20. The conversion rates of NH_3 to NH_2, NH and N are indeed greater for the Okafor mechanism.

The concentrations of NH_3 out of cluster 1 are 9985 and 7149 ppm (wet basis) for the Okafor and Tian mechanisms respectively. Therefore, the Okafor mechanism maintains a higher NH_3 concentration in the PFR until ~4 cm downstream, despite the higher rate of NH_3 consumption. At 4 cm, the NO values (wet basis) are 428 and 926 ppm for the Okafor and Tian mechanisms respectively. Therefore, the ultimate relative difference in the NO_x readings (i.e. ~double for Tian) is already established in the first 4 cm of the PFR.

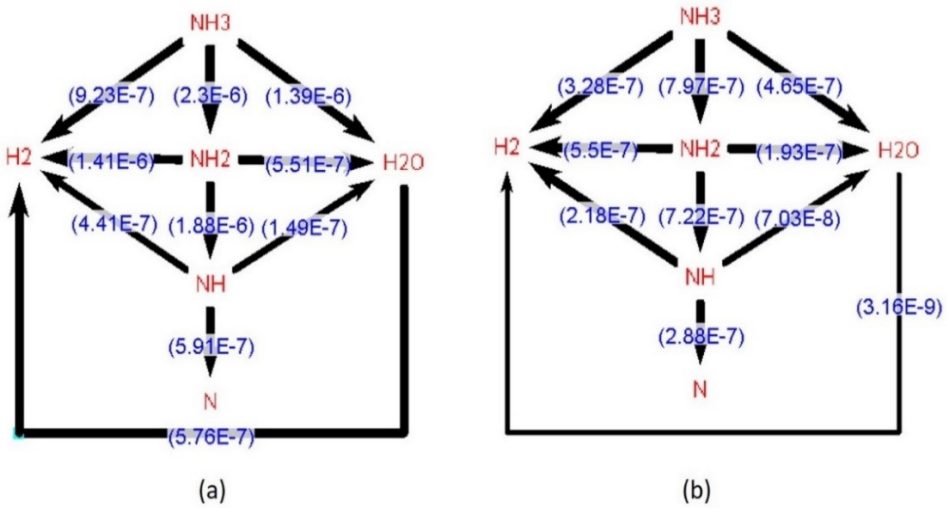

Figure 3.20 Reaction path analysis of NH_3 consumption 0.8 cm into the PFR for pure NH_3 at Φ = 1.2 (inlet 550 K, 1 atm) for the Okafor (a) and Tian (b) mechanisms.

This difference in modelling is because, although the Okafor mechanism has incorporated many important NH_3 oxidation reactions from the Tian mechanism into GRI-mech 3.0, the NH_3 reactions do differ nonetheless between the two mechanisms. For example, on brief inspection of the input files there are five reactions listed in the Tian mechanism for the forward conversion of NH_3 to NH_2 and only three for the Okafor mechanism. Two of these three shared reactions, have the same values in both mechanisms, but the values of the third reaction (NH_3+H = NH_2+H_2) differ. These are reversible reactions and there are other reversible reactions where NH_3 is described as a product, with NH_2 as a reactant, which will also contribute to the overall NH_3 consumption rate. Thus, differences in the many NH_3 conversion equations would account for the higher NH_3 consumption rates for the Okafor mechanism, influencing radicals production (NH_2, NH and N) and their availability for NO reduction reactions. It is likely that this tendency would hold true for all the AA blends and is just more pronounced for the pure AA case. As was described in Chapter 2, the Tian mechanism was validated for many blends including pure NH_3, whereas Okafor mechanism validation was conducted on blends of ≤ 30%$_{vol}$ NH_3. Hence, the effects of some of the Tian mechanism NH_3 oxidation reactions may not be fully recognised by the Okafor mechanism, when modelling high NH_3 percentage blends. This suggests the Tian mechanism may be a marginally more reliable emissions predictor for the high percentage NH_3 blends selected for this study.

In any event, for most cases the differences between mechanisms is minimal. Variation in NO_x levels across blends is modest, especially when excluding the results for the pure AA blend. For example, at Φ = 1.15, NO_x concentrations for the Tian mechanism are 329 ± 27 ppm across all blends, excepting pure AA. Thus, either mechanism is suitable for predicting NO_x values, especially for the more reactive blends.

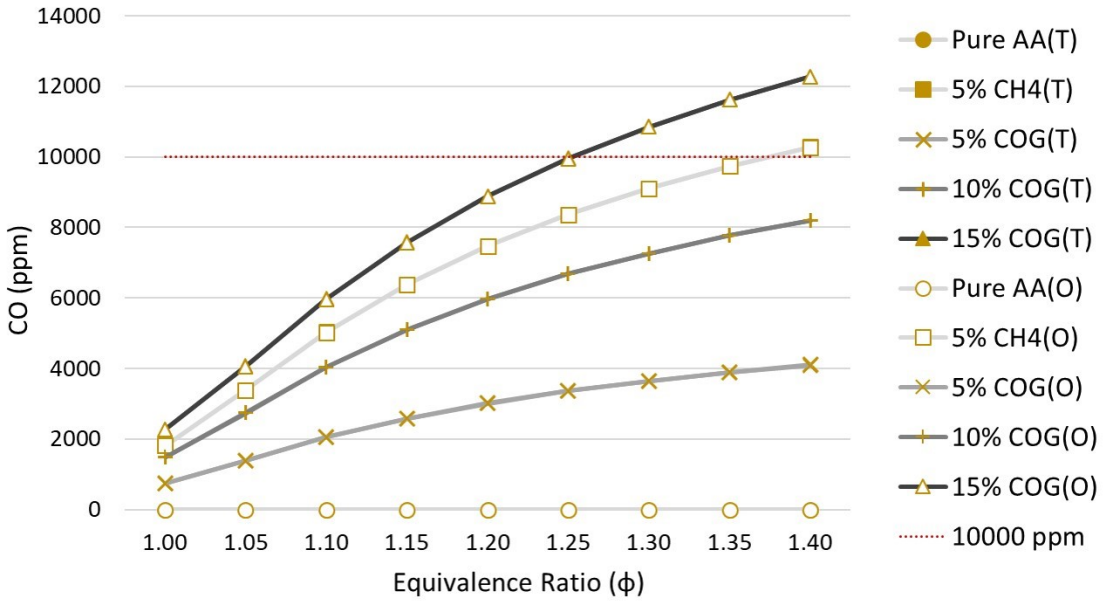

Figure 3.21 CO (dry) by Φ for AA blends – reactor network (1 atm, 550 K inlet).

As was the case for the AV blends, the CO results for the two mechanisms completely overlap, as shown in Figure 3.21, and so half of the plots are obscured by those of the alternative mechanism. As expected, CO concentrations for the AA blends are considerably lower than for the corresponding AV blends. At Φ < 1.25, all are simultaneously under the chosen CO threshold.

Again, as was the case for the AV blends, Figure 3.22 predicts that the least reactive AA blends are most prone to NH_3 slip. The Okafor mechanism predicts that NH_3 product concentrations for many of the AA blends breach 7 ppm (dry basis) at far leaner Φ values than for the Tian mechanism. Thus, limiting selection to the most reactive blends and an Φ < 1.3, should help to minimise the likelihood of excessive slip when factoring for heat losses. Once again, this difference can be accounted for in the difference in NH_3 consumption chemistry between the two mechanisms.

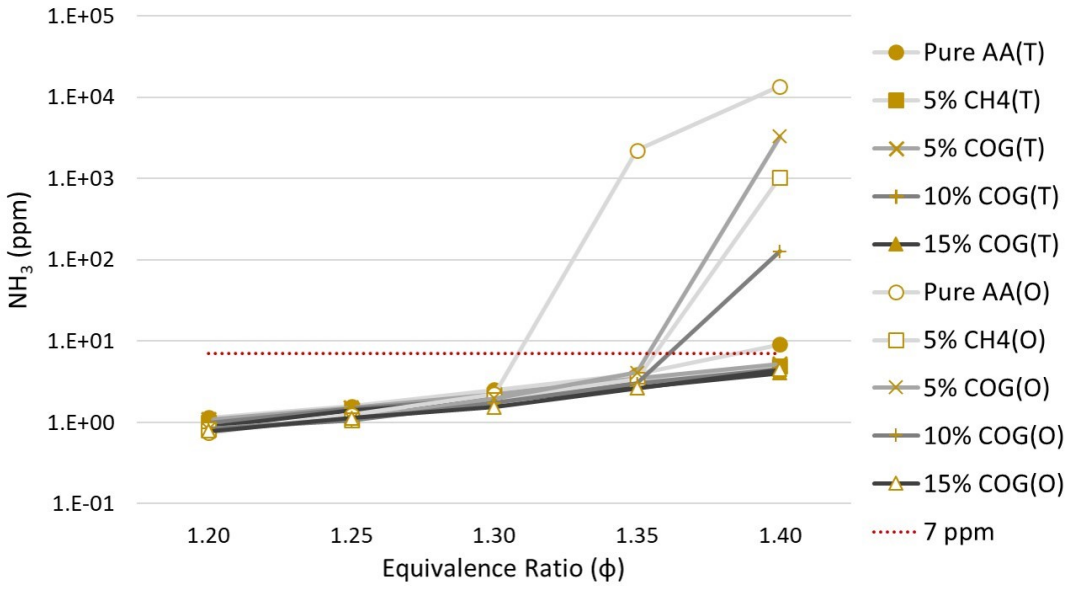

Figure 3.22 NH_3 (dry) by Φ for AA blends using Tian and Okafor mechanisms – reactor network (1 atm, 550 K inlet).

In summary, for all AA blends at an Φ = 1.25, the NO_x concentrations are < 200 ppm, the CO emissions are < 10,000 ppm (the chosen threshold) and the risk of excessive NH_3 slip is minimised for the most reactive blends. At this Φ, the 15%$_{vol}$ COG blend is the only blend for which both mechanisms agree a S_L within the range for fuel-lean CH_4 combustion in conventional gas turbines is achievable. Any differences in NO_x emissions between the most reactive blends is relatively modest. Consequently, the most reactive AA blend, 15%$_{vol}$ COG, is chosen for further investigation with a predicted Φ_{opt} of ~1.25.

3.5.4 NO_x Emissions at Elevated Pressures for the Selected Blends

This chapter has been concerned with selecting the best potential blends of AA and AV with the support fuels available (on a steelworks site) with which to proceed to experimental investigation. Thus, the emissions were modelled at atmospheric pressure, to reflect the conditions under which the subsequent experimental campaign was to be conducted. However, this did not take account of the potential for considerable NO_x reductions when operating at typical gas turbine pressures. This is investigated later in Chapter 5, using an improved reactor model, further developed utilising the experimental results discussed in the next Chapter (Chapter 4). The improved reactor model is also used to model the primary stage N_2O emissions.

3.6 Chapter Summary

- **Under equilibrium modelling**, five AV blends and pure AV simultaneously satisfied the stated NO_x and CO thresholds, within the Φ range modelled (inlet conditions of 550 K and 1 atm). Four AA blends and pure AA did the same. Therefore, from 78 initial potential NH_3 fuel blends, **11 blends progressed to the next stage of evaluation.**
- The **equilibrium modelling suggested** the optimal balance of NO_x versus CO product was centred between **Φ 1.05 to 1.1 for the selected AV blends** and **Φ 1.15 to 1.25 for the AA blends**, under the modelled conditions.
- The **carbonaceous components** of AV (CO_2 and HCN) only represent 4%$_{vol}$ of the AV composition. However, for the AV blends, the potential contribution of these components to CO (and ultimately CO_2) emissions is significant. **Their removal would carry significant advantages** for carbon emissions reduction.
- In consideration of the kinetic modelling results for S_L and emissions, **AA with 15%$_{vol}$ COG and AV with 15%$_{vol}$ COG were selected as the best blend of each type** with which to proceed to an experimental investigation. However, blends with ±5%$_{vol}$ COG support (i.e. 10 and 20%$_{vol}$ COG support) will also be investigated to verify the simulated results.
- The Okafor mechanism (having been validated for blends of ≤ 30%$_{vol}$ NH_3) lacks some NH_3 chemistry present in the Tian mechanism. This may lead to different emissions predictions for pure NH_3 in particular. Thus, the **Tian mechanism is preferred for modelling high NH_3 percentage blends**.
- For kinetic modelling (1 atm), the selected blends **Φ_{opt} values** were predicted to be **~1.15 for AV** with 15%$_{vol}$ COG and **~1.25 for AA** with 15%$_{vol}$ COG.
- The **simulated S_L** for the selected AA blend sat within the range for very fuel-lean natural gas combustion, **suggesting stable combustion of the AA blend may be possible in conventional systems**. This was not the case for the selected **AV blend**. A **halving of the water content** (simulated by a 50:50$_{vol}$ blending of AA/AV) increased S_L to within the aforementioned range, suggesting this level of water reduction may be necessary for achieving stable combustion. Chapter 4 discusses how a halving of the H_2O component can be practically achieved.

Chapter 4 Primary Stage Experimental Campaign

4.1 Experimental Campaign Method Introduction

The experimental campaign discussed in this chapter investigates the flame stability of the chosen blends in the primary combustion stage (i.e. whether stability reflects normal or abnormal operational flame behaviour in a gas turbine combustor) and also aims to find the experimental Φ_{opt} values for all blends tested. Operation of the primary combustion stage at a blend's Φ_{opt} simultaneously minimises the NO_x and NH_3 emissions leaving the primary stage of combustion, that in turn minimises NO_x exhaust emissions from the second stage (as NH_3 is a precursor for NO_x). The anhydrous (AA) and aqueous NH_3 (AV) blends are investigated with 10, 15 and 20%$_{vol}$ COG support to verify whether 15%$_{vol}$ support can be upheld as optimal, as was predicted by the simulations.

The experimental campaigns described in this thesis were conducted at Cardiff University's Gas Turbine Research Centre, known as the GTRC. The GTRC has a unique gas mixing facility, capable of blending up to five gaseous streams, in real time. A combination of needle valves and coriolis mass flow meters of varying capacity are on each of the five supply lines and are controlled and monitored remotely from the facility's control room.

The GTRC has a model gas turbine combustor rig. The premixed swirl burner assembly used in this rig is representative of a typical industrial gas turbine assembly. The geometry of the burner (discussed later in the chapter) is optimised for NH_3/H_2 combustion, in light of previous related studies conducted at the facility [89–93]. This assembly has been previously employed in the successful combustion of NH_3/H_2 blends with steam addition, with favourable NO_x and unburned fuel emissions [93].

4.2 Fuel Compositions

4.2.1 Ammonia Vapour (AV) Experimental Composition

In Section 2.4.2 a representative blend for industrial AV was derived from the literature. In steelworks the AV waste stream is produced and maintained as a vapour (e.g. at ~370 K for 39%$_{vol}$ NH_3) ahead of its destruction (or conversion), in a continuous process [58,

62]. For the experimental work in this study, there is no facility to store a representative AV blend as a vapour, and so a surrogate blend of steam and vapourised AA has been used instead, i.e. omitting the H_2S, CO_2 and HCN.

For this experimental campaign, it is the essential combustion properties of the original, representative AV blend, that are represented (as closely as practically feasible) using the steam and NH_3 vapour flows. This approach serves to make the combustion behaviour studied relevant to the results of the preliminary numerical modelling, which used the representative AV blend.

The AV blend components H_2O (61.8%$_{vol}$) and CO_2 (1.7%$_{vol}$) offer no heating value to the fuel. They do, however, absorb thermal energy from the flame, serving to cool the flame, thus lowering overall reactivity and therefore flame stability. At 2000 K (approximating the flame temperature), the specific heat capacity of CO_2 is 60.43 kJ/kmol-K versus 51.14 kJ/kmol-K for H_2O [75]. Therefore, to represent the cooling effects of the CO_2 via the substitution of additional water, the percentage of CO_2 in AV has been multiplied by the ratio of the heat capacities (i.e. 1.182) and added to the water component giving 63.8%$_{vol}$ H_2O. Naturally, any species substitution will kinetically effect intermediate chemistry. However, with such a small degree of CO_2 substitution, this is assumed to be negligible.

The H_2S and HCN components of AV, have LHVs of 517.9 kJ/mol and 623.3 kJ/mol respectively, as derived from the Aspen Plus program database [142]. Ammonia's LHV is comparatively low at 316.8 kJ/mol. Multiplying the H_2S component (2%$_{vol}$) by 517.9/316.8 and the HCN component (2.3%$_{vol}$) by 623.3/316.8 and adding them to the NH_3 percentage (32.2%$_{vol}$) can account for their thermal contribution in terms of a revised NH_3 fraction, giving a total NH_3 fraction of 40.0%$_{vol}$.

The sum of the H_2O and NH_3 percentage mole fractions is 103.8%, so both numbers were normalised to 100%, giving 61.5%$_{vol}$ H_2O and 38.5%$_{vol}$ NH_3 for the composition of the simplified experimental AV blend. When reflecting on the AV compositions found in the literature (see Section 2.4.2), the molar contributions of either of the two components in this simplified AV blend are not outside of the variations found in the AV produced in actual processes. It is noted that there is 4%$_{vol}$ more fuel-bound nitrogen in the simplified

AV blend (38.5%$_{vol}$) than the representative AV composition (34.5%$_{vol}$). This represents an 11.6% increase in the moles of fuel-bound nitrogen available for oxidation during combustion.

4.2.2 Humidified Ammonia

Given the issue of low predicted flame speeds, as identified in Section 3.4 for the AV with 15%$_{vol}$ COG blend, and the suggestion that halving the H_2O component would raise the flame speeds to within the range of fuel-lean CH_4 combustion in gas turbines, a low water (30%$_{vol}$ H_2O with 70%$_{vol}$ NH_3) blending has also been investigated in this experimental campaign (with 10, 15 and 20%$_{vol}$ COG support as for the AA and AV blends). This low water blend is henceforth termed humidified ammonia (HA). In composition terms (i.e. H_2O_{vol} content by volume) HA sits approximately halfway between the AA and AV blends, enabling the identification of trends in behaviour as water content changes for the humidified NH_3 blends. HA practically represents a blending of AA from the overhead stream of the fractionating tower in a Phosam plant, with the fractionating column inlet at the base of the tower (~80%$_{vol}$ H_2O with 20%$_{vol}$ NH_3). The HA blend therefore not only represents a blend free of the impurities H_2S, HCN and CO_2, with the associated benefit of minimising the formation of carbon and sulphur oxides, but also facilitates easy long term storage of the fuel (due to the modest partial pressures of NH_3 and H_2O and removal of highly toxic vapour phase HCN and H_2S). Direct use of the fractionating tower's inlet stream also saves energy from reduced flows through the tower. At 80%$_{vol}$ H_2O in the fractionator inlet stream, the relative molar blending for the HA blend would be 1.67 moles of overhead AA to every mole of fractionator inlet stream, saving 37.5% of the tower's energy when compared with processing all the H_2O/NH_3 stream to AA overhead product. Naturally, the H_2O fraction of 30%$_{vol}$ is easily modifiable with different proportions of the overhead and pre-fractionator streams.

The humidity of this study's HA blends was compared to that of NH_3 blends used in a previous study conducted using the same rig [93], to predict comparative effects of humidity on reactivity. The blends' relevant details are summarised in Table 4.1. The most humidified HA blend to be tested in this campaign (i.e. 10%$_{vol}$ COG/HA) comprised

8.3%$_{vol}$ of H_2O in the fuel/air premix. This is slightly less than the maximum humidification percentage of the 30%$_{vol}$ H_2/NH_3 blend successfully investigated in the study conducted by Pugh et al. (2019) [93] (at 9.6%$_{vol}$). Thus, while the HA blend is less reactive than the blend used in the Pugh et al. (2019) study (i.e. 10%$_{vol}$ COG versus 30%$_{vol}$ H_2), the HA blend is delivered at a much higher inlet temperature (550 K versus 423 K) and with lower H_2O, so the HA blend's reactivity could be considered broadly comparable, suggesting equivalent flame stability. In contrast, the 10%$_{vol}$ COG/AV blend's considerable H_2O component (22%$_{vol}$), makes it a far less reactive blend than those successfully, previously investigated.

Table 4.1 The comparative humidity of NH_3-air blends used in this rig [93].

Fuel blend	Φ	Inlet Temperature (K)	% H_2O in the fuel/air premix
10% COG/HA	1.2	~ 550	8.3
30% H_2/NH_3	1.2	423 ± 5	9.6
10% COG/AV	1.1	~ 550	22.0

4.2.3 Coke Oven Gas (COG) Experimental Composition

The COG gases were supplied, pre-mixed, in two 40 L cylinders. Due to the high costs of premixed gases, some blend simplification was required. The primary considerations for the blend simplification were as follows:

1. Hydrogen should differ as little as possible due to its influence on flame speed and its low combustion air requirements (which effects bulk mass flow).
2. Inert gases (N_2 and CO_2) should remain as close to the original percentages as possible.
3. The carbon content should be as representative as possible.

Therefore, it was decided that CH_4 could be substituted for the small amounts of ethene (C_2H_4) and ethane (C_2H_6) while the H_2 and inert gases were rounded up to their nearest volume percentages. The simplified composition requested from the supplier is given in Table 4.2 along with the certified compositions of the two cylinders provided and the comparative heating values.

Table 4.2 Comparative composition and heating values of experimental COG versus COG from the literature.

COG Composition	Mole Fractions of Component Gases							MJ/kg (LHV)	MJ/Nm^3 (LHV)
	H_2	CH_4	CO	N_2	CO_2	C_2H_4	C_2H_6		
COG - Literature	0.608	0.242	0.07	0.039	0.019	0.017	0.005	40.59	17.43
COG - Simplified	0.61	0.26	0.07	0.04	0.02	0	0	40.16	16.78
Cylinder 1	0.6063	0.262	0.0712	0.0401	0.0204	0	0	39.94	16.82
Cylinder 2	0.6043	0.263	0.0717	0.0405	0.0205	0	0	39.81	16.84

The LHVs of the two COG gas cylinders supplied were < 2% and < 3.5% lower than those of the literature derived composition, for mass and volumetric bases (273 K and 1 atm) respectively. Therefore the fuel blends are considered to adequately reproduce the representative composition derived from the literature.

Henceforth, all compositions given should be assumed to be on a volumetric/molar basis unless otherwise stated. The molar compositions of the three fuel blends (i.e. AA, HA and AV with 15% COG) experimentally investigated are summarised in Appendix A.2a (using the simplified AV and COG compositions). The compositions of the 20% and 10% COG experimental fuel blends, are to be found in Appendices A.2b and A.2c respectively. The proportion of the energy content provided by the NH_3 is 82.7% for the 15% COG/AA blend and 77.0% for the 15% COG/HA blend (LHV basis). It was much lower at 64.8% for the experimental 15% COG/AV blend.

4.3 Flame Power Selection

An interactive Excel workbook was created, containing all the data necessary for the calculation of the mass flows of fuel and air required to deliver any combination of the fuels mentioned in this study, at any specified power and Φ. This data includes molar masses for all reactants and their heating values (from the Aspen Plus database) and stoichiometric requirements for each component of the fuel blends. The composition of air was taken to be the same as was used in the equilibrium modelling. This workbook is submitted as supporting material.

To attain the intended 550 K fuel/air inlet temperature (e.g. simulating the recuperation of heat from the exhaust gases) the air and steam lines were preheated upstream of the

fuel/air mixing chamber. The fuels were not preheated, therefore it was necessary to overheat the air/steam line to compensate for the lower supply temperatures of the fuels.

Both NH_3 and COG have relatively low (and very similar) stoichiometric air requirements when compared with other gaseous fuels, at 3.58 for NH_3 (see Table 2.3) and calculated in Gaseq as 4.26 for COG (volumetric basis). The low air requirements of these fuels naturally limits the thermal capacity of the air supplied, especially under fuel-rich scenarios. While, overheating the air flow above 550 K was used to increase the thermal capacity, the air heater at the facility is limited to a maximum temperature of ~650 K. The high air temperature, coupled with low air flow rates, led to high heat losses, despite significant insulation. Hence, efforts were made to maximise air flows by maximising power.

The limiting factor for deciding the maximum power rating for this study concerns the maximum flowrate of NH_3 achievable. As was introduced in Section 2.1.2, the maximum sustained rate at which the NH_3 vapour can be withdrawn from its container is dictated by the heat transfer rate from the external environment. Considering the high latent heat of vapourisation of NH_3 represents approximately 7% of its LHV [79] the heat transfer required is significant for sustained vapour flows. For safety, the NH_3 container is stored outside the facility and is not externally heated other than by the ambient temperature (~20°C for this campaign), which translates to a theoretical maximum initial supply pressure of ~0.9 MPa from the container.

The fuel supply lines external to the building, leading from the container into the facility, are not heated, thus, temperature fluctuations along the pipework can arise for a combination of reasons. The first is the cooling of the NH_3 vapour due to the pronounced Joule-Thomson effect elicited from NH_3 vapour flows through constrictions/expansions, especially across the regulator valve. Secondly, there is intermittent cooling as the NH_3 passes through the sun-shaded portions of the pipework. The greater the delivery pressure, the greater the risk of liquid NH_3 condensing out of the vapour en route to the combustor, therefore, the exit pressure from the regulator for this testing was set to 0.4 MPa, which delivered a maximum sustainable NH_3 flow of ~1 g/s for the chosen blends.

This NH_3 flow (plus the relevant COG flow) is equivalent to a net thermal power of approximately 25 kW_{th}, almost twice the flow used in the reactor network numerical modelling. Aside from other effects on flame volume, the lower modelled flow makes the modelled flame volume comparatively smaller than the experimental flame volume, the implications of which are considered later in the model improvements, in Chapter 5 (Section 5.1.1). The NH_3 fuel line (line 4) is constructed from materials specifically rated for use with NH_3.

The NH_3 flows (< 1.2 g/s) were controlled and monitored using a needle valve and an Emerson CMF025 coriolis meter with base accuracy ±0.35% of reading. The product datasheet states that base accuracy only applies for flow rates above a specified level, calculated as per Equation 4.1 (taken from the data sheet):

$$\text{If flow rate} \geq \frac{\text{zero stability}}{(\text{base accuracy }\%) \div 100} \text{ then total accuracy} = \pm \text{base accuracy }\% \text{ of rate}$$

Equation 4.1

Zero stability is given as 0.027 kg/h for this model, requiring a flow rate of 7.714 kg/h or more for the base accuracy to apply. As flow rates for NH_3 were a maximum of 4.7 kg/h, total accuracy is instead calculated according to Equation 4.2:

$$\text{total accuracy} = \pm \left[\left(\frac{\text{zero stability}}{\text{flow rate}}\right) \times 100\right] \% \text{ of rate} \qquad \textit{Equation 4.2}$$

Therefore, the total accuracy values are calculated to be ±0.675%, ±0.725% and ±0.863% of rate for the 15% COG/AA, 15% COG/HA and 15% COG/AV blends respectively. The COG flow (of 0.07 to 0.27 g/s) was controlled remotely using a M14 Bronkhorst MFC with an accuracy of ± 0.5% of rate.

Air flow rates for 25 kW_{th} power, over the Φ ranges investigated for the fuel blends, were approximately 6-8 g/s. The Φ ranges experimentally investigated for the nine blends of COG with AA, HA and AV (at 20, 15 and 10% COG) were 1.05 to 1.3, 1.0 to 1.2 and 1.0 to 1.15, respectively, reflecting the differing predicted Φ_{opt} values and comparative reactivities of the blends, as found during the numerical modelling. The target mass flow rates of the air and fuels for all blends investigated, as calculated using the Excel workbook, are to be found in Appendix A.3.

4.4 The Steam and Air Delivery System

The steam fraction of the AV/COG and HA/COG blends was preheated and entrained with the preheated air, upstream of the mixing plenum of the combustion chamber. A schematic of the system is shown in Figure 4.1.

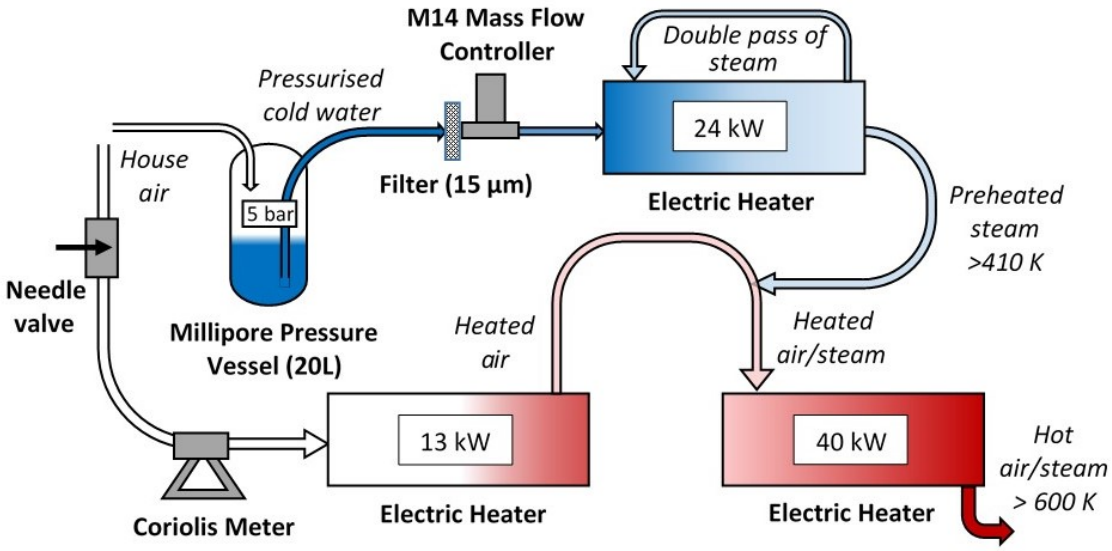

Figure 4.1 Schematic of the steam/air delivery system

In consideration of the anticipated high heat losses, all lines flowing heated gases were heavily insulated. The double-pass steam line (external to the 24 kW heater) and the preheated steam line (feeding into the heated air line) were thermally supported to sustain approximately 410 K, through the use of an external mesh heating system, wrapped around the lines, under the insulation.

Air at the facility (house air) is compressed to 7 bar_g (~0.8 MPa) using an Atlas Copco GA 45 variable speed drive compressor and is conditioned using a Beko Drypoint DPRA960 air dryer, so that it has a dew point of 256 K. A 20 L Millipore pressure vessel was pressurised using the house air regulated to ~ 5 bar_g (0.6 MPa). This facilitated the siphoning off of liquid water which then passed through a Bronkhorst M14 mass flow controller (MFC) with an accuracy of ±0.2% of flow rate (for liquids). The maximum required flow rate of steam was calculated as 1.7 g/s, or ~6 kg/h (for the 90% AV with 10% COG blend), thus, the pressure vessel provided ample capacity for several hours of testing. The needle valve for the air line (line 1 of 5) coupled with an Emerson CMF050

coriolis meter (base accuracy of ±0.35% of reading), enabled remote and accurate manipulation of the air mass flow (to 3 decimal places). As was the case for the NH_3 flows, the average air flows are too low to assume the base accuracy. The zero stability is given in the datasheet as 0.163 kg/h, so total accuracy is calculated as ±0.65% of reading (for an average flow of ~7 g/s). All fuel and air flow rates through the coriolis meters and MFCs are logged remotely, in the control room, as was all sensor data (e.g. thermocouple readings). All flowrate and sensor data was logged at 1 Hz. The fuel and air flows were averaged for each test sampling period and these averaged flows are given in Appendix A.4.

4.5 The High Pressure Optical Chamber and Swirl Burner

The in-line air heaters (as shown previously in Figure 4.1) were used to precondition the inlet plenum, burner and combustor to the specified inlet temperature of 550 K, prior to ignition. Ignition was achieved using a CH_4 pilot. The use of the pilot was continued until self-sustained combustion of the first experimental blend was assured. Subsequent test points were conducted without interruption, except for when reigniting for the second day of testing. On the second day of testing, the first test point was a repeat of a test point from the day before, to first establish equivalent conditions and results before further data points were investigated. Test points were sequenced between higher and lower percentages of COG and between richer and leaner test points to minimise the risk of sustained upstream cooling of the NH_3 fuel lines and also to increase air flows intermittently, to help sustain inlet temperatures.

Figure 4.2 is a diagrammatic representation of the combustion rig used in this study (as viewed from above). The inlet air/fuel flows are split upstream into two approximately equal flows that enter from opposite sides of the inlet plenum, to promote turbulence in the inlet flow, which in turn promotes turbulence and mixing downstream. The premixed blend then proceeds to the mixing plenum and on through the swirl burner, exiting at the burner nozzle. The primary purpose of the lance in the model gas turbine assembly is for liquid fuel injection, which is not relevant to this study. In this instance, the lance (outside diameter 18 mm) provides a bluff body stabilisation location within the swirl burner exit nozzle (internal diameter 40 mm).

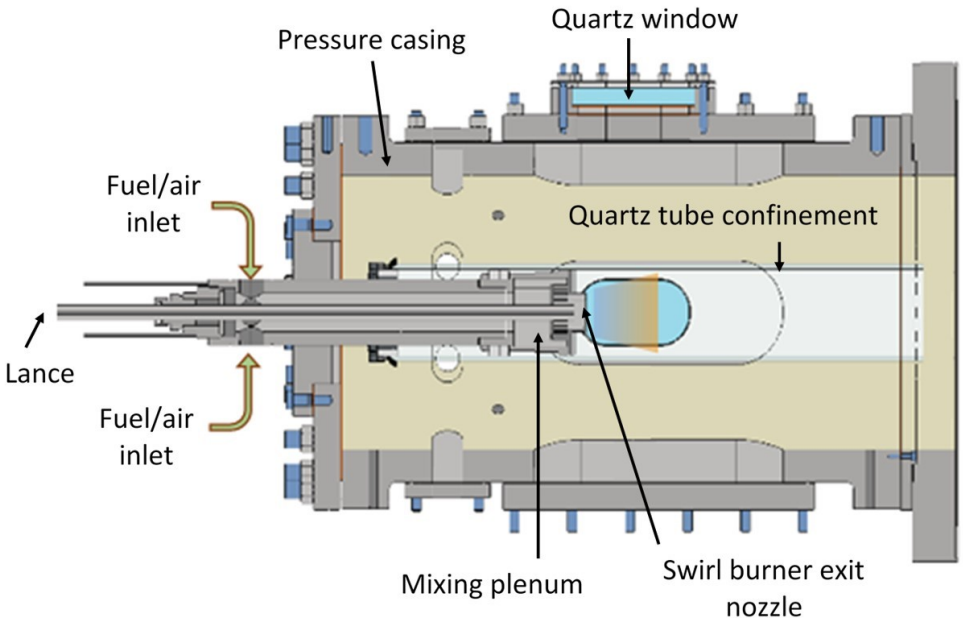

Figure 4.2 Diagrammatic representation of the combustion rig.

There are thermocouples inside the mixing plenum (for measuring the inlet temperature), at the lance tip and at the burner face. A ceramic covering of the burner face encircles the base of the nozzle, insulating the mixing plenum and swirl burner from the heat of the combustor. There are pressure transducers at the burner face and inside the mixing chamber that can, in combination, monitor changes in pressure between the two zones. Another two pressure transducers, situated towards the top edge of the circular burner face (90° apart), capture high frequency (kHz) dynamic pressure fluctuations from the system. The four transducers together facilitate the monitoring of thermoacoustic instabilities. The inlet temperature and combustor pressure were averaged for each sampling period and are also detailed in Appendices A.4.

The flame is contained within a 600 mm long, quartz tube confinement, 100 mm in diameter. Thus, the expansion ratio of the confinement's internal diameter to the internal diameter of the burner exit nozzle is 2.5. The open-ended quartz tube is housed inside a pressure vessel enabling the rig to be used for pressurised combustion experiments and eliminating any atmospheric dilution of the exhaust emissions. Figure 4.2 shows the quartz tube, which extends upstream beyond the burner face and downstream, beyond the limits of the pressure casing and towards the gas sampling zone. Thus, the length of tube between the nozzle exit and the tube's exit totals 385

mm. The tube is not enclosed as it passes out of the pressure chamber and into the ducting beyond. The pressure casing is fitted with quartz windows (one on top and one to the side) allowing for non-intrusive, optical observations of the flame structure in the axial plane. The heat transfer from inside the quartz tube to the surroundings at ambient temperature is buffered by the heated gases inside the pressure casing, reducing the quenching conditions at the quartz boundary when compared with an uncontained confinement. An exhaust thermocouple is situated at the exit of the quartz tube.

This study uses a nine-fin swirl burner of radial-tangential design, with a calculated geometric swirl number of 0.8 (see Section 2.2.1), as detailed in Figure 4.3.

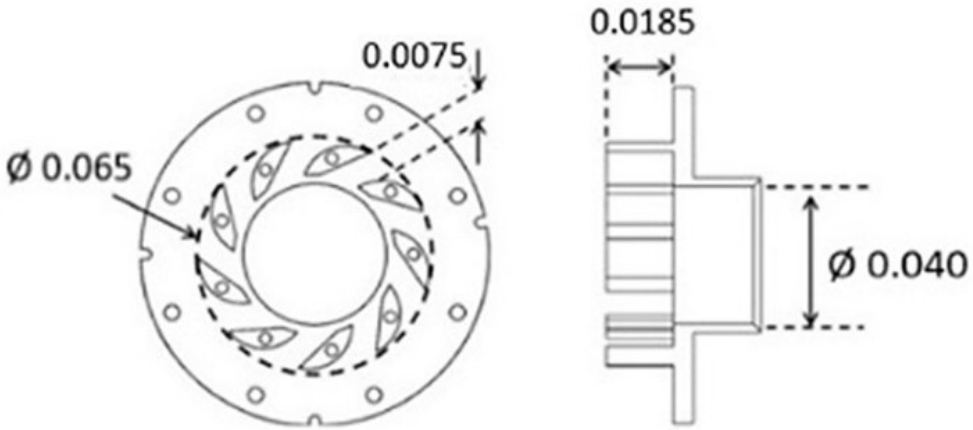

Figure 4.3 Geometry of the swirl burner (in metres).

4.6 Emissions Sampling and Measurement

4.6.1 Emissions Sampling

On exiting the quartz tube, the hot combustion gases enter water cooled pipework, internal diameter 150 mm, within which a water-cooled back-pressure valve is installed. Partial closure of this valve (via remote control) facilitates the incremental elevation of combustor pressure. For experiments at atmospheric pressure, elevation of pressure is extremely modest at < 0.1 bar (0.01 MPa), serving to restrict the entry of air from outside (i.e. wind), thus minimising consequential upstream turbulence effects. This valve is utilised to greater effect, for the elevated pressure work in Chapter 6.

Suspended in the centre of the water-cooled pipe and facing into the flow of combustion gases (~150 mm downstream of the quartz tube exit), is a multi-point equal area probe,

as shown in Figure 4.4. The holes are spaced to enable distributed sampling across the circular cross-section of the exhaust pipe, to ensure the sample is representative of the emissions concentrations throughout the entire exhaust flow. Thus, there are more holes further from the centre, so each hole can draw its sample from the same-sized cross-sectional area of the flow (described by the circular diagram in Figure 4.4).

Figure 4.4 Image of the multi-point equal area probe

All nine withdrawn samples are immediately combined and pass through a water-conditioned pipe (water bath) at 433 K. This rapid cooling of the sampled gases suspends progress of the combustion chemistry. An electrically heated (to 433 K) 25 m pipe carries the samples to the control room for analysis.

The temperature of 433 K is somewhat higher than that which would be necessary to maintain this study's samples above their dew point. This is because the emissions measurement system at the GTRC performs in accordance with ISO 11042 (gas turbines exhaust gas emissions measurement and evaluation) [108] and is therefore capable of maintaining unburned hydrocarbons in the vapour phase, which is of particular relevance to the aerospace and automobile industry. Adopting this sampling method is standard practice, making these measurements directly relevant to the industry.

4.6.2 Sample Gas Analysis Suite

As previously discussed (in Section 3.1.3) the CO emissions were predicted to greatly exceed the maximum measurement scale of the CO analyser (by approximately one order of magnitude) necessitating the addition of significant amounts of dilution air

upstream of the gas analysis suite. On reaching the control room, the diluted samples were filtered before entering the heated pump unit (with PTFE diaphragm) in the gas analysis suite. The flow of the samples through the suite is shown schematically in Figure 4.5.

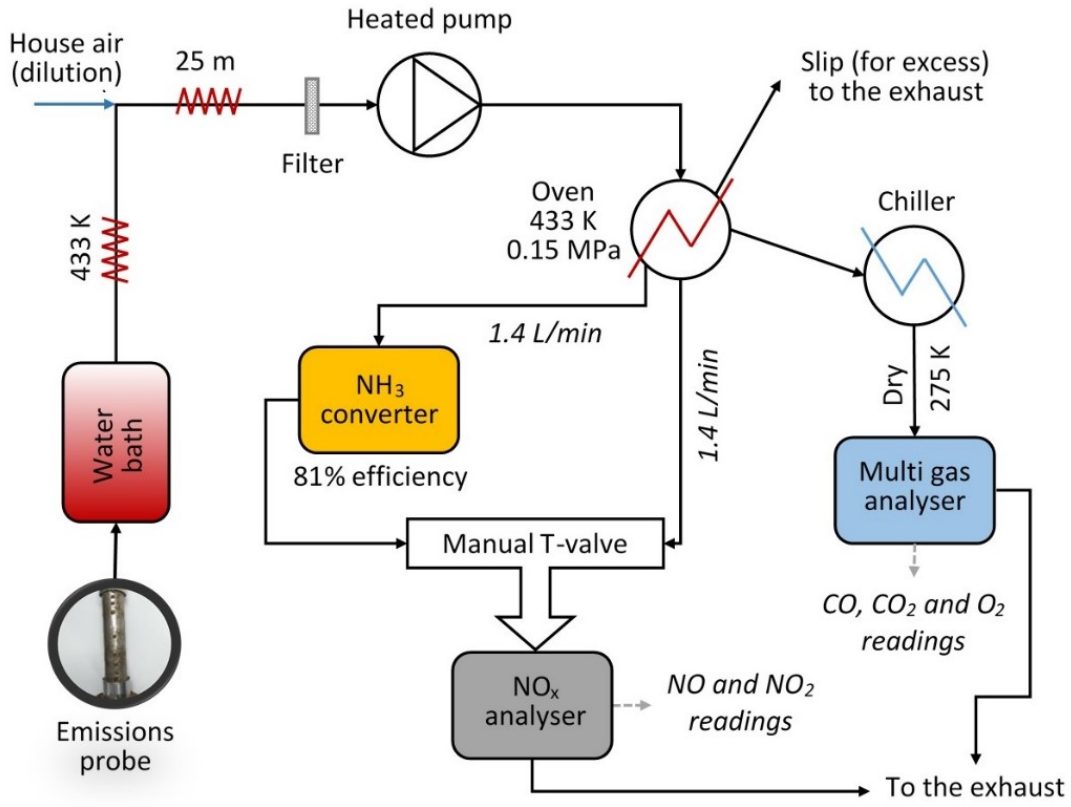

Figure 4.5 Flow diagram of samples through the gas analysis suite

The emissions gases sampled were NO, total NO_x, CO_2, CO, NH_3 and O_2. There was no facility for measuring N_2O or H_2O. The emissions were continuously logged (at 1 Hz) for the duration of the testing. Two analyser systems were used for the gas analyses, a Multi Gas Analyser (MGA) (Signal 9000) for CO_2, CO and O_2 and a heated vacuum chemiluminescence analyser (Signal 4000VM) for NO_x.

After the pump, the samples proceeded to the oven, which acted as a distribution facility for the suite. Four channels were used for the distribution of the sample. The first channel was available for either the NH_3 converter (converting NH_3 to NO) or for total (unburned) hydrocarbon (THC) measurement. As the analysis of NH_3 takes precedence in this study, the analysis of THC was sacrificed. The second channel was sent directly to

the NO_x analyser and the third was sent to the chiller prior to its use in the MGA. The fourth channel sends excess flow to the exhaust.

An NH_3 converter (Signal 410) with a conversion efficiency of 81% (as found during analyser calibration) was used to convert the samples' NH_3 emissions to NO in a one to one ratio according to Equation 4.3 below. Thus the concentration of NH_3 in the exhaust could be subsequently measured using the NO_x analyser. It can be seen from Equation 4.3 that the NH_3 converter needs O_2 (provided by the air) for the reaction to take place. The NH_3 is reacted with O_2 at 1023 K, over a platinum on alumina catalyst. As the combustion is fuel-rich, O_2 was provided by dilution air. The level of deoxygenation of the sample by the reaction remains relatively insignificant considering the NH_3 concentrations present, when compared to the total oxygen available from the air dilution, thus the NH_3 conversion is assumed to reach 81% efficiency.

Equation 4.3

$$4NH_3 + 5O_2 \rightleftharpoons 4NO + 6H_2O$$

The NO_x and NH_3 analyses were conducted hot and wet (i.e. no condensation of the water fraction). This was to prevent the loss of NO_2 from the gaseous sample, as NO_2 is readily soluble in water. Whether the NO_x analysis being performed at any particular instance was for a sample containing converted NH_3 or for one fed directly from the distribution oven, was dependent on the choice of inlet stream into the NO_x analyser. This choice was governed by the manual manipulation of a T-valve.

The samples sent to the MGA required a dew point of at least 10 K below the local ambient temperature. Thus, a chiller (operating at 275 K) condensed out the water vapour fraction upstream of the MGA, and the samples (CO_2, CO and O_2) were analysed on a dry basis. After sampling, all gases were sent to the exhaust.

4.6.3 Gas Analyser Measurement Methods

Details for the operation of the NO_x analyser are taken from the analyser's manual [143]. The NO_x analyser reacts ozone (O_3) with NO in a reaction chamber, to produce NO_2. The manufacture of the ozone takes place within the analyser in an ozoniser unit. Approximately 10% of the NO_2 produced is electronically excited as NO_2^*. The equation for the reaction is shown in Equation 4.4.

$$NO + O_3 \rightarrow NO_2^* + O_2 \qquad \textit{Equation 4.4}$$

$$NO_2^* \rightarrow NO_2 + h\nu \qquad \textit{Equation 4.5}$$

A photon with a wavelength of 300 to 600 nm is emitted on the return of the NO_2 to its ground state, as shown in Equation 4.5, where the energy of the photon is represented by Plank's constant (h) and the frequency of the photon (v). Thus, the process measures the chemiluminescence of the NO_2^* in the sample. The intensity of the emitted light is measured with a photomultiplier tube (PMT) and, as the intensity of the radiation emitted is proportional to the number of NO molecules in the optical path, the PMT signal is proportional to the concentration of NO in the sample. To maximise the proportion of NO_2^* emitting light (rather than losing the energy via collisions) low pressures (~1 kPa) are maintained within the reaction chamber. The NO_x analyser has an accuracy of better than ±1% of range. The uncertainty related to cross-interference from water in the sample, reduces NO_x readings by < 1% with $3\%_{vol}$ H_2O.

The NO_x analyser was calibrated using pure N_2 (for 0% NO concentration) and, having a linear relationship of intensity to sample concentration, one other gas of 40 ppm NO. The use of N_2 and one other calibration gas, was the calibration method used for all the other emissions analysed except CO_2, which is discussed later in this section. The calibration gases used had uncertainties of ±2% of their specified concentration. The measurement of sample NO_2 was achieved through the use of an NO_2 to NO converter unit (95% efficiency), also situated inside the NO_x analyser. Having initially established a measurement for NO, the sample is subsequently directed to the NO_2 to NO converter, before entry (once again) into the (ozone) reaction chamber, to obtain a total NO_x measurement. The analyser automatically subtracts the prior NO readings from the total NO_x readings and displays the difference as an NO_2 measurement.

The MGA uses non-dispersive infra-red for the measurement of CO and CO_2 and a paramagnetic sensor for the measurement of O_2. Most gases absorb infra-red radiation and the amount absorbed by different gases varies with wavelength. The CO and CO_2 analyser works by passing infra-red through a sample containing an absorbing gas and comparing the intensity of the radiation received by a detector, with the intensity of a

calibration gas or N_2, which does not (in a practical sense) absorb infra-red radiation. The analyser contains two infra-red optical sensors (for CO_2 and CO). It is necessary when measuring CO_2 to calibrate for slight deviation from a linearity between the output signal and concentration. Several calibration gases (3%, 6% and 9% CO_2 concentration and N_2), were used to input the calibration curve for CO_2 measurement.

O_2 is a highly paramagnetic molecule, meaning it is attracted to the strongest part of a magnetic field. The flow of O_2 in the analyser's magnetic field applies a force to sensing equipment. In resisting the force of the O_2 (via a self-correcting mechanism) the sensing equipment generates a current, proportional to the concentration of O_2 in the sample. NO and NO_2 are also paramagnetic, although to a much lesser extent. The influence of NO and NO_2 in the analyser's results are assumed to be negligible, due to their comparatively low sample concentrations.

Thus, maximum combined uncertainties for all emissions measurements are taken to be ± 5% of the temporally averaged reading, as used in similar published NH_3 combustion studies using the same rig and instrumentation [94, 103].

Maximum uncertainties in the calculation of experimental Φ are large, with maximum error bars capable of spanning much of the width of the plots. As the deviation of actual Φ from measured Φ is very similar between cases (because the fuel and air flows are similar), the plots simply shift together to a similar degree leaner or richer. Hence, comparative trends between blends will hold. Thus, at this stage, the uncertainty in Φ is not included. However, the uncertainty in Φ is considered in detail later, in Chapter 6, where the blends verified as optimal in this chapter's work, are again optimised in the primary zone, before the commencement of elevated pressure and secondary air-staging work.

4.6.4 Calculation of Sample Dilution

When combustion is fuel-rich it can be assumed that all O_2 in the sampled gases comes from dilution air, although this assumption becomes less valid as combustion approaches stoichiometry. The logged concentration of oxygen present in the dry samples was averaged for each experimental condition (test point). The oxygen concentration of the dry ambient air was measured ahead of each day's testing, so that

it could be used to calculate the dry dilution factor (DDF) for each test point sample obtained that day, according to Equation 4.6.

$$DDF = \frac{Ambient\ O_2\ \%\ Conc.}{(Ambient\ O_2\ \%\ Conc. - Sample\ \%\ Conc.)} \qquad \textit{Equation 4.6}$$

For CO and CO_2, analysed as dry, multiplying the measured emissions concentration by the DDF will give the undiluted concentration. For those samples that were measured wet (NH_3, NO and NO_2), it was also necessary to calculate a wet dilution factor (WDF).

The method for calculating the WDF is demonstrated using a simplified example, shown in Figure 4.6, where the wet undiluted sample has a H_2O fraction (a) of 40%$_{vol}$.

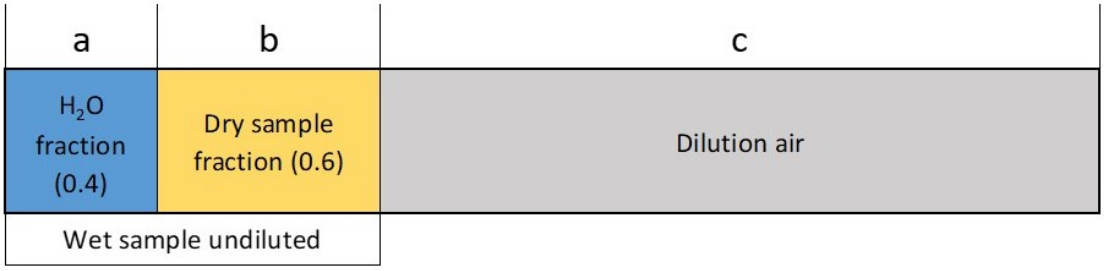

Figure 4.6 Example for the calculation of a sample's wet dilution factor

Taking the wet undiluted sample (a + b) as having a relative volume of 1, the dry fraction of the undiluted sample (b) has a volume of (1 – H_2O fraction), i.e. 0.6. The relative volume of the dry dilution air (c) to the sample volume is unknown, but the O_2 concentration for the dry diluted sample (b + c) is known and measured as 18%$_{vol}$. For simplicity, in this example the O_2 concentration of dry ambient air is taken to be 20%$_{vol}$.

The first stage of the WDF calculation is to find the DDF for 'b + c' using Equation 4.6, which in this case equals 10. Therefore, the ratio of dilution air to dry sample fraction in this example is 9:1. In other words, the relative volume of dilution air to the dry sample fraction is (DDF – 1) for this example and all cases calculated this way. The dry sample fraction (i.e. 'b') of the wet undiluted sample has a value of (1 - H_2O fraction), so in this example is 0.6. The dilution air in this example (c) therefore has a relative volume of (DDF – 1)*(1 - H_2O fraction) which is 5.4 times the volume of the wet undiluted sample.

Hence, the total volume of the wet diluted sample (a + b + c) = 6.4 times the volume of the wet undiluted sample (a + b), so the WDF is 6.4 for the example given.

Therefore, for the actual test results, the WDF is (a + b + c), where a + b = 1 and c = (DDF – 1)*(1 - H_2O fraction) and is calculated using Equation 4.7.

$$WDF = 1 + (DDF - 1) * (1 - mole\ fraction\ H_2O) \qquad \textit{Equation 4.7}$$

Therefore, the wet undiluted sample concentration of NO_x is calculated as shown in Equation 4.8.

$$[NO_x]\ undiluted = [NO_x]\ diluted * WDF \qquad \textit{Equation 4.8}$$

Emissions were continuously logged with time indents for synchronising emissions sampling with the other data loggers (e.g. fuel flows, etc.). This enabled averaged readings for all variables (e.g. temperature and air flow) to be calculated for any emissions sampling period. It was initially assumed that several seconds would be sufficient delay for readings to stabilise when switching between NO_x and NH_3 sampling periods when using the NO_x analyser. The aim was to have approximately 1 minute (i.e. ~60 data points) from which to average the readings for each sampling period. All emissions concentrations were calculated as undiluted in three ways, dry normalised to 15% O_2, dry without normalising for O_2 and wet (to enable experimental results to be used in Chemkin for the development of an improved model).

The O_2 readings specific to each measurement period (i.e. NO_x, NO, NH_3 in and NH_3 out) were averaged separately, to give precise dilution factors for each individual measurement. As NH_3 emissions are plotted alongside NO_x and NH_3 is a NO_x precursor, it is reported in the same way (i.e. $15\%_{vol}O_2$).

There was no facility for measuring the mole fraction of H_2O in the samples. Therefore, Gaseq was used to derive equilibrium values for the mole fraction of H_2O produced, by entering into the program the time-averaged fuel/air mass flows and the measured temperature and pressure readings, as logged for each individual test point. The slight

variation in COG compositions between cylinders was accounted for. It was assumed that any deviations of H_2O product concentrations from equilibrium would be insignificant.

4.7 Chemiluminescence Method

4.7.1 Chemiluminescence Observation Technique

High temperature combustion reactions are sufficiently energetic as to excite the electrons of the reacting species. Unlike for the NO_x analyser, which utilises a specific reaction, the emissions spectra of a flame will include a plethora of wavelengths. By filtering emissions spectra to include only those emissions within a narrow wavelength band, it is possible to characterise the structure of a flame in relation to a specific chemical species. However, some species e.g. CO_2, emit photons across a broad band of wavelengths and hence contribute to the signal intensity of any filtered light [144]. Given this fact and that the precise relationship of excited to non-excited species is an unknown, chemiluminescence intensity is indicative of the relative, rather than the absolute, concentration of any species.

The chemiluminescence of the excited OH radical (OH*) has been used in a number of recent studies to visualise flame structure in pure NH_3 [94, 103] and blended NH_3 flames [89, 90, 92–94]. Regions of highest OH* concentration are indicative of maximum localised heat release and flame front location [93] and thus OH* chemiluminescence is an established technique for appraising the structure of flames and locating where maximum NO formation is located. The images for this study were captured using a Phantom v1212 high-speed CMOS (complementary metal oxide semiconductor) camera, a Specialised Imaging SIL40HG50 high-speed image intensifier gated at 10µs, an ultra violet lens (78 mm, f/11) and a narrow bandpass filter selected specifically for measuring the often used $A^2\Sigma+\text{-}X^2\pi OH^*$ system of the OH* species (315 nm (±15 nm) FWHM) [103]. Full width half maximum (FWHM) indicates that at full width, the extremes of the wavelength range measured (i.e. 300 and 330 nm), the filter is allowing half of the maximum signal through. The camera was situated aiming horizontally through the side quartz window on the pressure casing and into the combustion

chamber. Images were captured such that the horizontal plane of the images represents the axial plane in the combustion chamber.

4.7.2 Chemiluminescence Image Processing

A manually focussed, single image of a target was captured to enable calibration. The target, a matrix of dots with a spacing of precisely 10mm horizontally and vertically, was positioned so that its central horizontal line of dots was in line with the radial centre of the burner nozzle exit. All image files for this study were captured in .cine 12 bit format. Phantom's PCC software program [145] was used to convert the image files to 12 bit .TIF format, for use with the programming language and numeric computing environment MATLAB (abbreviation of Matrix Laboratory), developed by MathWorks [146]. MATLAB's matrices oriented programming, makes it well suited to the mathematical manipulation of the 'grid' of pixel intensities, as found in images.

Once imported into MATLAB, adjustment of contrast and colourmap selection was used to enhance the target image for inspection. By counting the pixels between 7 dots (i.e. 60 mm) it was possible to scale for the test images giving an image resolution of 22.4 pixels/mm^2 or 4.733 pixels/mm. The burner centreline was located at pixel row 275.

All test point video files were captured at a frame rate of 4 kHz, giving a period of 0.5 s for each test case, equal to 2001 individual images. A shorter background video file was also captured, prior to combustion, and converted to 101 .TIF files. The background .TIF images were temporally averaged using MATLAB program BG_code.m (see Appendix C.1), to produce an unfiltered, average background image. This was achieved by summing the intensities of each pixel, across all 101 background images, into the corresponding co-ordinate of an empty matrix and then dividing all the resultant pixel values in the matrix by the total number of images. This temporally averaged background intensity was then removed from each temporally averaged test point .TIF image in turn, using another MATLAB program averaging_code.m (see Appendix C.2). The same code (i.e. averaging_code.m) also noise filters the background corrected test point image, such that each output pixel contains the median value in a 3-by-3 neighbourhood (around the corresponding pixel in the input image) and the image boundary is extended symmetrically. The code saves the original image grayscale

colourmap, for easy viewing of the output image matrices. These two programs were adapted from code obtained from Runyon (2017) [76].

Much of the original images' field of view included the casing surrounding the quartz window, the burner assembly and an area downstream of the flame, so the images required cropping before the next stage of processing. First, the brightest averaged image was displayed as a MATLAB figure, to give the greatest contrast between the flame and the edges of the viewing window. The top half of the image contained a sizeable flaw resulting from a deposit on the quartz tube. Fortunately, the subsequent stage of image processing assumes symmetry about the axial centreline of the flame, so requires only half an image (top or bottom), hence the lower half of the image was chosen for the subsequent processing stages. Row 488 marks the lower edge of the quartz window, so there were 213 pixels between the burner centreline and the bottom edge of the cropped image. The burner centreline (row 275) minus 213 pixels made row number 62 uppermost for the cropped image.

A sharp increase in the intensity gradient on the left-hand-side of the image, indicated that the fuel exited the burner at image column 120. The averaged images for the weakest flames were used to judge the approximate length for the longest flames (i.e. the slowest to burnout). Approximately 100 mm was deemed adequate to allow for the full inclusion of the OH* chemiluminescent areas of these flames. Therefore, given the scaling, the images were cropped downstream of the flame (at column 593). The cropping and scaling code is incorporated into the code for the next stage of image processing, that of Abel deconvolution.

Abel deconvolution is a technique widely used in the image processing of chemiluminescent signals from axially symmetric flames [76]. When observing the swirling conical flame structure, the line-of-sight signal received by the observing equipment, e.g. an eye, will include all light emitted in front of or behind the focal plane. The focal plane in this instance is a plane cutting vertically down through the burner centreline and projecting axially along the confinement tube. The open-source MATLAB algorithm for the Abel inversion processing method used in this study was created by Killer (2014) [147]. This code was modified by Runyon (2017) to provide spatial

representation of chemiluminescence measurements. The program is included in the relevant thesis under the program name HalfAbel.m [76]. The code assumes the distribution of the chemiluminescent signal is radially symmetric about its axis (i.e. as achieved through temporal averaging) and uses either half of the image. The code processes a matrix, containing the pixel intensities for the chosen half of a three-dimensional image, into another matrix, a two-dimensional spatially resolved projection representing the signal intensities in the focal plane, mirrored about the centreline. Figure 4.7 shows how the structure of the flame for one of the test cases (15% COG/AA at Φ = 1.2) is revealed by showing the same image before and after the Abel inversion algorithm has been applied to the image (flow direction is from left to right).

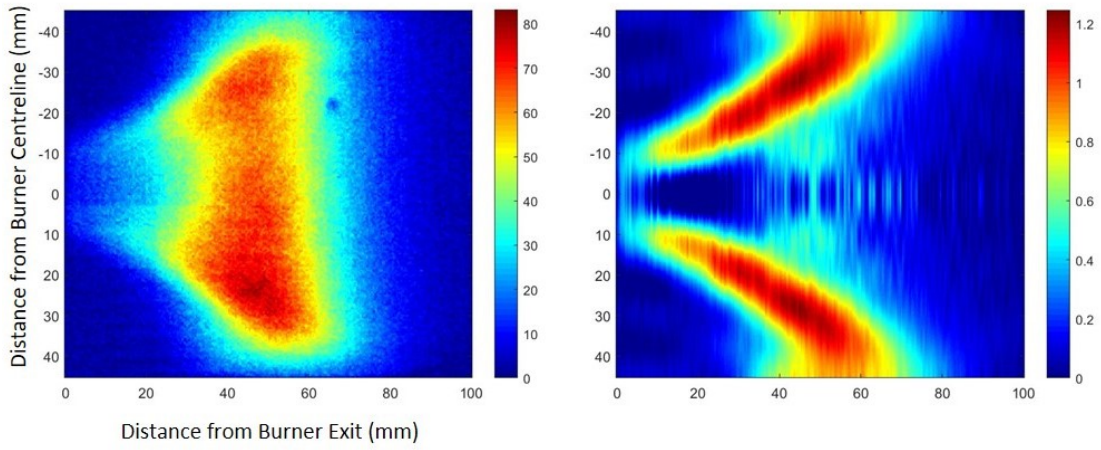

Figure 4.7 The relative pixel intensity for the OH* signal before (left) and after (right) Abel deconvolution (for 15% COG with AA flame at Φ = 1.2).

The relative maximum OH* intensities for the pixels before and after processing are also shown, indicating that the integral of the maximum signal intensity from a line-of-sight perspective (of > 80) is almost two orders of magnitude greater than for the planar projection (at ~1.2). The symmetrical image is equivalent to a viewable flame width of 90.4 mm. This is smaller than the internal diameter of the quartz tube (100 mm), due to the window edge slightly obscuring the very edges of the tube. However, the images show the vast majority of the OH* chemiluminescence data indicating flame structure.

The image cropping and Abel inversion were performed for each background corrected, noise filtered test point image in turn, run in batches. An example of the batch processing code is given in Appendix C.3. The code includes all necessary scaling

information to enable scaled plotting of the processed image about the burner centreline. It specifies the revised burner centreline pixel row of 213 (post image cropping) using the variable CentXPix, and designates the half of the original image to be processed via the WhichWay variable. The Abel inversion code processes the image in a vertical orientation, so some coding for matrix rotation before and after processing is necessary to display the images in their true orientation (hence negative values upwards for the y-axis in some images presented). The functions to which the HalfAbel.m code calls are available on the MATLAB Central File Exchange [147]. The final images displayed are scaled from 0 to each matrix maximum value by setting the colourmap minimum to zero, to exclude negative values.

4.8 Adaptations of the Method in Response to Data Appraisal

4.8.1 Issues Related to Sample Dilution

As anticipated from the numerical modelling, it was necessary to dilute the CO measurements to bring them on scale. Dilution was equivalent to a WDF of 7.0 to 9.3 across all test cases. The molar percentage of H_2O in the undiluted samples (from equilibrium modelling) is between 27 and 40%, so at this level of dilution, the H_2O in the wet samples is approximately 3 to 6% (across all cases). As this exceeds $3\%_{vol}$ (stated as having < 1% reduction in NO_x readings [143]), the manufacturer (Signal Instruments) was contacted. They advised that for every 10% H_2O, NO_x measurements are reduced by approximately 1%. Therefore, cross-interference effects from the H_2O component are still assumed to be minimal (at < 1% of reading) for these samples.

An unanticipated consequence to the significant air dilution of the emissions, which became evident after the conclusion of the test campaign, was the effect on NO_2 measurements. The NO_2 readings were as expected for the leaner values of Φ, being significantly lower than those of NO and so contributing a small minority of the NO_x emissions. However, as Φ was increased and as the NH_3 emissions started to climb, so did the NO_2 exhaust concentrations. This phenomenon is demonstrated by the plots in Figure 4.8, for the three AA blends at their target Φ. It was postulated that the rise in measured NO_2 was somehow related to the presence of high concentrations of NH_3 in conjunction with the addition of dilution air, as no other relevant publications (or the

numerical modelling) had shown this increase. Considering that the NO_x analyser calculates NO_2 as the increase in NO reading when a sample is passed through the NO_2 converter (see Section 4.6.3), it was theorised that the converter was reacting a portion of the NH_3 to NO, due to the presence of a considerable concentration of O_2 (from air). A subsequent, short experimental study was conducted to investigate this theory.

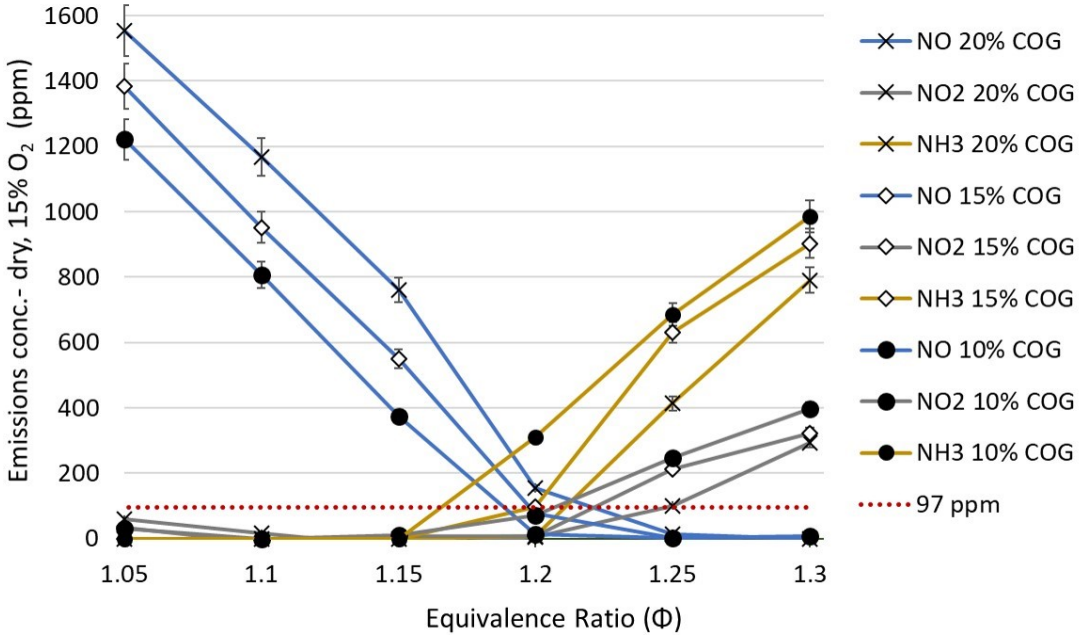

Figure 4.8 Rise in NO_2 emissions (dry, 15% O_2) with increase of Φ for the AA blends

The short study, was conducted at 0.11 MPa, with an inlet temperature of 469 K, using 15% COG with AA at a target Φ of 1.25. This test point was chosen for its high NH_3 measurements (632 ppm) in the aforementioned campaign (see Figure 4.8). The quartz tube design and installation differs slightly from that used in the previous sections of this chapter, but not in any way that would invalidate the findings (the tube design and installation is described later in Chapter 6). Table 4.3 shows the NH_3 results of this short study (631.4 ppm) are practically identical to those of the earlier campaign.

Table 4.3 Emissions concentrations with/without air dilution for 15% COG/AA

Average Φ	DDF	WDF	NO_x ppm (dry, 15% O_2)	NO ppm (dry, 15% O_2)	NO_2 ppm (dry, 15% O_2)	NH_3 ppm (dry, 15% O_2)
1.231	2.400	2.013	74.9	27.7	47.2	-
1.241	2.379	1.999	-	-	-	631.4
1.235	1	1	18.5	19.4	-0.9	-

The NO_2 reading without dilution was essentially zero (-0.9), while modest dilution resulted in an NO_2 reading of 47 ppm, representing the majority of the NO_x measured (the reason for negative results is discussed shortly). There is also a slight increase in NO with dilution, although this is likely due to the slightly lower Φ. The results show NO_2 to be a very minor contributor to measured NO_x when NH_3 concentrations are low (as would be expected) contributing a maximum of 3.7% of total NO_x for the blends in Figure 4.8. Therefore, NO emissions have been used as a proxy for NO_x in this chapter's results.

Having identified the cause of the increase in NO_2, the subsequent staged combustion study, discussed later in Chapter 6, did not use dilution air during the measurement of NO_x and thus, the NO_2 measurements in that chapter are valid. As some air dilution is necessary for measurement of NH_3, to provide the O_2 for the conversion of NH_3 to NO (see Equation 4.3), dilution was still required when measuring NH_3 in the later chapter.

The NO_2 measurements were frequently calculated as a negative value. This is because NO concentrations generally increase over the duration of a test point in line with a gradual decrease in Φ. This decrease is due to the continual cooling of the NH_3 container, which increases the restriction of NH_3 flow. The fuel flow valves were held at position for the duration of each test point. Although the decrease in Φ is slight, modest decreases can lead to a rapid increase in NO. When NO values are high, the subtraction of the higher NO value from the NO_x value (measured minutes earlier), gives a negative result for concentrations of NO_2. The y-axis in Figure 4.8 starts from zero, so the negative data points are not visible. Similarly, for high background NO readings and insignificant NH_3 concentrations (i.e. for the leanest cases), the increasing NO readings across a test point also led to negative readings for NH_3 (most often measured after NO_x). Negative

data points for NH_3 have been set to zero in this thesis (although the measured negative values are included in Appendix A.4).

4.8.2 NO_x Analyser Fluctuations and Sampling

When using the manual T-valve to switch between NH_3 and NO_x readings, there was significant delay in the settling of the readings, not least because high NH_3 readings are recorded for cases with low NO_x readings and vice-versa. It was originally intended that approximately one minute of measurement (~60 readings) would be averaged, but given the substantial settling delay, the timings were adjusted to achieve stable readings.

4.9 Experimental Results and Discussion

4.9.1 Flame Stability

There were significant issues with the combustion stability of the AV blends, as was anticipated from the earlier numerical modelling of the laminar flame speeds. AV with 20% COG was the only AV blend capable of sustaining a flame under the experimental operating conditions. The inlet temperatures for the premixed fuel and air were lower than had been intended and modelled for, despite significant insulation of the heated air and steam lines, due to the inability of the overheated preheated air to lift the premix temperature to 550 K. Across all cases, inlet temperatures ranged from 502 to 533 K. Inlet temperatures were highest for the AV with 20% COG at 529 to 533 K. Had inlet temperatures been modestly higher (at 550 K), the instabilities could have been marginally lessened for the 20% COG/AV blend. However, given the issues experienced by this more reactive blend, this minor elevation in temperature would not be sufficient to enable stable combustion of the 15% COG/AV blend. Figure 4.9 shows the time averaged OH* chemiluminescent images of the AV with 20% COG blend at the range of Φ investigated. Intensities are scaled to the maximum for each individual image. Combustor pressure was maintained 1.086 ± 0.004 bara.

As Φ increases the flame adopts a more ‘M’ shaped average structure due to the greater proportion of fuel consumption occurring in the outer recirculation zone and the detachment of the root of the flame as it lifts progressively further away from the burner exit. The far grainier image at Φ = 1.15 results from the lower signal intensity (increasing

the noise to signal ratio) and the more variable spatial distribution over time due to the more frequently transitioning flame structure, atypical for normal gas turbine operation. Had the target Φ range included higher values for the AV blends, these would not have been achievable for safety reasons, even for the more reactive 20% COG blend.

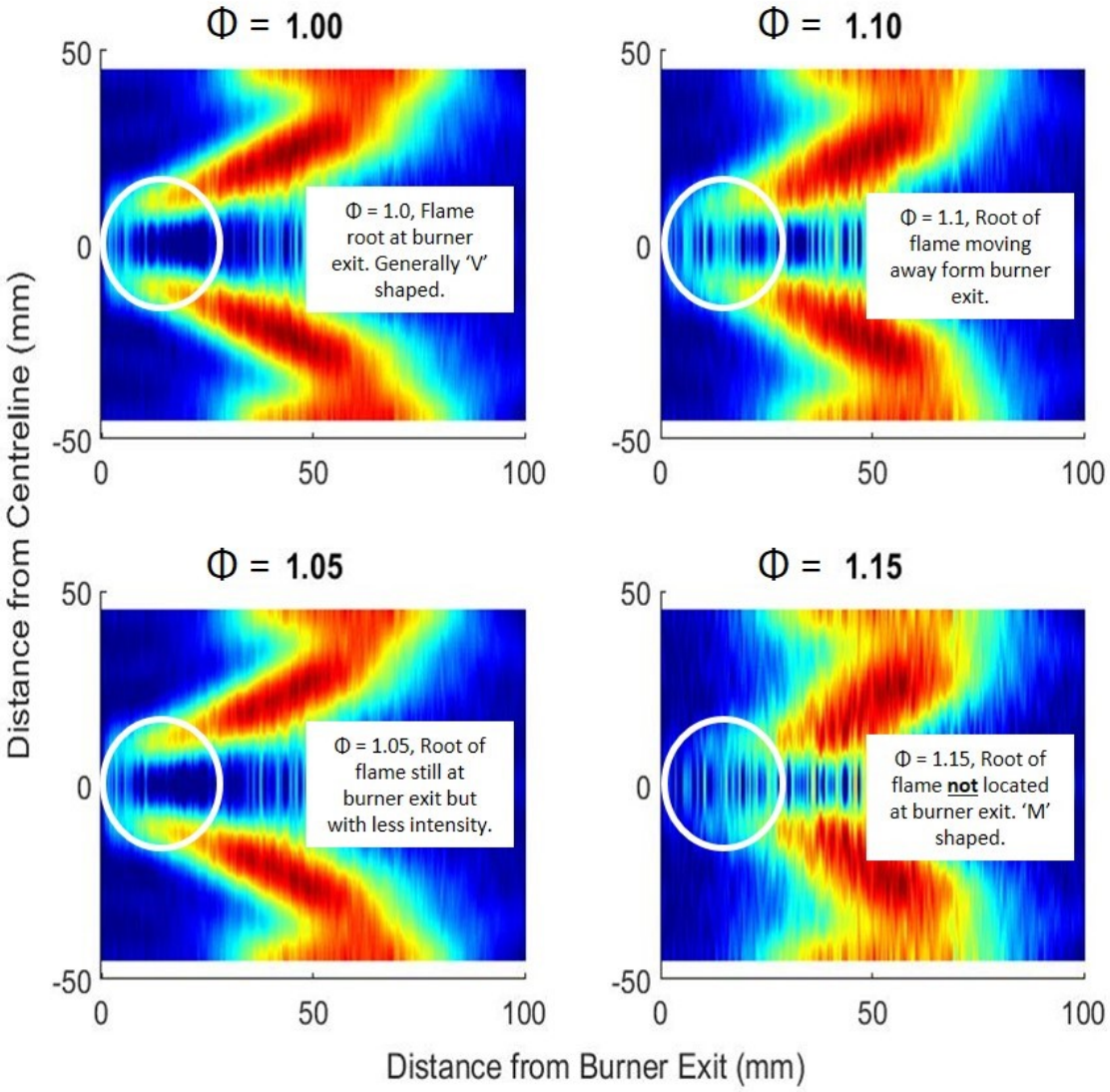

Figure 4.9 OH* Chemiluminescence of the AV with 20% COG blend at Φ = 1.00 to 1.15 (529 to 533 K inlet, 1.09 bara)

Only the 20% COG blends are available for direct comparison of flame structure between all three types of blend (i.e. AA, HA and AV). The structures of these flames are shown at Φ = 1.05 in Figure 4.10.

While the structures of the AA and HA blends are very similar and primarily 'V' shaped, the transition to a more distinctly 'M' structure for the AV blend is clear to see.

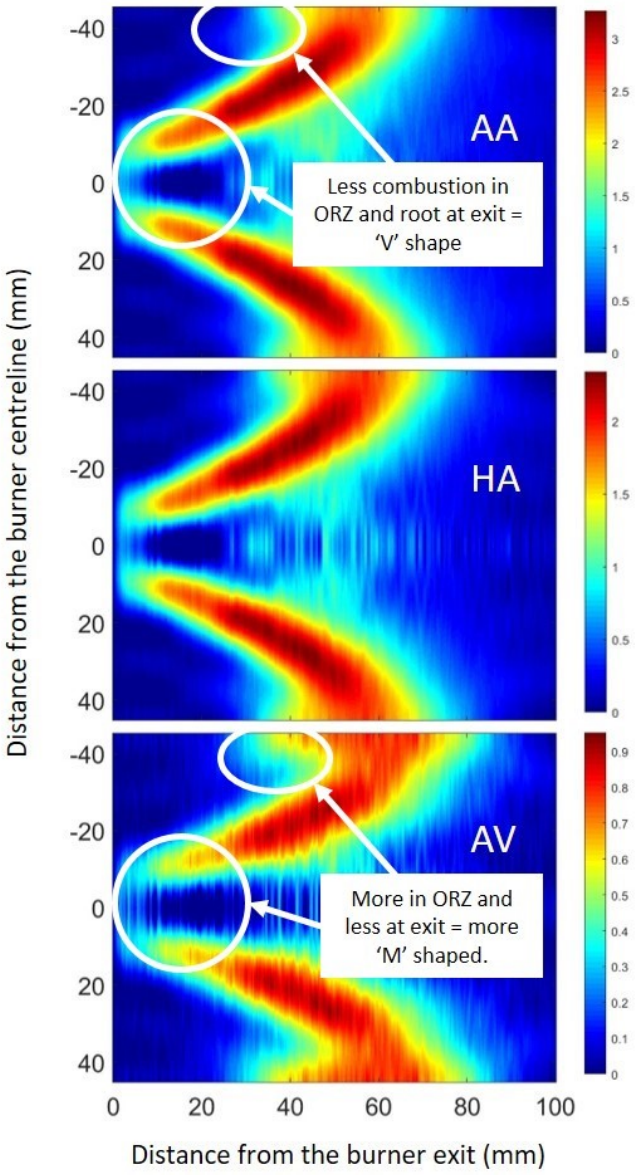

Figure 4.10 OH* Chemiluminescence for AA, HA and AV with 20% COG, at Φ = 1.05

For the AA and HA blends, only the 10% COG/HA blend experienced substantial instability, with the flame lifting off the burner at Φ = 1.2, preventing safe operation. Therefore, the richest Φ achieved for the 10% COG/HA blend was 1.15 (at 514 K). The inlet temperature for the HA blend at Φ = 1.2 was 507 K, 43 K lower than intended, so had this been 550 K, this could have stabilised the flame sufficiently for readings.

Using the same method as in Section 3.3 (and the Okafor mechanism), the laminar flame speed of the 10% COG/HA blend, at 514 K and 1.09 bara (the same inlet temperature and pressure and its richest stable combustion case Φ = 1.15) was modelled as 20.06 cm/s. The laminar flame speed of CH_4 for the same conditions and at the very lean Φ of

0.5 is 22.70 cm/s, so ~10 % higher. Similarly, for the 20% COG/AV blend at Φ = 1.15 and 529 K the laminar flame speed was 21.84 cm/s. The equivalent for CH_4 (at Φ= 0.5) is 24.90 cm/s, ~14% higher. Thus, the calculated flame speeds for the NH_3 blends at the borderline of stable combustion are slightly lower than those modelled for very lean CH_4 combustion. Given these results, and the experimentally validated prediction that the 15% COG/AV blend would not combust stably, comparison with the laminar flame speeds of CH_4 at Φ = 0.5 appears to be a good indicator of the approximate limits for stable combustion for NH_3 blends in this burner assembly.

4.9.2 CO Emissions

The emissions data for all blends across all test points reported in this chapter is given in Appendix A.4, calculated as undiluted. The H_2O product mole fractions, as well as the experimental Φ values calculated from the averaged air/fuel flows using Gaseq (accounting for the variation from the target Φ in the plots), are also given in Appendix A.4. Uncertainties in emissions concentrations are relatively small, being obscured by the data points themselves in many cases.

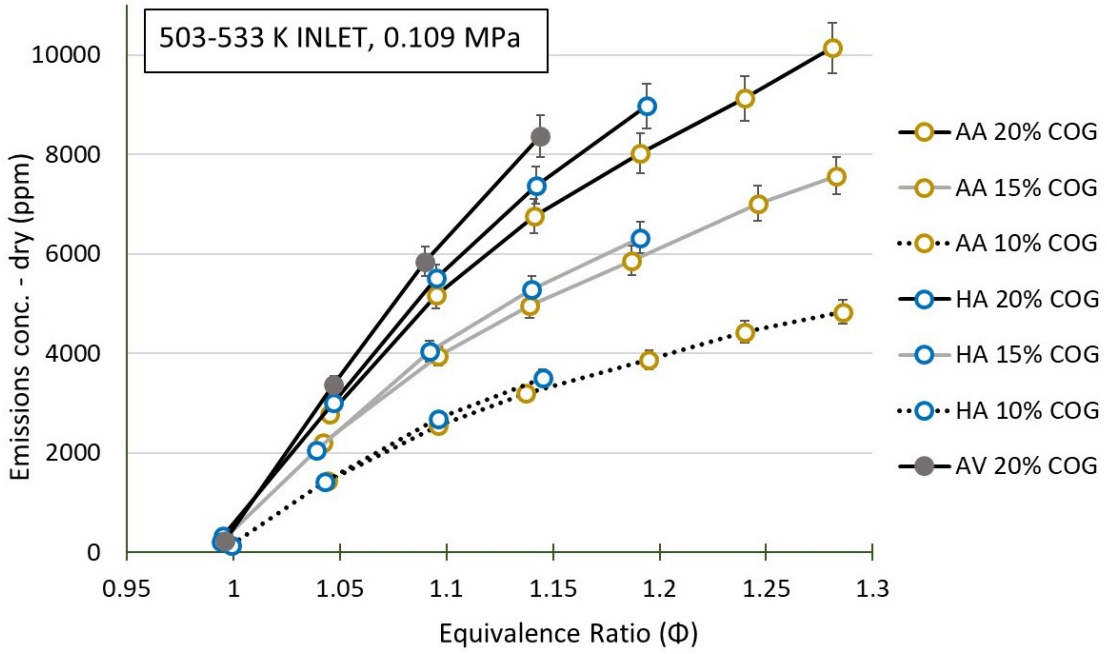

Figure 4.11 CO emissions for all blends (dry basis)

Figure 4.11 shows the results for the dry, undiluted CO concentrations for all successful cases. As anticipated by the numerical modelling, CO emissions for the humidified

blends exceed those of the anhydrous blends due to the higher ratio of carbonaceous fuel to NH_3. The CO for the 20% COG blends is naturally one third higher than that of the equivalent 15% COG blends and twice that of the equivalent 10% blends. The difference in CO (and ultimately CO_2) emissions between blends with the same volume percentage of COG is comparatively modest. CO will eventually convert to CO_2 and the purpose of this study is to mitigate for GHG emissions, therefore, all other measures being equal, the 10% blends are preferred.

Naturally, with such high concentrations of CO exiting the primary stage, efficient mixing with the oxidant in the second stage is crucial to bringing these CO concentrations down to acceptable levels and enabling efficient combustion.

4.9.3 Nitric Oxide (NO) and Ammonia (NH_3) Emissions

The NO and NH_3 emissions concentrations for the AA blends are shown in Figure 4.12, focusing on the Φ range close to the three blends' values of Φ_{opt}.

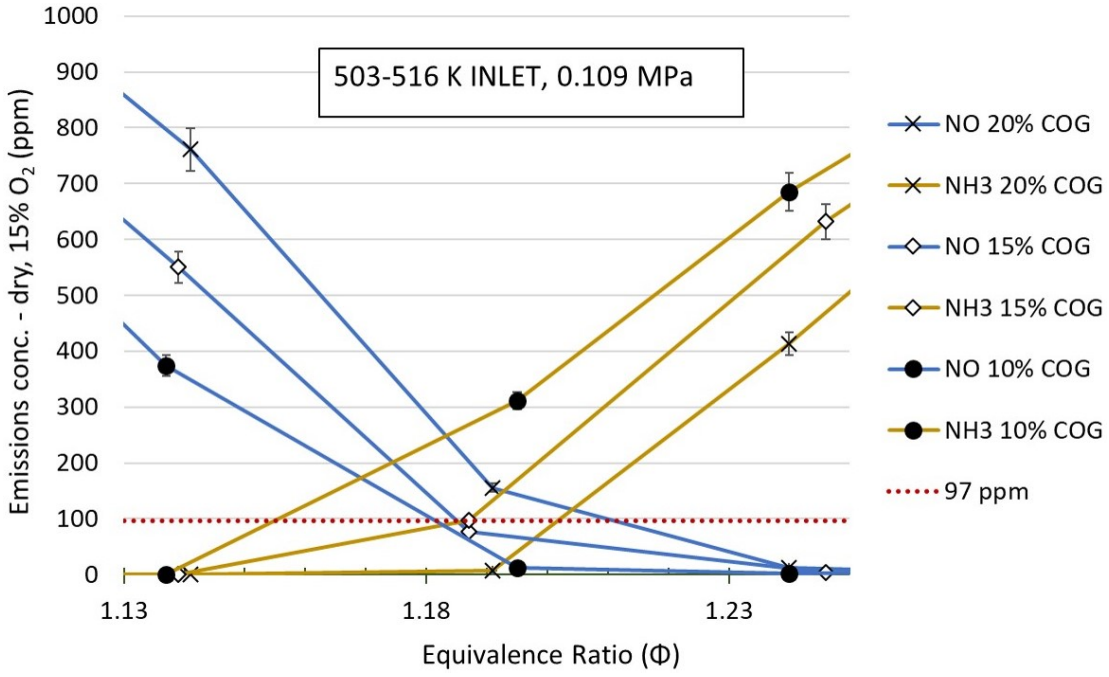

Figure 4.12 NO and NH_3 emissions concentrations for the AA blends (dry, 15% O_2)

Concentrations for both NO and NH_3 are presented as dry, 15% O_2 to facilitate comparison of NO emissions with UK regulatory requirements and to compare the two emissions on an equivalent basis, appreciating that NH_3 leaving the primary stage is a potential source of NO in the lean secondary stage.

The lowest combined NO/NH_3 emissions (from Figure 4.12) are given in Table 4.4, for the values of Φ investigated. As the resolution of Φ is limited to increments of ~0.05, the lowest possible combined emissions achievable are possibly lower at Φ values between those measured. For this reason the subsequent experimental study in Chapter 6 improves on this resolution by targeting increments of 0.01 for a range close to the predicted Φ_{opt}. The values of Φ at which the NO/NH_3 lines intersect are assumed to be indicative of the approximate Φ_{opt} for each blend under the conditions investigated. Thus, the Φ values for the intersects are also approximated in Table 4.4 with the approximate value of their combined emissions (obtained from visual inspection of the plots).

Table 4.4 The Φ values for the measured minimum combined NO and NH_3 emissions (AA blends) and the intersects for the plotted emissions values.

COG $\%_{vol}$	Φ for emissions measured	NO (ppm)	NH_3 (ppm)	Combined (NO/NH_3)	Φ at Intersect	Combined NO/NH_3 (ppm) at intersect
20	1.191	155	7	162	1.205	~230
15	1.187	76	98	174	1.185	~188
10	1.195	12	311	323	1.17	~344

Although two of the blends in Table 4.4 achieve NO readings of < 97 ppm, none have low enough combined NO/NH_3 readings, exiting the primary stage of combustion, to satisfy the regulatory limit in a staged configuration, should all the NH_3 ultimately be converted to NO_x in a second leaner stage. The lowest combined emissions values measured for the 20% and 15% COG/AA blends are very similar (< 200 pm) and superior to the 10% COG/AA blend (> 300 ppm). The combined emissions at the NO/NH_3 intersects for each blend are also similar and much lower for the 15 and 20% COG blends. The 10% COG blend is therefore least favoured. The predicted Φ_{opt} of each blend (the NO/NH_3 intersect) increases as the percentage of COG increases with an approximately linear rate of increase.

Figure 4.13 shows the NO and NH_3 results for the HA blends, once again focusing the range of Φ near the blends' Φ_{opt} values.

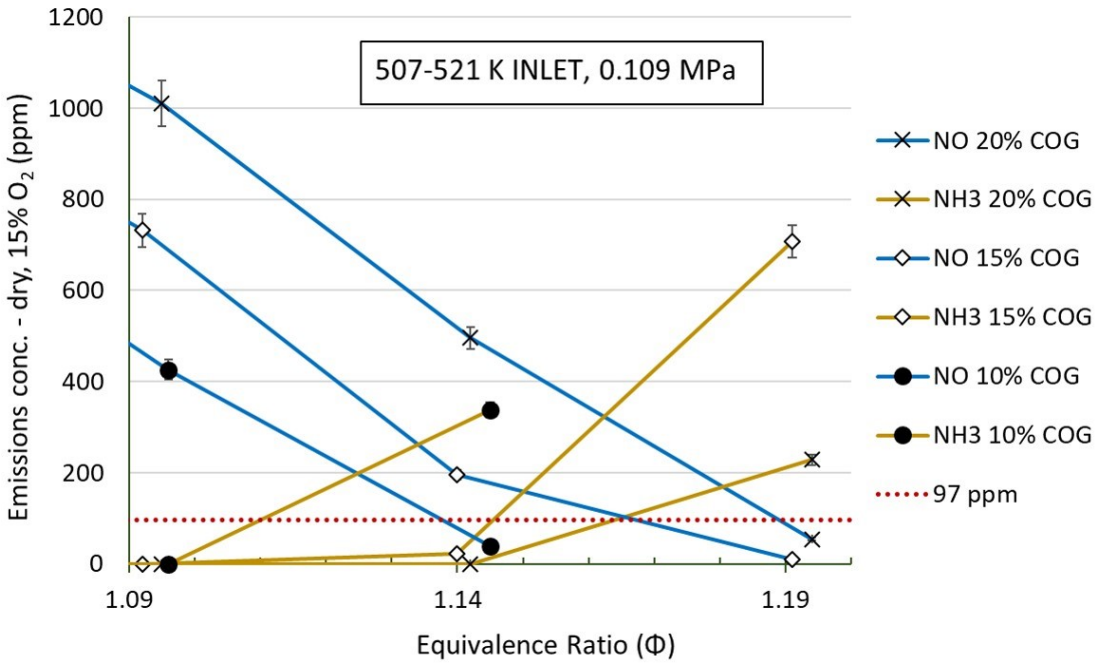

Figure 4.13 NO and NH_3 emissions (dry, 15% O_2) by Φ for the HA blends.

The emission results for the HA blends are summarised in Table 4.5.

Table 4.5 The Φ values for the measured minimum combined NO and NH_3 emissions (HA blends) and the intersects for the plotted emissions values.

COG $\%_{vol}$	Φ for emissions measured	NO (ppm)	NH_3 (ppm)	Combined (NO/NH_3)	Φ at Intersect	Combined (NO/NH_3) at intersect
20	1.194	54	229	283	1.18	~340
15	1.14	196	23	219	1.15	~320
10	1.145	338	38	376	1.125	~400

The 15% and 20% COG/HA blends have measured combined emissions of < 300 ppm (219 and 283 ppm respectively), and approximately equal combined values at their respective intersects. The 10% blend's measured combined concentrations are significantly higher than for the other blends (~380 ppm). For the values of Φ investigated, the results for the 15% COG blend are best overall. Similar to the AA blends, there is an almost linear increase in Φ_{opt} with percentage COG, with a slightly larger increment between the 15 and 20% blends. The combined emissions for the AA blends are lower than for the HA blends for all equivalent blends.

Figure 4.14 shows the NO and NH_3 results for the only COG/AV blend (20% COG), for the target range of Φ = 1.0 to 1.15.

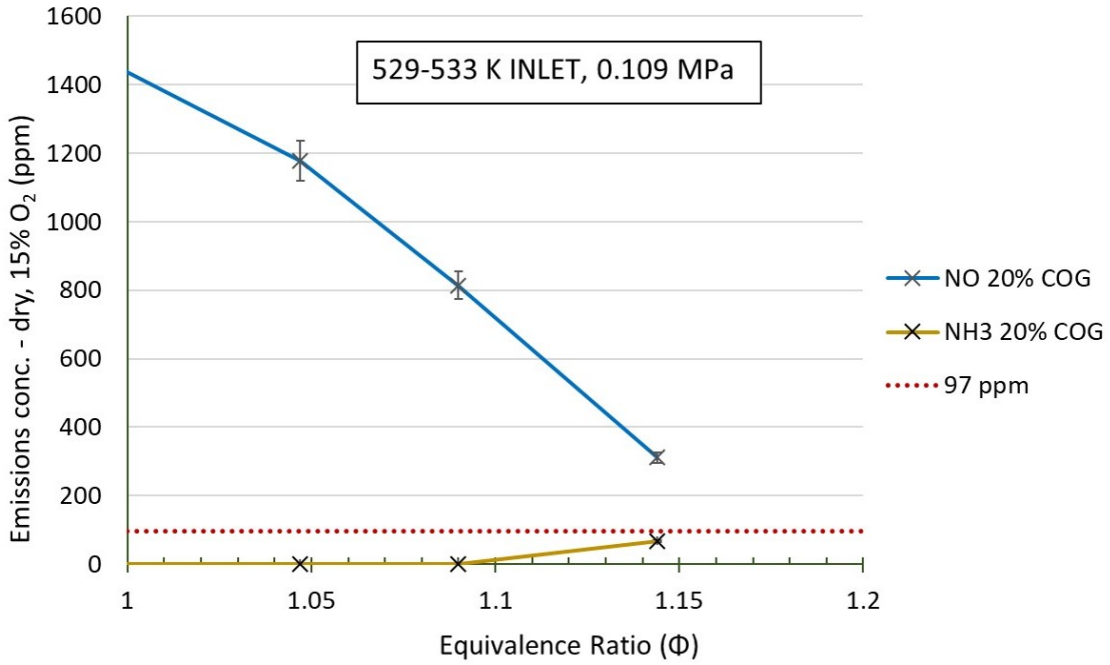

Figure 4.14 NO and NH_3 emissions (dry, 15% O_2) by Φ for 20% COG with AV.

The lowest combined emissions for the AV blend occurred at Φ = 1.144, where combined emissions were 380 ppm (312 ppm for NO and 68 ppm NH_3). Although the fuel-bound nitrogen is 11.6% higher for the simplified AV blend than for the AV derived from the literature (see Section 4.2.1), even if this translated to a proportional reduction in NO and NH_3, instabilities would prevent safe operation at this or greater Φ.

4.9.4 Overall Evaluation of Blends' Performance

For stable combustion, AV blends require greater COG volume percentages, lower Φ or higher inlet temperatures than those investigated, but these measures would result in either higher NO_x or CO_2 emissions (or both), as seen from the numerical modelling. As this study seeks to minimise both of these emissions under stable combustion conditions, the AV blends are excluded from further investigation.

Aside from the problems of flame stability and NO_x/CO emissions given above, there are other compelling reasons to exclude AV blends in favour of HA and AA blends, some of which were alluded to when the potential benefits of utilising HA were introduced in Section 4.2.2. The other perceived operational and environmental benefits resulting

from the exclusion of AV blends, and the consequential removal of acid gases (H_2S, HCN and CO_2) in the ammonia fuel, are as follows:

- Mitigation of the production of sulphur oxides; precursors to acid rain.
- Greatly reducing the effects of catalyst poisoning in the event that SCR is used for NO_x control.
- Easier, safer storage of the ammonia-based fuel.

Further dehydration of AV vapour in the by-product plant, via additional condensing, would only serve to increase the acid gas components in AV, therefore selective removal of the NH_3 from the waste stream (e.g. via the Phosam process) is necessary before the NH_3 component can be converted into a form useable as a fuel.

Having excluded the AV blends the comparative evaluation of the AA and HA blends follows. In consideration of the flame stability, CO, NO and NH_3 emissions results, it is predicted that, with sufficient resolution of Φ, the best performance would be achieved by the two 15% COG blends and that under similar conditions of inlet temperature and pressure, the anhydrous blend would out-perform the humidified blend at each blends' respective Φ_{opt}. It is predicted that for the operating conditions investigated, lowest combined emissions would be achieved at Φ ~1.185 and ~1.15 for the AA and HA blends respectively.

4.9.5 Emissions Trends with Changes in Fuel Humidification

Having successfully tested all three blend types with 20% COG enables examination of performance and emissions trends, allowing predictions for blends with water fractions between those tested, under similar operating conditions. Figure 4.15 directly compares the NO and NH_3 emissions results for the three blends with 20% COG. A key feature to note from Figure 4.15 is that the more humidified the blend, the lower the NO emissions values, for any one specified Φ. This relationship appears to approximate linearity over the range of humidification investigated, such that the NO emissions for the HA (30% H_2O) blend lie approximately halfway between the AA (anhydrous) and AV (~60% H_2O) blends. This finding enables predictions to be made concerning the likely NO_x emissions

for all compositions lying in-between those of the AA and AV blends for the range of Φ investigated.

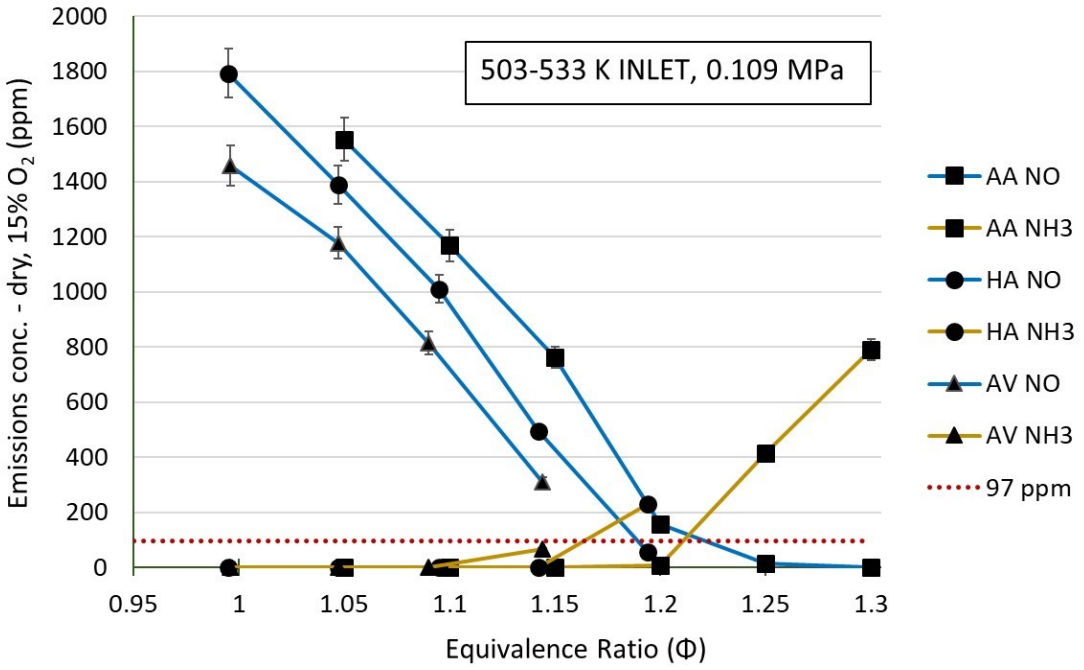

Figure 4.15 NO and NH_3 emissions concentrations by Φ for 20% COG with AA, HA and AV blends.

That lowered NO emissions are found through NH_3 humidification is in agreement with the findings of Pugh et al (2019) [93]. However, as has been discussed in this chapter, equivalence in NO emissions between humidified and anhydrous blends can be achieved when the anhydrous (or less humidified) blends are operated under a more fuel-rich combustion regime, and this action carries no apparent disadvantages as, for each blend combusted at its respective Φ_{opt}, efficiency is not compromised, provided combustion is completed in a second stage. Consequently, active humidification of AA, solely for the purpose of NO_x control, is not supported by these results. However, in the case of steelworks by-product NH_3, without complete dehumidification of the aqueous ammonia stream, which carries an energy penalty, there inevitably already exists a partially humidified fuel. Aside from energy savings from partial dehumidification, a potential benefit from utilising humidified NH_3 yet to be considered is that of higher power and efficiency, from increased bulk flow. Power and efficiency comparisons are investigated later in Chapter 7 in the development of a power cycle, utilising the chosen AA and HA blends. From the data obtained in this campaign it can be assumed that

instabilities would not feature for any NH_3 blend of ≥ 15% COG with a water fraction between 0 and 30% and that it is possible to operate at the Φ_{opt} for any such blend.

Therefore, although this chapters results predict NO_x emissions to be greater for the HA than AA blends, there are potential advantages to continuing to pursue HA blend investigations, especially as NO_x mitigation opportunities remain to be investigated. The mitigation measures include pressure elevation and thermal de-NO_x which could lower emissions to acceptable levels for the AA and HA blends alike. Thus, despite the apparent poorer emissions performance of HA blends, both the 15% COG/AA and 15% COG/HA blends are investigated further.

4.10 Chapter Summary

- Simplified, **representative AV and COG compositions were designed** for the experimental investigation.
- Flame speed modelling in Chapter 3 supported the idea of a halving of the water content of the AV blends. Thus, a **humidified NH_3 blend (30% H_2O) was investigated** in addition to the AV (~60% H_2O) and AA blends.
- The **blends investigated were chosen from the earlier numerical modelling** (i.e. with 15% COG support) and additionally **with 5% more or less COG**, as a proportion of their composition.
- To maximise the preheat capability (i.e. overheating air flows) and to simultaneously account for NH_3 flow restrictions, **25 kW_{th}** power was adopted.
- All flowrates and measurements (e.g. temperature, emissions, etc.) were averaged for each test point. These measurements were used to **derive the experimental Φ** and to account for sample dilution (bringing emissions readings on-scale) to calculate **industry relevant emissions data**.
- Abel deconvolution of OH^* chemiluminescence images was performed to **assess changes in flame structure** across the blends at different Φ. Transitioning of structure from a 'V' to an 'M' shape, was evident for the least reactive flames.
- Sustainable combustion of the 15% COG/AV blend was not achieved. Inlet temperatures were lower than intended, but performance of the 20% COG/**AV blend was sufficiently poor to preclude AV blends** from further investigation.

- **All NH_3/H_2O blends** of 0 to 30%$_{vol}$ H_2O can be **predicted to burn stably at their Φ_{opt} when supported by 15% COG** under the conditions tested. Their emissions can be estimated from the demonstrated trend (i.e. 30% H_2O gave NO readings halfway between ~60% and 0% H_2O).
- The modelled **laminar flame speed of CH_4 at $\Phi = 0.5$** is an approximate **indicator** as to the minimum flame speed **for stable combustion of ammonia blends** in this burner assembly (at the same inlet temperature and pressure).
- The trends suggest a **positive linear correlation between blend reactivity and Φ_{opt}.**
- The **15% COG/AA and 15% COG/HA blends were the best** when balancing stability with emissions. Combined NO/NH_3 emissions for these two blends were found to be two to three times the assumed regulatory limit for NO_x.
- The **AA blend's emissions were lower than the HA blend's** when each blend was operating at its Φ_{opt} and the proportion of the energy content from the NH_3 is marginally higher for the AA blend. The differences in CO (and ultimately CO_2) emissions is very modest.
- Although HA's primary stage emissions performance is generally poorer than AA's, there may yet be **other benefits in using HA worth consideration** (e.g. increased cycle efficiency), especially once pressure elevation and de-NOx treatments are considered.

Chapter 5 Reactor Model Improvement

5.1 Reactor Model Development - Method

Significant elevations of pressure, representative of those used in industrial gas turbines, are not feasible at the GTRC. Therefore, the best way to predict the likely effects of pressure elevation on emissions, for the chosen blends, was to further develop the reactor model from Chapter 3, using the experimental data from Chapter 4. The chemiluminescence images and experimental emissions results (subsequently calculated as wet and undiluted) were used as reference data, from which to train and improve the model. Several model variables were manipulated so that the model generated emissions values approximating those of the Chapter 4 experimental work at atmospheric pressure and for the limited range of Φ tested (i.e. 1.05 to 1.3 for 15% COG/AA and 1.0 to 1.2 for 15% COG/HA). This improved model was then used to numerically predict approximate emissions values for the blends under elevated pressure conditions. The Okafor [96] and Tian [130] mechanisms were used in the modelling.

The improved model reflects the product concentrations for fuel-rich combustion. Therefore, in preparation for the experimental secondary air staging work, the improved model was also used to predict product concentration profiles along the PFR (representing the post flame zone). A decision regarding the appropriate locations for the secondary air-staging inlet holes was made using these profiles.

5.1.1 Approximation of Flame Volume

The images obtained from the chemiluminescence work in Chapter 4 were used to approximate an average flame volume. In the numerical modelling of Chapter 3, the residence times and adiabatic temperatures of the model produced an overall volume for the PSRs in cluster 1 of approximately 68 cm^3 for 15% COG/AA at Φ = 1.2 and 61 cm^3 for 20% COG/AV at Φ = 1.05. The OH* chemiluminescence images for these two cases are shown in Figure 5.1.

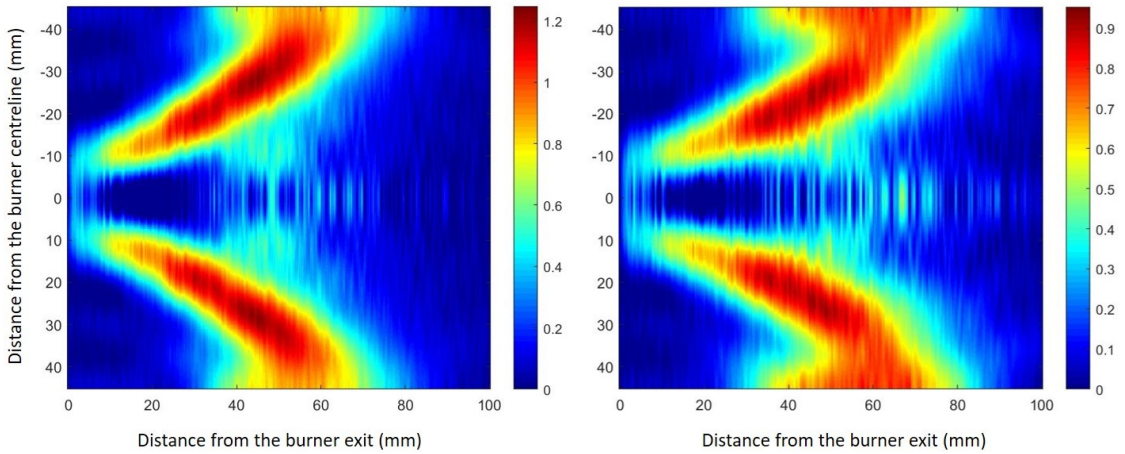

Figure 5.1 Abel deconvoluted OH*chemiluminescence images for 15% COG/AA (Φ = 1.2) and 20% COG/AV (Φ = 1.05)

The OH* chemiluminescence of the flames persists for approximately 80 to 90 mm downstream of the burner exit. The volume of confinement occupied by 80 and 90 mm axially is 628 to 707 cm^3. However, the outer boundary of the flame does not occupy the entire volume. Therefore, an average flame volume of ~500 cm^3 was assumed for the revised model, ~7 times greater than for the original model. The premixed flowrates for the original modelling were 5 g/s, whereas the experimental flowrates were 7.5 and 10.4 g/s, so the increase in bulk flow accounts for a minority of the flame volume increase.

5.1.2 Heat Loss and Residence Time Revisions

It is recognised that producing one model, to give best average fit for the data, will have its limitations. Heat losses and residence times will vary between blends, but are fixed for the model. However, one model that can approximate the performance of different blends at different Φ (incorporating their differing inlet temperatures and flowrates) is a more robust method for creating a simulation representing reality, than creating individualised models for each case, which happen to fit the data.

In reality, the most reactive blends at leanest Φ would have higher relative heat losses than the average blend, due to their higher flame temperatures. Additionally, residence times in cluster 1 would in reality be marginally greater for the flames with lowest reactivity (humidified and at highest Φ) than for the average, as can be seen in the flame elongation of AV compared with AA in Figure 5.1. Hence, the heat loss and residence times chosen need to be a compromise for achieving reasonable agreement across the

blends. Choosing values that simultaneously represent a best compromise between the 15% COG/AA and 15% COG/HA at their respective Φ_{opt}, is the approach adopted here.

As there was no reliable heat loss data available for the burner assembly, or flow profiles (i.e. describing strength of recirculation) for the blends tested, a method for approximating these values based on average reactant flowrates, approximate temperatures, etc. was adopted. The temperature of the flow in the first 80 mm of tube (measured axially from the burner exit) was assumed to be an average of approximately 1900 K (based on modelled adiabatic temperatures of ~2000 K). Using the ideal gas equation, at this temperature, 1 mole of an ideal gas occupies ~0.14 m^3. The fuel/air flow was approximately 0.29 mol/s (calculated from the Excel interactive workbook), hence one second of flow would occupy (0.29 * 0.14) = 0.041 m^3. As discussed in Section 5.1.1 the flame volume is assumed to be approximately 500 cm^3 (5.0 x 10^{-4} m^3), therefore the average residence time is ~0.012 s. Although this value has been arrived at via a rather crude method, in the absence of hard data (such as particle image velocimetry data), it is considered a valid step for enabling model improvement, helping to account for the order of magnitude disparity in flame volumes between those modelled by the original model and those evident from the visual observations obtained experimentally.

The residence times between the flame zone and the CRZ are assumed to be approximately equal (as they were in Chapter 3). Minor changes in overall residence times made very little difference to the emissions predictions. Residence times ultimately chosen were 0.0015 s in PSR1, and 0.005 s each in PSRs 2 and 3, to approximate the ~0.012 s total average residence time in the flame (as derived in the previous paragraph). Thus, the modelled flame volumes are now more representative of those observed experimentally.

By far the most crucial manipulation of the flow variables was the variation of heat loss. However, it was found that the division of the proportion of the heat losses between the flame zone and CRZ made no significant difference to the emissions entering the PFR. For example, a heat loss of 0.5 kW/s in the flame zone and 1.5 kW/s in the CRZ gave practically identical results as 0 kW/s in the flame zone and 2.0 kW/s in the CRZ.

Adiabatic temperatures originally modelled for PSR1 were ~600 K, whereas those in PSRs 2 and 3 averaged ~ 2000 K. Therefore, heat losses from PSR 1 were assumed to be relatively insignificant. A range of heat loss values in cluster 1 were investigated. Heat losses in PSR1 were held at 0.1 kW/s, while losses from PSRs 2 and 3 combined were varied between 1.3 and 2.3 kW/s. The results for combined heat losses of 2.0 kW/s were the best at resembling the emissions results from the experimental campaign. These losses were split as follows: the flame zone, 1.5 kW/s and the CRZ, 0.5 kW/s. A modification of recirculation between PSRs of 30% from 20% gave marginally more representative emissions results, but as was the case for residence times, these changes were fairly insignificant, compared with the changes when manipulating heat losses.

5.1.3 PFR Profile Revisions

The PFR residence time is dictated by the PFR geometry, mass flows and temperatures and cannot be set (unlike for the PSRs). Greater heat losses will increase residence times as the volume of product gases is less. However, the approximate doubling of the mass flows from those of the original modelling, greatly reduces the residence time in the PFR despite the fact that heat losses are now being considered. The PFR in the original model assumed a constant 10 cm diameter, 40 cm in length, without heat losses. The maximum length of flame observed experimentally (in Chapter 4), occupied the first ~10 cm of the quartz confinement. As the confinement projects 40 cm downstream of the burner, the PFR profile was modelled as 30 cm long and 10 cm diameter. Following after the PFR, was an approximate representation of the water-cooled pipework ahead of the gas analysis probe. This length of 6 inch pipe was modelled as having length 15 cm and diameter 15 cm. Heat losses were manipulated until exhaust temperatures reasonably matched the exhaust thermocouple measurements, at ~0.3 kJ/cm-s.

5.2 Improved Reactor Model Results and Discussion

5.2.1 Emissions Concentration Results at Atmospheric Pressure

The modelled results (broken lines) versus experimental results (solid points), for the two chosen blends, are shown in Figure 5.2 and Figure 5.3 for the AA and HA blends respectively.

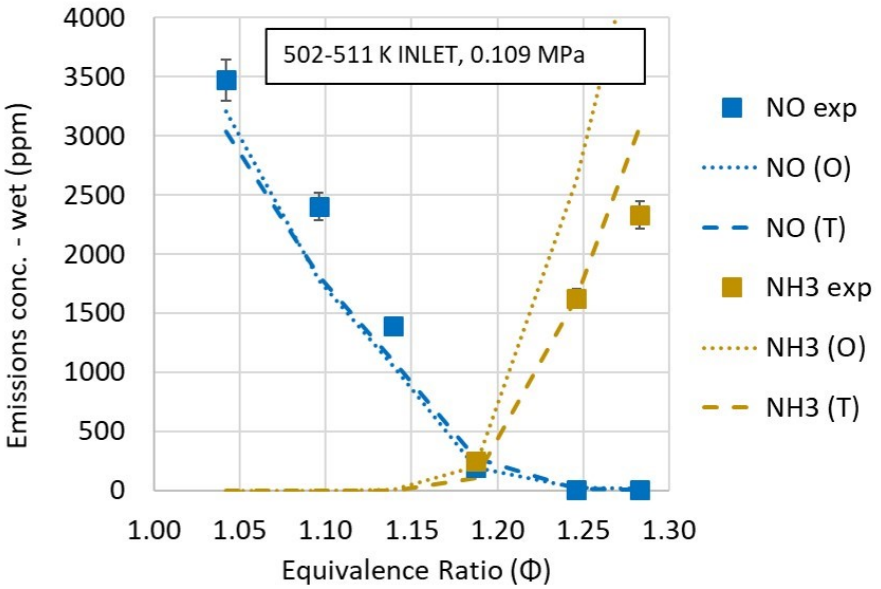

Figure 5.2 Experimental NO and NH_3 results versus improved reactor model for 15% COG/AA (wet basis) – using the Okafor and Tian mechanisms.

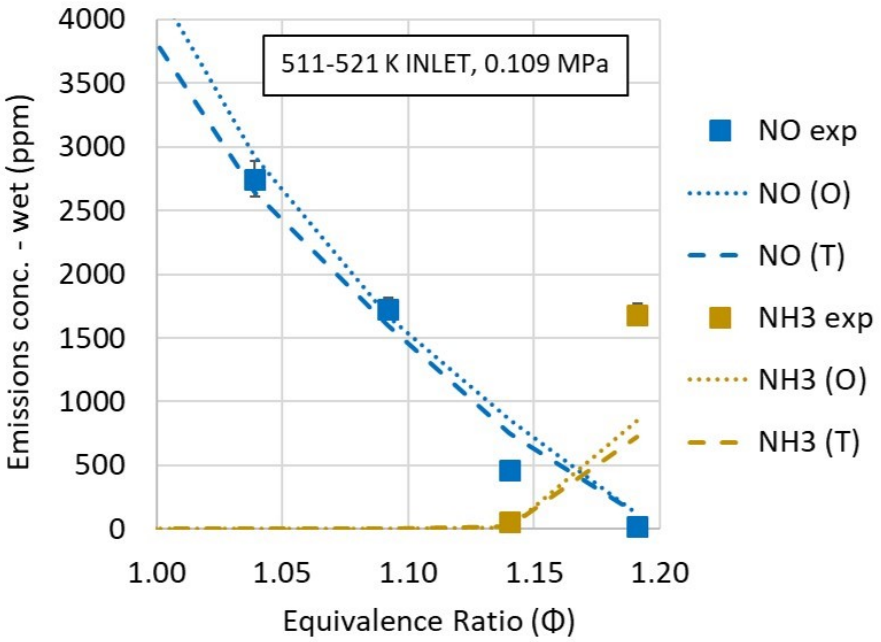

Figure 5.3 Experimental NO and NH_3 results versus improved reactor model for 15% COG/HA (wet basis) – using the Okafor and Tian mechanisms.

It can be seen from Figure 5.2 and Figure 5.3 that, although modelled results were up to 450% higher at the lower concentrations (e.g. 22 ppm experimental versus 121 ppm for the AA blend at Φ = 1.191), the improved model produces NO emissions values broadly in line with the experimental results (± 25% for experimental and modelled NO values > 1000 ppm), for both blends and both mechanisms. The model is marginally better at

predicting NO for the HA blend than for the AA blend and a better predictor of degree of NH_3 slip for the AA blend than the HA blend. The Φ above which NH_3 slip occurs is correctly predicted by both mechanisms for both blends, but the accuracy of the modelling of slip is much better for the AA blend, than the HA blend (maximum error of +32% and -57% of experimental reading respectively, using the Tian mechanism). Over the range of Φ investigated and with the variable settings used, the Tian mechanism's predictions for the blends' emissions are the closest to the experimental results, so this was the mechanism used to model the behaviour at elevated pressure.

5.2.2 Emissions Concentration Results at Elevated Pressures

When simulating an increase in pressure, reactant mass flows need to be scaled accordingly, to maintain the original residence times while changing the density. An elevated pressure of 12 atm was simulated. This is a typical operating pressure for a ~5MW industrial combined cycle gas turbine (see Section 2.4.2). Additionally a pressure halfway between this and atmospheric was modelled to show the trend for change in emissions with pressure elevation. To scale from 1.075 atm (0.109 MPa) to 6 atm (0.605 MPa) and 12 atm (1.21 MPa) required multiplying the mass flows by 5.58 and 11.16 to give LHVs of 150 and 300 kW respectively. Total heat losses were held constant across pressures, so relative heat losses were lower at elevated pressure (i.e. for the greater mass flows). Thus, the modelled flame volumes do increase accordingly, by 7% to 9% for 6 atm and 12 atm of pressure respectively.

Figure 5.4 and Figure 5.5 show the 15% COG/AA and 15% COG/HA blends' NO and NH_3 emissions predictions at the elevated pressures, compared with 0.11 MPa (atmospheric pressure experimental and modelled results). As was discussed in Section 2.3.1, the rationale for calculating NO_x emissions from NH_3 combustion in the same way as for carbon-based fuels combustion is in question. Therefore, for a more complete assessment, all the emissions results, experimental and modelled, for wet basis, dry basis and normalised to dry, 15% O_2 concentrations, are made available in Appendix A.5. The water fractions used in the emissions calculations for the modelled data were those obtained from the Chemkin (kinetic) results and are also included in Appendix A.5.

The evidence for predicting considerable reduction in NO_x at elevated pressures was described in Section 2.3.3. The modelling supports these predictions, with considerable improvements in NO emissions shown at the elevated pressures. Combined emissions easily attain levels below the assumed regulatory limit of 97 ppm (see Section 2.3.1).

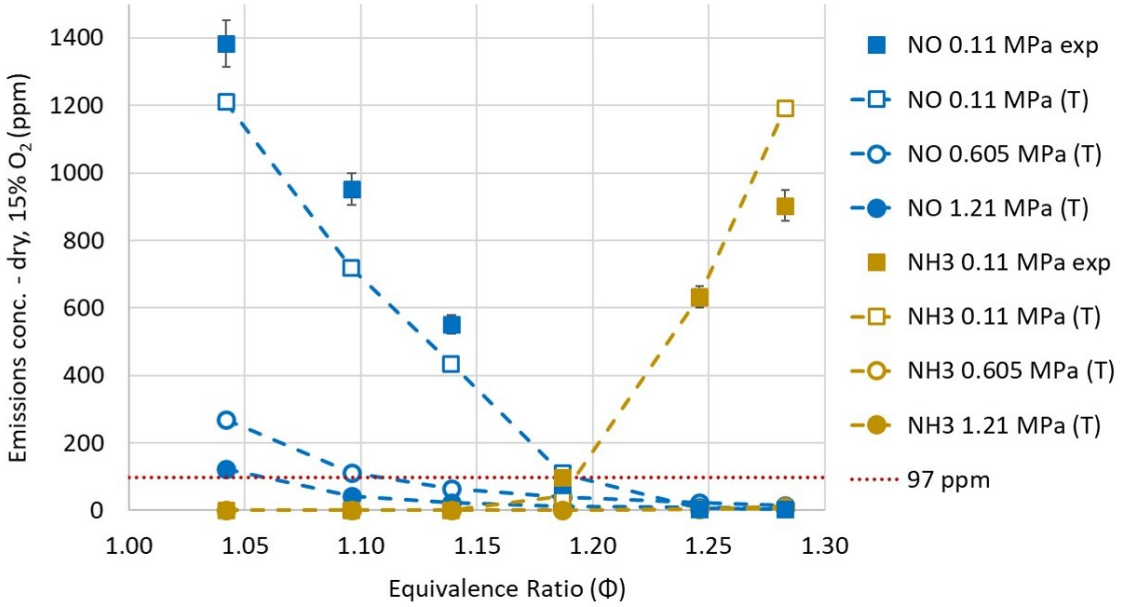

Figure 5.4 Modelled effect of elevated pressure on NO and NH_3 emissions showing experimental results (Tian mechanism) for the 15% COG/AA blend.

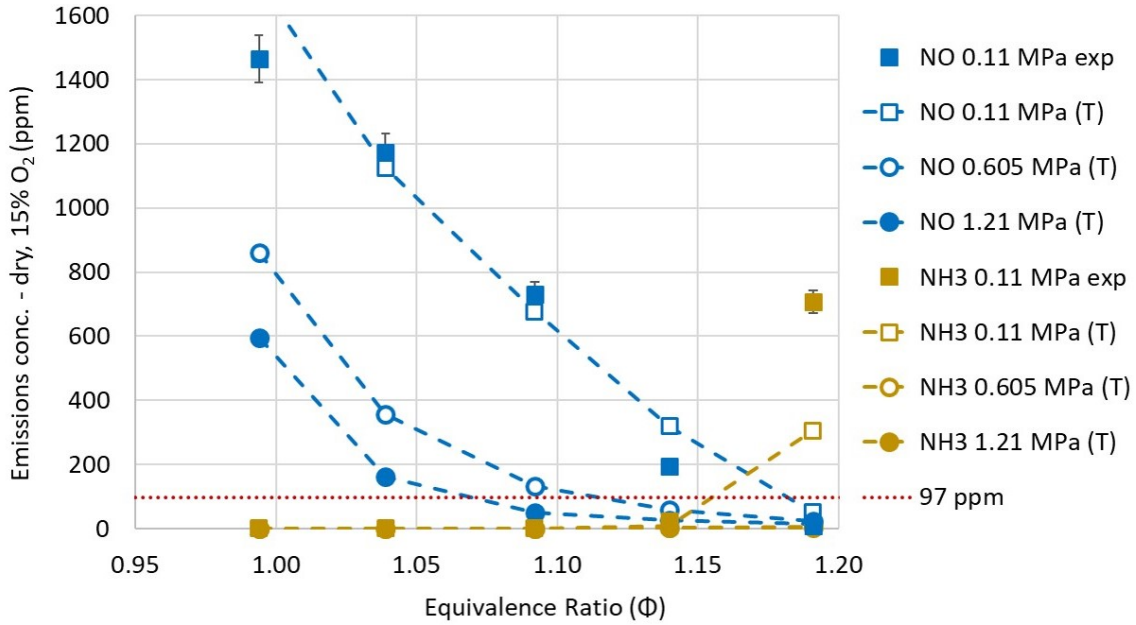

Figure 5.5 Modelled effect of elevated pressure on NO and NH_3 emissions showing experimental results (Tian mechanism) for the 15% COG/HA blend.

5.2.2.1 NO Emissions Discussion

In Figure 5.4 and Figure 5.5, the reductions achieved for NO at 6 atm (i.e. below the typical pressures for gas turbine technology) represent a major proportion of the reductions achievable at 12 atm. For example, at Φ = 1.19, the AA blend NO is modelled as 109 ppm at atmospheric pressure, 39 ppm at 6 atm and 14 ppm at 12 atm, showing that 64% of the reduction is achieved at 6 atm with a further 23% reduction (to 87% overall) at 12 atm. Although the NO reductions with pressure elevation appear significantly more pronounced for the AA blend, this is an illusion due to modelling under a different range of Φ (although the NO reductions at elevated pressure are indeed marginally greater for the AA blend than the HA blend). For example there are 84% and 80.5% reductions for NO for the AA and HA blends respectively, at Φ ~ 1.1 (for modelled data between 0.11 and 0.605 MPa).

5.2.2.2 NH_3 Emissions Discussion

Being very similar, the NH_3 concentrations at 6 atm are obscured by those at 12 atm. Therefore, the NH_3 results for the different pressures modelled are provided in Table 5.1. At elevated pressure, at the blends' richest Φ values, NH_3 slip begins to climb. With secondary air-staging this unburned fraction would be consumed.

Table 5.1 Modelled NH_3 emissions by Φ for the AA and HA blends using the Tian mechanism (dry, 15% O_2).

Blend	Φ	NH_3 emissions concentrations (ppm)		
		~1 atm	6 atm	12 atm
15% COG/AA	1.042	0	0	0
	1.096	0	1	0
	1.139	0	2	1
	1.187	43	2	2
	1.246	633	4	4
	1.283	1191	12	6
15% COG/HA	0.994	0	0	0
	1.039	0	0	0
	1.092	0	1	1
	1.140	10	2	2
	1.191	306	7	4

What is most significant about the observed trends in Table 5.1 is that NH_3 concentrations are predicted to decrease significantly with increasing pressure. This agrees with the findings of Somarathne et al. (2017) who also modelled a reduction in NH_3 at a pressure elevation from 0.1 to 0.5 MPa [106]. However, that study was modelled without scaling flows (corresponding to the elevation of pressure) and hence resulted in a much shorter modelled flame, shortening residence times.

The modelled results of Pugh et al. (2019) [93] contradict the above findings, showing increased NH_3 emissions with increasing pressure (scaled flows). Heat losses were modelled as a fixed percentage (10%) of LHV. The same paper [93] also included elevated pressure experiments and while these results also indicated a general trend for higher NH_3 with higher pressures (0.158 MPa versus 0.105 MPa), the uncertainties prevented any robust conclusions being drawn. A possible explanation for an increase in NH_3 at higher pressures is that reduced flame thickness at higher pressures could lead to lower NH_3 oxidation efficiency (being slow to react) and that unburned NH_2 may reform to NH_3 in the post-flame zone. While this could explain the experimental trends of Pugh et al. (2019) [93] it does not explain the modelled trends, as using perfectly stirred reactors for simulating the flame zone would not account for changes in flame thickness.

Therefore, an alternative explanation for these contradictory modelled findings is offered. Using Fourier's Law of Heat Conduction, the rate of heat conduction (q) is expressed in terms of conductive area (A), the thermal conductivity of the material (k) and the temperature differential through the material (dT/dx) as shown in Equation 5.1 [75].

$$\dot{q} = -Ak\frac{dT}{dx} \qquad \textit{Equation 5.1}$$

The assumption can be made that the AFT is practically constant for a premixed blend across different operating pressures. For example, for Φ = 1.0 and an inlet temperature of 298 K, the AFT values for an NH_3/air blend are 2074 and 2091 K for 1 and 10 atm respectively (as modelled in Gaseq). Thus, dT/dx (between the combustor and its surroundings), would remain virtually constant across the different pressures modelled.

In accordance with Equation 5.1, as heat transfer (q) from the system is proportional to dT/dx (for any one system), heat transfer is also approximately constant across these pressures.

If combustor heat losses are assumed to be approximately constant (i.e. of a fixed power) across pressures, but the thermal power into the system is scaled up with increases in pressure, the *relative* heat loss (i.e. as a proportion of LHV) must decrease as pressure increases. In reality, this can be observed as an increase in measured temperatures at elevated pressure (as observed and discussed in the next chapter, Section 6.6.2). As Pugh et al. modelled with losses as a fixed percentage of LHV, the modelling would not account for a reduction in *relative* heat losses (and increase in flame temperature), when scaling up flows for pressure elevation.

Naturally, small, low powered research combustors have much higher relative heat losses than large, industrial systems (i.e. due to larger surface area to power ratios and practical difficulties reaching thermal equilibrium with their surroundings). Hence, accounting for changes in relative heat loss is especially useful when modelling smaller research combustors at low pressures

Therefore, ever increasing pressures (i.e. thermal power) and thus lower relative heat loss, would increase combustion temperature. This, in turn, would increase heat transfer rate, but the rate of increase would gradually decrease, levelling off to zero as the system approaches adiabatic conditions. Unlike other studies, this study has sought to acknowledge this heat transfer rate curve (albeit rather crudely) by factoring in heat losses at the one fixed power, in line with atmospheric testing results, and keeping this constant to allow for decreases in relative heat loss with upscaling of flows/pressure. For example, for the 15% COG/AA blend at Φ ~1.3, when fixing absolute heat losses at those modelled for atmospheric pressure, the modelled maximum flame temperatures are 1897, 2052 and 2074 K at 1, 6 and 12 atm respectively. Thus, there is a far more significant increase in temperature between 1 and 6 atm than for 6 and 12 atm. Higher combustion temperatures lead to more efficient consumption of NH_3. Therefore, for the same case, NH_3 emissions were modelled as 3074, 30 and 16 ppm (wet basis) at 1, 6 and 12 atm respectively, thus showing a decreasing trend of NH_3 with increasing pressure.

Modelled adiabatically, i.e. losses as a fixed percentage (i.e. 0% of LHV), with little change in temperature, the same model predicts 1.5, 4.4 and 6.2 ppm for 1, 6 and 12 atm respectively, a ~400% increase across the range.

In summary, lower *relative* heat losses at higher pressure (i.e. higher power) gives higher combustion temperatures in the modelling and it is these higher temperatures that are suggested as the reason for the lowering of NH_3 concentrations at elevated pressures in this numerical study. In reality, and as evidenced (albeit with large uncertainties) by the Pugh et al. (2019) study, a decrease in flame thickness with pressure elevation, potentially leading to reforming of NH_3 in the post flame zone, could work to oppose the increase in NH_3 consumption from the higher temperatures at higher flame power.

5.2.2.3 Combined Emissions Including N_2O - Discussion

At 6 atm and the highest values of Φ modelled (~1.3 for the AA blend and 1.2 for the HA blend), NO and NH_3 emissions are 14 and 12 ppm for the AA blend and 24 and 7 ppm for the HA blend (dry, 15% O_2). Although these values only relate to emissions from the fuel-rich primary stage, (i.e. without staging, so with some unburned fuel), such low levels at such modest pressures does suggest all gas turbines would be capable of sub-regulatory limits when utilising either of these blends, potentially even meeting those for natural gas in gas turbine combustion, i.e. < 25 ppm (50 mg/Nm^3 NO_2e) [107].

The modelled concentrations of N_2O for these examples (wet basis) were very low at 2 and 0.3 ppb for the AA and HA blends respectively. Likewise, CH_4 concentrations were two to three orders of magnitude lower than those of the N_2O. As there is no facility to measure N_2O or CH_4, this modelling serves to show that concentrations of these species exiting the primary stage are of little concern under these modestly elevated conditions. Even at atmospheric pressure N_2O was modelled at < 1 ppm for these blends (with CH_4 an order of magnitude lower). As was described in Section 2.3.6, as it is less prone to decomposition in the primary stage, HCN has a greater capacity than NH_3 for N_2O production in the burnout stage. However, the low contribution of fuel carbon in the blend would minimising HCN formation in the primary stage, and temperatures >1300 K in the second stage, would facilitate rapid N_2O decomposition. Thus, the global

warming potential of these blends is practically confined to the concentrations of CO_2 emissions, especially at gas turbine relevant pressures.

5.2.3 Changes in Emissions Concentrations through the PFR

Figure 5.6 shows the change in emissions concentrations and temperature along the length of the PFR for a typical case at atmospheric pressure. It can be seen that temperatures are >1300 K until ~30cm into the PFR.

The modelled results show that the majority of the change in NH_3 and NO emissions concentrations occurs in the first 10 cm of the PFR, with a significantly decreased rate of change in concentrations thereafter. The very high NH_3 concentrations entering the PFR (~4000 ppm) suggest air staging, to create lean conditions, should be delayed until at least 10 cm after the flame (~255 ppm), to avoid considerable conversion of the NH_3 to NO.

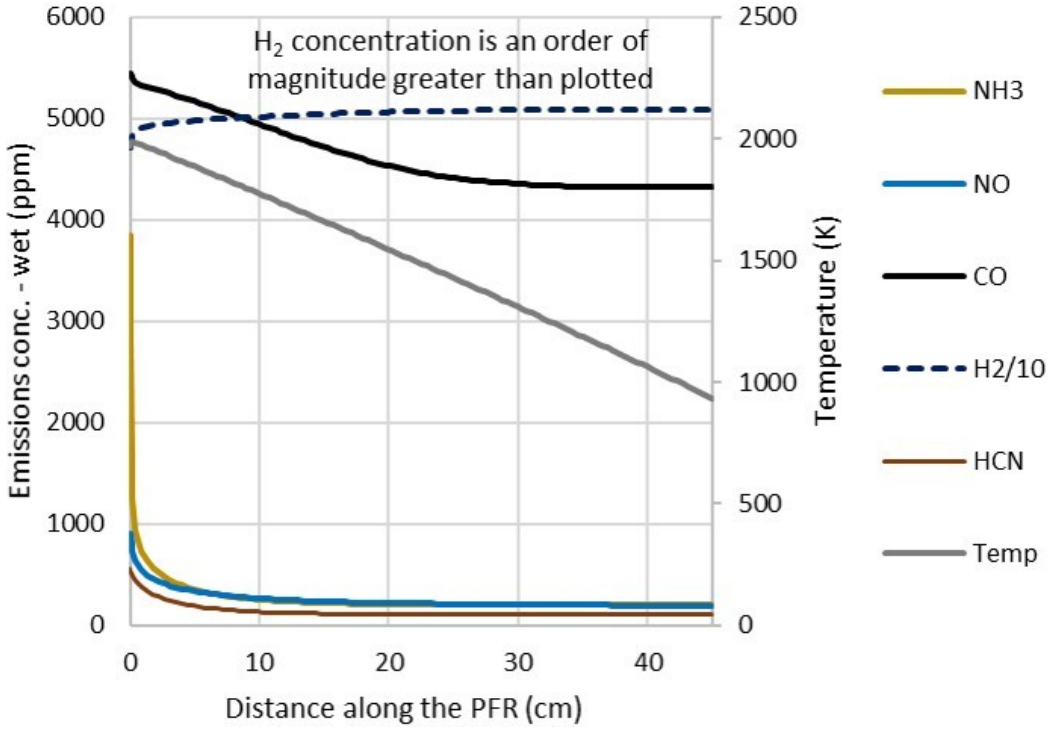

Figure 5.6 Emissions concentrations by distance along the PFR for 15% COG/AA blend at Φ = 1.187 and 0.109 MPa.

The decrease in NH_3 is primarily due to its thermal decomposition to H_2 that, in this example case, increases from 4.7 to 5.0% of the product volume in the first 10 cm. HCN is also reduced from 229 to 56 ppm (~75%) over this distance. The NO concentration

itself is also predicted to decrease dramatically in the first 10 cm of tube post flame (909 to 267 ppm in the example). The decrease in CO is more protracted, due to the low oxygen availability under rich conditions, for its conversion to CO_2. A lean second stage would greatly reduce the CO conversion time. All other cases modelled behave similarly.

There are no facilities to measure H_2 leaving the primary stage in the experimental work. The model was therefore used to find the $H_2\%_{vol}$ leaving the primary stage. For the Φ closest to the AA and HA blends' predicted Φ_{opt} values, the modelling predicted the H_2 fraction to be ~5 and ~3.5$\%_{vol}$, respectively (across pressures). The H_2 (with its high flammability) aids the reactivity of the other unburned gases, such as CO, in the second stage.

Assuming the modelled PFR emissions concentration profile reflects actual conditions post-flame, one would expect to see significantly higher NO_x and N_2O production with air-staging at 5 cm post flame than for 15 cm post flame with little change thereafter. Therefore, a decision was made to investigate air-staging at distances 5 cm and 15 cm downstream of the flame zone. With reference to the OH* chemiluminescence images for the two chosen blends, the post flame zone is assumed to begin ~10 cm from the burner face (~8.5 cm from the burner nozzle exit). Thus staging holes at 15cm and 25cm downstream of the burner face are used in the air-staged work to follow.

5.3 Chapter Summary

- Using OH* chemiluminescence imagery, experimental flows, conditions and emissions data from Chapter 4, a revised and more representative PFR profile and the Tian and Okafor mechanisms, the heat losses and residence times were modified to **develop a more representative reactor model**.
- Flows for the model were then **scaled for elevated pressures** of 6 and 12 atm, to simulate an effect on emissions under gas turbine relevant conditions, using the Tian mechanism.
- The emissions were processed and analysed according to UK regulations (dry, 15% O_2). The results predict that, under typical gas turbine operating pressures, both the **AA and HA blends could be capable of meeting emissions limits for**

NO_x. However, it is recognised that the modelling is for fuel-rich combustion only.

- Thermal power was scaled with **increases in pressure** leading to **a reduction in relative heat losses** (i.e. as a proportion of LHV) in the modelling. Consequently, **NH_3 emissions are reduced with elevations of pressure**, due to an increase in modelled combustion temperature and its positive effect on NH_3 consumption rates.
- The modelled concentrations of **N_2O in the products** leaving the primary stage are three orders of magnitude lower at very modest gas turbine pressures than at atmospheric. Even atmospheric concentrations are **< 1 ppm**. Therefore, the **global warming potential** of these fuel blends is **essentially related to CO_2** product concentrations alone, when combusted under preheated, rich-lean staged conditions, especially at elevated pressures.
- The emissions profile in the modelled PFR suggests **significant decreases in NO_x precursors over the first 10 cm of the post flame zone reactor length**. It is therefore assumed that delays of air-staging would reduce NO_x emissions in the exhaust. It is predicted that locating air-staging at 5cm downstream of the flame zone (~15 cm from the burner face) would show notably higher NO_x emissions than at 15 cm (~25 cm from the burner face).

Chapter 6 Staged Combustion Experiments

6.1 Overview of Second Experimental Campaign

The experimental campaign described in this chapter investigates the effects of elevated pressure and different air-staging configurations on emissions concentrations, for the two blends selected in Chapter 4. A brief overview of the approach adopted, is described below.

1. Earlier chapters demonstrated a variability of Φ_{opt} (i.e. the Φ where combined NO_x and NH_3 emissions are minimised) with changes in blend reactivity. It is therefore reasonable to assume that, at the target inlet temperature of 550 K (higher than the temperatures achieved in the previous experimental campaign), marginally different Φ_{opt} values for the blends could result. Therefore, primary zone optimisation of Φ was repeated at atmospheric pressure (~1.1 bara) for the higher inlet temperature, for both of the chosen blends (15% COG/AA and 15% COG/HA), prior to the air-staging work. Additionally, due to the rapid rate of increase in measured NO_x and NH_3 emissions either side of a blend's Φ_{opt}, the resolution of Φ_{opt} was increased to every ~0.01 (up from ~0.05), to achieve a more precise value for Φ_{opt}.
2. A short study was conducted to experimentally verify the beneficial effects of elevated pressure (to ~1.3 bara) on NO_x and NH_3 emissions (as predicted in the numerical modelling). This study was conducted using the 15% COG/AA blend, without staging, for comparison with atmospheric pressure results from point 1.
3. Having optimised the primary zone Φ in point 1, air-staging was introduced via four Ø20 mm holes cut into a quartz tube confinement designed specifically for this work. This is reminiscent of a rich-quench-lean configuration, but with a premix rather than diffusion flame. The flame polished staging holes were located 25 cm downstream of the burner face as shown in Figure 6.1, quartz tube staging design 1. Confinement dimensions were otherwise identical to those used in the Chapter 4 experiments. The optimised Φ for the primary zone (Φ_{prim}) was held stable while the global Φ (Φ_{gl}) was varied, to see how varying Φ in the second stage effects overall product concentrations of NO_x and unburned fuel

(indicative of how efficient mixing is). The variation in Φ_{gl} was achieved by having an air only staging case as the leanest Φ_{gl} and then progressively substituting more N_2 for a portion of the staged air, thus increasing Φ_{gl}. This was performed for both fuel blends.

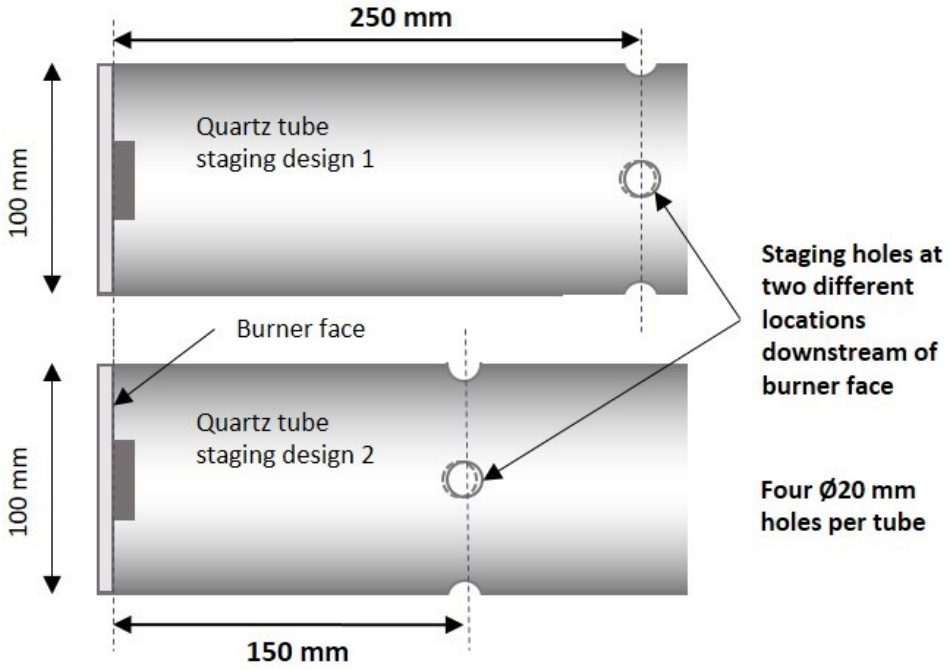

Figure 6.1 Quartz tube designs for staging work.

4. An alternative quartz confinement was then installed with flame polished holes located 15 cm downstream as shown in Figure 6.1, quartz tube staging design 2. Tube dimensions were otherwise identical to those of the other design. On this occasion Φ_{gl} was held stable, using air-only in the second stage, and Φ_{prim} was varied to obtain minimum combined (NO_x/NH_3) emissions for both blends. There was deliberate crossover between these values of Φ_{prim} and Φ_{gl} and those used for the air-only staging in point 3, such that the staging location was able to be investigated as the only changing variable.
5. An emissions comparison was made using the different staging locations at elevated pressure, for the 15% COG/AA blend at ~Φ = 1.2. This was to compare the effect of staging location on emissions under elevated pressure conditions.

Naturally, the method is similar to that of the previous experimental campaign in Chapter 4. The variations on the earlier method are described in the following sections.

6.2 Air-Staging Mass Flow Calculations

The relative heat losses in the model combustor are much higher than those of a full-scale industrial system, largely due to the greatly reduced reactant flow densities and greater surface area to volume ratio. To keep exhaust temperatures for the model combustor relevant to those of full-scale turbine inlet temperatures, Φ_{gl} values for the model combustor are necessarily higher (i.e. providing less second stage cooling). Maintaining industrially relevant temperatures avoids excessive quenching, making progress of the combustion chemistry in the model rig representative of a real system.

The fuel-rich combustion of the previous campaign (Chapter 4) naturally resulted in considerable unburned fuel emissions. To maintain exhaust temperatures, and therefore system losses, to approximately the same as in Chapter 4, it was necessary to adopt a crude method for matching the increase in heat release from the previously unburned fuel (now being consumed in a fuel-lean second stage), with the cooling effects of the oxidant entering the second stage. Thus, for this chapter's campaign, it is necessary to assume that, with the secondary air-staging (equivalent to $\Phi_{gl} < 1$) and sufficient mixing, the previously unburned fuel is now completely consumed, leading to an additional heat release equivalent to a ~100% combustion efficiency. This assumption is tested later via measurement of CO and NH_3 in the exhaust. Therefore, the mass of air (or air/N_2) introduced in the second stage was calculated so as to have a specific heat capacity approximately equivalent to the increase in heat release from the previously unburned fuel.

Using the 15% COG/AA blend as an example, approximately one sixth of the fuel will remain unburned after the primary stage (i.e. at a Φ_{opt} of ~1.2). Thus, for a 25 kW_{th} flame power, the unburned portion is equivalent to ~4.2 kW_{th}. This energy heats the staged air from a target inlet temperature of ~550 K up to an exhaust temperature of ~1250 K (i.e. an increase of ~700 K). The approximate exhaust temperature of ~1250 K was arrived at via observations from the previous experimental campaign and the improved reactor network modelling results. Values of specific heat capacity (C_p) change with temperature. At 550 K, the target inlet temperature into the second stage, the C_p of air is 1.040 kJ/kgK for air. At an exhaust temperature of ~1250 K, the C_p of air is 1.182 kJ/kgK

[75]. Thus, the average C_p for the air is taken to be 1.111 kJ/kgK. Assuming no change in overall heat transfer from the system compared with the previous campaign, an air flow of 5.36 g/s would approximately negate any temperature increase resulting from the increase in heat release due to complete combustion for the 15% COG/AA blend. This air flow is equivalent to a Φ_{gl} of 0.67. For convenience, a Φ_{gl} of 0.7 was adopted for the air-staged cases. Hence, the precise calculated flow for Φ = 0.7 is 4.84 g/s of air for this blend.

To enable variation of Φ_{gl}, a portion of the second-stage air was replaced with a very similar flow rate of N_2, thus maintaining the flow structures in the combustor. The precise flows of N_2 were calculated to account for the modest difference in specific heat capacity (C_p) between N_2 and air, keeping product gas temperatures and hence system heat losses, near equivalent across the variations in Φ_{gl}. At 550 K, the target inlet temperature in the second stage, the C_p of N_2 is 1.065 kJ/kgK and at an exhaust temperature of ~1250 K, the C_p is 1.210 kJ/kgK [75]. Thus, the average C_p for the N_2 is taken to be 1.138 kJ/kgK. Hence, when substituting N_2 for some of the air, the replaced portion of the air flow rate is multiplied by 0.976. Considering the moles of N_2 added account for 97.6% of the moles of air they replace, product species concentrations in the exhaust are also approximately maintained.

With a Φ_{gl} of 0.7 for the air-staged cases, increases to 0.8, 0.9 and 0.95 were used for the air/N_2 staging. The fuel, primary air and secondary air/N_2 target flowrates are given in Appendix B.1a for the AA blend (Φ_{prim} 1.15 to 1.25) and Appendix B.1b for the HA blend (Φ_{prim} 1.10 to 1.20). These values relate to the flows at 1.1 bara (approximating atmospheric pressure). The wide ranges of Φ_{prim} given above were calculated in preparation of possible movement of Φ_{opt} with the anticipated change in inlet temperature, compared with the previous campaign.

6.2.1 Elevated Pressure Material Flows

To maintain nozzle exit velocities and residence times the same as those of the atmospheric testing (~1.1 bara), flows were scaled in line with the increase in pressure, with pressure controlled via the incremental partial closing of the back-pressure valve.

An initial attempt was made to flow the reactants at one third higher power than for the atmospheric cases. However, it soon became apparent that this was not sustainable, even for a short testing period, due to the restriction on the NH_3 inlet flows. The tests were conducted in October, so ambient temperatures were only ~13°C maximum, enabling just 0.35 MPa exit pressure on the NH_3 drum regulator. Therefore, mass flowrates ~17% higher (~one sixth) were ultimately used for all material flows for the pressure work. This scaling for pressure meant the pressure work was conducted at 1.3 bara, hence just over a one quarter increase above ambient pressure.

6.2.2 Predicting Φ_{opt} for Different Blends/Inlet Temperatures

It was found possible to use past data collection to predict the likely value of Φ_{opt} for the different blends at different inlet temperatures.

As was found in Chapter 4, the Φ_{prim} values at the NO/NH_3 intersects (approximating the Φ_{opt} values) increase with percentage COG. This indicates that Φ_{opt} is influenced by the reactivity of the blends. Essentially, Φ_{opt} is shifted to a richer value for the more reactive blends. As S_L is a predictor of the reactivity of a blend, S_L values for each of the six blends investigated in Chapter 4 were simulated at their respective Φ_{opt} (using Chemkin and the Okafor mechanism) under the specific experimental conditions recorded for each case (e.g. in consideration of varying inlet temperature). These simulated S_L values are shown in Table 6.1.

Table 6.1 Simulated flame speeds (S_L) for the Chapter 4 experimental blends at their respective Φ_{opt} values (Okafor mechanism).

Fuel		P (MPa)	Inlet T (K)	Φ_{opt}	S_L (cm/s)
COG %	Ammonia				
20% COG	AA	0.1088	512.5	1.205	29.157
15% COG	AA	0.1088	506.3	1.185	26.461
10% COG	AA	0.1089	507.4	1.170	24.623
20% COG	HA	0.1086	506.8	1.180	24.946
15% COG	HA	0.1085	513.3	1.150	23.078
10% COG	HA	0.1084	515.3	1.125	20.577

The S_L values from Table 6.1 are plotted (at their Φ_{opt} values) as round markers in Figure 6.2, linking with the colour scheme from the table. A straight line of best fit passes through these points (dotted line). The correlation between Φ_{opt} and S_L is shown to be strong across the two blends for the conditions tested.

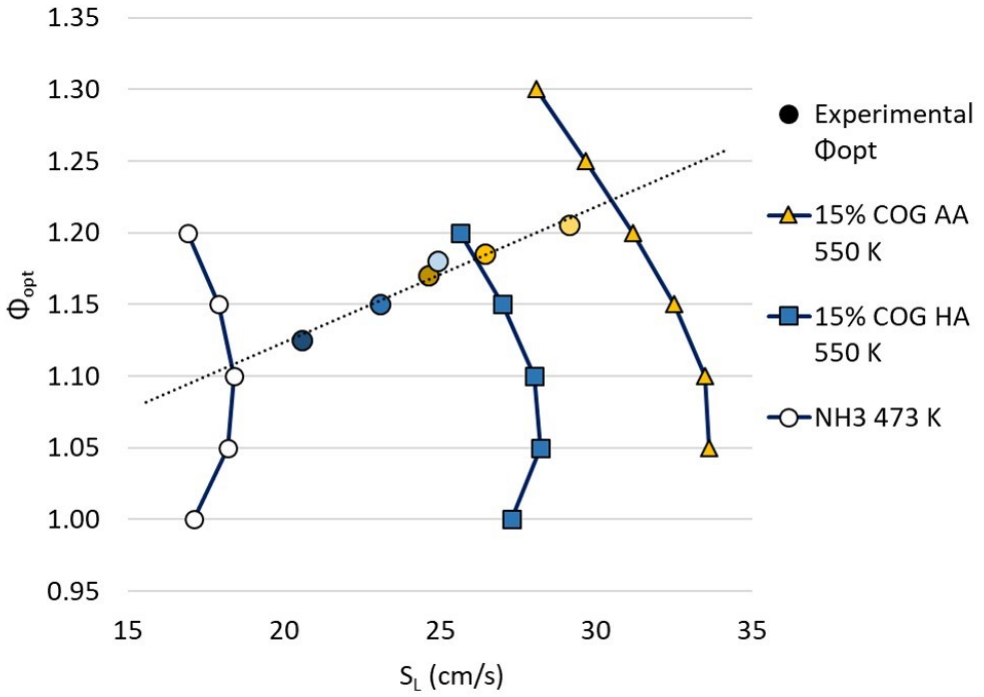

Figure 6.2 Φ_{opt} by S_L at atmospheric pressure (modelled using Chemkin and the Okafor mechanism).

To further assess the strength of the correlation, the S_L values for a pure AA blend with an inlet temperature of 473 K (Φ_{prim} of 1.0 to 1.2) were also plotted in Figure 6.2 (as white circular markers). The S_L curve intersects the correlation line at a predicted Φ_{opt} of ~1.1 for pure NH_3, which is supported by the findings of another study under similar operating conditions [40].

Such a strong correlation suggests that plots of Φ_{opt} against S_L, which could be obtained during commissioning, could potentially be used to predict the likely Φ_{opt} of NH_3 based blends under varying inlet temperatures and blend compositions.

The correlation was thus utilised for the prediction of Φ_{opt} values for the 15% COG AA and HA blends at the higher inlet temperature of 550 K. The simulated S_L curves, obtained for a range of Φ, intersected the correlation line at Φ_{opt} values of 1.22 and 1.18

for the AA and HA blends respectively (plotted as orange triangles and blue squares respectively). This is up from 1.185 and 1.15 at the lower inlet temperatures (of 506 and 513 K for AA and HA respectively). Hence, these revised values of Φ_{opt} were considered appropriate starting values of Φ for testing (assuming an inlet temperature of 550 K).

6.3 Quartz Confinement Design and Installation

As discussed in Section 5.2.3, the holes for the introduction of second stage air should be located at 15 and 25 cm downstream of the burner face, to verify the beneficial effect on NO_x reduction arising from the rapid decrease in NO precursor concentrations predicted between these locations.

Figure 6.3 shows the combustor assembly. Each of the two tube designs had four holes at one location only (i.e. either 15 or 25 cm downstream of the burner face). The two staging hole locations are illustrated on a single tube for convenience (not to scale).

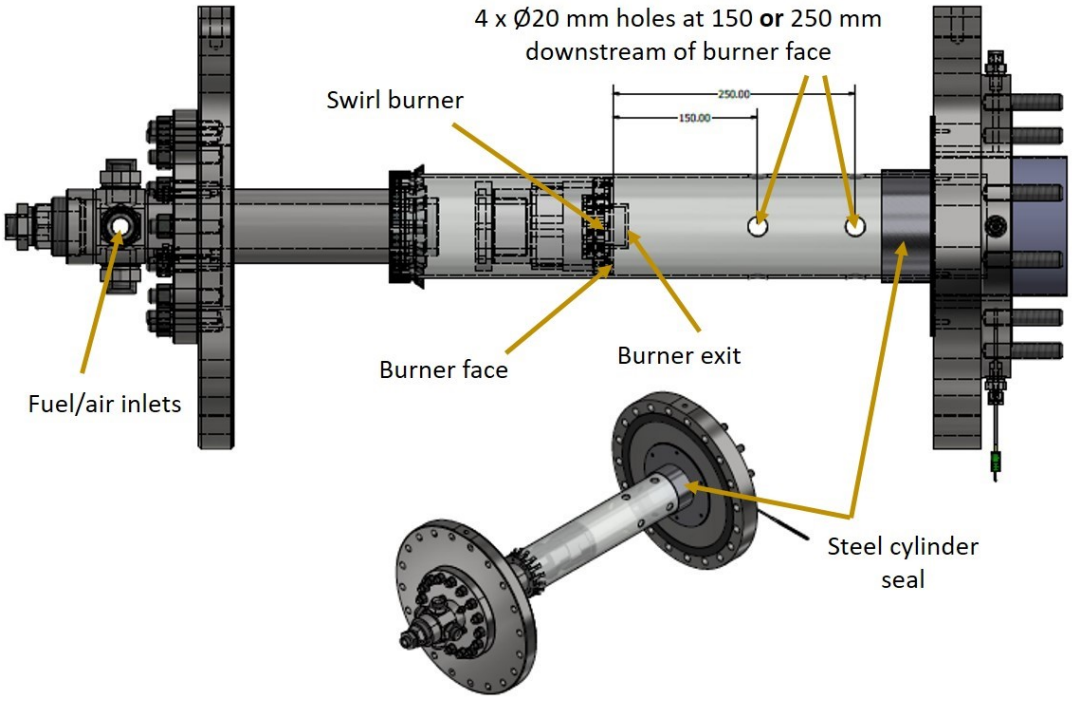

Figure 6.3 Sealed confinement with staging holes assembly

Unlike in the first campaign, the tube exit required sealing. This ensured that all the secondary staged flows passed through the inlet holes. The seal was achieved by installing a short cylinder of steel, encircling the quartz tube as it exited the pressure

casing. The short steel cylinder was attached to the inside of the pressure casing via a flange on the back end of the casing. The cylinder was cut along part of its length in several places around its circumference allowing it to be bent inwards as the cut sections (or 'petals') overlapped. Heat resistant wadding was installed between the quartz tube and the steel cylinder to prevent gaseous leakage and to enable a jubilee band to be tightened around the steel cylinder for a secure fit. Enclosing the tube risks creating pressure differentials between the inside and outside of the tube and the potential for failure of tube integrity. Therefore, the holes need to be of sufficient size to limit the risk of this pressure differential occurring. However, sufficient penetration of the staged air into the primary stage products is also necessary for sufficient mixing to take place, ensuring high combustion efficiency ahead of gas sampling. Additionally, for even penetration across the flow, the holes should be positioned axi-symmetrically. As the inlets are simply holes, all flows are naturally directed to the centre of the product gas flow. No examples of air-staging directly into a quartz confinement could be found in the literature, making this a novel design.

A 50 kW_e micro combustor employed successfully by Kurata et al. (2017) achieved combustion efficiencies of 96.5% for NH_3 only combustion [78]. The geometry of the same combustor is described in detail in a later CH_4/NH_3 study by Okafor et al. (2019) where efficiencies of 99.8% were achieved (at an elevated pressure 0.25 MPa) [98]. The combustor is of a similar scale to the one used in this study having Ø130 mm narrowing to Ø88 mm, with a length of 238 mm. Dilution holes in these studies are situated ~150 mm downstream of the burner face and total 2,500 mm^2 in inlet area, with all primary stage air provided by the swirler. Halving this, to reflect the lower power for this chapter's study, gives an inlet area ~ 1,250 mm^2. Thus four equal holes of Ø20 mm are used here (1,256 mm^2) and the combined area of the air-staging holes is equivalent to the primary inlet nozzle area.

Calculations of flow velocities, suggests broadly equivalent flow velocities of ~5.9 m/s for products leaving the primary zone and ~5.8 m/s for the staging holes inlet (at atmospheric pressure). It was assumed that this equivalence of flow would enable sufficient penetration of the staged inlets and adequate mixing ahead of the sampling

probe. Volumetric flows for the staged cases increased by ~16% after the staging point. These calculations are detailed in Appendix B.2.

6.4 Changes in the Rig Inlet Flows

Figure 6.4 shows an image of the inlet flow pipework for the combustion rig. All inlets were preheated and insulated en route to the combustor. The secondary air/N_2 was split and entered the pressure casing from both sides of the rig at the burner end. The fuel and primary air entered in opposition from either side of the inlet plenum, upstream of the burner.

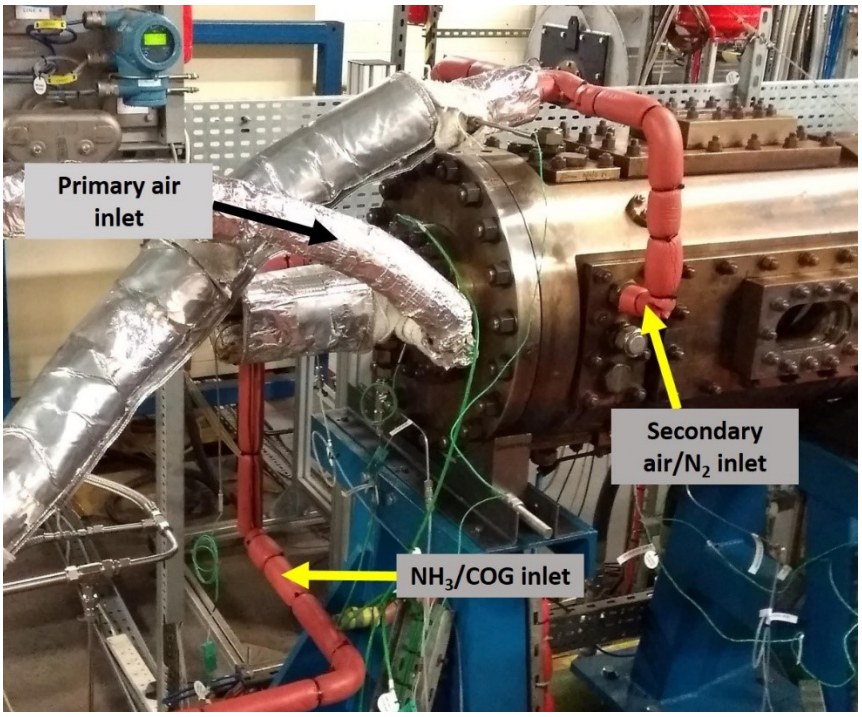

Figure 6.4 Inlet flows into the combustion rig

6.4.1 Changes in the Air/Steam Flow Paths and Measurement

The passage of the preheated secondary air/N_2 flows into the burner end of the pressure casing and alongside the hot quartz confinement, inevitably lead to additional heating of the flows prior to their ingress into the tube. Naturally, the longer the journey of the air/N_2 before entry into the tube holes, the greater the heat transfer from the flame via the quartz tube. The secondary inlet flows increased in temperature by approximately 132 to 209 degrees between entry into the pressure casing and passing into the staging holes. A second stage inlet temperature of ~550 K was maintained for the two different

staging locations as follows. The preheat temperature (upstream of the pressure casing) was monitored (using a thermocouple in the flow stream). By manually altering the level of secondary inlet preheat, in response to the readings of a newly installed thermocouple positioned close to the secondary inlet holes, the secondary inlet temperature was maintained at 550.7 ± 17 K for all staged cases.

The revised air/steam preheat system is shown in Figure 6.5.

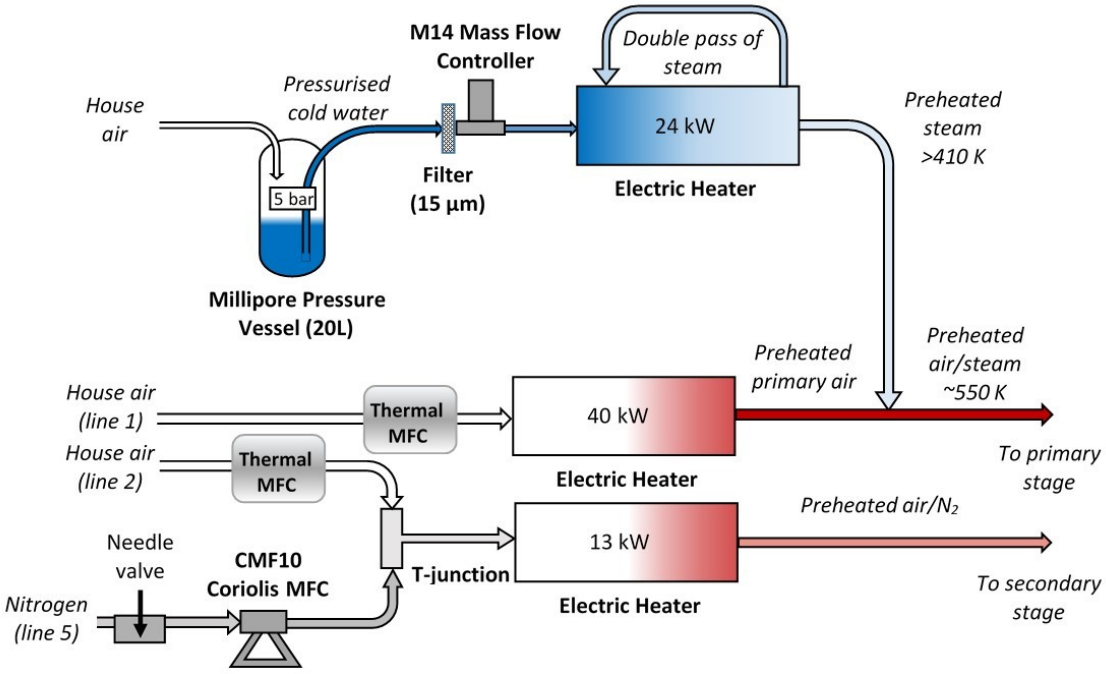

Figure 6.5 Schematic of the air/steam/nitrogen delivery system for staged combustion.

For the staging work, the secondary air/N_2 inlet flows were mingled using a T-junction downstream of their individual MFCs (for independent control of mass flow) before passing through a 13 kW heater. The manual control of this heater (to help regulate the temperature of the air/N_2 into the staging holes) meant that the preheat temperature upstream of the pressure casing was 347 to 424 K, varying with staging location and rig temperature (which increased over the duration of testing).

Addition of the steam to the primary air (at ambient temperature) upstream of the 40 kW heater led to condensation of the steam ahead of the heater inlet, resulting in unstable pulsing in the combustor. Therefore, it was necessary to entrain the steam into the primary air flow after the 40 kW heater, sacrificing additional steam preheating by

the 40 kW heater and reducing the potential premix inlet temperature (further discussed in Section 6.4.3).

The air line MFCs were Bronkhorst In-Flow F203 thermal MFCs with a rated accuracy of ±0.5% of reading ± 0.1% of full-scale. Air flows were averaged and the uncertainties accounted for, having significant bearing on both Φ_{prim} (for the primary air flow) and the calculations for product species concentrations (after second stage air dilution). The N_2 flows were temporally averaged, but having no influence on Φ and minimal impact on species dilution, uncertainties were assumed to be insignificant for the N_2 flow measurements. All other air/steam metering remained unchanged.

6.4.2 Changes in Fuel Inlet Temperature and Composition

A shell and tube counter-current heat exchanger was constructed to preheat the combined NH_3/COG fuel inlet stream (from lines 4 and 3 respectively). The heater used to provide the heated water for the exchanger, is built for the same primary purpose as the one used for the rapid cooling of the sampled product gases and therefore maintains a temperature of 433 K. Hence, this is the approximate maximum temperature to which the fuel gases could be preheated. The COG gas composition was, as before, simplified with the omission of the ethane and ethene components, with the same requested composition as for the previous experimental campaign. The precise compositions for the three cylinders supplied are given in Appendix B.3.

6.4.3 Premix Inlet Temperature

As in the previous campaign there was difficulty reaching a preheat temperature of 550 K for the primary air/fuel inlet for both the HA and AA blends. As the minimum inlet temperature achievable across all cases is associated with the lowest air flowrate (i.e. minimum heat capacity and highest heat losses) the richest AA case was run first (Φ = 1.25), to establish an approximate standardised inlet temperature of ~530 K across all subsequent tests. Inlet temperature was therefore 533.2 ± 4.8 K across all tests reported in this chapter. At this inlet temperature and using the method described in Figure 6.2 (modelling flame speed versus Φ_{opt}), the predicted Φ_{opt} values were 1.205 and 1.17 for the AA and HA blends respectively. Hence testing was centred at these values of Φ_{prim}.

6.5 Modifications in Emissions Measurement and Observation

6.5.1 Sample Dilution and Emissions Uncertainties

The optimisation of the primary stage is achieved by the minimisation of NH_3 and NO_x emissions. The CO emissions were not of interest for this primary stage optimisation and were on-scale (i.e. below the CO analyser's maximum limit of 10,000 ppm) for the staged work. Therefore, sample air dilution was only necessary to provide O_2 for the NH_3 converter when not staging (< 0.1 g/s) and could be stopped during all NO_x measurement, removing the issue of flawed NO_2 readings as discussed in Section 4.8.1. Concentrations of NH_3, undiluted, were calculated as in Section 4.6.4, using the dilution factor equations.

The concentration of H_2O product in the undiluted samples of NH_3 combustion is much higher than for hydrocarbon work. As was stated in Section 4.8.1, an assumption of a 1% reduction in measured reading for every 10%$_{vol}$ H_2O in the sample was given (by the manufacturer) as appropriate for consideration of the cross-interference of water in the NO_x analyser samples. Therefore, Gaseq was again used to calculate the equilibrium concentrations of H_2O for the precise mass flows (at the logged operating conditions) and this was used for each individual test point (for NO_x and NH_3 readings separately) to ascertain the NO_x uncertainties due to H_2O cross-interference. Gaseq was also used to calculate all experimental Φ values (Φ_{prim} and Φ_{gl}) and their uncertainties (for the NO_x and NH_3 readings separately), from the temporally averaged reactant flows. For the optimisation of the primary zone (no staging), the concentrations of H_2O in the undiluted product stream were ~28 and ~33%$_{vol}$ for the AA and HA blends respectively. For the staged work, the concentrations of H_2O in the undiluted product stream were ~22 and ~26%$_{vol}$ for the AA and HA blends respectively. Thus, uncertainties related to H_2O cross-interference, ranged from approximately +2.2% to +3.3% for the NO_x readings, across all tests. This uncertainty is in addition to that of ±1% for the NO_x analyser and consequently makes positive uncertainties much greater than negative. NO_x analyser cross-interference from CO_2 (< 1% reduction with 10% CO_2) is not considered due to the very low concentrations of CO_2 (~1%) in the samples. For the MGA, uncertainties of ±0.01% in O_2 readings and 1% of range (or 0.5 ppm if greater) for CO_2 and CO readings

are considered insignificant (or irrelevant) and are thus ignored. Therefore, whereas maximum combined uncertainties for the diluted samples in Chapter 4 (and other studies using the same experimental setup [94, 103]) used ±5% measurement uncertainty, maximum combined uncertainties for NO_x and NH_3 emissions measurements in this chapter's work are modified to be between +8 and –5%, to account for the potential for increased H_2O cross-interference.

6.5.2 Calculating Equivalence Ratio Uncertainties

The practice of accounting for uncertainty in Φ is not evident in any of the relevant literature. However, it is reported in this chapter because of the high sensitivity of emissions to changes in Φ. The inclusion of Φ uncertainties may serve to explain differences in values of Φ_{opt} between studies.

Uncertainty in Φ is relatively large due to the need for high resolution of Φ in this work. However, any error can be assumed to be very consistent between data points (given the same set up and similar flows) shifting all data points leaner or richer by an equivalent degree, so as to enable meaningful, precise comparison for trending between cases. Hence, to dispense with the need to show numerous near equivalent horizontal error bars of considerable span, the uncertainties are reported under the plots, so maintaining clarity within the plots.

6.5.3 Chemiluminescence Observations

In addition to OH* chemiluminescence, NH_2* chemiluminescence observations were made. Regions of high NH_2* production facilitate the consumption of NO, as discussed in detail in Section 3.5.3. Significant optical emission bands for the NH_2 radical are found at 610 to 670 nm (peaking at 630 nm) and 720 to 780 nm (peaking at 760 nm), with a peak in H radical also present at 656.3 nm [148]. Therefore, as in similar studies [94, 103], a bandpass filter centred at 632 nm (±10 nm FWHM) was used for the NH_2* chemiluminescence observations.

6.6 Experimental Results and Discussion

6.6.1 Optimising the Primary Zone

Figure 6.6 shows the emissions results for both the AA and HA blends (with 15% COG) at atmospheric pressure. The averaged reactant flowrates, important operating conditions and emissions results for the optimising of the primary zone at atmospheric pressure, are included in Appendix B.4. The emissions in the Appendices are given as wet, complete with $H_2O\%_{vol}$ in the sample (modelled in Gaseq) to enable adjustments depending on local regulations and for numerical modelling purposes. This optimisation was performed using the confinement with staging holes at 25 cm downstream of the burner face, although no staging took place.

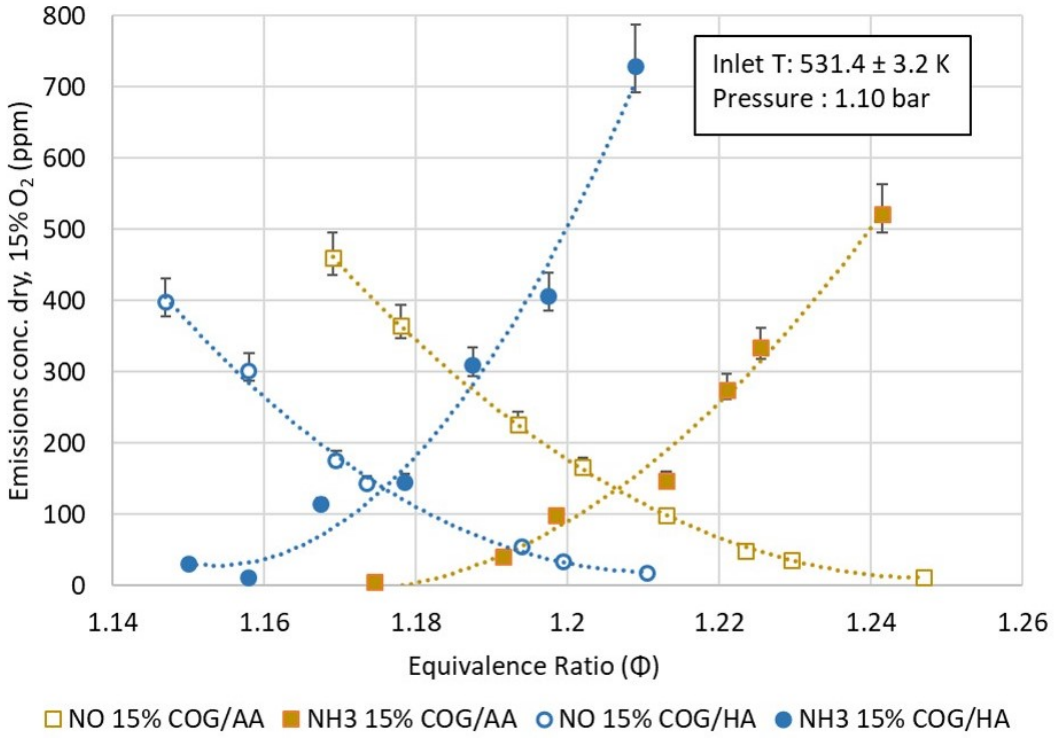

Figure 6.6 NO and NH_3 emissions concentrations by Φ for 15% COG/AA and 15% COG/HA (dry, 15% O_2)

Readings for NO_2 were insignificant and thus sometimes negative, again due to decreases in Φ over the duration of a test point, resulting from NH_3 restrictions from supply drum cooling. This fact was observed in the first few test points and so NO_2 measurements were excluded for the primary zone optimisation. Negative values for NH_3 are once again excluded for the same reason, from all plots in this chapter.

The data trends are indicated using polynomial trendlines of order 2 (dotted lines). Calculated uncertainty in Φ is ±0.02 to 0.0215 (increasing with richer Φ). Many emissions uncertainties were entirely obscured by the data points (being comparatively small), but are visible for the highest emissions values. The emissions results are in good agreement with those of the improved numerical model and the results from the first experimental campaign. For example, the AA blend was predicted by the model to have NH_3 concentrations of 630 ppm (dry, 15% O_2) at atmospheric pressure and Φ ~1.25, albeit with a marginally lower inlet temperature of 503.3 K.

The Φ_{opt} of the HA blend (Φ = 1.175) is approximately 0.03 less than the Φ_{opt} of the AA blend (Φ = 1.205). These values are very close to those predicted at the end of Section 6.4 using the flame speed/Φ_{opt} correlation (i.e. 1.17 and 1.205), further supporting that approach to approximating Φ_{opt}. At their respective Φ_{opt} values, the combined NO and NH_3 emissions are approximately equivalent for the AA and HA blends at ~ 260 ppm (130 ppm NO and 130 ppm NH_3). This equivalence of combined emissions at Φ_{opt} was not demonstrated in the earlier study, possibly due to the poorer resolution of Φ. Based on this finding, either blend is equally suitable for emissions. However, for $\Phi > \Phi_{opt}$, the rate of increase in NH_3 emissions concentrations with Φ is greater for the HA fuel. Thus, optimising Φ for HA blends demands greater control of combustion variables (e.g. fuel flow) than for anhydrous blends.

The minimum combined emissions for the blends are higher than in Chapter 4, despite the higher resolution of Φ. The minimum combined NO and NH_3 emissions were previously 174 and 219 ppm for 15% COG/AA and 15% COG/HA respectively. For this optimisation of the primary zone, all variables except inlet temperature have been closely maintained (i.e. fuel compositions, pressure, etc.). According to the trend in Figure 6.6, when the AA blend has NH_3 emissions ~ 100 ppm, NO is ~190 ppm, whereas it was previously 76 ppm. This suggests that, in aiming to increase reactivity via a modest increase in premix inlet temperature (~30 K), the resulting higher peak flame temperatures are increasing NO_x production in the primary stage.

6.6.2 Investigating Elevated Pressure Effects on Emissions

The NO and NH_3 emissions results for the 15% COG/AA blend at pressure 1.1 bara (as in Figure 6.6) are now compared with the same blend at the modestly elevated pressure of 1.3 bara (~17% higher) and higher power of 29.2 kW, in Figure 6.7, using the same confinement. Averaged reactant flowrates, important operating conditions and emissions results (again wet with stated $H_2O\%_{vol}$) for the optimising of the primary zone at elevated pressure are included in Appendix B.5.

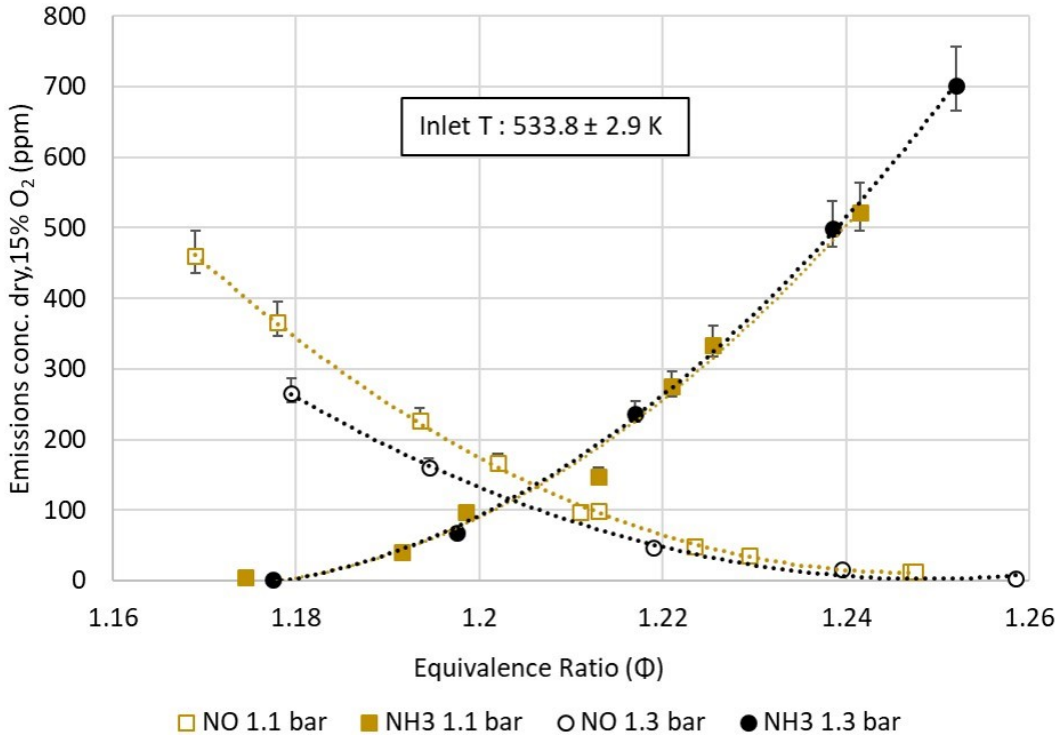

Figure 6.7 NO and NH_3 emissions at 1.1 and 1.3 bara by Φ for 15% COG/AA blend (inlet 533.8 ± 2.9 K).

Calculated uncertainty in Φ is ±0.0185 to 0.02 (increasing with richer Φ). As discussed in Section 5.2.2.1, the modelling suggested reduced NH_3 with elevated pressure (due to higher temperatures from lower relative heat losses) and combustion exhaust temperatures for 1.3 bara were 34 K higher than for 1.1 bara (at ~ 1.24) and yet there was no discernible difference in NH_3 emissions between pressures. While the data cannot support the modelling results of Chapter 5, which like the work of Somarathne et al. (2017) [106] showed a trend of decreasing NH_3 with increases in pressure, neither can it support the findings of Pugh et al. (2019) which showed a trend for increases in

NH_3 emissions with pressure elevation, albeit with high uncertainties [93]. It is possible that the pressure elevations were too modest to effect the NH_3 emissions either way. It is also possible that a reduction in NH_3 emissions due to temperature increase (at the higher power), was so slight, as to only be capable of off-setting a possible pressure induced increase in NH_3 from a narrowing of the flame front.

Although the absence of an observed NH_3 reduction is assumed to be related to the difficulties in flowing sufficient power, to reveal the trends predicted by the modelling, it is possible that there is actually an issue with the mechanisms' treatment of NH_3 emissions at elevated pressure, as both mechanisms were originally developed and verified at or below atmospheric pressure [96, 130]. Thus, performance in modelling at elevated pressures may be poor for these mechanisms. Unsurprisingly, most appraisals of these mechanisms have been more concerned with their ability to predict NO_x [112, 113].

In summary, Section 5.2.2.1 detailed the existing conflicting evidence regarding changes in NH_3 emissions with pressure elevation. This study has been unable to advance this work due to fuel flow restrictions. Thus, there is currently no robust evidence for whether pressure elevation increases or decreases NH_3 in gas turbine systems at industrially relevant pressure ratios. Therefore, further work, beyond the scope of this study, investigating much higher pressures, scaled at higher powers, is required to answer this important question.

As predicted, NO production does decrease noticeably with the increase in pressure, such that at $\Phi = 1.2$ it is ~25% lower at the higher pressure. Consequently, the Φ_{opt} shifts to a slightly lower value, closer to $\Phi = 1.2$, showing that Φ_{opt} is modified by pressure. Minimum combined readings of NO and NH_3 are approximately 235 ppm at the elevated pressure. This is ~13% lower than for 1.1 bara (~260 ppm). Therefore, despite only modest pressure elevation, there is sufficient data to show clear overall improvement in NO, and thus combined emissions, with elevated pressure.

The OH* and NH_2* chemiluminescence at the two different pressures is shown in Figure 6.8, for 15% COG/AA, with a Φ_{prim} of 1.195 ± 0.003. Colour scaling is to the maximum intensity for each image. As previously discussed (Section 4.7.1), regions of greatest OH*

concentration are considered the most reactive, highest temperature regions. The images for OH* chemiluminescence in Figure 6.8 show there is little difference in the structure of the regions of highest temperature across the two pressures. At the higher pressure, there is a slight narrowing and elongation of the flame brush at the tip.

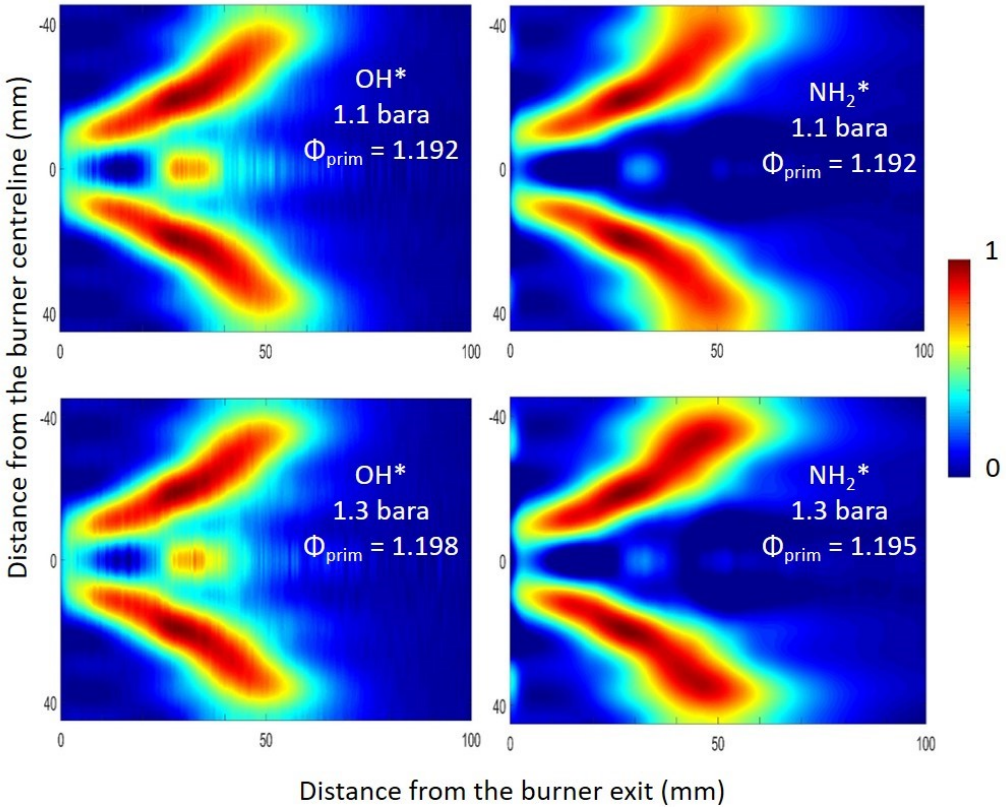

Figure 6.8 OH* and NH_2* Chemiluminescence for 15% COG/AA without secondary staging at varying pressure (1.1 to 1.3 bara)

Were it not for the increase in pressure, the concentration of excited OH* radicals would normally be expected to increase at the higher power, due to higher temperatures. The OH* chemiluminescence maximum intensity was in fact measured as 4% lower for the higher pressure case in Figure 6.8. This decrease (assuming no change in background CO_2 readings) could reflect the promotion to the right, with increase in pressure, of the chain terminating reaction H + OH + M ↔ H_2O + M (Equation 2.12), in apparent agreement with the literature (see Section 2.3.3). This reduction in OH radical concentrations would consequently result in lower NO_x production.

The NH_2* chemiluminescence shows the conversion of NH_3 to NH_2 starts as soon as NH_3 exits the burner. The NH_2 is mostly consumed at < 70 mm downstream of the burner

exit for both pressures (assuming NH_2* is proportional to NH_2 radical concentration). At the higher pressure, the flow field has a more pronounced 'V' shape, with less NH_2* flowing into the ORZ. The higher pressure shows a more localised distribution of NH_2* in the flame (a narrower flame thickness), suggesting a more rapid consumption of NH_2 (reacting with NO) is taking place at the slightly elevated pressure. The regions of greatest OH*, are the same regions in which the NH_2 radical is most concentrated, especially at the elevated pressure. This means that in the regions of highest temperature (leading to thermal NO_x production) and highest fuel oxidation (leading to fuel NO_x production), NH_2 is readily available for consuming the NO and minimising NO_x leaving the primary stage.

6.6.3 Varying Global Equivalence Ratio in Staging

Averaged reactant flowrates, important operating conditions (including sample O_2 concentrations) and emissions results (wet with $H_2O\%_{vol}$) for the staged combustion of the AA and HA blends, whilst varying Φ_{gl} at atmospheric pressure, are included in Appendix B.6. The scheduling of the experimental campaign did not allow for sufficient time to establish the precise values of Φ_{opt} in the primary zone (as shown in Figure 6.6) ahead of the staging work. Ideally this would be obtained via detailed analysis of the prior primary zone optimisation data before continuation (e.g. averaging flows in the logs, etc.). Hence, visual inspection of the spot values (approximated values as observed during testing) was performed to judge the approximate values of Φ_{opt} for the two blends. From the visual inspection, the Φ_{opt} values for the primary zone were therefore approximated as 1.18 and 1.22 for the HA and AA blends respectively, so these were the target primary zone Φ values (Φ_{prim}) used for the staging work for the variation of Φ_{gl}.

Figure 6.9 shows the NO_x and NH_3 emissions results for both fuels, optimised for the primary zone when varying Φ_{gl}. The global Φ values are plotted at their calculated average, with uncertainties of ±0.0125 to 0.0185 (increasing with Φ_{gl}), and were the same for both fuel blends. The Φ_{prim} values for the AA blend were 1.215 ± 0.003, (~0.01 higher than the later derived Φ_{opt}) with a measurement uncertainty of ±0.021. The Φ_{prim} values for the HA blend were between 1.178 ± 0.004 (~0.003 higher than the later derived Φ_{opt}), with the same measurement uncertainty of ±0.021.

As previously described, Φ_{gl} for these cases was varied from 0.7, using simple air-staging, up to 0.95, via the reduction of air and equivalent replacement of N_2 in the second stage (based on the thermal capacity of N_2 versus air). Aside from maintaining flow fields and providing an equivalent thermal heat capacity when cooling combustion products in the second stage, the N_2 also kept the dilution of emissions equivalent, in place of the missing air.

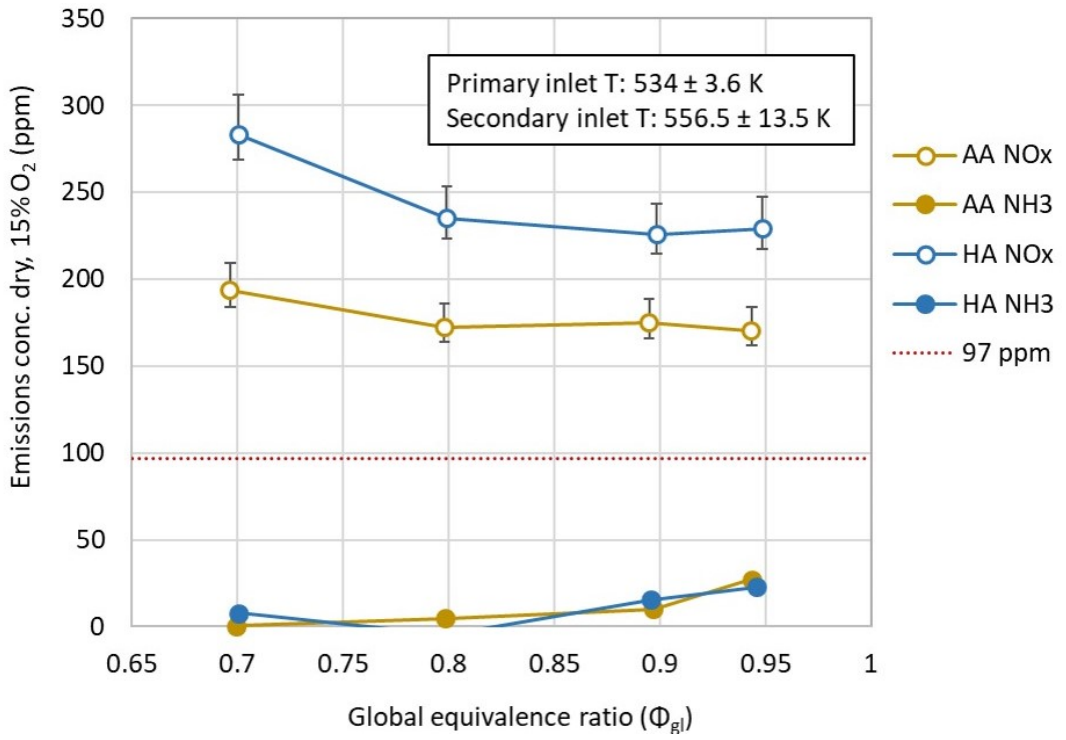

Figure 6.9 Emissions concentrations of NO_x and NH_3 by Φ_{gl}, for the staged combustion of the AA and HA blends, optimised in the primary stage (dry, 15% O_2), 1.1 bara.

The usual approach to measuring emissions concentration (i.e. measuring exhaust sample O_2 and relating this to 15% O_2 as per the regulations) could not be used for the air/N_2 staged cases (i.e. Φ = 0.8, 0.9 and 0.95), as the inherently lower percentages of exhaust O_2 (when using N_2 in the staging) would distort the calculated emissions concentration values, artificially lowering them. Considering the molar flows of N_2 were near equivalent to those of the air they replaced (97.6%$_{mol}$), any difference in sampled product concentrations was considered negligible. Thus, the O_2 percentage from the air-staged case at 0.7 (for both fuel blends independently) was used to establish a consistent and representative approach to measuring relative NO_x and NH_3 concentrations, across the range of Φ_{gl} investigated.

For the AA blend at Φ_{prim} = 1.215, NO_x emissions have increased from ~100 ppm without staging (see Figure 6.6) to ~190 ppm with the introduction of pure air-staging, while reducing unburned NH_3 from ~220 ppm to practically zero. Similarly, for the HA blend at Φ = 1.178, air-staging has increased NO_x from ~120 ppm to ~280 ppm and decreased NH_3 from ~160 ppm to practically zero. This suggests a much higher conversion rate of NH_3 to NO_x for the HA blend in this configuration.

The NO_x emissions for the HA blend are consistently higher than for the AA blend across the Φ_{gl} range. As combustion temperatures are lower for HA (i.e. lower thermal NO_x), this suggests that larger concentrations of unburned NH_3 are leaving the primary zone and being converted to NO_x in the second stage for this blend. This finding agrees with those of Okafor et al. (2020) [98], that in cases of rich-lean combustion, the fuels with higher flame speeds (in this case AA) produce lower fuel NO emissions when $\Phi_{prim} = \Phi_{opt}$, due to the more efficient consumption of NH_3 in the primary zone. As previously stated, the Φ_{prim} of the two blends was actually marginally higher than the assumed Φ_{opt}, slightly more so for the AA blend, but then NH_3 emissions were also shown to increase more rapidly for the HA blend above Φ_{opt} (see Figure 6.6).

For both fuels, NO_x measurements decrease between a Φ_{gl} of 0.7 and 0.8, by 11% and 17% for the AA and HA blends respectively, although for AA, variability is within the measurement uncertainties. It is not clear why there is a more pronounced decrease for HA. It is possible that because there is only one data point for either blend at Φ_{gl} = 0.7, with repeat testing, the difference may no longer be observed. At a Φ_{gl} of 0.7 and 0.8 the average NO readings for the HA blend are 231 and 221 ppm, only 10 ppm different, whereas total NO_x readings are 283 and 235 ppm, so 48 ppm different, showing the majority of the difference lies with the NO_2 reading. At Φ_{gl} = 0.7, NO_2 contributed 18.4% of the NO_x reading for the HA blend. For all the other staged cases (seven in total) NO_2 accounted for between 3.5% and 9.6% of NO_x, making the NO_2 emissions for the HA blend at Φ_{gl} = 0.7, at least double the expected contribution. For AA at Φ_{gl} = 0.7, NO_2 contributed just 3.5% of NO_x, so the pure air-staging at this Φ_{gl} could not account for the apparent discrepancy in the HA blend NO_2 reading. Given the difficulties experienced with NO_2 measurement in the earlier experiments of Chapter 4, and the scheduling of

this particular test, it is possible some NH_3 contamination in the NO_2 to NO converter is responsible for a higher than expected NO_2 for this particular reading. If the assumption was made the NO_2 reading was at least double that expected, a revised NO_2 value of < 24 ppm would be anticipated, making NO_x of ~259 ppm a reasonable prediction. With the same assumption, the AA blend NO_x concentrations are ~25% lower than for the HA blend, across the range of Φ_{gl}. Also, had the reading been 259 ppm, the variability in HA readings would have fallen within the measurement uncertainties.

The measured NO_x concentrations plateau as Φ_{gl} is increased above $\Phi_{gl} = 0.8$, for both blends. At Φ_{gl} ~0.8, the observed optimal Φ_{gl} for emissions, NO_x is 172 and 235 ppm for the AA and HA blends respectively, with NH_3 of < 5 ppm for both blends. These AA results are the lowest emissions results for atmospheric staged work in this thesis. At $\Phi_{gl} > 0.8$ there is a gradual increase in unburned products in the exhaust, rising to ~ 25 ppm NH_3 for both blends at Φ_{gl} ~ 0.95. Average CO readings (dry basis) were ≤ 4 ppm from Φ_{gl} 0.7 to 0.9, rising to 10 and 8 ppm at Φ_{gl} ~0.95 for the AA and HA blends respectively. As this confinement had holes located at 25 cm, the further of the two locations from the burner face, and CO emissions were previously measured as ~6,000 ppm for the rich primary zone products (see Figure 4.11), the very low CO emissions with air-staging show satisfactory mixing is possible between the staging locations and the gas analyser, for both staged confinements. This degree of mixing enables effective consumption of the unburned fuels leaving the primary stage and therefore efficient overall combustion, especially for Φ_{gl} of < 0.95. Thus, the earlier assumption of ~100% combustion in the second stage (see Section 6.2) was reasonable.

Although variability of NO_x with Φ_{gl} is within the limits of the measurement uncertainties, the same observed trend for the two blends (of decreasing NO_x as Φ_{gl} increases from 0.7 to 0.8) suggests there may be some minor benefit in substituting a portion of the air in favour of N_2 in the second stage. An explanation offered here is that by lowering the mole fraction of O_2 in the second stage, while maintaining the molar flow rates, reactivity is modestly decreased. The N_2 may serve to slow the consumption of the unburned fuel from the primary stage when it comes into contact with the staged air. The slower consumption of unburned fuel would distribute the resulting heat

release more widely, reducing peak temperatures, and thus the thermal NO_x production when compared with a more localised heat release. This could be particularly significant when mitigating for the rapid high temperature heat release of H_2, of which there is several percent by volume entering the second stage (as modelled in Chapter 5). The plateauing of the NO_x above Φ_{gl} = 0.8 could be because any gains from reducing peak temperatures are already realised with the amounts of N_2 substitution at Φ_{gl} = 0.8, i.e. peak temperatures are sufficiently reduced below the NO_x formation range due to the slower consumption of the unburned fuels. The hypothesis that higher and lower mole fractions of O_2 in the second stage influence reactivity, and hence peak temperatures and NO_x production, requires further investigation, beyond the scope of this study.

This study has shown that N_2 inclusion in the second stage, in combination with elevated pressures, could potentially be more effective than pressure elevation alone. Once the H_2O component is condensed out of the products of pure NH_3 or NH_3/H_2 combustion with air, the product gas is essentially N_2 and O_2 (with small amounts of argon), akin to a rarefied air mixture, that when compressed, could in theory be used to provide a richer Φ_{gl} than air alone, for the cooling of product gases ahead of the turbine inlet.

Despite the possibility of minor improvements in NO_x with N_2 inclusion in the second stage, NO_x levels are still significantly higher than the 97 ppm limit set in this thesis.

6.6.4 Varying Primary Equivalence Ratio in Staging

Figure 6.10 shows the results for the combustion of both fuels at a Φ_{gl} of ~0.7, with small variations in Φ_{prim}, to find the minimum Φ_{prim} for NO_x emissions with air-staging at 15 cm downstream of the burner face, using the alternative staging confinement. Averaged reactant flowrates, important operating conditions and emissions results are included in Appendix B.7. The Φ_{prim} values are plotted at their calculated average with uncertainties of ± 0.021 to 0.022 for the AA blend and ± 0.02 to 0.021 for the HA blend, increasing with Φ_{prim}. The Φ_{gl} values ranged from 0.6905 to 0.7005, with a measurement uncertainty of ± 0.0125.

Minimum NO_x concentrations were ~260 and ~310 ppm for the AA and HA blends respectively, with AA once again having the lower emissions (~16% lower). These values

are ~20 to 34 % higher than those for the staging holes at 25 cm for the HA and AA blends respectively (i.e. for Φ_{gl} of 0.7 and assuming the revised HA blend NO_x ~259 ppm).

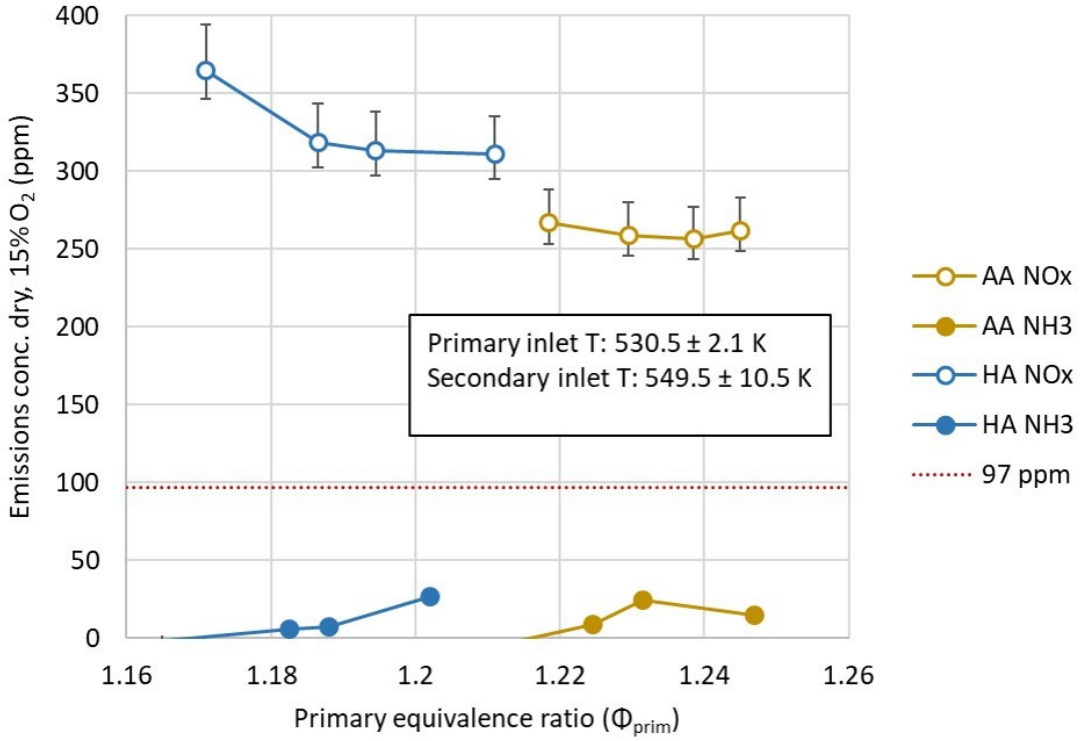

Figure 6.10 Emissions concentrations of NO_x and NH_3 by Φ_{prim}, for staged combustion of the AA and HA blends, Φ_{gl} held at 0.7 (dry, 15% O_2), 1.1 bara.

It is interesting to note that NO_x concentrations for HA at 25 cm staging are the same as for AA at 15 cm staging (~260 ppm). This suggests that the longer residence times offered by the 10 cm delay in staging has successfully mitigated for the lower reactivity of the HA blend, offering a simple strategy for accommodating varying amounts of humidification between 0 and 30%$_{vol}$.

NO_x emissions do not increase with an increase in Φ above Φ_{opt}, for either blend, for the Φ_{prim} ranges investigated, suggesting NO formation from NH_3 exiting the primary zone does not increase rapidly as Φ_{prim} increases above Φ_{opt}. This is unexpected and significant as, for the non-staged work (Section 6.6.1), NH_3 was > 500 ppm (dry, 15% O_2) for the AA blend at Φ_{prim} of ~1.24, twice that at Φ_{prim} of ~1.22. More NH_3 will be exiting the primary zone, at the higher Φ, and one might anticipate that much of this NH_3 would quickly be converted to NO at the lean staging point, leading to higher overall NO_x when compared to a lower Φ_{prim}. As overall NO_x does not appear to increase, the rate of

formation of NO from the unburned NH_3 must be approximately equivalent to the consumption of NO by the unburned NH_3, for this range of Φ_{prim}. Alternatively, concentrations of NH_3 leaving the primary zone for Φ values marginally higher than Φ_{opt}, could be far more similar at this location, than can be evidenced by the gas sampling in the non-staged work. It is possible that, only when residence times are extended without secondary air, that the difference in NH_3 concentrations is generated, perhaps via the gradual consumption of NO by NH_3 in the post-flame zone.

For whichever reason, at this staging location, NO_x formation in the second stage is apparently insensitive to small elevations of Φ_{prim}, giving a margin for Φ_{opt} of > +0.03 for lowest NO_x operating Φ_{prim}. For $\Phi_{prim} < \Phi_{opt}$ this is not the case. The potential rise in NO_x below Φ_{opt} is indicated by the leanest HA data point (Φ_{prim} of ~1.17), showing that there is no margin for minimising NO_x at a Φ_{prim} below Φ_{opt}, only above. For leaner Φ, NO_x exiting the primary zone has no second-stage NH_3 with which to combine.

As noted earlier in this section, the measured exhaust NO_x concentrations (for the same blend and conditions) were higher for the staging location nearest the burner (15 cm downstream). To directly compare the blends' performances at the two staging locations, the relevant results from Figure 6.9 and Figure 6.10 are summarised in Table 6.2 (with the revised value of 259 ppm adopted for the HA blend NO_x, as explained in Section 6.6.3). Relating these results to the modelling of the PFR performed in Chapter 5, the results in Figure 6.9 and Figure 6.10 represent staging at ~15 cm and ~5 cm into the PFR respectively (i.e. for cluster 1, the PSRs, represented the first ~10 cm of the confinement). With the 10 cm delay in staging, Table 6.2 shows there is a 27% and 19% reduction in NO_x concentrations for the AA and HA blends respectively.

Table 6.2 Percentage NO_x decrease with change in staging location for Φ_{gl} ~0.7

Blend	Staging position along PFR (cm)	Φ_{prim}	NO_x (ppm)	NO_x decrease with 10 cm staging delay
AA	5	1.219	267	27%
	15	1.213	194	
HA	5	1.187	318	19%
	15	1.181	259	

Figure 6.11 shows the concentration profiles for the NO_x precursors, NH_3 and HCN, along the PFR, as modelled in Chapter 5 for the AA blend (see Figure 5.6), focussing on the region of interest (i.e. 5 to 15 cm along the PFR).

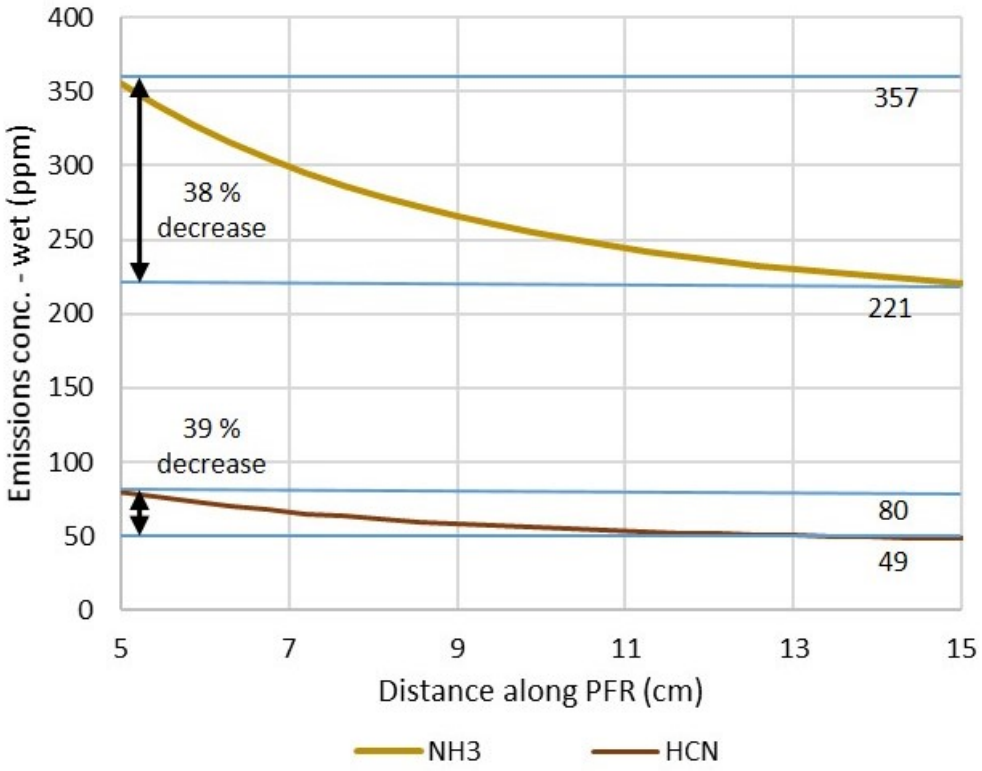

Figure 6.11 Concentrations of NH_3 and HCN (wet) as modelled between 5 and 15 cm along the PFR for 15% COG/AA blend at Φ = 1.187 and 0.109 MPa.

Figure 6.11 shows a ~38% reduction in NH_3 and HCN modelled concentrations over the intervening 10 cm. Thus, the experimental results support the predicted trend in the modelling, such that with significantly less NH_3 and HCN available for oxidation at the latter staging location (~38% less), there is a 27% reduction in overall NO_x. Hence, increasing residence time by delaying staging (in this case by an additional 10 cm) could be an effective method for reducing overall NO_x emissions. Additionally, with delayed staging, NO formed upstream in the primary combustion zone, has longer to react with amine radicals from the decomposition of NH_3 (to progress to N_2), as described by the fuel-rich NH_3 oxidation paths in Figure 1.3.

However, delays in staging prolong high temperatures in the post combustion zone. In the 25 cm staging case, the temperatures for this region (5 to 15 cm into the PFR) are modelled as between 1660 and 1890 K (see Figure 5.6), thus, of a temperature range

capable of thermal NO_x formation [46, 116]. Therefore, while later staging is beneficial in this case, further investigation is required before this trend can be assumed to hold for all staging locations, as prolonged high temperatures may lead to an increased contribution from thermal NO_x, which may negate the benefits of decline in NO_x precursors along the PFR.

6.6.5 Staging at Elevated Pressure

The AA blend was used to compare the NO, NH_3 and CO emissions at modest pressure elevation (1.305 ± 0.001 bara) at the two different staging locations. The averaged reactant flowrates, important operating conditions and emissions results are included in Appendix B.8. The target Φ_{prim} was 1.2 and the Φ_{gl} was 0.7. NO_2 readings were taken for one of the staging locations only (15 cm), due to the NH_3 restrictions, but were found to contribute only 3.2% of NO_x, so it is assumed that the NO concentrations are approximately equal to the NO_x concentrations for both locations. Table 6.3 lists the emissions results and average Φ values (primary zone and global) for the two different staging locations. The uncertainties for Φ_{prim} and Φ_{gl} were ±0.0185 and ±0.0115 respectively. The negative value for NH_3 in the 25 cm staging is indicative of the aforementioned issue of NH_3 flow restrictions. How flow restrictions lead to negative NH_3 and NO_2 readings was explained earlier (see Section 4.8.1).

Table 6.3 Emissions results for the AA blend at the two different staging locations under elevated pressure (1.3 bara)

Measured Variable	Staging Location	
	25 cm	15 cm
Average Φ_{prim} during NO measurement	1.194	1.192
Average Φ_{gl} during NO measurement	0.696	0.695
NO (dry, 15% O_2)	294	292
Average Φ_{prim} during NH_3 measurement	1.188	1.183
Average Φ_{gl} during NH_3 measurement	0.693	0.690
NH_3 (dry, 15% O_2)	-20	12
CO (dry)	4.1	0.2

At 1.3 bara, the NO concentrations were virtually identical at ~290 ppm, for both staging locations. This was not the case for the air-only staging at 1.1 bara, where concentrations were 34% higher for the staging at 15 cm. Thus, lower NO_x for the furthest staging location is no longer observed with the modest elevation of pressure to 1.3 bara. The reader is to note that the NO readings themselves are not directly comparable across the pressures, as the Φ_{prim} of ~1.19 reached for these two points at 1.3 bara, was not investigated at 1.1 bara (i.e. where target Φ_{prim} values for the staged cases were 1.22 to 1.25).

Reasons why the staging location has no effect on NO_x for the pressure elevated cases could be that, because higher pressure leads to an increase in fluid density, turbulence is increased and also that higher temperatures (from lower relative heat loss) accelerate the rates of reaction (i.e. resulting in a narrower flame thickness) when compared with the lower pressure cases. Hence, the combustion products may be achieving an approximate equilibrium before the earliest (15 cm) staging location, such that there is little change in species concentrations between the 15 cm and 25 cm staging points and hence no difference in overall NO_x product. Higher elevations of pressure could therefore enable staging at locations closer to the burner without increasing NO_x product concentrations. However, this finding is limited to only two data points and requires replication and further study, beyond the scope of this thesis.

6.6.6 Effects of Staging on Flame Structure

Figure 6.12 shows the OH* and NH_2* images for the 15% COG/AA with and without staging at Φ_{prim} ~ 1.22. The images in Figure 6.12 reveal that there is some disruption to the flame structure in the primary stage due to the secondary air-staging. As the staging moves closer to the burner exit, the flame brush gets thinner and the tips of the flame move inwards, away from the confinement. There are more excited radicals of both types at the mouth of the burner, showing that the reaction zones appear as though pushed further upstream. For the cases in Figure 6.12, the burner face temperature without staging was 656 K, rising to 752 K and 762 K, with staging at 25 cm and 15 cm respectively, thus an increase of ~ 100 K due to staging. The shape of the NH_2* distribution more closely approximates that of the OH* image as the staging moves

closer to the burner, suggesting the entire upstream flow field is undergoing a compression of the reacting regions due to the staging.

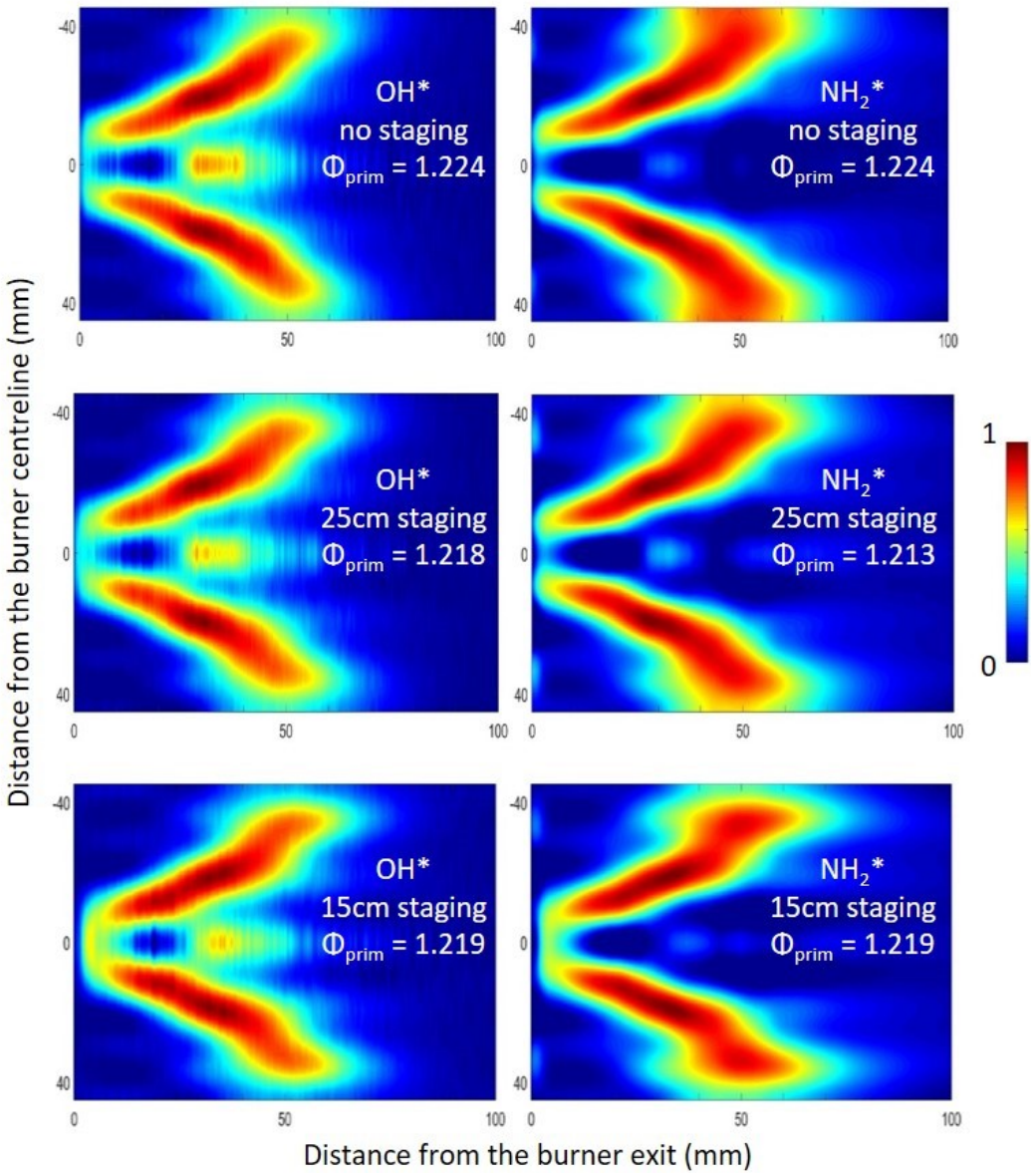

Figure 6.12 OH* and NH_2* chemiluminescence for 15% AA/COG with Φ_{prim} ~ 1.22 at 1.1 bara - without air-staging and with air-staging (Φ_{gl} = 0.7) at 25 and 15 cm downstream of burner exit.

Figure 6.8 showed that even a modest pressure increase led to a change in NH_2* distribution in the primary zone and Figure 6.12 showed that staging position also influences flame structure. Thus, these two influences will have a combined effect on species distribution and flame structure in the primary stage.

Visual observations of the flame showed a faint flame forming just after the staging locations. This visible flame revealed that the combustion gases from the primary zone were experiencing a four-way pinching action, shaped by the flows of secondary air through the four staging holes, immediately upstream of the staging location. If the inflows of secondary air are impinging on each other this could itself have implications for flame structure. In the premixed NH_3/air numerical modelling work by Somarathne et al. (2017)[106], it was stated that secondary inlet jets should not impinge on each other, as this would destroy the recirculation zones and thereby flame stabilisation. The study was conducted at Φ_{prim} 1.15 to 1.4, staging at 10 cm, inlet temperature of 500 K and 0.1 and 0.5 MPa pressure. The flowrates of secondary air in that study were modelled at low velocity and did not appear to penetrate to the centre of the primary products' flow before exiting the combustion chamber. However, it is clear from the OH* chemiluminescence in Figure 6.12, that the CRZ (located in the centre of the 'V' shape) is still intact for all staging investigated here, despite the visually observed impingement, so stability has not been compromised for staging up to a Φ_{gl} of 0.7. The more reactive blends, later staging locations and marginally higher inlet temperatures used here may have helped to preserve flame stability.

Axially symmetric, secondary flow inlet tubes, penetrating into the confinement and directing secondary inlet flows away from the confinement centre, could address this issue as Φ_{gl} increases. An increase in Φ_{gl} would be necessary to reach Φ_{gl} values capable of cooling product gases ahead of the turbine inlet in industrial applications (this is investigated later in the cycle analysis in Chapter 7). However, a study by Makida et al. (2006) [149] investigating the use of inlet tubes, whereby the inlet jets were not in direct opposition, found that the resulting swirl effects enhanced the swirl of the upstream flow fields, lowering combustion efficiency. Therefore, the potential of this strategy to effect the upstream swirl structures needs consideration. In addition, this approach may be technically challenging for manufacture in quartz (bonding of inlet tubes to the quartz confinement) or for a combined quartz/metal alloy confinement (due to differing thermal expansion rates). Alternatively, more holes of the same size would enable lower velocities into the second stage, and/or holes ~180° apart could be located at marginally

different distances downstream, distributing the inflows more widely, thereby reducing the jet impingement.

Investigating the impingement effects of various air-staging configurations on upstream swirling flows requires flow-field measurement techniques, such as particle image velocimetry, which is beyond the scope of this study.

6.7 Chapter Summary

- A correlation between S_L (as an measure of reactivity) and Φ_{opt} was demonstrated, suggesting **a method for predicting Φ_{opt}** for high fraction NH_3 fuel blends at varying inlet temperatures.
- Combined emissions from the primary stage (without staging) were higher than for the previous experiment. This is due to the higher inlet temperatures (~30 K higher) leading to higher thermal NO_x formation. **Inlet temperatures ~ 500 K** are therefore recommended for these blends in future work, to lower emissions while maintaining reactivity.
- The 15% COG/**AA blend consistently outperformed** the 15% COG/HA blend for emissions, achieving between 16 and 25% lower NO_x emissions for the two staging locations.
- The **modest elevation of pressure** of ~17% was demonstrated to **reduce NO_x by ~25%**. NH_3 emissions were unaffected by the modest pressure increase. Thus, combined emissions decreased by ~13% and Φ_{opt} appeared to reduce marginally with the pressure elevation.
- **Partial substitution of N_2** for air (changing Φ_{gl} from 0.7 to 0.8) may lower NO_x product concentrations by > 10%, without any increase in unburned NH_3 (< 5 ppm) or CO (≤ 4 ppm) emissions, for both blends.
- **NO_x emissions were unchanged for Φ_{prim} marginally above Φ_{opt}** (increase of < 0.03), but increased below Φ_{opt}.
- **At atmospheric pressure, the later air-staging (25 cm) produced lower NO_x**. No difference in NO_x was observed between the two staging locations at elevated pressure, suggesting an approximate equilibrium in primary stage products is

reached before 15 cm downstream at the elevated pressure. Hence**, higher pressures could allow for earlier staging** where residence times are maintained.

- Both **staging locations showed adequate mixing and oxidation of unburned fuels** ahead of the gas sampling probe, with CO reduced from ~6000 ppm without secondary air to < 5 ppm at the furthest air-staging location (25 cm).
- **Humidified blends can achieve similar NO_x** concentrations to AA blends **with delays in secondary air-staging**.
- Chemiluminescence images show that the **flame structure was modestly influenced as the staging moved upstream**.
- Lowest emissions results were achieved for 15% COG/AA at Φ_{prim} 1.22 and Φ_{gl} 0.8, at a pressure of 1.1 bara and with air-staging introduced 25 cm downstream of the burner face**. Lowest emissions were 172 ppm NO_x and 5 ppm NH_3 on a dry, 15% O_2 basis and 1 ppm CO on a dry basis.**

Chapter 7 Cycle Analyses

7.1 Software Overview

This chapter uses the process simulation software program Aspen Plus (version 12) [142], developed by AspenTech, to design a novel $NH_3(H_2O)$/COG-air power cycle, to predict the net power values and cycle efficiencies achievable when utilising typical steelworks mass flows of waste stream NH_3. This program and its sister program Aspen HYSYS are commonly used to model steady-state power cycles [150–154]. A brief introduction to the program's user interface characteristics and fundamental modelling approach (e.g. choosing a property method) is provided in Appendix D.1.

There are numerous Aspen programming resources available. An Aspen Plus tutorial developed by J. Jechura (2015) [155] which models a simple natural gas burner/boiler with a steam bottoming cycle (using Aspen Plus version 8.6), was modified for this study. Naturally, the fuel-side of the cycle required a radical redesign for this chapter's investigation, being the novel element. However, the proposed cycle does include a steam cycle (discussed in the next section), so modelling methodology remains essentially unchanged for the steam cycle section. For the detailed methodology of the steam cycle, the reader is directed to this tutorial [155].

7.2 Cycle Overview

Although the emissions performance of the AA blend was shown to consistently outperform the HA blend in earlier chapters, the modelling in Chapter 5 showed that, under industry relevant pressures, either fuel has the potential to comply with emissions regulations. The impact of ammonia humidification on cycle efficiency has yet to be investigated. Hence, steady-state thermodynamic cycle simulations were performed for both of the two chosen fuels (15% COG/AA and 15% COG/HA) at compression ratios of 8 and 12. This range of operating pressures is fairly modest for industrial gas turbines, to reflect the anticipated scale of operation (i.e. ~2 to 5 MW, depending on the availability of by-product NH_3).

The process flow diagram for the modelled combined cycle is shown in Figure 7.1. Most of the labels used in Figure 7.1 are fairly intuitive, e.g. W- or Q- streams (dashed and

dotted lines) leaving an item of equipment, indicate the work done or heat lost/gained by that equipment and LP or HP indicates lower or higher pressure material streams. Stream labels (material, work and heat flows) are enclosed within textboxes, equipment labels are not. Labels whose meaning may not be not immediately obvious are discussed in the subsequent text as the process flows are described. All labels are included in the thesis nomenclature section.

The combined cycle consists of a Brayton cycle (i.e. gas turbine power/heat generation), followed by a Rankine bottoming cycle (i.e. steam turbine power generation), via the use of a heat recovery steam generator (HRSG).

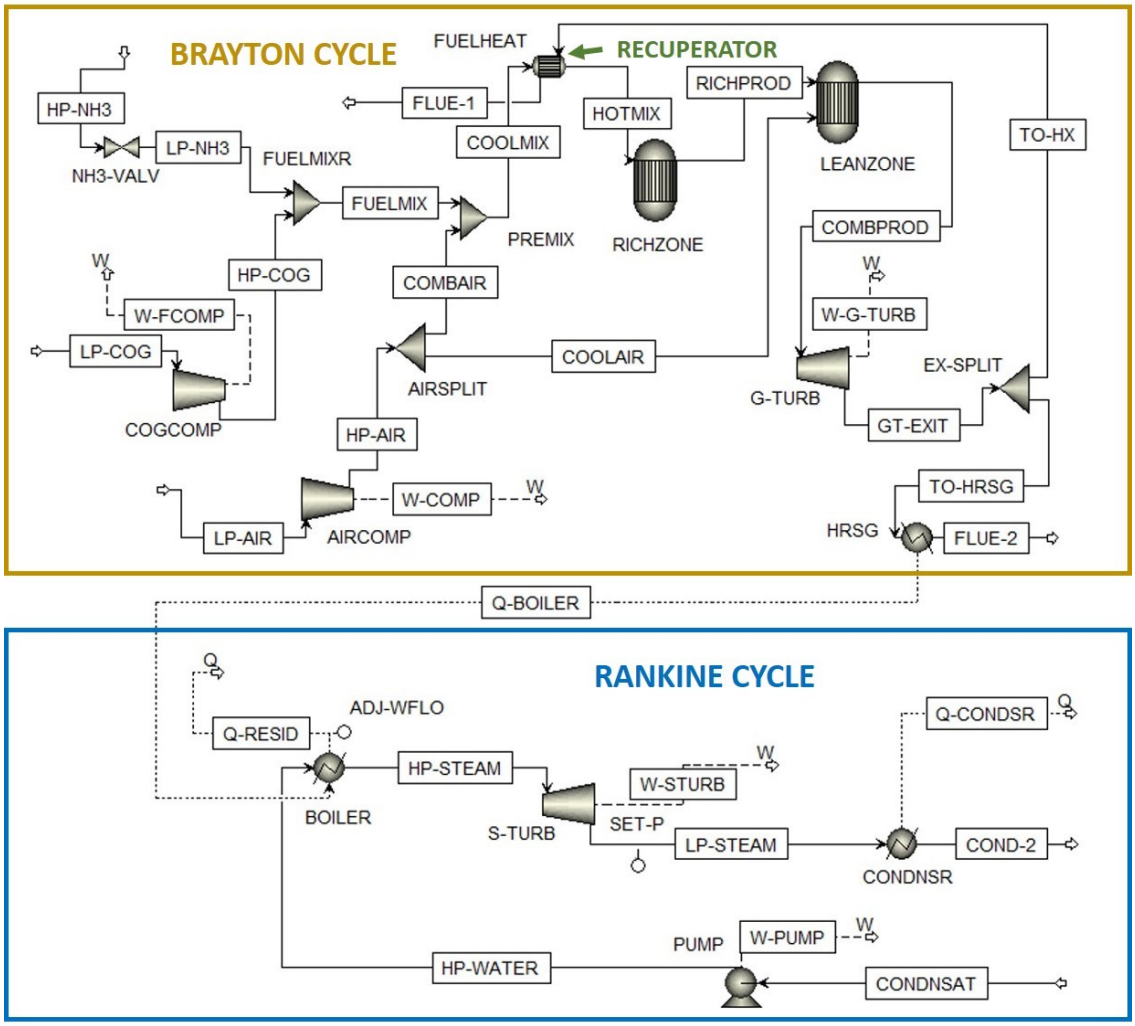

Figure 7.1 Combined cycle process flow diagram (Aspen Plus)

The Brayton cycle incorporates the use of a recuperator, utilising a portion of the thermal energy of the exhaust (TO-HX) to preheat the fuel/air premix immediately

upstream of the combustor, for a self-sustaining cycle. An alternative arrangement whereby the recuperator is used to heat the NH_3 (H_2O) fuel only, before its entrainment with the COG and compressed air, is also investigated. For ease of reference, this alternative arrangement is shown later, alongside the related results (Figure 7.3). As recuperators are normally used for preheating air only, these arrangements are a novel concept and would require materials in the recuperator design, chosen to cope with the corrosivity of the fuel. The material, heat and work flows of the cycle are represented by solid, dotted and dashed lines respectively.

Although the sizing of the gas turbine (discussed later) is unlikely to warrant the use of a dedicated Rankine cycle, its inclusion is to allow for efficiency comparisons with existing larger-scale combined cycles. Naturally, the rejected heat from the gas turbine exit could augment heat from nearby plant which is being used to raise steam. Efficiencies for the Brayton cycle with recuperation, but without a bottoming cycle, are also obtained, as is the efficiency of a gas turbine cycle with the turbine exhaust heat being used to produce process steam.

While kinetics modelling in Aspen is available, it is not practically achievable for the complex reactions of combustion, not least because the reaction mechanism files and Aspen software are incompatible. Hence, the product concentrations which rely heavily on combustion kinetics (e.g. fuel NO_x) were not evaluated using Aspen Plus, but were instead obtained via the Chemkin reactor network kinetic modelling and the experimental data in earlier chapters. The experimental data showed very high combustion efficiencies, so CO_2 emissions predictions are considered valid using equilibrium modelling. Therefore, as for other combustion/gasification studies using Aspen Plus [150, 153, 154], the combustion chamber is modelled using a Gibbs (i.e. equilibrium) reactor. As combustion is staged, two Gibbs reactors were modelled in sequence, one for each stage, labelled RICHZONE and LEANZONE. Modelling two reactors for the combustion process is technically unnecessary, as two successive equilibrium reactors will give much the same exit temperature and CO_2 concentrations as one. However, when using the recuperator to preheat the fuel/air premix, the portion of the exhaust gases required by the recuperator, is dependent on the mass flow of

primary air only, so it is necessary to direct the flow for the primary air separately from that of the secondary air. The Φ_{prim} values of 1.15 and 1.2 were used to calculate the primary air flows for the HA and AA blends respectively. Modelling the two stages of combustion separately, using two reactors, also makes the two distinct air flow paths easier to visualise and provides adiabatic flame temperature data for each reactor, before and after the introduction of cooling air.

7.3 Model Properties

The property method describes the rules governing the behaviour of the species modelled under the specified conditions. Since the appearance of the Van der Waals equation of state (EOS) in 1873, many authors have sought to further improve on the relationship by modifying the equation. The 'Property Methods Assistant' facility provided by Aspen, recommends the most appropriate EOS from the many available, based primarily on application. Recommended for power generation, the Peng-Robinson EOS [156] with Boston-Mathias modifications (PR-BM) [157] is stated as being suited to nonpolar or mildly polar mixtures. These types of mixtures are typical in hydrocarbon and power systems, which explains its use in other combustion simulations [150, 152, 154]. The Peng-Robinson equation and the equations associated with its derivation are detailed in Appendix D.2.

Although Section 2.1.1 describes NH_3 as a polar molecule, the fuel/air mixtures entering the combustor are assumed to be only mildly polar, for, once combined with air, NH_3 represents a minor component of the fuel/air mixture entering the combustor (i.e. 21 and 17.5%$_{vol}$ for the AA and HA blends respectively). Also, the polar nature of NH_3 is assumed to have insignificant effect when in the vapour phase, at high temperature and pressure, because under these conditions the effects of intermolecular attraction are minimised. The high temperature and pressure conditions found in an NH_3 plant may serve to explain why the Peng-Robinson (PR) EOS (this time without the Boston-Mathias modification) is recommended for simulating NH_3 plant, despite the same statement for this method regarding non-polar and mildly polar mixes. For context, the example of a polar mixture given in the relevant Aspen documentation is a liquid blend of alcohol and water.

The cycle was simulated using both the PR-BM and PR methods for the fuel-side (using the AA blend at 12 atm) and there was no difference in the results. Therefore, for all cycle simulations, the PR EOS was selected for the fuel-side modelling and the standard used by the International Association for the Properties of Water and Steam (IAPWS-95) was selected for modelling the steam cycle.

7.4 Cycle Description

7.4.1 Brayton/Recuperator Cycle - Reactant Flows

The compositions of the reactants used in the Aspen simulation were very similar those used in the Chapter 6 experimental campaign. Having been excluded in the experimental campaigns, due to cost, ethene (C_2H_4) and ethane (C_2H_6) were reintroduced to the COG composition. A comparison of the target composition of COG for the experimental campaigns, versus the COG composition used in the Aspen Plus modelling, is given in Table 7.1. The HA blend was 70%$_{vol}$ NH_3 with 30%$_{vol}$ H_2O and air was modelled as 78%$_{vol}$ N_2, 21%$_{vol}$ O_2 and 1%$_{vol}$ argon.

Table 7.1 Compositions of COG used in experimental work versus Aspen Plus modelling

Use of COG	Component species percentage (volumetric)						
	H_2	CH_4	CO	N_2	CO_2	C_2H_4	C_2H_6
Experimental	61	26	7	4	2	-	-
Aspen Plus	60.8	24.2	7	3.9	1.9	1.7	0.5

The fuel and air material streams are introduced to the cycle at an ambient temperature of 284 K, the average temperature of the South Wales region in the UK where the largest UK steelworks is situated. Liquid NH_3 is pumped from the bottom of its storage container at a pressure of 20 bara to a letdown valve, reducing the pressure to the operating pressure of the gas turbine. The COG is taken from the steelworks' COG line and compressed up to operating pressure of the turbine in a dedicated compressor. The air is compressed to the same operating pressure before being split between the primary and secondary stages.

Fuel and primary air mass flows into the Brayton cycle were calculated in the Excel interactive workbook, with calculations scaled to an NH_3 availability of 10 tonnes/day,

approximately equivalent to the by-product NH_3 of a modest-sized steelworks site with a crude steel output of 2 Mt per annum (see Section 2.4.2). Storage of one day's recovered NH_3 (in the event of temporary shutdowns) would therefore require ~ 7 m^3 of storage capacity for the AA (see Table 2.2). With NH_3 representing 69% of the mass of HA, storage of the additional 4.5 tonnes of H_2O brings the total storage requirement of HA to ~ 11.5 m^3/day at 288 K.

The NH_3 and COG flows are brought together in a stream labelled FUELMIX. The results for the FUELMIX stream show the gross (HHV) and net (LHV) calorific values and mass flowrates of the fuel blends which are used to calculate the gross (HHV) and net (LHV) power into the cycle, according to Equation 7.1. In reality, these streams could be injected into the primary air separately.

$$P_{in}(kW) = calorific\ value\left(\frac{kJ}{kg}\right) \times mass\ flow\ rate\left(\frac{kg}{s}\right) \qquad \textit{Equation 7.1}$$

Gross and net power for the two fuel blends into the cycle are summarised in Table 7.2.

Table 7.2 Calculating power into the cycle for the AA and HA fuel blends

Fuel Blend	Fuel LHV (kJ/kg)	Fuel HHV (kJ/kg)	Fuel flow rate (kg/s)	Net power in (kJ/s)	Gross Power in (kJ/s)
15% COG/AA	20598	24595	0.1273	2622	3130
15% COG/HA	15282	18176	0.1847	2822	3357

Thus, as the HA fuel is a combination of 10 tonnes/day NH_3 plus H_2O (representing 85%$_{vol}$ of the fuel), the 15%$_{vol}$ COG in the HA blend has a higher mass flowrate than for the AA blend. Gross power entering the cycle is over 3 MW, for both blends. The greater recruitment of COG when using the HA blend leads to 7.6% higher flows of energy into the cycle as shown in Table 7.2.

7.4.2 Brayton/Recuperator Cycle – Operating Conditions

In response to the Chapter 6 findings, the target premix temperature into the combustor (HOTMIX) is 500 K. The exhaust temperatures out of 'FLUE-1' (the recuperator) and 'FLUE-2' (the HRSG) are set to a minimum of 393 K, to achieve a temperature well above

the dew point of water, enabling effective dispersal of all the combustion products. The recuperator is of counter-current design and has an approach temperature of 25 K [150], so on occasions where the cold reactants enter the recuperator with a temperature within 25 K of 393 K, the hot exhaust feed into the recuperator is increased to maintain the 25 K temperature difference, so increasing the flue exit temperature. The proportion of the gas turbine exhaust mass flows directed to the recuperator (TO-HX) rather than the HRSG is manipulated manually in the 'EX-SPLIT' block to the minimum required to reach the 500 K needed for the cold-side outlet (i.e. primary reactor inlet). This proportion (TO-HX) reflects the proportion of the heat transfer required from the entire exhaust, rather than a physical split of the exhaust flows. In reality, the recuperator would be located within the single exhaust stream, after the turbine exit and before the HRSG. Therefore, the two flue exit temperatures are kept equivalent.

While primary air mass flows are known (calculated in the Excel workbook), secondary air flows are dependent on the cooling required to obtain the necessary turbine entry temperature (TET). The block 'AIRSPLIT' splits the air compressor outlet sending a specified primary air mass flow 'COMBAIR' to the primary reactor, while the remaining air 'COOLAIR' is sent to the second reactor. Hence, the air mass flow entering the air compressor (i.e. LP_AIR) is manipulated, until the correct TET is achieved.

A TET of 1273 K (1000 °C) was used. This is lower than in similar studies 1328 to 1425 K [150, 152–154] to reflect the smaller size gas turbine and the less technologically advanced turbine blade materials and design likely for such a unit. It is also the optimum temperature for NO_x reduction via the SNCR process [95, 158]. Therefore, if the SNCR process was applied just before the turbine inlet, reductions in NO_x emissions of 30 to 75% could be achieved [48]. The air required to cool the combustion products to this temperature (i.e. COOLAIR) is far in excess of that required for the combustion of the unburned products from the primary stage, giving Φ_{gl} values well below 1.

The smallest gas turbines from the Siemens range were used to benchmark likely pressure ratios for gas turbines used in cycles of a relevant scale. The SGT-100 industrial gas turbine and SGT-A05 aeroderivative gas turbine have power outputs of 5.1 and 4 MW_e and pressure ratios of 14:1 and 10.3:1 respectively [124]. Hence pressure ratios of

8:1 and 12:1 were investigated to give the likely span of performance figures for this scale of cycle. Gas turbine discharge pressure was set to 1 atm (1.013 bara).

The turbine exhaust heat not transferred via the recuperator is recovered via the HRSG and transferred to the Rankine cycle (while allowing for the minimum flue gas temperature of 393 K).

7.4.3 Rankine Cycle – Operating Conditions

The steam circuit is a closed loop. The steam leaving the boiler is characterised as a saturated vapour (i.e. no superheating). The amount of water circulating through the steam loop is ultimately calculated by Aspen Plus, but, as with many other variables in the loop, an initial value is entered from which to iterate. Thus, the condensate flow entering the pump (and therefore leaving the condenser) is initially characterised as 1 kg/s of pure water at 293 K, with no vapour fraction.

The condensate pump operating pressure, and therefore the steam turbine inlet pressure, is set at 100 bara, as per a similar study by Liu and Karimi (2018) [152]. The steam turbine discharge pressure is initially unknown and is designated an arbitrary value from which to iterate (i.e. 0.1 bara). Using the program's 'CALCULATOR' operation, FORTRAN coding feeds forward the vapour pressure of the stream CONDNSAT at 293 K, calculated by Aspen Plus, assigning this value to the steam turbine discharge pressure automatically. The CALCULATOR is shown in the process flow diagram (Figure 7.1) as SET-P.

The thermal energy from the Brayton cycle is capable of heating a specific mass of water in the steam cycle, at the specified pressure, with zero degrees of superheating. The thermal energy available will vary by case (e.g. as percentage exhaust to the recuperator is varied), so the water mass also varies to account for this. To automatically find the correct mass of steam circulating the loop, a second CALCULATOR operation is required. The CALCULATOR is shown in the process flow diagram (Figure 7.1) as ADJ-WFLO. This operation minimises the residual heat rejected by the boiler to calculate the maximum steam mass flow for the Rankine cycle.

7.4.4 Equipment Efficiencies

Although the operating conditions are assumed to be mostly ideal, some important and predictable efficiencies were considered. These efficiencies are given in Table 7.3 together with their referenced sources. Being a hypothetical cycle, there are no pressure drops modelled, as pressure drops would be system specific. However, the potential implications of this are not ignored and are addressed later in Section 7.7.

Table 7.3 Modelled equipment efficiencies

Equipment	Isentropic Efficiency (%) [Ref]	Mechanical Efficiency (%) [Ref]
Compressors	88 [150, 152, 154]	99 [152]
Gas Turbine	90 [150, 153, 154]	99 [153]
Steam Turbine	75 [151–153]	97 [151, 153]
Condensate Pump	80 [151, 159]	95 [153]

7.5 Data Processing Method.

The tables of results for the material, heat and work streams were copied into excel workbooks, making three tables (data sheets) for each case. A summary worksheet was designed and added to each workbook, its function being to retrieve the relevant values from the streams tables and use them to calculate several important results. These results include power into the cycle, Φ_{gl} and efficiency values for the Brayton cycle, the steam cycle and the combined cycle. The summary sheets for the two blends, at the two pressures investigated, are provided in Appendix E.

The formulae used to calculate the efficiencies of the gas turbine cycle (i.e. including boiler duty), a standalone Brayton cycle, the steam cycle, the combined cycle net power and the overall efficiency of the combined cycle are given in Equations 7.2 to 7.6 respectively. The derivation of P_{in} which features in these equations, was described earlier in Equation 7.1.

$$\text{Gas turbine cycle efficiency (\%)} = \frac{GT + Boiler - AIR - COG}{P_{in}} \times 100 \qquad \textit{Equation 7.2}$$

$$\text{Brayton cycle efficiency (\%)} = \frac{GT - AIR - COG}{P_{in}} \times 100 \qquad \textit{Equation 7.3}$$

$$\text{Steam cycle efficiency (\%)} = \frac{ST - Pump}{Boiler} \times 100 \qquad \textit{Equation 7.4}$$

$$\text{Combined cycle net power (kW)} = GT + ST - Pump - AIR - COG \qquad \textit{Equation 7.5}$$

$$\text{Combined cycle efficiency (\%)} = \frac{Combined\ cycle\ net\ power}{P_{in}} \times 100 \qquad \textit{Equation 7.6}$$

Where GT = power from the gas turbine, ST = power from the steam turbine, Boiler = boiler duty, AIR = power to the air compressor, COG = power to the COG compressor and Pump = power to the condensate pump.

The Φ_{gl} values for the AA cases and HA cases were calculated according to Equation 7.7a and 7.7b respectively (to reflect the different Φ_{prim} in the primary reactor).

$$\Phi_{gl}\text{ for the AA blend} = \frac{Primary\ air\ flow}{Total\ air\ flow} \times 1.2 \qquad \textit{Equation 7.7a}$$

$$\Phi_{gl}\text{ for the HA blend} = \frac{Primary\ air\ flow}{Total\ air\ flow} \times 1.15 \qquad \textit{Equation 7.7b}$$

7.6 Cycle Results and Discussion

7.6.1 Premix Recuperator Preheat – Air/Fuel Delivery Configuration 1

The first part of the Brayton cycle, the fuel/air delivery system as described in Figure 7.1, is expanded in Figure 7.2, for ease of reference. The results for this arrangement are summarised in Table 7.4 for the two fuels 15% COG/AA and 15% COG/HA at 8 and 12 atm pressure.

As anticipated, the heat from the compressed primary air alone is insufficient to heat the fuel/air mix to the required inlet temperature of 500 K (see COOLMIX), achieving a maximum of 386 K for the AA blend premix at 12 atm.

At 8 and 12 atm compression, the HP-COG stream reached temperatures of 510 and 565 K respectively (not included in Table 7.4). However, being such a minor component, the compressed COG does nothing to raise the temperature of the LP-NH3 stream from its starting temperature of 284 K (the same temperature as HP-NH3, as LP-NH3 is still in the liquid phase).

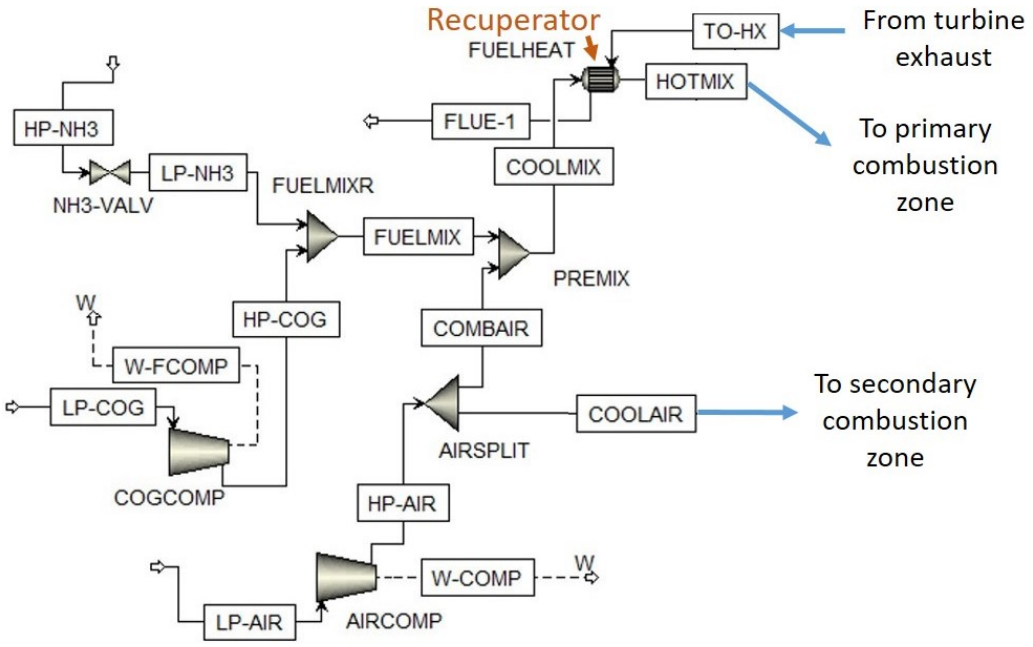

Figure 7.2 Process flow diagram for the fuel/air delivery system

Table 7.4 Fuel/air delivery results – premix through the recuperator.

Results Stream	15% COG/AA		15% COG/HA	
	8 atm	12 atm	8 atm	12 atm
HP-AIR temperature (K)	541	608	541	608
FUELMIX temperature (K)	266	275	275	283
FUELMIX vapour fraction (molar)	0.254	0.241	0.225	0.215
COOLMIX temperature (K)	333	386	324	348
COOLMIX vapour fraction (molar)	1	1	0.919	0.938
Percentage exhaust to recuperator	12.4	10.2	23.2	21.6
FLUE-1 exit temperature (K)	393	411	393	393

In fact, as the NH_3 and COG combine (FUELMIX), the temperature is lowered to below 284 K, in all cases, due to the vapourisation of the NH_3 (e.g. ~11% for the higher pressure

AA blend). The blended fuel is in two phases (liquid phase ~75-80%$_{mol}$), so it is recommended that the COG and NH_3 are injected independently in their own phase.

The heat of the compressed air is sufficient to enable the AA/COG premix to become vapour upstream of the recuperator (at both pressures). This is not the case for the HA/COG blend where ~6 to 8%$_{mol}$ of the blend still remains in the liquid phase. Hence, unless the HA fuel is injected into the air within the recuperator itself, there is the potential for a build-up of liquid fuel in the lines upstream of the recuperator.

Reaching 500 K after the recuperator (HOTMIX), all cases are 100% vapour before entering the combustor. The 25 K temperature approach for the recuperator necessitated a higher outlet temperature (411 K versus 393 K) for the AA/COG blend at 12 atm. A higher flue temperature will naturally lower the cycle efficiency.

7.6.2 Fuel Only Recuperator Preheat – Air/Fuel Configuration 2.

To address the issue of approach temperature and to investigate other potential benefits, an alternative configuration, where only the NH_3 fuel is heated in the recuperator (effectively using the recuperator as a boiler), was investigated. The process flow diagram for the reconfigured system is shown in Figure 7.3.

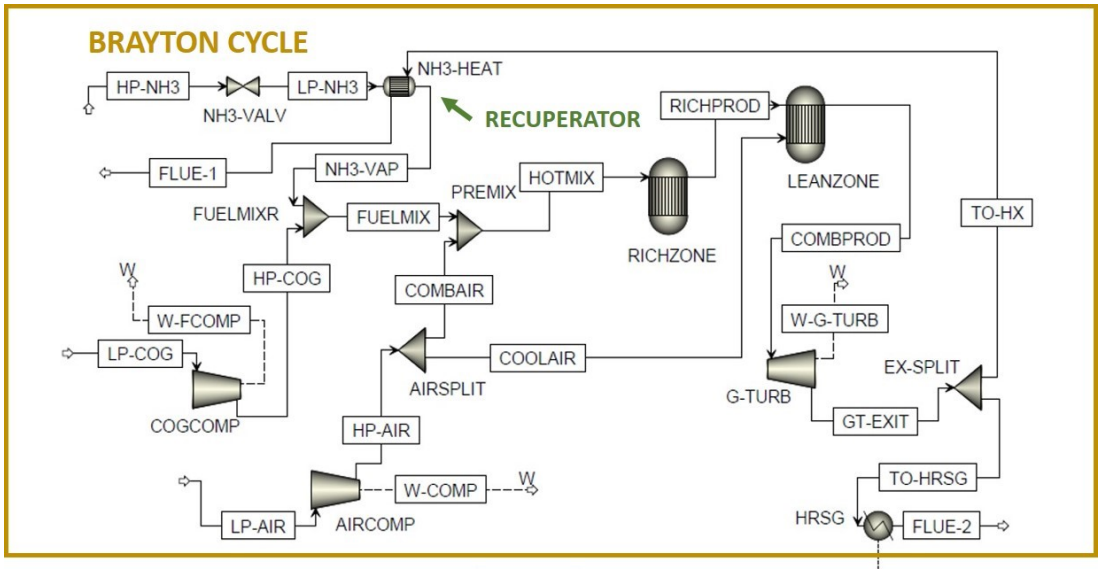

Figure 7.3 Alternative recuperator configuration - NH_3 fuel heat only

Without the heat gains from the compressed air, the approach temperature within the recuperator is consistently greater than the set minimum of 25 K for all cases, avoiding the need to raise the flue temperature for the AA, 12 atm case.

Table 7.5 shows the results when reconfiguring for an NH_3 (or NH_3/H_2O) only recuperator preheat, using the same exhaust return percentages (see Table 7.4) and therefore maintaining a premix inlet temperature of 500 K. Flue temperatures are now 393 K for all cases.

Table 7.5 Fuel stream results for NH_3 (or NH_3/H_2O) only through recuperator.

Results Stream	15% COG/AA		15% COG/HA	
	8 atm	12 atm	8 atm	12 atm
Temperature of hot NH_3 (K)	393	305	416	408
Vapour fraction of hot NH_3	1	0.79	1	0.84
Temperature of FUELMIX (K)	407	298	428	404
Vapour fraction of FUELMIX	1	0.90	1	0.89

The AA blend at 8 atm can be completely vapourised and superheated at the point of injection (this time within the recuperator), using the same exhaust percentages as before. This configuration has also enabled complete vapourisation and superheat of the HA blend at 8 atm, due to the high percentage of exhaust recuperation (~23%). Therefore, this is a simpler arrangement for the HA blend at 8 atm as it completely avoids the potential for a build-up of fuel in the air line, that necessitated injection into the air within the recuperator in the previous configuration.

At 12 atm pressure, both blends have a ~20%$_{mol}$ liquid component leaving the recuperator. This mix of phases could present operational issues related to uneven fuel delivery and build-up in the recuperator. Considering the AA at 12 atm was fully vapourised with the previous configuration, it is clearly more reliant on heat from the compressed air than on the returned exhaust heat for its vapourisation. The potential for build-up of liquid fuel in the lines thus negates any potential benefit from a small increase in cycle efficiency (i.e. 0.7%). Between the two configurations, and under the set inlet temperature constraints, the first is preferred for the AA blend at 12 atm.

One is bound to consider the implications of adopting the approach of complete vapourisation of the NH_3 fuel at 12 atm, within the recuperator (before combining with the air). This approach would require an increase in minimum exhaust return to 11.89% for AA (+1.7%) and 25.65% for HA (+4%), that would in turn result in higher combustor inlet temperatures (527 K for AA and 547 K for HA), increasing the potential for thermal NO_x. Whilst this increase in inlet temperature is only marginal for the AA blend, so was the elevation in flue temperature for the previous configuration, and as this study seeks to prioritise the minimisation of emissions, the first configuration is preferred for the AA/COG blend at 12 atm. Injection of HA into air, within the recuperator remains the best option for that blend at 12 atm when maintaining the 500 K inlet to the combustor.

Therefore, the suggested configurations for each of the four cases investigated, in light of the low emissions priority and in consideration of operating an even rate of fuel delivery, can be summarised as follows:

- Both configurations are suitable for the AA/COG blend at 8 atm.
- At 8 atm, the HA alone should be heated in the recuperator, prior to mixing with COG and air.
- At 12 atm the liquid AA and gaseous COG should be injected separately into the compressed air upstream of the recuperator (giving a flue temperature of 411 K).
- At 12 atm, the liquid HA should be injected into the compressed air within the recuperator (COG injection can take place anywhere upstream of the combustor).

The subsequent cycle results are therefore based on these suggested arrangements, assuming their operational feasibility. In essence, this statement is only relevant to the AA/COG blend at the higher pressure, because, as the inlet and flue temperatures are maintained at 500 and 393 K for the other three cases, the cycle efficiencies, etc. are the same whichever configuration is chosen.

7.6.3 Combustor/Recuperator Results

Figure 7.4 shows the combustor, gas turbine and HRSG process flows. Table 7.6 summarises the important results from this part of the cycle. Adiabatic flame

temperatures of the blends in the primary zone (RICHZONE) were 2149 and 2070 K for the AA and HA blends respectively. Modelling these blends in Gaseq at 500 K inlet and elevated pressure (which also models equilibrium by minimising Gibbs free energy) gives AFTs of 2144 and 2067 K, showing consistency between the programs and robustness in the data.

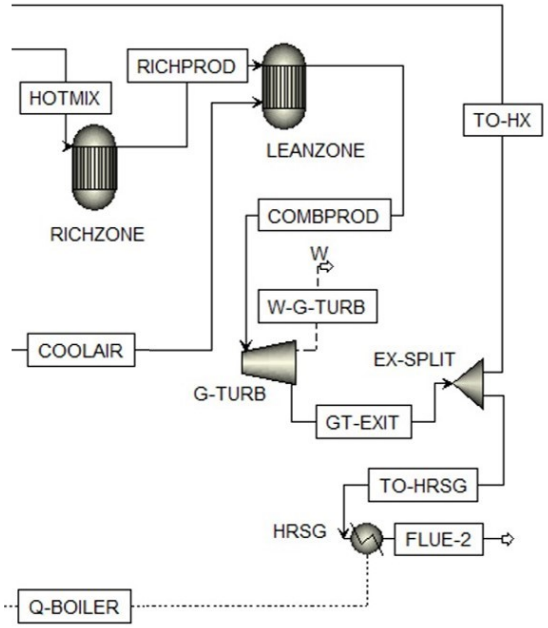

Figure 7.4 Process flow diagram for the combustor and gas turbine.

Table 7.6 Combustor and gas turbine results.

Results Stream	15% COG/AA		15% COG/HA	
	8 atm	12 atm	8 atm	12 atm
Primary air flow (kg/s)	0.710	0.710	0.796	0.796
Secondary air flow (kg/s)	2.070	2.265	2.099	2.294
Global equivalence ratio	0.31	0.29	0.32	0.30
Turbine exit temperature (K)	817	749	819	751
Percentage exhaust to recuperator	12.4	10.2	23.2	21.6
Heat to Rankine cycle (MW_{th})	1.23	1.06	1.16	1.05

The Φ_{gl} varies little between cases (0.305 ± 0.015), with secondary air accounting for 74.3 ± 1.8% of total air. The mole fraction of O_2 in the exhaust was ~13%. Although the exhaust percentages needed for the recuperator, for the HA blend, are double those of

the AA blend, the heat energy transferred to the Rankine cycle is very similar for the same pressure. This is explained by the higher recruitment of COG for the HA blends making more energy available for the combined cycle.

7.6.4 Cycle Efficiencies, Power Availability and Matching Demand

Table 7.7 gives the cycle efficiencies, net power and the specific gas turbine power for several cycle configurations, to enable a comparison of the NH_3/COG cycle under a range of scenarios:

- Brayton cycle with recuperator (i.e. no turbine exhaust heat utilisation).
- Brayton cycle with turbine direct exhaust heat utilisation (i.e. combined heat and power (CHP)).
- A combined Brayton/Rankine cycle (with recuperator).

The net power is also detailed for the combined cycle, to enable comparison with natural gas combined cycles. Lastly, the gas turbine power output is given, to indicate the scale of gas turbine which would be required in any of the above configurations (the Brayton cycle being a common element to all three scenarios).

Table 7.7 Cycle efficiencies (LHV basis), net power and gas turbine output results.

Cycle Efficiencies and Power	AA/COG		HA/COG	
	8 atm	12 atm	8 atm	12 atm
Stand-alone Brayton cycle efficiency (% of LHV)	33.5	36.5	33.9	37.0
Brayton cycle plus use of waste heat efficiency (% of LHV)	80.3	76.9	75.1	74.1
Combined cycle efficiency (% of LHV)	47.3	48.4	46.0	47.9
Combined cycle net power (kW)	1,239	1,268	1,299	1,352
Gas turbine power (kW)	1,623	1,971	1,737	2,102

The steam cycle efficiency was calculated to be 29.5% and the mass of water circulating in the Rankine cycle ranged from 0.4 to 0.47 kg/s. Turbine power output ranged from 1.6 to 2.1 MW.

The results in Table 7.7 show that the blend and operating pressure with the highest efficiency varies with the cycle configuration adopted. The energy flow into the Brayton cycle was lower for the AA blend than the HA blend (see Table 7.2) and yet the energy

leaving the Brayton cycle and entering the Rankine cycle is greater for the AA blend (see Table 7.6). Therefore, the energy leaving the Brayton cycle is a greater proportion of the energy input into the cycle for the AA blend. This has negative consequences for the efficiency of using the AA blend in a stand-alone Brayton cycle, when compared with the HA blend. Thus, in the absence of a use for the exhaust waste heat (other than preheating the fuel), the HA blend at the higher pressure is the most efficient (37%), 0.5% higher than for the AA blend at the same pressure. The HA blend at 12 atm also offers greatest power output from the gas turbine, which may serve demand better, and reduces the energy needs of the Phosam process (as discussed in Section 4.2.2). However, there are disadvantages which need to be weighed against these benefits. Fully vapourising this fuel at 12 atm, was not as simple as for the other cases, in either of the preheat configurations. When using the humidified blend, the need for additional COG is also a factor for consideration, i.e. whether the COG has an alternative use, as is the larger storage volume of HA versus AA during shutdowns. Last, but not least, the HA blend has also been shown to produce higher NO_x although delays in secondary staging have been shown to potentially overcome this issue. Hence, for a stand-alone Brayton cycle, the AA blend at 12 atm could offer a better solution than the HA blend at 12 atm, depending on the perceived relative importance of all these factors. A typical reported value for the thermal efficiency of existing natural gas, stand-alone Brayton cycle systems, at a pressure ratio of 20 and with a TET of 1400 K, is 36% [160].

The second scenario results (as shown in Table 7.7), describe the comparative efficiencies when there is the opportunity for utilisation of the waste heat exiting the gas turbine, such as when raising steam for contaminants stripping in the COG by-product plant. Thus, when the cycle favours the direct use of waste heat over maximum power generation, the AA blend at 8 atm is the most efficient, accounting for 80.3% of the LHV. The high efficiency of this CHP cycle make this case very attractive, especially when one considers the ease with which either recuperator configuration was able to vapourise the fuel.

For a combined cycle (Brayton and Rankine), the AA blend at the higher pressure commanded the highest efficiency, at > 48%. This compares with a reported figure of 45

to 57% for a natural gas combined cycle plant [161]. Hence, the efficiencies of the cycles modelled here are reasonably typical when compared with existing systems.

7.7 Greenhouse Gas Emissions – Cycle Evaluation

The Intergovernmental Panel on Climate Change have introduced international guidelines for compiling GHG inventories [162]. These guidelines suggest tiers of increasingly accurate default GHG emissions factors (EF) based on fuel (LHV basis), country and technology, in that order. Carbon dioxide emissions can be satisfactorily calculated via amounts of a fuel consumed. Natural gas combustion is therefore assigned a 56,100 kg CO_2 per TJ default emissions factor, irrespective of technology used. However, when using the same fuel in differing technologies, N_2O and CH_4 emissions can vary considerably, so EF is best derived using the tier 3 technology default.

As NH_3 is not yet commercially exploited as a fuel, no EF values are presented in the guidelines to enable inclusion in a GHG inventory, hence the need for kinetic modelling for the N_2O and CH_4 emissions as performed in Chapter 5, where these emissions were found to be practically insignificant to the global warming potential of these fuels. However, this modelling was for the fuel-rich primary stage only. There is the potential for increased N_2O resulting from NH_3 and HCN oxidation in a lean burnout stage. However, concentrations of these two species exiting the primary stage are already minimised and turbine entry temperatures are ~ 1300 K, the approximate minimum temperature for effective N_2O decomposition [119]. It is possible that turbine entry temperatures could be marginally raised if desired (~100 K) and still be within the range of other similar studies [150, 152–154]. Maximum turbine entry temperatures have increased significantly in recent years with advances in materials science and blade cooling technologies, as shown in Figure 7.5. It is not clear how this trend applies across the full range of machines of varying scale.

The default values for N_2O and CH_4 in natural gas combustion in the energy industry are 1 kg and 0.1 kg CO_2e respectively, to include not only the combustion, but also the fugitive releases of fuels [162]. Being only minor contributors to GHG emissions (as discussed in Section 5.2.2.3) and because this study has not considered fugitive

emissions in the $NH_3(H_2O)$/COG cycle, comparison of the global warming potential of the cycles is limited to the CO_2 emissions.

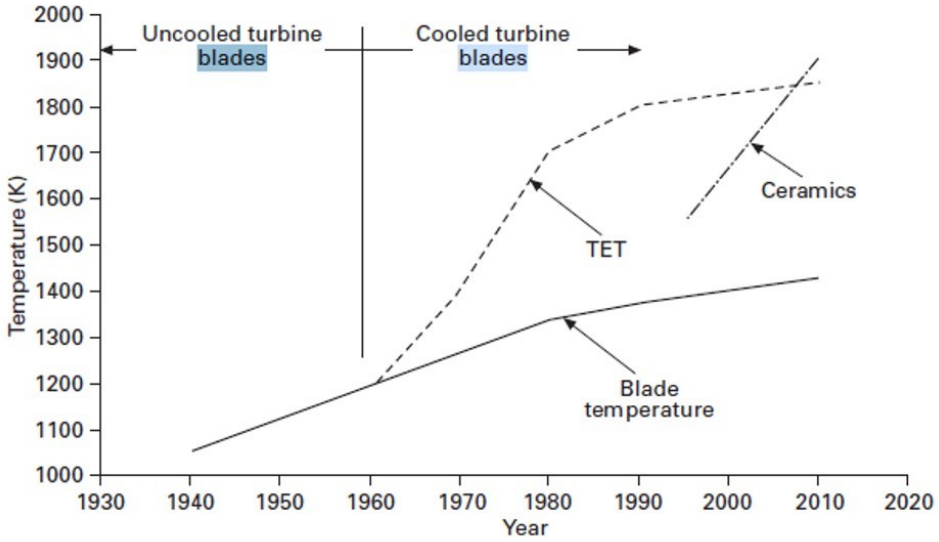

Figure 7.5 Trends in high temperature material technology for turbine blades (reproduced from [160])

The CO_2 emissions from the Aspen Plus simulations were 1.98 x 10^{-2} kg/s for the AA blend and 2.83 x 10^{-2} kg/s for the HA blend, with inputs of 2622 and 2822 kJ/s for the AA and HA blends (LHV basis) respectively (see Table 7.2). Therefore, for 1 TJ (10^{12} J) of energy input, the CO_2 emissions are 7,551 kg for the AA blend and 10,028 kg for the HA blend. This is 13.5% and 17.9% of the CO_2 emissions of natural gas combustion. Assuming the simple gas turbine (i.e. Brayton) cycle has been modelled accurately (e.g. equipment efficiencies and other operating parameters) and that ~36% is a typical cycle efficiency for natural gas, gas turbine combustion, the 15% COG/HA and 15% COG/AA cycles could reduce the global warming potential of the power produced by approximately 82 to 86% when compared with natural gas. Updating the model to include case study specific factors, such as pressure losses, would naturally decrease the CO_2 mitigation percentages, although not significantly, as combustion pressure losses vary from about 1% of the compressor discharge pressure for an industrial gas turbine to about 5% for an aeroderived gas turbine [160], the higher pressure losses being associated with higher flow velocities [99]. Flow velocities are likely to be relatively low for NH_3 combustion as comparatively long residence times are needed due to low

burning velocities and the time taken to chemically complete NO_x reduction in primary combustion.

In a final consideration about potential losses, heat losses from the combustor have not been investigated here. These are generally ignored in gas turbine literature, presumably as they are relatively low and dependent on operating conditions (e.g. load). However, it is worth noting that, as the blend proposed here is low carbon, radiative heat transfer from the flame to the combustor liner (which is unlikely to be significant feature of NH_3 or H_2 combustion) is predicted to be generally lower than that of natural gas combustion [95].

7.8 Chapter Summary

- A combined cycle (with recuperator in the Brayton cycle) was successfully modelled for 15% COG/AA and 15% COG/HA blends using relevant equipment efficiencies and a TET of 1273 K (to enable both the use of SNCR and to facilitate rapid N_2O decomposition). Two different configurations for preheating the air/fuel (using the recuperator) were investigated, at 8 atm and 12 atm.
- It was found that the **best air/fuel preheat configuration was dependent on blend and pressure**, with a recommended configuration made for each case investigated. Recommendations were based on effective vapourisation for even fuel delivery, while controlling for thermal NO_x (by limiting premix inlet temperature to 500 K).
- Global equivalence ratios and percentage exhaust returns to the recuperator were calculated. The energy available from the exhaust heat greatly exceeds that needed for the recuperator as **the recuperator utilised a maximum of 23.2% of the exhaust heat available**. This was achieved whilst allowing for a 393 K (120 °C) dew point for effective products dispersal to the atmosphere.
- Which blend and operating pressure was optimal, depended on a combination of which cycle is best suited to the end use and the technical challenges associated with vapourising the fuel. **Cycle efficiencies** ranged from **a maximum 80.3% (combined heat and power)** down to 33.5% (simple Brayton with

recuperator) both **for the AA blend at 8 atm**. Therefore, in a combined heat and power arrangement, the AA blend at 8 atm is recommended.

- The best cycle efficiencies modelled were typical for existing natural gas plant. **At 12 atm both blends achieved efficiencies of 36% for Brayton with recuperator and 48% for a combined cycle.** Pressure losses are unlikely to have a significant impact on these efficiencies.
- **For the simple Brayton cycle** (with recuperator) the marginally higher efficiency, greater gas turbine power output and greater energy savings of less distillation in the Phosam process, makes **the HA blend (at 12 atm) most attractive**. **However**, this has to be weighed against the **more challenging fuel vapourisation, higher modelled NO_x emissions** and the **greater COG demand** (i.e. whether the COG has an alternative use). The choice must therefore be made on a case by case basis.
- Combined cycle efficiency is greatest for the AA blend at 12 atm, despite the higher flue dew point temperature. **Therefore, the AA blend at 12 atm is preferred for the combined cycle arrangement**.
- Given that cycle efficiencies modelled here are within the range of those typical in existing natural gas, gas turbine cycles, GHG emissions for the $NH_3(H_2O)$/COG cycles can be compared directly with those of existing gas turbine plant. **For the AA blend, GHG emissions are lowest, modelled as 13.5% those of natural gas combustion (17.9% for the HA blend).**

Chapter 8 Conclusions

This thesis has aimed to establish whether by-product NH_3 from COG has the potential to be utilised in gas turbine technology for power generation and, if so, how this may be best achieved whilst simultaneously minimising pollutant emissions and maximising power.

This study has established that the Phosam process, which has been commercially exploited on steelworks sites, offers the pre-treatment required to convert concentrated by-product NH_3 (a potential waste stream from any coking plant) into a form which, with the minority support of an indigenous process gas (i.e. COG), can achieve stable combustion in a representative gas turbine combustor swirl burner.

With near complete combustion, in two novel air-staged combustors, lowest NO_x emissions experimentally achieved (172 ppm as dry, 15% O_2) were far above regulatory limits. However, these measurements were obtained at atmospheric pressure and modelling suggests substantial decreases in NO_x of approximately 60 to 80% at relevant operating pressures (of 6 to 12 atm). These modelling predictions are supported by the experimental work (i.e. a 25% reduction in NO_x with a 17% pressure elevation) and also by the experimental work of others [81, 92, 93, 114]. However, this prediction and the question of continued flame stability at industrially relevant pressures, will only be properly investigated when the issue of NH_3 flow restrictions is addressed to enable the required upscaling of flows. If predictions are approximately accurate and a 70% reduction in NO_x is achievable at these elevated pressures, NO_x emissions for the best case investigated here could reduce to ~50 ppm (dry, 15% O_2). According to this study's findings, other emissions should remain at acceptable levels. However, there is some evidence in the literature for a potential for increases in NH_3 at elevated pressure [93].

This study has highlighted inconsistencies in the literature in the approach to reporting emissions (e.g. wet or dry and percentage O_2 in exhaust). If the effectiveness of NO_x reduction strategies are to be effectively compared, to advance this important aspect of NH_3 combustion, a universal approach must be adopted. There are many examples of studies reporting NO_x emissions in isolation, this study has shown that reporting NH_3

emissions alongside those of NO_x is crucial, as conditions capable of lowest NO_x emissions (fuel-rich) are often associated with unacceptable levels of unburned NH_3.

Aside from pressure elevation, other strategies for limiting NO_x, suggested by this study's findings, are to restrict inlet temperatures to 500 K or below (to reduce thermal NO_x formation) and to alter the Φ_{gl} via the partial substitution of air in favour of N_2 in the second stage (leading to ~10% NO_x reduction). Both these strategies warrant further investigation. The addition of steam was also found to lower NO_x, but only where the Φ was fixed. Where Φ was varied, anhydrous blends offered lowest NO_x across the range of Φ and the lowest overall emissions (i.e. NO_x and NH_3 combined).

Post combustion NO_x reduction technique SNCR, is also considered in the cycle design, by ensuring appropriate temperatures for its administration. SNCR has the potential to more than halve NO_x exhaust concentrations [48]. This was demonstrated in a study by Kurata et al. (2017) [78] where the addition of 800 ppm NH_3 using SNCR reduced 600 ppm of NO_x down to 10 ppm. They found that the low requirement of NH_3, in an approximate ratio of 1:1 NH_3 to NO made little impact on efficiency. In consideration of all the above findings and suggested measures, an NH_3/COG cycle appears to have the potential for legally acceptable NO_x and unburned fuel emissions.

In consideration of GHG emissions, rich, primary stage modelled N_2O emissions were shown to be negligible. Whether they remain negligible for complete, staged combustion requires further investigation, beyond the capabilities of the facilities used in this study. However, maintaining the TET >1300 K supports the assumption that N_2O emissions would remain negligible and that GHG emissions are limited to an evaluation of the CO_2 produced. When compared with a natural gas Brayton cycle, CO_2 was reduced by >80% when utilising recovered by-product NH_3 with 15%$_{vol}$ COG support.

Having demonstrated how pollutant emissions can be minimised, the maximisation of power (and potentially heat) was investigated. A recuperator, to efficiently utilise gas turbine exhaust heat, was an obvious solution for overcoming the chilling effects of NH_3 vapourisation upstream of the combustor (i.e. due to liquid phase storage) and was thus proposed for all cycle scenarios. Of all cycles modelled, maximum net power of 1.35 MW_e was simulated for the HA blend in a combined cycle operating at 12 atm. However,

this cycle efficiency (47.9% of LHV) is lower than that for the AA blend, in the same cycle (48.4%), because the HA blend utilises more COG (i.e. fuel flows are based on the fixed NH_3 availability of 10 tonnes per day), raising questions about the alternative uses the additional COG might otherwise be put to. Additionally, a decision about whether HA or AA is preferred necessitates a decision about the relative importance of greater power production versus predicted inferior emissions. In any event, the question of how best to maximise power is primarily dependant on cycle scenario, which will be dictated by the existing site infrastructure (e.g. the presence of a steam turbine to export heat to) and local demands for power and heat. Thus, this study has modelled and evaluated a number of anticipated scenarios to answer this question.

As pressure to reduce carbon emissions increases, steelworks will need to innovate. A pilot plant operating on recovered by-product NH_3 and COG could have the potential to reduce the carbon emissions for over 1 MW of its power usage by >80%, which may seem insignificant for a steelworks site. However, steelworks offer an interesting proposition. COG is a rich source of H_2 and the economic separation of H_2 from COG (e.g. membrane technologies and cryogenics) is an active field of research [57, 163]. Separation of H_2 from COG before the COG combustion also offers a more concentrated CO_2 exhaust, facilitating more efficient CO_2 capture and storage. Air separation, to provide O_2 to the basic oxygen furnace, produces by-product N_2, which is of course the other chief component required for NH_3 manufacture. Thus, steelworks could become manufacturers of NH_3. This NH_3, possibly with H_2 support, could be used to provide carbon free gas turbine power (albeit originally sourced from coal). Should this come to pass, the experience gained from running a small-scale pilot plant could become invaluable. Naturally, green NH_3 could also be imported to steelworks sites and used to augment the indigenous NH_3 available, regardless of whether this indigenous NH_3 is recovered from the by-product stream or manufactured from the H_2 in COG (as just described). Additionally, the aqueous stream that would normally be fed to the bottom of the fractionating tower in the Phosam process could be blended with anhydrous NH_3 (green or manufactured from COG H_2) to achieve the desired $H_2O\%_{vol}$, negating the need for the Phosam fractionating tower, saving the associated capital costs and the energy required by the dehydrating process.

Chapter 9 Suggested Further Work

To progress the research, a crucial next step is the investigation of the effect of pressure elevation on NH_3 emissions. Flow restrictions have thus far prevented significant pressure elevation above atmospheric. Given the findings for $15\%_{vol}$ COG/AA at 8 atm (Table 7.4), it is recommended that, for pressures approaching this compression ratio (i.e. 8) and lower, a liquid NH_3 spray be injected into hot compressed air (~540 K at a compression ratio of 8) prior to COG vapour addition and that the premix (NH_3/COG/air) be further heated to an inlet temperature of ~500 K. This configuration should enable even vapourisation, avoiding the potential for pulsing in the combustor and to provide a homogenous premix. Results would thus be relevant to a practically relevant cycle, utilising a recuperator.

Primary zone NO_x emissions at inlet ~500 K were found to be significantly lower than for ~530 K. Therefore, inlet temperature versus NO_x should be investigated, reducing inlet temperatures below 500 K, while taking care to maintain flame stability. The results could help mitigate for thermal NO_x, resulting from unnecessarily high preheating of the premix.

Further investigation is required to understand how significantly the configuration and location of the confinements' secondary air staging effects the structures of upstream swirling flows (e.g. using particle image velocimetry), and particularly how impingement of opposing air inlet flows may disrupt flame structure.

Partial secondary air substitution (using N_2) showed decreases in NO_x exhaust emissions. This suggests a potential NO_x mitigation strategy. However, data was extremely limited so replication is required. Similarly, due to very few data points, repeat testing is required to verify whether modest pressure elevation (~1.3 bara) does indeed lead to the same NO_x for both staging locations, as earlier staging facilitates shorter combustors. As the HA blend emissions from later staging resembled those of AA with earlier staging, it could be that higher pressures can improve HA emissions without the need for significantly delayed staging.

The discovered correlation between Φ_{opt} and laminar flame speed, across the full range of blends investigated, proved useful in predicting an optimal operating Φ prior to testing blends. This tool should be further validated on this and other equipment to ascertain its general usefulness as it could potentially prove useful in similar studies and ultimately to industry during commissioning of NH_3 fuelled gas turbines.

The N_2O and HCN emissions need to be measured experimentally. This will require gas analysis equipment capable of these measurements such as a fourier-transform infrared (FTIR) spectroscopy gas analyser, which would also facilitate H_2O readings that have in this study needed to be derived from equilibrium modelling. An FTIR analyser would also enable simultaneous readings of NO, NO_2 and NH_3 at the same Φ, overcoming the issue of negative readings due to decreases in NH_3 flow (and consequently increasing lean Φ) across test cases.

Given the individual nature of the by-product NH_3 plant to each steelworks, a case study is required for a techno-economic evaluation of the proposed ammonia cycles. Thus, a willing industrial partner with a plant in need of updating (such as either of the UK sites) needs to be sourced to assess the economic viability of the proposed cycle. While the final assessment would be largely limited to that specific case, it would help to inform others regarding any common aspects in the redesign of their own processes.

If Chemkin mechanism files can be modified to be compatible with Aspen Plus software and if Aspen Plus is found capable of utilising such large mechanism files, it would mean that cycles developed in Aspen Plus could simulate, not only cycle efficiencies and power, but also generate emissions results which acknowledge the kinetic aspect of NO_x formation, dispensing with the need for separate Chemkin analyses.

Finally, a case needs to be made for the creation of NH_3 and H_2 specific NO_x standards. As was discussed in this thesis, the absence of CO_2 in the exhaust (acting as an emissions diluent) disadvantages these two fuels, when being held to the same regulations as natural gas, in gas turbine technology. Lastly, a universal standard for the reporting of NO_x AND NH_3 emissions needs to be established to enable proper comparison between studies, thus generating competitive improvement in the development of emissions limiting strategies.

References

[1] IPCC. (2018). "2018: Summary for Policymakers", Masson-Delmotte, V., Zhai, P., Pörtner, H.-O., Roberts D., Skea, J., Shukla, P. R., Pirani, A., Moufouma-Okia, W., Péan, C., Pidcock, R., Connors, S., Matthews, J. B. R., Chen, Y., Zhou, X., Gomis, M. I., Lonnoy, E., Maycock, T., Tignor, M., Waterfield, T. (Eds.), *An IPCC Special Report on the Impacts of Global Warming of 1.5°C above Pre-Industrial Levels and Related Global Greenhouse Gas Emission Pathways, in the Context of Strengthening the Global Response to the Threat of Climate Change, Sustainable Development,* World Meteorological Organization, Geneva, Switzerland, pp. 6

[2] Nerem, R. S., Beckley, B. D., Fasullo, J. T., Hamlington, B. D., Masters, D., Mitchum, G. T. (2018). "Climate-change-driven accelerated sea-level rise detected in the altimeter era.", *Proceedings of the National Academy of Sciences of the United States of America*, Vol. 115, No. 9, pp. 2022–2025. doi:10.1073/pnas.1717312115

[3] The Royal Society. (2005). "Ocean acidification due to increasing atmospheric carbon dioxide", from https://royalsociety.org/topics-policy/publications/2005/ocean-acidification/

[4] European Environment Agency. (2017). "Atmospheric greenhouse gas concentrations", from https://www.eea.europa.eu/data-and-maps/indicators/atmospheric-greenhouse-gas-concentrations-6/assessment-1, accessed 3-12-2019

[5] US Department of Commerce, NOAA, E. S. R. L. (2020). "NOAA ESRL Global Monitoring Division", from https://www.esrl.noaa.gov/gmd/ccgg/trends/, accessed 14-12-2020

[6] International Energy Agency. (2019). *World Energy Outlook 2019*, International Energy Agency

[7] Sönnichsen, N. (2020). "UK: Fossil fuel dependence 2019 | Statista", from https://www.statista.com/statistics/418202/fossil-fuel-dependence-united-kingdom/, accessed 14-12-2020

[8] Myhre, G., Shindell, D., Bréon, F.-M., Collins, W., Fuglestvedt, J., Huang, J., Koch, D., Lamarque, J.-F., Lee, D., Mendoza, B., Nakajima, T., Robock, A., Stephens, G., Takemura, T., Zhang, H. (2013). "Anthropogenic and natural radiative forcing", T. F. Stocker; D. Qin; G.-K. Plattner; M. Tignor; S. K. Allen; J. Boschung; A. Nauels; Y. Xia; V. Bex; P. M. Midgley (Eds.), *Climate Change 2013: The Physical Science Basis. Contribution of Working Group I to the Fifth Assessment Report of the Intergovernmental Panel on Climate Change*, Cambridge University Press, Cambridge, United Kingdom and New York, NY, USA, pp. 731

[9] United Nations Framework Convention on Climate Change. (2015). "Historic Paris agreement on climate change: 195 nations set path to keep temperature rise well below 2 degrees celsius", from https://unfccc.int/news/finale-cop21, accessed 2-5-2019

[10] United Nations Framework Convention on Climate Change. (2019). "What is the United Nations Framework Convention on Climate Change? | UNFCCC", from https://unfccc.int/process-and-meetings/the-convention/what-is-the-united-nations-framework-convention-on-climate-change, accessed 2-1-2020

[11] WSP and Parsons Brinckerhoff. (2015). *Industrial Decarbonisation and Energy Efficiency Roadmaps to 2050 - A report prepared for the Department of Energy and Climate Change and the Department for Business, Innovation and Skills*

[12] Gummer, R. H. J., Brown, B., Bell, K., Chater, N., Forster, P., Heaton, R., Johnson, P., FRS, C. L. Q. (2019). *Net Zero The UK's Contribution to Stopping Global Warming*, © Committee on Climate Change Copyright 2019

[13] UK Government. (2019). *Climate Change Act 2008 (2050 Target Amendment) Order 2019*, © Crown copyright 2019

[14] UK Cabinet Office. (2021). "Companies bidding for major government contracts face green rules - GOV.UK", *Crown Copyright*, from https://www.gov.uk/government/news/companies-bidding-for-major-government-contracts-face-green-rules, accessed 1-10-2021

[15] Dickins, S. (2021). "Climate change: Tata Steel wants roadmap to make industry greener", *BBC News*, from https://www.bbc.co.uk/news/uk-wales-59010674, accessed 25-10-2021

[16] Worldsteel Association. (2021). "Energy use in the steel industry - fact sheet 2021", from https://www.worldsteel.org, accessed 9-7-2021

[17] Worldsteel Association. (2019). "Energy use in the steel industry - fact sheet 2019", from https://www.worldsteel.org, accessed 8-5-2019

[18] Worldsteel Association. (2019). "Steel and raw materials - fact sheet 2019", from https://www.worldsteel.org, accessed 16-12-2020

[19] International Energy Agency. (2020). "Iron and Steel Technology Roadmap – Analysis", from https://www.iea.org/reports/iron-and-steel-technology-roadmap, accessed 16-12-2020

[20] Allwood, J. M. (2016). "A bright future for UK steel: A strategy for innovation and leadership through up-cycling and integration", *University of Cambridge*, pp. 1–16

[21] Committee on Climate Change. (2019). "Reducing UK emissions - 2019 Progress Report to Parliament", © Committee on Climate Change Copyright 2019

[22] Committee on Climate Change. (2017). "2017 Report to Parliament - Meeting Carbon Budgets: Closing the policy gap", © Committee on Climate Change Copyright 2017

[23] Flavell-While, C. (2010). "Fritz Haber and Carl Bosch feed the world", from https://www.thechemicalengineer.com/features/cewctw-fritz-haber-and-carl-bosch-feed-the-world/, accessed 8-1-2020

[24] U.S. Geological Survey. (2020). "Mineral Commodity Summaries 2020", pp. 116–117, from https://pubs.er.usgs.gov/publication/mcs2020, accessed 16-12-2020

[25] International Energy Agency. (2019). *The Future of Hydrogen - Seizing Today's Opportunities*. doi:10.1787/1e0514c4-en

[26] Djinović, P., Schüth, F. (2014). "Energy carriers made from hydrogen", P. and G. Moseley (Ed.), *Electrochemical Energy Storage for Renewable Sources and Grid Balancing*, pp. 183–199. doi:10.1016/B978-0-444-62616-5.00012-7

[27] Zamfirescu, C., Dincer, I. (2008). "Using ammonia as a sustainable fuel", *Journal of Power Sources*, Vol. 185, No. 1, pp. 459–465. doi:10.1016/j.jpowsour.2008.02.097

[28] Giddey, S., Badwal, S. P. S., Munnings, C., Dolan, M. (2017). "Ammonia as a Renewable Energy Transportation Media", *ACS Sustainable Chemistry & Engineering*, Vol. 5, No. 11, pp. 10231–10239. doi:10.1021/acssuschemeng.7b02219

[29] Kojima, Y. (2013). "A Green Ammonia Economy", *10th Annual NH3 Fuel Conference*, from https://nh3fuelassociation.org/wp-content/uploads/2013/10/nh3fcx-yoshitsugu-kojima.pdf, accessed 14-5-2020

[30] Ahlgren, W. L. (2012). "The dual-fuel strategy: an energy transition plan", *Proceedings of the IEEE*, Vol. 100, No. 11, pp. 3001–3052. doi:10.1109/JPROC.2012.2192469

[31] Green, L. (1967). "Energy needs versus environmental pollution: A reconciliation?", *Science*, Vol. 156, No. 3781, pp. 1448–1450. doi:10.1126/science.156.3781.1448

[32] Philibert, C. (2017). "Producing ammonia and fertilizers: new opportunities from renewables", *IEA Report*, pp. 1–6

[33] Crolius, S. H. (2019). "Technology Advances for Blue Hydrogen and Blue Ammonia - Ammonia Energy Association", from https://www.ammoniaenergy.org/articles/technology-advances-for-blue-hydrogen-and-blue-ammonia/, accessed 14-12-2020

[34] Zamfirescu, C., Dincer, I. (2009). "Ammonia as a green fuel and hydrogen source for vehicular applications", *Fuel Processing Technology*, Vol. 90, No. 5, pp. 729–737. doi:10.1016/j.fuproc.2009.02.004

[35] Hughes, T., Wilkinson, I., Tsang, E., Mcpherson, I., Sudmeier, T., Fellowes, J., Liao, F., Wu, S., Valera-Medina, A., Metz, S. (2015). "Green Ammonia", from http://www.energy.ox.ac.uk/wordpress/wp-content/uploads/2016/03/Green-Ammonia-Hughes-8.3.16.pdf, accessed 18-9-2018

[36] Wilkinson, I. (2017). "The Role of "Green" Ammonia in Decarbonising Energy Systems: Practical Demonstration and Economic Considerations", *NH3 Fuel Conference*, Minneapolis, from https://nh3fuelassociation.org/2017/09/26/the-role-of-green-ammonia-in-decarbonising-energy-systems-practical-demonstration-and-economic-considerations/

[37] Gill, S. S., Chatha, G. S., Tsolakis, A., Golunski, S. E., York, A. P. E. (2012). "Assessing the effects of partially decarbonising a diesel engine by co-fuelling with dissociated ammonia", *International Journal of Hydrogen Energy*, Vol. 37, No. 7, pp. 6074–6083. doi:10.1016/j.ijhydene.2011.12.137

[38] Valera-Medina, A., Xiao, H., Owen-Jones, M., David, W. I. F., Bowen, P. J. (2018). "Ammonia for power", *Progress in Energy and Combustion Science*, Vol. 69, pp. 63–102. doi:10.1016/j.pecs.2018.07.001

[39] Cheddie, D. (2012). "Ammonia as a Hydrogen Source for Fuel Cells: A Review", *Hydrogen Energy - Challenges and Perspectives*. doi:10.5772/47759

[40] Kobayashi, H., Hayakawa, A., Somarathne, K. D. K. A., Okafor, E. C. (2019). "Science and technology of ammonia combustion", *Proceedings of the Combustion Institute*, Vol. 37, No. 1, pp. 109–133. doi:10.1016/j.proci.2018.09.029

[41] Verkamp, F. J., Hardin, M. C., Williams, J. R. (1967). "Ammonia combustion properties and performance in gas-turbine burners", *Symposium (International) on Combustion*, Vol. 11, pp. 985–992. doi:https://doi.org/10.1016/S0082-0784(67)80225-X

[42] Pratt, D. . (1967). "Performance of ammonia-fired gas-turbine combustors", *University of California, Berkley*, from https://apps.dtic.mil/dtic/tr/fulltext/u2/657585.pdf

[43] Miller, J., Bowman, C. (1989). "Mechanism and Modeling of Nitrogen Chemistry in Combustion", *Progress in Energy and Combustion Science*, Vol. 15, No. 4, pp. 287–338

[44] Glassman, I., Yetter, R., Glumac, N. (2015). *Combustion* (Fifth edit.), Academic Press, Waltham, MA

[45] Zel'dovich, Y. B. (1946). "The Oxidation of Nitrogen in Combustion Explosions", *Acta Physecochem*, Vol. 21, pp. 577

[46] Glarborg, P., Miller, J. A., Ruscic, B., Klippenstein, S. J. (2018). "Modeling nitrogen chemistry in combustion", *Progress in Energy and Combustion Science*. doi:10.1016/j.pecs.2018.01.002

[47] Fenimore, C. P. (1971). "Formation of nitric oxide in premixed hydrocarbon flames", *Symposium (International) on Combustion*, Vol. 13, No. 1, pp. 373–380. doi:10.1016/S0082-0784(71)80040-1

[48] Gómez-García, M. A., Pitchon, V., Kiennemann, A. (2005). "Pollution by nitrogen oxides: an approach to NOx abatement by using sorbing catalytic materials", Vol. 31, pp. 445–467. doi:10.1016/j.envint.2004.09.006

[49] Adam, M. R., Othman, M. H. D., Abu Samah, R., Puteh, M. H., Ismail, A. F., Mustafa, A., A. Rahman, M., Jaafar, J. (2019). "Current trends and future prospects of ammonia removal in wastewater: A comprehensive review on adsorptive membrane development", *Separation and Purification Technology*, Vol. 213, pp. 114–132. doi:10.1016/J.SEPPUR.2018.12.030

[50] Air Quality Expert Group. (2018). "Air Pollution from Agriculture Prepared for: Department for Environment, Food and Rural Affairs; Scottish Government; Welsh Government; and Department of the Environment in Northern Ireland", from https://uk-air.defra.gov.uk/assets/documents/reports/aqeg/2800829_Agricultural_emissions_vfinal2.pdf

[51] The Royal Society. (2020). "Ammonia: zero-carbon fertiliser, fuel and energy store. Policy Briefing.", from https://royalsociety.org/topics-policy/projects/low-carbon-energy-programme/green-ammonia/

[52] Misselbrook, T. H., Gilhespy, S. L., Cardenas, L. M., Williams, J., Dragosits, U. (2015). "Inventory of Ammonia Emissions from UK Agriculture 2015: DEFRA Contract Report (SCF0102)", No. November, pp. 36

[53] Gude, V. G. (2015). "Energy and water autarky of wastewater treatment and power generation systems", *Renewable and Sustainable Energy Reviews*, Elsevier Ltd, pp. 52–68. doi:10.1016/j.rser.2015.01.055

[54] Anderson, M., Ray, M. (2017). "Elimination of Hydrogen Sulphide in Aqueous Ammonia", European Patent Office

[55] The Institute for Industrial Productivity. (2020). "Coke Making", from http://www.iipinetwork.org/wp-content/Ietd/content/coke-making.html, accessed 18-12-2020

[56] Remus, R., Roudier, S., Aguado-Monsonet, M. A., Delgado Sancho, L. (2013). "Best available techniques - iron and steel production", *Industrial Emissions Directive 2010/75/EU*. doi:10.2791/97469

[57] Bermúdez, J. M., Arenillas, A., Luque, R., Menéndez, J. A. (2013). "An overview of novel technologies to valorise coke oven gas surplus", *Fuel Processing Technology*, Vol. 110, pp. 150–159. doi:10.1016/J.FUPROC.2012.12.007

[58] Kohl, A. L., Nielsen, R. (1997). *Gas Purification.*, Gulf Publishing, Houston

[59] US Energy Information Administration. (n.d.). "United States Natural Gas Industrial Price (Dollars per Thousand Cubic Feet)", from https://www.eia.gov/dnav/ng/hist/n3035us3m.htm, accessed 1-10-2021

[60] Reuters. (2021). "Yara brings ammonia to Europe after gas price hike, CEO says", from https://www.reuters.com/business/energy/yara-brings-ammonia-europe-after-gas-price-hike-ceo-says-2021-09-20/, accessed 6-10-2021

[61] Platts, M. (n.d.). "The Coke Oven By-Product Plant", American Coke and Coal Chemicals Institute, from http://www.accci.org/industry.html, accessed 13-10-2021

[62] Svoboda, K., Diemer, P. (1990). "Catalytic decomposition of ammonia from coke-oven gas", *Iron and Steel Engineer*, Vol. 67, No. 12, pp. 42–46

[63] European Commission. (1996). "Study on the technical and economical aspects to reduce (on the basis of the best available technologies) the pollution (of water and other environmental areas) from the industrial emissions of cokeries", from ttps://policycommons.net/artifacts/298814/study-on-the-technical-and-economical-aspects-of-measures-to-reduce-on-the-basis-of-the-best-available-technologies-the-pollution-of-water-and-other-environmental-areas-from-the-industrial-emissions-of-cokeries/12, accessed 13-10-2021

[64] Natural Resources Wales. (2016). "Permit with introductory note No. EPR/BL7108IM", from https://naturalresources.wales/media/676099/20160208-eprbl7108imv015-tata-port-talbot-permit-signed.pdf, accessed 8-10-2018

[65] Teng, H. (1996). "Combustion modifications of batch annealing furnaces and ammonia combustion ovens for NOx abatement in steel plants", *Journal of the Air and Waste Management Association*, Vol. 46, No. 12, pp. 1171–1178. doi:10.1080/10473289.1996.10467552

[66] "Thermophysical Properties of Fluid Systems". (n.d.), from https://webbook.nist.gov/chemistry/fluid/, accessed 17-6-2020

[67] Health & Safety Executive. (n.d.). "COMAH - Guidance - Technical Aspects - Measures Documents - Corrosion / selection of materials", from http://www.hse.gov.uk/comah/sragtech/techmeasmaterial.htm, accessed 1-3-2018

[68] Cole-Parmer Instrument Company. (2021). "Chemical Compatibility Database from Cole-Parmer United Kingdom", from https://www.coleparmer.co.uk/Chemical-Resistance, accessed 2-6-2021

[69] National Academies. (2008). "Ammonia Final AEGL Document", from

http://www.nap.edu/catalog/12018.html, accessed 2-6-2021

[70] Health and Safety Executive. (2011). *EH40/2005 Workplace Exposure Limits*, *EH40 Second Edition*, HSE Books

[71] Advanced Motor Fuels. (n.d.). "Technology collaboration programme on advanced motor fuels - Composition of gasoline and diesel", from https://www.iea-amf.org/content/fuel_information/diesel_gasoline, accessed 18-6-2020

[72] European Commission. (2009). "European Parliament Directive 2009/30/EC", *Official Journal of the European Union*, pp. 88–113, from https://www.legislation.gov.uk/eudr/2009/30/introduction/adopted

[73] Mabanaft UK. (n.d.). "Products", from https://www.mabanaft.co.uk/, accessed 3-6-2021

[74] International Energy Agency. (2004). *Energy Statistics Manual*, *Energy Statistics Manual*, OECD. doi:10.1787/9789264033986-en

[75] McAllister, S., Chen, J.-Y., Fernandez-Pello, A. C. (2011). *Fundamentals of Combustion Processes*. doi:10.1007/978-1-4419-7943-8

[76] Runyon, J. (2017). *Gas turbine fuel flexibility: pressurized swirl flame stability, thermoacoustics, and emissions*, *Cardiff University*Cardiff

[77] Encyclopedia Britannica. (2021). "Joule-Thomson effect", from https://www.britannica.com/science/Joule-Thomson-effect, accessed 8-6-2020

[78] Kurata, O., Iki, N., Matsunuma, T., Inoue, T., Tsujimura, T., Furutani, H., Hayakawa, A., Kobayashi, H. (2017). "Success of ammonia-fired, regenerator-heated, diffusion combustion gas turbine power generation and prospect of low NOx combustion with high combustion efficiency", *American Society of Mechanical Engineers, Power Division (Publication) Power* (Vol. 1), American Society of Mechanical Engineers (ASME). doi:10.1115/POWER-ICOPE2017-3277

[79] Okafor, E. C., Yamashita, H., Hayakawa, A., Somarathne, K. D. K. A., Kudo, T., Tsujimura, T., Uchida, M., Ito, S., Kobayashi, H. (2021). "Flame stability and emissions characteristics of liquid ammonia spray co-fired with methane in a single stage swirl combustor", *Fuel*, Vol. 287, pp. 119433. doi:10.1016/j.fuel.2020.119433

[80] Reiter, A. J., Kong, S. C. (2011). "Combustion and emissions characteristics of compression-ignition engine using dual ammonia-diesel fuel", *Fuel*, Vol. 90, No. 1, pp. 87–97. doi:10.1016/j.fuel.2010.07.055

[81] Hayakawa, A., Goto, T., Mimoto, R., Kudo, T., Kobayashi, H. (2015). "NO formation/reduction mechanisms of ammonia/air premixed flames at various equivalence ratios and pressures", *Mechanical Engineering Journal*, Vol. 2, No. 1, pp. 14- 00402-14–00402. doi:10.1299/mej.14-00402

[82] Kondo, S., Takizawa, K., Takahashi, A., Tokuhashi, K. (2011). "On the temperature dependence of flammability limits of gases", *Journal of Hazardous Materials*, Vol. 187, Nos. 1–3, pp. 585–590. doi:10.1016/j.jhazmat.2011.01.037

[83] Ciccarelli, G., Jackson, D., Verreault, J. (2006). "Flammability limits of NH3-H2-N2-air mixtures at elevated initial temperatures", *Combustion and Flame*, Vol. 144, Nos. 1–2, pp. 53–63. doi:10.1016/j.combustflame.2005.06.010

[84] Lees, F. P. (1977). "Electrostatic hazards: Their evaluation and control", *The Chemical Engineering Journal*, Vol. 14, No. 3, pp. 229. doi:10.1016/0300-9467(77)85022-3

[85] Eckhoff, R. K., Ngo, M., Olsen, W. (2010). "On the minimum ignition energy (MIE) for propane/air", *Journal of Hazardous Materials*, Vol. 175, Nos. 1–3, pp. 293–297. doi:10.1016/j.jhazmat.2009.09.162

[86] Hayakawa, A., Goto, T., Mimoto, R., Arakawa, Y., Kudo, T., Kobayashi, H. (2015). "Laminar burning velocity and Markstein length of ammonia/air premixed flames at various pressures", *Fuel*, Vol. 159, pp. 98–106. doi:10.1016/J.FUEL.2015.06.070

[87] Amirante, R., Distaso, E., Tamburrano, P., Reitz, R. D. (2017). "Laminar flame speed correlations for methane, ethane, propane and their mixtures, and natural gas and gasoline for spark-ignition engine simulations", *International Journal of Engine Research*, Vol. 18, No. 9, pp. 951–970. doi:10.1177/1468087417720018

[88] Morley, C. (n.d.). "Gaseq - A chemical equilibrium program for Windows", from http://www.gaseq.co.uk/

[89] Valera-Medina, A., Morris, S., Runyon, J., Pugh, D. G., Marsh, R., Beasley, P., Hughes, T. (2015). "Ammonia, methane and hydrogen for gas turbines", *Energy Procedia*, Vol. 75, pp. 118–123. doi:https://doi.org/10.1016/j.egypro.2015.07.205

[90] Valera-Medina, A., Gutesa, M., Xiao, H., Pugh, D., Giles, A., Goktepe, B., Marsh, R., Bowen, P. (2019). "Premixed ammonia/hydrogen swirl combustion under rich fuel conditions for gas turbines operation", *International Journal of Hydrogen Energy*, Vol. 44, No. 16. doi:10.1016/j.ijhydene.2019.02.041

[91] Valera-Medina, A., Pugh, D. G., Marsh, P., Bulat, G., Bowen, P. (2017). "Preliminary study on lean premixed combustion of ammonia-hydrogen for swirling gas turbine combustors", *International Journal of Hydrogen Energy*, Vol. 42, No. 38. doi:10.1016/j.ijhydene.2017.08.028

[92] Valera-Medina, A., Marsh, R., Runyon, J., Pugh, D., Beasley, P., Hughes, T., Bowen, P. (2017). "Ammonia–methane combustion in tangential swirl burners for gas turbine power generation", *Applied Energy*, Vol. 185, pp. 1362–1371. doi:10.1016/j.apenergy.2016.02.073

[93] Pugh, D., Bowen, P., Valera-Medina, A., Giles, A., Runyon, J., Marsh, R. (2019). "Influence of steam addition and elevated ambient conditions on NOx reduction in a staged premixed swirling NH3/H2 flame", *Proceedings of the Combustion Institute*, Vol. 37, No. 4, pp. 5401–5409. doi:10.1016/j.proci.2018.07.091

[94] Pugh, D., Runyon, J., Bowen, P., Giles, A., Valera-Medina, A., Marsh, R., Goktepe, B., Hewlett, S. (2020). "An investigation of ammonia primary flame combustor concepts for emissions reduction with OH*, NH2* and NH* chemiluminescence at elevated conditions", *Proceedings of the Combustion Institute*, Vol. 38, No. 4, pp. 6451–6459. doi:10.1016/j.proci.2020.06.310

[95] Kurata, O., Iki, N., Matsunuma, T., Inoue, T., Tsujimura, T., Furutani, H., Kobayashi, H., Hayakawa, A. (2017). "Performances and emission characteristics of NH3–air and NH3 CH4–air combustion gas-turbine power generations", *Proceedings of the Combustion Institute*, Vol. 36, No. 3, pp. 3351–3359. doi:10.1016/J.PROCI.2016.07.088

[96] Okafor, E. C., Naito, Y., Colson, S., Ichikawa, A., Kudo, T., Hayakawa, A., Kobayashi, H. (2018). "Experimental and numerical study of the laminar burning velocity of CH4–NH3–air premixed flames", *Combustion and Flame*, Vol. 187, pp. 185–198. doi:10.1016/j.combustflame.2017.09.002

[97] Li, S., Zhang, S., Zhou, H., Ren, Z. (2019). "Analysis of air-staged combustion of NH3/CH4 mixture with low NOx emission at gas turbine conditions in model combustors", *Fuel*, Vol. 237. doi:10.1016/j.fuel.2018.09.131

[98] Okafor, E. C., Somarathne, K. D. K. A., Ratthanan, R., Hayakawa, A., Kudo, T., Kurata, O., Iki, N., Tsujimura, T., Furutani, H., Kobayashi, H. (2020). "Control of NOx and other emissions in micro gas turbine combustors fuelled with mixtures of methane and ammonia", *Combustion and Flame*. doi:10.1016/j.combustflame.2019.10.012

[99] Lefebvre, A. H. (Arthur H., Ballal, D. R. (2010). *Gas Turbine Combustion : Alternative Fuels and Emissions*, Taylor & Francis

[100] Gupta, A. K., Lilley, D. G., Syred, N. (1984). *Swirl Flows*, Abacus Press, Tunbridge Wells, UK

[101] Syred, N. (2006). "A review of oscillation mechanisms and the role of the precessing vortex core (PVC) in swirl combustion systems", *Progress in Energy and Combustion Science*, Vol. 32, No. 2, pp. 93–161. doi:10.1016/J.PECS.2005.10.002

[102] Hayakawa, A., Arakawa, Y., Mimoto, R., Somarathne, K. D. K. A., Kudo, T., Kobayashi, H. (2017). "Experimental investigation of stabilization and emission characteristics of ammonia/air premixed

flames in a swirl combustor", *International Journal of Hydrogen Energy*, Vol. 42, No. 19, pp. 14010–14018. doi:10.1016/J.IJHYDENE.2017.01.046

[103] Pugh, D., Valera-Medina, A., Bowen, P., Giles, A., Goktepe, B., Runyon, J., Morris, S., Hewlett, S., Marsh, R. (2020). "Emissions performance of staged premixed and diffusion combustor concepts for an NH3/AIR flame with and without reactant humidification", *Proceedings of the ASME Turbo Expo* (Vol. 4A-2020), American Society of Mechanical Engineers (ASME). doi:10.1115/GT2020-14953

[104] Palies, P., Durox, D., Schuller, T., Candel, S. (2011). "Experimental Study on the Effect of Swirler Geometry and Swirl Number on Flame Describing Functions", *Combustion Science and Technology*, Vol. 183, No. 7, pp. 704–717. doi:10.1080/00102202.2010.538103

[105] Syred, N., Beér, J. M. (1974). "Combustion in swirling flows: A review", *Combustion and Flame*, Vol. 23, No. 2, pp. 143–201. doi:10.1016/0010-2180(74)90057-1

[106] Somarathne, K. D. K. A., Hatakeyama, S., Hayakawa, A., Kobayashi, H. (2017). "Numerical study of a low emission gas turbine like combustor for turbulent ammonia/air premixed swirl flames with a secondary air injection at high pressure", *International Journal of Hydrogen Energy*, Vol. 42, No. 44, pp. 27388–27399. doi:10.1016/j.ijhydene.2017.09.089

[107] European Union. (2014). "Directive (EU) 2015/ 2193 of the European Parliament and of the Council on the limitation of emissions of certain pollutants into the air from medium combustion plants", *Official Journal of the European Union EN*, Vol. 451, No. 354, pp. 134–23

[108] International Organization for Standardization. (n.d.). "ISO 11042-1:1996 - Gas turbines - Exhaust gas emission - Part 1: Measurement and evaluation", from https://www.iso.org/standard/19022.html, accessed 18-11-2019

[109] Kurata, O., Iki, N., Inoue, T., Matsunuma, T., Tsujimura, T., Furutani, H., Kawano, M., Arai, K., Okafor, E. C., Hayakawa, A., Kobayashi, H. (2019). "Development of a wide range-operable, rich-lean low-NOx combustor for NH 3 fuel gas-turbine power generation", *Proceedings of the Combustion Institute*, Vol. 37, No. 4, pp. 4587–4595. doi:10.1016/j.proci.2018.09.012

[110] Khateeb, A. A., Guiberti, T. F., Zhu, X., Younes, M., Jamal, A., Roberts, W. L. (2020). "Stability limits and exhaust NO performances of ammonia-methane-air swirl flames", *Experimental Thermal and Fluid Science*, Vol. 114, pp. 110058. doi:10.1016/j.expthermflusci.2020.110058

[111] Khateeb, A. A., Guiberti, T. F., Zhu, X., Younes, M., Jamal, A., Roberts, W. L. (2020). "Stability limits and NO emissions of technically-premixed ammonia-hydrogen-nitrogen-air swirl flames", *International Journal of Hydrogen Energy*, Vol. 45, No. 41, pp. 22008–22018. doi:10.1016/j.ijhydene.2020.05.236

[112] Xiao, H., Valera-Medina, A., Marsh, R., Bowen, P. J. (2017). "Numerical study assessing various ammonia/methane reaction models for use under gas turbine conditions", *Fuel*, Vol. 196, pp. 344–351. doi:https://doi.org/10.1016/j.fuel.2017.01.095

[113] Xiao, H., Valera-Medina, A., Bowen, P. J. (2017). "Study on premixed combustion characteristics of co-firing ammonia/methane fuels", *Energy*, Vol. 140, pp. 125–135. doi:10.1016/J.ENERGY.2017.08.077

[114] Okafor, E. C., Somarathne, K. D. K. A., Hayakawa, A., Kudo, T., Kurata, O., Iki, N., Kobayashi, H. (2019). "Towards the development of an efficient low-NOx ammonia combustor for a micro gas turbine", *Proceedings of the Combustion Institute*, Vol. 37, No. 4, pp. 4597–4606. doi:10.1016/j.proci.2018.07.083

[115] Wendt, J. O. L., Sternling, C. V. (1974). "Effect of ammonia in gaseous fuels on nitrogen oxide emissions", *Journal of the Air Pollution Control Association*, Vol. 24, pp. 1055–1058. doi:10.1080/00022470.1974.10470013

[116] Law, C. K. (2006). *Combustion Physics*, *Combustion Physics* (Vol. 9780521870), Cambridge University Press. doi:10.1017/CBO9780511754517

[117] Dagaut, P., Glarborg, P., Alzueta, M. U. (2008, February 1). "The oxidation of hydrogen cyanide

and related chemistry", *Progress in Energy and Combustion Science*, Pergamon, pp. 1–46. doi:10.1016/j.pecs.2007.02.004

[118] Takagi, T., Tatsumi, T., Ogasawara, M. (1979). "Nitric oxide formation from fuel nitrogen in staged combustion: Roles of HCN and NHi", *Combustion and Flame*, Vol. 35, No. C, pp. 17–25. doi:10.1016/0010-2180(79)90003-8

[119] Kristensen, P. G., Glarborg, P., Dam-Johansen, K. (1996). "Nitrogen chemistry during burnout in fuel-staged combustion", *Combustion and Flame*, Vol. 107, No. 3, pp. 211–222. doi:10.1016/S0010-2180(96)00081-8

[120] Sowa, F., Otten, B., Kamp, J., Proface, E. (2009). "Advanced technologies for desulphurisation of coke oven gas", *ICC International Conference on Coking Coals and Coke Making: Challenges and Opportunities*, Ranchi, India

[121] Jensen, F. (2019). "Phenol", *ICIS Chemical Business*, Vol. 296, No. 6, pp. 37

[122] Hewlett, S. (2019). "SurveyMonkey By-Product Ammonia Survey", from https://www.surveymonkey.co.uk/r/GZRWDBD

[123] Tata Steel. (n.d.). "Sustainable performance at our Port Talbot site", from https://www.tatasteeleurope.com/construction/sustainability/performance-at-our-sites/port-talbot, accessed 5-10-2021

[124] Siemens. (n.d.). "Siemens Energy Global - Gas Turbines", from https://www.siemens-energy.com/global/en/offerings/power-generation/gas-turbines.html, accessed 28-5-2021

[125] Pugh, D. (2013). *Combustion characterisation of compositionally dynamic steelworks gases*Cardiff UniversityRetrieved from http://orca.cf.ac.uk/58006/

[126] European Commission. (2001). "Integrated Pollution Prevention and Control (IPPC) Best Available Techniques Reference Document on the Production of Iron and Steel"

[127] European Union. (2010). "Directive 2010/75/EU of the European Parliament and of the Council of 24 November 2010 on industrial emissions (integrated pollution prevention and control)", *Official Journal of the European Union*, from https://eur-lex.europa.eu/legal-content/EN/TXT/PDF/?uri=OJ:L:2010:334:FULL&from=EN, accessed 31-5-2018

[128] DVSA. (2017). *In service exhaust emission standards for road vehicles: 19th edition*

[129] Gordon, S., Mcbride, B. J. (1994). *NASA Reference Computer Program for Calculation Complex Chemical Equilibrium Compositions and Applications*

[130] Tian, Z., Li, Y., Zhang, L., Glarborg, P., Qi, F. (2009). "An experimental and kinetic modeling study of premixed NH3/CH4/O2/Ar flames at low pressure", *Combustion and Flame*, Vol. 156, No. 7, pp. 1413–1426. doi:10.1016/j.combustflame.2009.03.005

[131] Xiao, H., Valera-Medina, A., Bowen, P. J. (2017). "Modeling combustion of ammonia/hydrogen fuel blends under gas turbine conditions", *Energy and Fuels*, Vol. 31, pp. 8631–8642. doi:10.1021/acs.energyfuels.7b00709

[132] Mathieu, O., Petersen, E. L. (2015). "Experimental and modeling study on the high-temperature oxidation of Ammonia and related NOx chemistry", *Combustion and Flame*, Vol. 162, No. 3, pp. 554–570. doi:10.1016/j.combustflame.2014.08.022

[133] Ansys Inc. (n.d.). "Chemkin-Pro - Chemical Kinetics Simulation Software", from https://www.ansys.com/products/fluids/ansys-chemkin-pro

[134] Smith, G. P., Golden, D. M., Frenklach, M., Moriarty, N. W., Eiteneer, B., Goldenberg, M., Bowman, C. T., Hanson, R. K., Song, S., Gardiner, Jr., W. C., Lissianski, V. V., Qin, Z. (n.d.). "GRI-Mech 3.0", from http://www.me.berkeley.edu/gri_mech/, accessed 5-2-2020

[135] Skreiberg, Ø., Kilpinen, P., Glarborg, P. (2004). "Ammonia chemistry below 1400 K under fuel-rich conditions in a flow reactor", *Combustion and Flame*, Vol. 136, No. 4, pp. 501–518. doi:10.1016/J.COMBUSTFLAME.2003.12.008

[136] Williams, C. L. (2015). *A Waste Heat Recovery Strategy for An Integrated Steelworks*Retrieved from https://orca.cf.ac.uk/87146/1/Final version PhD Thesis Chris Williams Waste Heat Steelworks.pdf

[137] Miró, L., Gasia, J., Cabeza, L. F. (2016). "Thermal energy storage (TES) for industrial waste heat (IWH) recovery: A review", *Applied Energy*, Vol. 179, pp. 284–301. doi:10.1016/j.apenergy.2016.06.147

[138] Reynolds, W. C. (1986). "The Element Potential Method for Chemical Equilibrium Analysis: Implementation in the Interactive Program STANJAN"

[139] Mei, B., Ma, S., Zhang, Y., Zhang, X., Li, W., Li, Y. (2020). "Exploration on laminar flame propagation of ammonia and syngas mixtures up to 10 atm", *Combustion and Flame*, Vol. 220, pp. 368–377. doi:10.1016/j.combustflame.2020.07.011

[140] Kumar, P., Meyer, T. R. (2013). "Experimental and modeling study of chemical-kinetics mechanisms for H2–NH3–air mixtures in laminar premixed jet flames", *Fuel*, Vol. 108, pp. 166–176. doi:10.1016/J.FUEL.2012.06.103

[141] Miller, J. A., Smooke, M. D., Green, R. M., Kee, R. J. (1983). "Kinetic Modeling of the Oxidation of Ammonia in Flames", *Http://Dx.Doi.Org/10.1080/00102208308923691*, Vol. 34, Nos. 1–6, pp. 149–176. doi:10.1080/00102208308923691

[142] Aspentech. (2021). "Aspen Plus", from https://www.aspentech.com/en/products/engineering/aspen-plus

[143] The Signal Instrument Co. Ltd. (1998). "4000VM Heated Vacuum NOx Analyser Operating Manual", from https://signal-group.com/index.php/legacy-instruments/legacy-chemiluminescence/mchemilun4000vm-2

[144] Kopp, M., Brower, M., Mathieu, O., Petersen, E., Güthe, F. (2012). "CO2* chemiluminescence study at low and elevated pressures", *Applied Physics B: Lasers and Optics*, Vol. 107, No. 3, pp. 529–538. doi:10.1007/S00340-012-5051-4/FIGURES/11

[145] Phantom. (2021). "PCC Software", from https://www.phantomhighspeed.com/resourcesandsupport/phantomresources/pccsoftware

[146] MathWorks. (2021). "MATLAB", from https://uk.mathworks.com/products/matlab.html

[147] Killer, C. (2014). "Abel Inversion Algorithm - File Exchange - MATLAB Central", MATLAB Central File Exchange, from https://www.mathworks.com/matlabcentral/fileexchange/43639-abel-inversion-algorithm, accessed 25-1-2021

[148] Yi, Y., Zhang, R., Wang, L., Yan, J., Zhang, J., Guo, H. (2017). "Plasma-Triggered CH4/NH3 Coupling Reaction for Direct Synthesis of Liquid Nitrogen-Containing Organic Chemicals", *ACS Omega*, Vol. 2, No. 12, pp. 9199–9210. doi:10.1021/acsomega.7b01060

[149] Makida, M., Yamada, H., Kurosawa, Y., Yamamoto, T., Matsuura, K., Hayashi, S. (2006). "Preliminary experimental research to develop a combustor for small class aircraft engine utilizing primary rich combustion approach", *Proceedings of the ASME Turbo Expo* (Vol. 1), American Society of Mechanical Engineers Digital Collection, pp. 835–842. doi:10.1115/GT2006-91156

[150] Canepa, R., Wang, M., Biliyok, C., Satta, A. (2013). "Thermodynamic analysis of combined cycle gas turbine power plant with post-combustion CO_2 capture and exhaust gas recirculation", *Proceedings of the Institution of Mechanical Engineers, Part E: Journal of Process Mechanical Engineering*, Vol. 227, No. 2, pp. 89–105. doi:10.1177/0954408912469165

[151] Dogbe, E. S., Mandegari, M., Görgens, J. F. (2019). "Assessment of the thermodynamic performance improvement of a typical sugar mill through the integration of waste-heat recovery technologies", *Applied Thermal Engineering*, Vol. 158, pp. 113768. doi:10.1016/j.applthermaleng.2019.113768

[152] Liu, Z., Karimi, I. A. (2018). "Simulating combined cycle gas turbine power plants in Aspen HYSYS", *Energy Conversion and Management*, Vol. 171, pp. 1213–1225. doi:10.1016/j.enconman.2018.06.049

[153] Zheng, H., Kaliyan, N., Morey, R. V. (2013). "Aspen Plus simulation of biomass integrated gasification combined cycle systems at corn ethanol plants", *Biomass and Bioenergy*, Vol. 56, pp. 197–210. doi:10.1016/j.biombioe.2013.04.032

[154] Lan, W., Chen, G., Zhu, X., Wang, X., Liu, C., Xu, B. (2018). "Biomass gasification-gas turbine combustion for power generation system model based on ASPEN PLUS", *Science of The Total Environment*, Vols 628–629, pp. 1278–1286. doi:10.1016/j.scitotenv.2018.02.159

[155] Jechura, J. (2015). "Steam Cycle Simulation - Aspen Plus v8.6", from https://inside.mines.edu/~jjechura/EnergyTech/Boiler_Steam_Cycle_AspenPlusv8.pdf

[156] Peng, D. Y., Robinson, D. B. (1976). "A New Two-Constant Equation of State", *Industrial and Engineering Chemistry Fundamentals*, Vol. 15, No. 1, pp. 59–64. doi:10.1021/i160057a011

[157] Boston, J. F., Mathias, P. M. (1980). "Phase equilibria in a third generation process simulator", *Proceedings of the 2nd International Conference on Phase Equilibria and Fluid Properties in the Chemical Process Industries.*, Berlin, pp. 823–849

[158] Tayyeb Javed, M., Irfan, N., Gibbs, B. M. (2007). "Control of combustion-generated nitrogen oxides by selective non-catalytic reduction", *Journal of Environmental Management*, Vol. 83, No. 3, pp. 251–289. doi:10.1016/j.jenvman.2006.03.006

[159] Papa, F., Radulj, D., Karney, B., Robertson, M. (2014). "Pump energy efficiency field testing and benchmarking in Canada", *Journal of Water Supply: Research and Technology - AQUA*, Vol. 63, No. 7, pp. 570–577. doi:10.2166/aqua.2014.095

[160] Razak, A. M. Y. (2007). "Thermodynamics of gas turbine cycles", *Industrial Gas Turbines*, Elsevier, pp. 13–59. doi:10.1533/9781845693404.1.11

[161] Storm, K. (2020). "Combined cycle power plant (1×1) labor estimate", *Industrial Construction Estimating Manual*, Elsevier, pp. 95–159. doi:10.1016/b978-0-12-823362-7.00006-5

[162] Gómez, D. R., Watterson, J. D., Americano, B. B., Ha, C., Marland, G., Matsika, E., Nenge Namayanga, L., Osman-Elasha, B., Kalenga Saka, J. D., Treanton, K., Quadrelli, R. (2006). *Chapter 2: Stationary Combustion 2006 IPCC Guidelines for National Greenhouse Gas Inventories*

[163] Razzaq, R., Li, C., Zhang, S. (2013). "Coke oven gas: availability, properties, purification, and utilization in China", *Fuel*, Vol. 113, pp. 287–299. doi:10.1016/J.FUEL.2013.05.070

APPENDICES

Appendix A.

Appendix A.1 Compositions of the selected blends - numerical modelling

a) Compositions of the 6 selected AV blends - Chapter 3 equilibrium modelling

Blend Description	Mole Fraction in Blend										
	NH_3	CO_2	H_2O	CH_4	H_2	CO	N_2	C_2H_4	C_2H_6	H_2S	HCN
Pure AV	0.32200	0.01700	0.61800	0	0	0	0	0	0	0.02000	0.02300
AV w/ 5% CH_4	0.30590	0.01615	0.58710	0.05000	0	0	0	0	0	0.01900	0.02185
AV w/ 10% CH_4	0.28980	0.01530	0.55620	0.10000	0	0	0	0	0	0.01800	0.02070
AV w/ 5% COG	0.30590	0.01710	0.58710	0.01210	0.03040	0.00350	0.00195	0.00085	0.00025	0.01900	0.02185
AV w/ 10% COG	0.28980	0.01720	0.55620	0.02420	0.06080	0.00700	0.00390	0.00170	0.00050	0.01800	0.02070
AV w/ 15% COG	0.27370	0.01730	0.52530	0.03630	0.09120	0.01050	0.00585	0.00255	0.00075	0.01700	0.01955

b) Compositions of the 5 selected AA blends - all Chapter 3 modelling

Blend Description	Mole Fraction in Blend							
	NH_3	CO_2	CH_4	H_2	CO	N_2	C_2H_4	C_2H_6
Pure AA	1.00000	0	0	0	0	0	0	0
AA w/ 5% CH_4	0.95000	0	0	0	0	0	0	0
AA w/ 5% COG	0.95000	0.00095	0.01210	0.03040	0.00350	0.00195	0.00085	0.00025
AA w/ 10% COG	0.90000	0.00190	0.02420	0.06080	0.00700	0.00390	0.00170	0.00050
AA w/ 15% COG	0.85000	0.00285	0.03630	0.09120	0.01050	0.00585	0.00255	0.00075

c) Normalised (w/o H_2S) AV blends - Chapter 3 kinetic modelling

Blend Description	Mole Fraction in Blend									
	NH_3	CO_2	H_2O	CH_4	H_2	CO	N_2	C_2H_4	C_2H_6	HCN
Pure AV	0.32857	0.01735	0.63061	0	0	0	0	0	0	0.02347
AV w/ 5% CH_4	0.31182	0.01646	0.59847	0.05097	0	0	0	0	0	0.02227
AV w/ 10% CH_4	0.29511	0.01558	0.56640	0.10183	0	0	0	0	0	0.02108
AV w/ 5% COG	0.31182	0.01743	0.59847	0.01233	0.03099	0.00357	0.00199	0.00087	0.00025	0.02227
AV w/ 10% COG	0.29511	0.01752	0.56640	0.02464	0.06191	0.00713	0.00397	0.00173	0.00051	0.02108
AV w/ 15% COG	0.27843	0.01760	0.53438	0.03693	0.09278	0.01068	0.00595	0.00259	0.00076	0.01989

Appendix A.2
Molar compositions of the Chapter 4 experimental blends.

a.) 15% COG blends

Component	Mole Fraction (%)		
	AA:15% COG	HA:15% COG	AV:15% COG
NH_3	85	59.5	32.7
H_2O	0	25.5	52.3
H_2	9.15	9.15	9.15
CH_4	3.9	3.9	3.9
CO	1.05	1.05	1.05
N_2	0.6	0.6	0.6
CO_2	0.3	0.3	0.3

b.) 20% COG blends

Component	Mole Fraction (%)		
	AA:20% COG	HA:20% COG	AV:20% COG
NH_3	80	56	30.8
H_2O	0	24	49.2
H_2	12.2	12.2	12.2
CH_4	5.2	5.2	5.2
CO	1.4	1.4	1.4
N_2	0.8	0.8	0.8
CO_2	0.4	0.4	0.4

c.) 10% COG blends

Component	Mole Fraction (%)		
	AA:10% COG	HA:10% COG	AV:10% COG
NH_3	90	63	34.7
H_2O	0	27	55.3
H_2	6.1	6.1	6.1
CH_4	2.6	2.6	2.6
CO	0.7	0.7	0.7
N_2	0.4	0.4	0.4
CO_2	0.2	0.2	0.2

Appendix A.3
Target mass flows of the Chapter 4 experimental blends (25 kW_{th} LHV).
a.) AA with COG

Composition	Φ	Air (g/s)	NH_3 (g/s)	COG (g/s)
$20\%_{vol}$ COG	1.05	7.715	1.036	0.1424
	1.1	7.364		
	1.15	7.044		
	1.2	6.751		
	1.25	6.481		
	1.3	6.231		
$15\%_{vol}$ COG	1.05	7.730	1.111	0.1078
	1.1	7.378		
	1.15	7.057		
	1.2	6.763		
	1.25	6.493		
	1.3	6.243		
$10\%_{vol}$ COG	1.05	7.745	1.187	0.0725
	1.1	7.392		
	1.15	7.071		
	1.2	6.776		
	1.25	6.505		
	1.3	6.255		

b.) HA (70% NH_3 : 30% H_2O) with COG

Composition	Φ	Air (g/s)	NH_3 (g/s)	COG (g/s)	H_2O (g/s)
$20\%_{vol}$ COG	1	8.082	0.944	0.1853	0.428
	1.05	7.697			
	1.1	7.347			
	1.15	7.028			
	1.2	6.735			
$15\%_{vol}$ COG	1	8.100	1.034	0.1433	0.469
	1.05	7.715			
	1.1	7.364			
	1.15	7.044			
	1.2	6.750			
$10\%_{vol}$ COG	1	8.120	1.131	0.0987	0.513
	1.05	7.733			
	1.1	7.382			
	1.15	7.061			
	1.2	6.767			

c.) AV with COG

Composition	Φ	Air (g/s)	NH_3 (g/s)	COG (g/s)	H_2O (g/s)
$20\%_{vol}$ COG	1 1.05 1.1 1.15	8.061 7.677 7.328 7.010	0.759	0.2709	1.282
$15\%_{vol}$ COG	1 1.05 1.1 1.15	8.084 7.699 7.349 7.030	0.870	0.2193	1.471
$10\%_{vol}$ COG	1 1.05 1.1 1.15	8.111 7.725 7.374 7.053	1.001	0.1588	1.691

Appendix A.4 Averaged operating conditions, reactant flows and undiluted product concentrations for all Chapter 4 test cases.

a.) ANHYDROUS CASES

Composition		Target ϕ	Calculated Φ	Test Point No.	Combust. P (bara)	Inlet T (K)	Primary Zone Air (g/s)	NH_3 (g/s)	H_2O as steam (g/s)	COG (g/s)[1]	Undiluted NO_x[2] (wet) ppm	Undiluted (wet) NO ppm	Undiluted (wet) NH_3 converted[3] - ppm	Undiluted CO_2 (dry) ppm	Undiluted CO (dry) ppm	Undiluted MF H_2O (from Gaseq)
Anhydrous Ammonia (AA)	80% NH3: 20% COG	1.05	1.045	11	1.090	521.1	7.744	1.033	-	0.1424	4067	3919	-164	21339	2783	0.2879
		1.1	1.095	12	1.087	519.2	7.382	1.033	-	0.1424	2997	2958	-70	19792	5165	0.2852
		1.15	1.141	13	1.088	516.7	7.087	1.033	-	0.1424	1874	1937	-89	19224	6756	0.2817
		1.2	1.191	14	1.088	512.6	6.788	1.032	-	0.1424	413	398	15	18468	8020	0.2774
		1.25	1.24	15	1.087	508.0	6.526	1.033	-	0.1424	294	34	863	17367	9123	0.2729
		1.3	1.281	16	1.086	502.8	6.307	1.032	-	0.1424	759	1	1657	16376	10140	0.2690
	85% NH3: 15% COG	1.05	1.042	17	1.089	510.9	7.804	1.112	-	0.1078	3551	3469	-140	18566	2213	0.2917
		1.1	1.096	18	1.088	510.3	7.414	1.111	-	0.1078	2372	2401	-77	16824	3945	0.2883
		1.15	1.139	19	1.088	508.9	7.130	1.110	-	0.1078	1418	1394	-111	15336	4955	0.2847
		1.2	1.187	20	1.088	506.3	6.839	1.110	-	0.1078	213	194	202	14237	5863	0.2802
		1.25	1.246	21	1.087	503.3	6.528	1.113	-	0.1078	557	9	1315	12949	7011	0.2746
		1.3	1.283	22	1.084	501.9	6.336	1.111	-	0.1078	846	11	1889	12047	7570	0.2712
	90% NH3: 10% COG	1.05	1.044	23	1.090	511.8	7.794	1.186	-	0.0725	3124	3049	-176	12998	1435	0.2951
		1.1	1.096	24	1.089	510.1	7.414	1.184	-	0.0725	2029	2028	-125	9992	2543	0.2912
		1.15	1.137	25	1.089	507.4	7.141	1.183	-	0.0725	976	947	-30	7949	3196	0.2875
		1.2	1.195	26	1.088	505.4	6.803	1.184	-	0.0725	216	32	641	6582	3871	0.2820
		1.25	1.24	27	1.086	504.9	6.545	1.183	-	0.0725	641	7	1421	5823	4429	0.2775
		1.3	1.286	28	1.083	502.8	6.316	1.184	-	0.0725	1041	20	2055	4981	4828	0.2730

(1) COG cylinder 1 was used on day 1 and cylinder 2 was used on day 2 (for compositions see Chapter 4).

(2) NO_x readings were invalidated due to measurement issues for NO2 when NH3 at high levels with air dilution (see Chapter 4)

DAY 1 DAY 2

(3) This is the difference between the NO reading when the NH3 converter is on and when it is off. The converter is assumed to have an efficiency of 81%, so actual [NH3] was assumed 23.5% higher than the figures listed here. Negative values result from background NO fluctuations when NH_3 concentrations are low, so can assumed to be zero.

b.) HUMIDIFIED CASES

Composition		Target ϕ	Calculated Φ	Test Point No.	Combust. P (bara)	Inlet T (K)	Primary Zone Air (g/s)	NH_3 (g/s)	H_2O as steam (g/s)	COG (g/s)[1]	Undiluted NO_x[2] (wet) ppm	Undiluted (wet) NO ppm	Undiluted (wet) NH_3 converted[3] - ppm	Undiluted CO_2 (dry) ppm	Undiluted CO (dry) ppm	Undiluted MF H_2O (from Gaseq)
Humidified Ammonia (HA)	80% NH3: 20% COG	1	0.995	7	1.084	523.6	8.128	0.943	0.428	0.1853	4529	4271	-195	28570	333	0.3279
		1.05	1.047	8	1.087	524.1	7.724	0.943	0.428	0.1853	3471	3295	-51	28153	3009	0.3299
		1.1	1.095	9	1.086	521.3	7.381	0.943	0.428	0.1853	2424	2403	-26	26547	5511	0.3282
		1.15	1.142	10	1.086	517.4	7.068	0.942	0.428	0.1853	1122	1184	-62	25389	7380	0.3257
		1.2	1.194	11a	1.086	506.8	6.747	0.939	0.428	0.1853	447	131	445	29153	8975	0.3226
	85% NH3: 15% COG	1	0.994	2a	1.088	520.9	8.123	1.030	0.469	0.1433	3510	3444	-151	29245	212	0.3360
		1.05	1.039	3a	1.087	516.8	7.770	1.029	0.469	0.1433	2866	2749	-121	27569	2059	0.3379
		1.1	1.092	4a	1.086	513.8	7.387	1.029	0.469	0.1433	1643	1726	-68	25966	4040	0.3344
		1.15	1.14	5a	1.085	513.3	7.080	1.029	0.469	0.1433	463	462	45	25819	5293	0.3329
		1.2	1.191	6a	1.086	510.9	6.790	1.031	0.469	0.1433	705	22	1363	26719	6321	0.3296
	90% NH3: 10% COG	1	0.999	7a	1.086	516.5	8.143	1.131	0.512	0.0987	2813	2780	-46	28073	145	0.3448
		1.05	1.043	8a	1.085	515.7	7.796	1.132	0.512	0.0987	2255	2182	-150	27547	1426	0.3454
		1.1	1.096	9a	1.084	515.3	7.412	1.131	0.512	0.0987	1009	993	-41	26846	2683	0.3427
		1.15	1.145	10a	1.083	513.8	7.088	1.129	0.512	0.0987	317	90	641	27194	3503	0.3396
		1.2	-	lift off	-	-	-	-	-	-	-	-	-	-	-	-
Ammonia Vapour (AV)	80% NH3: 20% COG	1	0.996	6	1.085	533.2	8.079	0.758	1.288	0.2715	3074	3108	2	42075	232	0.3985
		1.05	1.047	5	1.086	532.9	7.694	0.759	1.288	0.2715	2505	2499	-114	39475	3376	0.4012
		1.1	1.09	4	1.085	530.8	7.379	0.757	1.288	0.2715	1783	1727	-63	21820	5845	0.4011
		1.15	1.144	3	1.090	529.0	7.022	0.756	1.288	0.2715	717	662	117	41098	8369	0.4001

Repeat

HA	20% COG	1.05	1.043	1a	1.086	521.9	7.759	0.946	0.428	0.1853	3475	3325	-184	33237	3135	0.3300

(1) COG cylinder 1 was used on day 1 and cylinder 2 was used on day 2 (for compositions see Chapter 4).

DAY 1 **DAY 2**

(2) NO_x readings were invalidated due to measurement issues for NO2 when NH3 at high levels with air dilution (see Chapter 4)

(3) This is the difference between the NO reading when the NH3 converter is on and when it is off. The converter is assumed to have an efficiency of 81%, so actual [NH3] was assumed 23.5% higher than the figures listed here. Negative values result from background NO fluctuations when NH_3 concentrations are low, so can assumed to be zero.

Appendix A.5 Chapter 5 Experimental and Chemkin-Pro Model Results (Tian and Okafor mechanisms) for NO and NH3, 15% COG blends (AA and HA) at atmospheric and elevated pressure (wet, dry, and dry - 15% O2).

Blend	Φ	WET (ppm)									
		Atmospheric						6 atm		12 atm	
		NO experimental	NH_3 experimental	NO (Okafor)	NH_3 (Okafor)	NO (Tian)	NH_3 (Tian)	NO (Tian)	NH_3 (Tian)	NO (Tian)	NH_3 (Tian)
15% COG/AA	1.042	3469	-172	3206	0	3032	0	673	0	306	0
	1.096	2401	-95	1777	2	1810	1	282	2	106	1
	1.139	1394	-137	1054	5	1101	1	164	4	59	2
	1.187	194	249	195	201	279	109	99	6	35	5
	1.246	9	1623	21	2615	19	1628	61	11	22	9
	1.283	10	2332	12	4826	7	3074	37	30	20	16
15% COG/HA	0.994	3444	-186	4456	0	3989	0	2013	0	1398	0
	1.039	2749	-149	2927	0	2641	0	837	0	380	0
	1.092	1726	-84	1671	2	1598	0	310	2	120	2
	1.140	462	55	857	13	755	24	137	4	62	4
	1.191	22	1682	116	849	121	727	57	17	37	9

Blend	Φ	Water Mole Fraction				
		experimental (Gaseq)	~1 atm (O)	~1 atm (T)	~6 atm (T)	~12 atm (T)
15% COG/AA	1.042	0.2917	0.2918	0.292	0.2945	0.2947
	1.096	0.2883	0.2876	0.2876	0.2897	0.29
	1.139	0.2847	0.2839	0.2839	0.2855	0.2858
	1.187	0.2802	0.2798	0.2797	0.2807	0.2809
	1.246	0.2746	0.2751	0.2744	0.2747	0.275
	1.283	0.2712	0.2725	0.2712	0.2711	0.2714
15% COG/HA	0.994	0.3360	0.3383	0.3388	0.339	0.3387
	1.039	0.3379	0.3368	0.3371	0.3392	0.3396
	1.092	0.3344	0.3343	0.3344	0.3363	0.3366
	1.140	0.3329	0.3316	0.3318	0.3331	0.3334
	1.191	0.3296	0.3293	0.329	0.3295	0.3298

Blend	Φ	DRY (ppm)									
		Atmospheric						6 atm		12 atm	
		NO experimental	NH_3 experimental	NO (Okafor)	NH_3 (Okafor)	NO (Tian)	NH_3 (Tian)	NO (Tian)	NH_3 (Tian)	NO (Tian)	NH_3 (Tian)
15% COG/AA	1.042	4898	-243	4527	1	4282	0	954	1	434	0
	1.096	3374	-133	2494	3	2541	1	397	3	149	1
	1.139	1949	-192	1472	7	1537	1	230	6	83	3
	1.187	270	346	271	279	387	151	138	8	49	7
	1.246	12	2238	29	3607	26	2244	84	15	30	12
	1.283	14	3200	16	6634	10	4218	51	41	27	22
15% COG/HA	0.994	5187	-280	6734	0	6033	0	3045	0	2114	0
	1.039	4152	-225	4413	0	3984	0	1267	1	575	1
	1.092	2593	-126	2510	3	2401	1	467	3	181	3
	1.140	693	82	1282	19	1130	36	205	6	93	6
	1.191	33	2509	173	1266	180	1083	85	25	55	13

Blend	Φ	DRY, 15% O2 (ppm)									
		Atmospheric						6 atm		12 atm	
		NO experimental	NH_3 experimental	NO (Okafor)	NH_3 (Okafor)	NO (Tian)	NH_3 (Tian)	NO (Tian)	NH_3 (Tian)	NO (Tian)	NH_3 (Tian)
15% COG/AA	1.042	1383	-69	1278	0	1209	0	269	0	122	0
	1.096	952	-38	704	1	717	0	112	1	42	0
	1.139	550	-54	416	2	434	0	65	2	23	1
	1.187	76	98	76	79	109	43	39	2	14	2
	1.246	4	632	8	1018	7	633	24	4	9	4
	1.283	4	903	5	1873	3	1191	14	12	8	6
15% COG/HA	0.994	1464	-79	1901	0	1703	0	860	0	597	0
	1.039	1172	-64	1246	0	1125	0	358	0	162	0
	1.092	732	-36	709	1	678	0	132	1	51	1
	1.140	196	23	362	5	319	10	58	2	26	2
	1.191	9	708	49	357	51	306	24	7	16	4

Appendix B.

Appendix B.1a – Chapter 6 mass flowrates (g/s) of 15% COG/AA blend for staging at atmospheric pressure.

Composition	Φ	Primary Air (g/s)	NH_3 (g/s)	COG (g/s)
85% NH_3: 15% COG	1.15	7.073	1.1111	0.1078
	1.16	7.012		
	1.17	6.952		
	1.18	6.893		
	1.19	6.835		
	1.20	6.778		
	1.21	6.722		
	1.22	6.667		
	1.23	6.613		
	1.24	6.559		
	1.25	6.507		

		Air staging (Φ_{gl} = 0.7)		Air/N_2 Φ_{gl} = 0.8			Air/N_2 Φ_{gl} = 0.9			Air/N_2 Φ_{gl} = 0.95		
Composition	Φ	Total air for Φ_{gl} 0.7	Air into 2nd stage	Total air for Φ_{gl} 0.8	Air into 2nd stage	N_2 into 2nd stage	Total air for Φ_{gl} 0.9	Air into 2nd stage	N_2 into 2nd stage	Total air for Φ_{gl} 0.95	Air into 2nd stage	N_2 into 2nd stage
85% NH_3 : 15% COG	1.15	11.619	4.547	10.167	3.094	1.418	9.037	1.965	2.521	8.562	1.489	2.985
	1.16	11.619	4.608	10.167	3.155	1.418	9.037	2.026	2.521	8.562	1.550	2.985
	1.17	11.619	4.668	10.167	3.215	1.418	9.037	2.086	2.521	8.562	1.610	2.985
	1.18	11.619	4.727	10.167	3.274	1.418	9.037	2.144	2.521	8.562	1.669	2.985
	1.19	11.619	4.784	10.167	3.332	1.418	9.037	2.202	2.521	8.562	1.727	2.985
	1.20	11.619	4.841	10.167	3.389	1.418	9.037	2.259	2.521	8.562	1.784	2.985
	1.21	11.619	4.897	10.167	3.445	1.418	9.037	2.315	2.521	8.562	1.840	2.985
	1.22	11.619	4.953	10.167	3.500	1.418	9.037	2.370	2.521	8.562	1.895	2.985
	1.23	11.619	5.007	10.167	3.554	1.418	9.037	2.425	2.521	8.562	1.949	2.985
	1.24	11.619	5.060	10.167	3.608	1.418	9.037	2.478	2.521	8.562	2.002	2.985
	1.25	11.619	5.113	10.167	3.660	1.418	9.037	2.530	2.521	8.562	2.055	2.985

Appendix B.1b – Chapter 6 mass flowrates (g/s) of 15% COG/HA blend for staging at atmospheric pressure.

Composition	Φ	Primary Air (g/s)	NH_3 (g/s)	COG (g/s)	H2O (g/s)
85% HA: 15% COG	1.10	7.380	1.0344	0.1433	0.469
	1.11	7.313			
	1.12	7.248			
	1.13	7.184			
	1.14	7.121			
	1.15	7.059			
	1.16	6.998			
	1.17	6.938			
	1.18	6.879			
	1.19	6.822			
	1.20	6.765			
	1.21	6.709			
	1.22	6.654			

		Air staging (Φ_{gl} = 0.7)		Air/N_2 Φ_{gl} = 0.8			Air/N_2 Φ_{gl} = 0.9			Air/N_2 Φ_{gl} = 0.95		
Composition	Φ	Total air for Φ_{gl} 0.7	Air into 2nd stage	Total air for Φ_{gl} 0.8	Air into 2nd stage	N_2 into 2nd stage	Total air for Φ_{gl} 0.9	Air into 2nd stage	N_2 into 2nd stage	Total air for Φ_{gl} 0.95	Air into 2nd stage	N_2 into 2nd stage
85% HA : 15% COG	1.10	11.597	4.217	10.147	2.767	1.415	9.020	1.640	2.516	8.545	1.165	2.979
	1.11	11.597	4.284	10.147	2.834	1.415	9.020	1.706	2.516	8.545	1.232	2.979
	1.12	11.597	4.349	10.147	2.899	1.415	9.020	1.772	2.516	8.545	1.297	2.979
	1.13	11.597	4.413	10.147	2.963	1.415	9.020	1.836	2.516	8.545	1.361	2.979
	1.14	11.597	4.476	10.147	3.026	1.415	9.020	1.899	2.516	8.545	1.424	2.979
	1.15	11.597	4.538	10.147	3.088	1.415	9.020	1.961	2.516	8.545	1.486	2.979
	1.16	11.597	4.599	10.147	3.149	1.415	9.020	2.022	2.516	8.545	1.547	2.979
	1.17	11.597	4.659	10.147	3.209	1.415	9.020	2.081	2.516	8.545	1.607	2.979
	1.18	11.597	4.717	10.147	3.268	1.415	9.020	2.140	2.516	8.545	1.666	2.979
	1.19	11.597	4.775	10.147	3.326	1.415	9.020	2.198	2.516	8.545	1.723	2.979
	1.20	11.597	4.832	10.147	3.382	1.415	9.020	2.255	2.516	8.545	1.780	2.979

Appendix B.2
Chapter 6 staging tube design - Calculating approximate velocity flows along the quartz tube and through the dilution holes.

The volumetric flowrates and velocities of the product gases from the primary stage compared with those of the air entering the staging holes.

Exiting the primary stage:

Using 15% COG/AA at Φ = 1.2

Between approximately 15 and 25 cm from the burner face (assuming a post flame zone starting at 10 cm from the burner face) the average molecular mass of the blend is modelled to be 24.096 ± 0.0005. The mass flowrate is 8.056 g/s and therefore molar flow within the tube and prior to staging is ~ 0.334 mol/s. For the modelled temperature of ~1800 K and assuming ideal gas behaviour, each mole occupies ~ 0.137 m^3, thus volumetric flow is calculated to be ~ 0.046 m^3/s.

Using 15% COG/HA at Φ = 1.2

As for the above case: average molecular mass = 23.744, mass flowrate = 8.43 g/s, molar flow in tube = ~ 0.355 mol/s. Temperature ~ 1700 K, ~ 0.130 m^3/mol, thus volumetric flow ~ 0.046 m^3/s.

Calculating velocity in the tube

The cross-sectional area of the quartz tube is 7,854 mm^2 (0.007854 m^2). Volumetric flow ~ 0.046 m3/s for both cases. Velocity = ~5.9 m/s.

Entering through the holes:

The mass flow of staged air/N_2 across all blends totals ~5 g/s. The average molecular mass of air is 28.963 g, so molar flow is ~ 0.173 mol/s. One mole of air at 550 K occupies 0.042 m^3, so volumetric flow for the staged air/N_2 through the staging holes is ~0.0073 m^3/s.

Volumetric flows after the staging increase by ~ 16%.

With four Ø20 mm holes total area = 1,257 mm^2 (0.001257 m^2).

Velocity through holes = ~5.8 m/s.

Appendix B.3
Composition of the COG cylinders used in Chapter 6 experimental campaign.

COG Compositions	Mole Fraction				
	CO2	CH4	H2	CO	N2
Simplified COG	0.02	0.26	0.61	0.07	0.04
Cylinder ending 2700	0.02003	0.2591	0.61164	0.0693	0.03989
Cylinder ending 2684	0.02005	0.2584	0.61197	0.06994	0.03962
Cylinder ending 2287	0.01982	0.2592	0.61222	0.06906	0.03967

Uncertainty of ± 0.5%$_{molar}$ (relative) for all components except H_2 (± 0.1%$_{molar}$ rel).

Appendix B.4

Chapter 6: Primary zone optimisation at atmospheric P - averaged reactant flowrates, important operating conditions and emissions results.

Blend	Target Φ	Average calculated Φ	Test point No.	Primary inlet T (K)	Combust. P (bara)	Average Prim zone air (g/s)	Average NH_3 (g/s)	Average H_2O as steam (g/s)	Average COG (g/s)	Average NO (ppm) wet	Average NH_3 (ppm) wet[1]	Average undiluted fraction H_2O[2]
15% COG/AA (COG cylinder 2700)	1.18	1.167	13	533.2	1.122	6.893	1.096	0	0.1078	1169	0	0.2819
	1.19	1.176	12	534.6	1.122	6.835	1.095	0	0.1078	931	12	0.2810
	1.2	1.193	11	533.5	1.122	6.778	1.102	0	0.1078	577	104	0.2796
	1.21	1.200	10	534.2	1.122	6.722	1.100	0	0.1078	426	250	0.2789
	1.22	1.213	9	533.8	1.121	6.667	1.103	0	0.1078	253	378	0.2777
	1.23	1.222	8	533.7	1.121	6.613	1.102	0	0.1078	126	704	0.2768
	1.24	1.228	7	533.1	1.121	6.559	1.097	0	0.1078	93	857	0.2763
	1.25	1.244	6	534.1	1.121	6.511	1.105	0	0.1078	32	1339	0.2748
15% COG/HA (COG cylinder 2287)	1.15	1.1485	32 and 41	532.4	1.118	7.060	1.031	0.4693	0.1433	943	71	0.3323
	1.16	1.158	31 and 40	533.0	1.118	6.998	1.030	0.4692	0.1433	715	27	0.3317
	1.17	1.1685	30 and 39	532.2	1.117	6.939	1.031	0.4694	0.1433	416	269	0.3310
	1.18	1.176	29 and 38	532.8	1.117	6.879	1.028	0.4692	0.1433	338	343	0.3306
	1.19	1.19075	33 and 37	530.9	1.117	6.822	1.034	0.4694	0.1433	129	733	0.3295
	1.2	1.1985	34 and 36	531.9	1.117	6.770	1.033	0.4695	0.1433	79	965	0.3290
	1.21	1.20975	35	531.9	1.117	6.709	1.033	0.4695	0.1433	41	1735	0.3283

For conciseness (and because values varied little) average Φ, H_2O product and flowrates are given for each test point. However, for precision, the flowrates specific to each individual measure of NO and NH3 were used for plotting (hence slight shift in Φ between NO and NH_3 measures on plots).

1 This measurement is the value after factoring in the conversion efficiency of 81% in the NH_3 converter.

2 As calculated in Gaseq using experimental data.

Appendix B.5
Chapter 6: 15% COG/AA - primary zone at elevated P (1.3 bara) - averaged reactant flowrates, important operating conditions and emissions results.

Blend	Target Φ	Average calculated Φ	Test point No.	Primary inlet T (K)	Combust. P (bara)	Average Prim zone air (g/s)*	Average NH_3 (g/s)	Average H_2O as steam (g/s)	Average COG (g/s)	Average NO (ppm) wet	Average NH_3 (ppm) wet[1]	Average undiluted fraction H_2O[2]
15% COG/AA (COG cylinder 2287)	1.18	1.179	22 & 28	535.6	1.312	8.050	1.294	0	0.1259	678	5	0.2810
	1.2	1.196	21 & 27	533.0	1.311	7.920	1.292	0	0.1259	411	173	0.2788
	1.22	1.218	20 & 26	531.7	1.311	7.790	1.295	0	0.1259	120	605	0.2773
	1.24	1.239	23 &25	533.0	1.311	7.660	1.295	0	0.1259	40	1280	0.2751
	1.26	1.255	24	530.9	1.310	7.540	1.291	0	0.1259	11	1803	0.2736

* The primary zone mass flows are accurate to 3 decimal places, it is pure coincidence that the final decimal place is consistently zero.

For conciseness (and because values varied little) average Φ, H_2O product and flowrates are given for each test point. However, for precision, the flowrates specific to each individual measure of NO and NH_3 were used for plotting (hence slight shift in Φ between NO and NH_3 measures on

1 This measurement is the value after factoring in the conversion efficiency of 81% in the NH_3 converter.

2 As calculated in Gaseq using experimental data.

Appendix B.6: Chapter 6 staged combustion at atmospheric pressure - staging holes 25 cm downstream of burner face.

Variation of Φ_{gl} (Φ_{prim} fixed) - averaged reactant flowrates, important operating conditions and emissions results.

Blend	Test point No.	Target Φ_{gl}	Average calculated Φ_{gl}	Target Φ_{prim}	Average calculated Φ_{prim}	Averaged primary inlet T (K)	Averaged secondary inlet T (K)	Averaged Combust. P (bara)	Average Prim zone air (g/s)	Average Sec zone air (g/s)	Average Sec zone N_2 (g/s)
15% COG/AA (COG cylinder 2287)	44 & 50	0.70	0.698	1.22	1.216	535.3	557.2	1.113	6.671	4.952	0.000
	45 & 49	0.80	0.798	1.22	1.217	534.0	563.4	1.114	6.671	3.500	1.379
	46 & 48	0.90	0.896	1.22	1.215	536.2	563.9	1.113	6.670	2.370	2.512
	47	0.95	0.944	1.22	1.212	535.2	561.5	1.113	6.671	1.900	2.972
15% COG/HA (COG cylinder 2684)	57	0.7	0.701	1.18	1.171	531.6	554.1	1.124	6.879	4.717	0.000
	58	0.8	0.799	1.18	1.168	531.1	559.6	1.125	6.879	3.268	1.432
	59	0.9	0.897	1.18	1.166	532.9	564.0	1.125	6.879	2.140	2.551
	60	0.95	0.947	1.18	1.166	534.6	567.7	1.125	6.879	1.665	3.013

Continued:

Blend	Test point No.	Target Φ_{gl}	Average NH_3 (g/s)	Average H_2O as steam (g/s)	Average COG (g/s)	Average O_2 in sample (ppm)*	Average NO (ppm) wet	Average NO_2 (ppm) wet	Average NH_3 (ppm) wet(1)	Average CO (ppm) wet	Average undiluted fraction H_2O(2)
15% COG/AA (COG cylinder 2287)	44 & 50	0.70	1.106	0	0.1078	67936	346	13	1	0	0.2244
	45 & 49	0.80	1.108	0	0.1078	39738	288	31	7	1	0.2247
	46 & 48	0.90	1.105	0	0.1078	18689	306	18	15	3	0.2238
	47	0.95	1.102	0	0.1078	10231	302	13	39	8	0.2235
15% COG/HA (COG cylinder 2684)	57	0.7	1.035	0.469	0.1433	67188	411	91	10	3	0.2618
	58	0.8	1.032	0.469	0.1433	39590	393	23	-7	1	0.2610
	59	0.9	1.030	0.469	0.1433	18629	366	34	21	2	0.2603
	60	0.95	1.030	0.469	0.1433	9768	383	22	31	6	0.2604

* Background O_2 was 207299 ppm for the AA blend and 208073 ppm for the HA blend (tested the day after).

For conciseness (and because values varied little) average Φ, H_2O product and flowrates are given for each test case. However, for precision, the measures specific to each individual measure of NO and NH_3 were used for plotting (hence slight shift in Φ between NO and NH_3 measures on plots).

1. This measurement is the value after factoring in the conversion efficiency of 81% in the NH_3 converter.
2. As calculated in Gaseq using experimental data.

Appendix B.7: Chapter 6 staged combustion at atmospheric pressure staging holes 15 cm downstream of burner face. Variation of Φ_{prim} (Φ_{gl} fixed at 0.7) - averaged reactant flowrates, important operating conditions and emissions results.

Blend	Test point No.	Target Φ_{prim}	Average calculated Φ_{prim}	Average calculated Φ_{gl}	Averaged primary inlet T (K)	Averaged secondary inlet T (K)	Averaged Combust. P (bara)	Average Prim zone air (g/s)	Average Sec zone air (g/s)
15% COG/AA (COG cylinder 2684)	64	1.22	1.214	0.697	531.8	540.4	1.128	6.666	4.953
	65	1.23	1.227	0.6985	532.6	544.6	1.127	6.613	5.007
	66	1.24	1.235	0.6975	532.3	548.4	1.127	6.559	5.060
	67	1.25	1.246	0.698	530.7	551.0	1.127	6.506	5.113
15% COG/HA (COG cylinder 2684)	71	1.18	1.168	0.693	532.6	560.8	1.127	6.880	4.720
	70	1.19	1.185	0.697	532.4	559.9	1.127	6.821	4.779
	69	1.2	1.191	0.696	530.5	556.0	1.127	6.770	4.829
	68	1.21	1.207	0.698	528.4	556.0	1.127	6.709	4.888

Continued:

Blend	Test point No.	Average NH_3 (g/s)	Average H_2O as steam (g/s)	Average COG (g/s)	Average O_2 in sample (ppm)*	Average NO (ppm) wet	Average NO_2 (ppm) wet	Average NH_3 (ppm) wet(1)	Average CO (ppm) wet	Average undiluted fraction H_2O(2)
15% COG/AA (COG cylinder 2684)	64	1.104	0	0.1078	68125	456	39	-9	0	0.2242
	65	1.108	0	0.1078	67627	439	44	12	0	0.2247
	66	1.105	0	0.1078	67816	432	46	34	1	0.2243
	67	1.106	0	0.1078	67719	432	56	21	0	0.2245
15% COG/HA (COG cylinder 2684)	71	1.021	0.469	0.1433	68881	612	32	-3	1	0.2598
	70	1.028	0.469	0.1433	68230	529	34	8	0	0.2607
	69	1.025	0.469	0.1433	68911	508	43	9	0	0.2604
	68	1.030	0.469	0.1433	68284	520	29	35	0	0.2611

* Background O_2 was 208411 ppm for both blends.

For conciseness (and because values varied little) average Φ, H_2O product and flowrates are given for each test case. However, for precision, the measures specific to each individual measure of NO and NH_3 were used for plotting (hence slight shift in Φ between NO and NH_3 measures on plots).

1. This measurement is the value after factoring in the conversion efficiency of 81% in the NH_3 converter.
2. As calculated in Gaseq using experimental data.

Appendix B.8: Chapter 6 staged combustion at 2 different locations for 15% COG/AA blend (COG cylinder 2684) at elevated pressure (~1.3 bara)
Φ_{prim} ~ 1.2, Φ_{gl} ~ 0.7 - averaged reactant flowrates, important operating conditions and emissions results.

Staging location (cm downstream of burner face)	Test point No.	Background O_2 (ppm)	Average calculated Φ_{prim}	Average calculated Φ_{gl}	Averaged primary inlet T (K)	Averaged secondary inlet T (K)	Averaged Combust. P (bara)	Average Prim zone air (g/s)	Average Sec zone air (g/s)
25	55	208073	1.191	0.694	533.2	547.9	1.305	7.920	5.660
15	63	208411	1.187	0.693	538.0	533.7	1.304	7.920	5.656

Continued:

Staging Location (cm downstream of burner face)	Test point No.	Average NH_3 (g/s)	Average COG (g/s)	Average O_2 in sample (ppm)	Average NO (ppm) wet	Average NO_2 (ppm) wet	Average NH_3 (ppm) wet[(1)]	Average CO (ppm) wet	Average undiluted fraction H_2O[(2)]
25	55	1.286	0.1259	68813	545	N/A	-28	3	0.2236
15	63	1.281	0.1259	69105	540	18	17	0	0.2231

For conciseness (and because values varied little) average Φ, H_2O product and flowrates are given for each test case. However, for precision, the measures specific to each individual measure of NO and NH_3 were used for plotting (hence slight shift in Φ between NO and NH_3 measures on plots).

1. This measurement is the value after factoring in the conversion efficiency of 81% in the NH_3 converter.
2. As calculated in Gaseq using experimental data.

Appendix C.

Image Processing Code

C.1 Obtaining temporally averaged unfiltered background image

Program: BG_code.m

```
clear all
%Open a dialogue box for creating a cell 'FileList' containing all file names
[FileList, path] = uigetfile ('*.tif', 'Select your Background Images', 'MultiSelect', 'on');
%Picking the first file name 'Filename' from the 'FileList'
FileName = fullfile(path, FileList{1});
%Creating a matrix I from the 1st image file
[I, cmap] = imread(FileName);
%Finding the dimension variables for the new matrix I
[rows, columns] = size(I);
% Creating a zero matrix to hold average image data in later on
UHoldmat = zeros(rows,columns);
%Finding out how many files have been downloaded to 'FileList'
numfiles = length (FileList);
%Creating a cell into which the image data for each image can be written
ImageData = cell(1,numfiles);
%Creating a variable 'TifFilies' pointing to all tif files in the current
%directory
TifFiles = dir('*.tif');
%Filling the cell 'ImageData' with the data for each image
for k = 1:numfiles
   ImageData{k}=imread(TifFiles(k).name);
end
%Sequentially processing the data from each image file to get an unfiltered
%image which is a sum of all entered images
for j = 1:numfiles
   %Creating a matrix for the current file
   A = ImageData{j};
   %Converting the data to double format for mathmatical manipulation
   Adoub = double(A);
   %Adding each iteration of j to the previous data to give a sum of all
   %images in matrix, unfiltered
   UHoldmat = UHoldmat + Adoub;
end
%Finding the average intensity unfiltered background image
UAvBGImg = UHoldmat./numfiles;
%Displaying unfiltered background image
f1 = figure('name','Unfiltered');
imshow(UAvBGImg,cmap)
save('AvBGImg.mat','UAvBGImg')
```

Appendix C.2 – Obtaining temporally averaged filtered test point image corrected for background

Program: averaging_code.m

```
clear all
%Open a dialogue box for creating a cell 'FileList' containing all file names
[FileList, path] = uigetfile ('*.tif', 'Select your Test Images', 'MultiSelect', 'on');
%Picking the first file name 'Filename' from the 'FileList'
FileName = fullfile(path, FileList{1});
%Creating a matrix I from the 1st image file
[I, cmap] = imread(FileName);
%Finding the dimension variables for the new matrix I
[rows, columns] = size(I);
% Creating a zero matrix to hold average image data in later on
Holdmat = zeros(rows,columns);
%Loading matrix containing background image file from another folder
[BGImgFile,folder] = uigetfile('*.mat','Select your Background Image File');
UBGFileLoc = fullfile(folder, BGImgFile);
UBGFile = load(UBGFileLoc);
%Changing format of image file from struct to occupying cell 1, to a matrix
UBGFileCell = struct2cell(UBGFile);
UBGImgCell = UBGFileCell(1);
UBGImg = cell2mat(UBGImgCell);
%Finding out how many files have been downloaded to 'FileList'
numfiles = length (FileList);
%Creating a cell into which the image data for each image can be written
ImageData = cell(1,numfiles);
%Creating a variable 'TifFilies' pointing to all tif files in the current
%directory
TifFiles = dir('*.tif');
%Filling the cell ImageData with the data for each image
for k = 1:numfiles
   ImageData{k}=imread(TifFiles(k).name);
end
%Sequentially processing the data from each image file
for j = 1:numfiles
   %Creating a matrix for the current file
   A = ImageData{j};
   %Converting the data to double format for mathmatical manipulation
   Adoub = double(A);
   %Adding each iteration of j to the previous data to give a sum of all
   %images matrix
   Holdmat = Holdmat + Adoub;
end
%Finding the average unfiltered image and its sum intensity value.
AvImg = Holdmat./numfiles;
```

```
%Correcting Average unfiltered image for background
AvUImgCorBG = AvImg - UBGImg;
%Filtering the above image, median 3x3 filter with symmetrical padding at
%border
AvFImgCorBG = medfilt2(AvUImgCorBG, 'symmetric');
imshow(AvFImgCorBG,cmap)
%Saving filtered average images corrected for background
save('AvTP6OH.mat','AvFImgCorBG','cmap')
```

Appendix C.3 – Abel inversion code for cropping and batch processing images

Program code: abeldeconv_bottom.m

```
%%%%%%%%%%%%%%%%%%%%%%%%%%%%%%%%%%%%
%R=mm? CentXPIX=?, WhichWay=?     %
%Y direction refers to direction once image is rotated vertically as this
%is the normal orientation for Abel deconvolution image processing%
Y_in_mm=100.15              %
X_in_mm= 90.4               %
R=X_in_mm/2                 %
%CentXPix is the pixel for the burner centreline AFTER image is cropped%
CentXPix=213                %
%WhichWay is 2 for top (i.e. LHS when vertical) and 1 for bottom (RHS)%
WhichWay=1                  %
Numb_of_y_pixels=474        %
Numb_of_x_pixels=428        %
%%%%%%%%%%%%%%%%%%%%%%%%%%%%%%%%%%%%%%%%%%%%%%%%%%%%%%%%%%%%%%%%%%%%%%%
Y = linspace(Y_in_mm, 0, Numb_of_y_pixels)%
X = linspace(-R, R, Numb_of_x_pixels)     %
%%%%%%%%%%%%%%%%%%%%%%%%%%%%%%%%%%%%%%%%%%%%%%%%%%%%%%%%%%%%%%%%%%%%%%%
%load image .mat for each image in turn, rotate (anti-clockwise) to vertical, process %
%HalfAbel and then rotate anticlockwise 270degrees (3x90) back to original
orientation).%
%%%%%%%%%%%%%%%%%%%%%%%%%%%%%%%%%%%%%%%%%%%%%%%%%%%%%%%%%%%%%%%%%%%%%%%
Av1crop=Av1(62:488,120:593);
Image=rot90(Av1crop)                        %
[Abel1vert] = HalfAbel(Image, R, CentXPix, WhichWay) %
Abel1horz= rot90(Abel1vert,3); %
%%%%%%%%%%%%%%%%%%%%%%%%%%%%%%%%%%%%%%%%%%%%%%%%%%%%%%%%%%%%%%%%%%%%%%%
Av2crop=Av2(62:488,120:593);
Image=rot90(Av2crop) ;                      %
[Abel2vert] = HalfAbel(Image, R, CentXPix, WhichWay); %
Abel2horz= rot90(Abel2vert,3);    %
%%%%%%%%%%%%%%%%%%%%%%%%%%%%%%%%%%%%%%%%%%%%%%%%%%%%%%%%%%%%%%%%%%%%%%%
%Save all images post Abel processing to matrix AbelImgsHorz.mat)%
%%%%%%%%%%%%%%%%%%%%%%%%%%%%%%%%%%%%%%%%%%%%%%%%%%%%%%%%%%%%%%%%%%%%%%%
save Abel_bottom_horz.mat
```

Appendix D.

Appendix D.1 - A brief introduction to using Aspen Plus.

The Aspen Plus program has a number of templates from which to select. In this instance, the 'gas processing' template was selected (with metric units).

There are two main interface modes within the Aspen Plus program, 'Properties' and 'Simulation'. The properties mode is where all the chemical species involved in the simulation are searched and selected from within the program's database, providing the simulation with the relevant species properties from which to make its calculations. This includes all important reactant and product species (e.g. NO_x and argon). It is also where the property method, describing the rules governing the behaviour of these species under specified conditions (e.g. temperature and pressure) is selected. Selection of an appropriate property method is facilitated by a decision tree in the Aspen help function.

The simulation mode is a window into which various 'blocks' and 'streams' can be placed and connected, to represent the process flow diagram of the system being modelled. The blocks represent the items of equipment and the streams represent the flows of material or energy into and out of the blocks. The settings for each block or stream can be manually directed, however, in a steady-state process, it is only the initial conditions for the cycle inlets (e.g. ambient temperature), equipment specifications (e.g. compressor discharge pressure) and necessary equipment performance variables (e.g. isentropic efficiency) which are set manually. The software then calculates the temperatures achieved, vapour fractions, work done, etc. FORTRAN coding is used to refer calculated variables automatically from one part of a cycle to another to take account of inherent interdependency. For example, stoichiometric air requirements are dictated by fuel composition, so if air to fuel values are coded for (using FORTRAN), the mass flows of fuel can be referred to an air 'CALCULATOR', which updates the air flow as required. If the simulation is designed correctly, in keeping with process engineering principles, it is able to calculate all downstream variables and iterate to accurate steady-state results.

Appendix D.2 - The Peng-Robinson Equation of State.

The Peng-Robinson equation of state is defined as follows:

$$P = \frac{RT}{\upsilon - b} - \frac{a\alpha}{\upsilon^2 + 2b\upsilon - b^2}$$

Where P = pressure, R = universal gas constant, T = absolute temperature, υ = molar volume. Values α (attraction parameter) and b (Van der Waals covolume) are substance specific constants obtained using the universal gas constant, the critical temperature (T_c) and the critical pressure (P_c) for the substance. Above the critical temperature, no amount of additional pressure will liquefy the vapour. The α term is a scaling factor. The equations for α, b and α are shown below.

Attraction parameter (α) equation:

$$a = \frac{0.45724\, R^2 {T_c}^2}{P_c}$$

Van der Waals covolume (b) equation:

$$b = \frac{0.07780 RT_c}{P_c}$$

Scaling factor α equation:

$$\alpha = \left(1 + \kappa \left(1 - {T_r}^{0.5}\right)\right)^2$$

Where $T_r = (T/T_c)$ and κ is defined as follows:

$$\kappa = 0.37464 + 1.54226\omega + 0.26992\omega^2$$

The term ω is the acentric factor (measure of the non-sphericity of molecules). As it increases, the vapour curve is "pulled" down, resulting in higher boiling points.

Appendix E.

Aspen results - material, heat and work streams, Φ_{gl} and efficiency values for equipment, cycles and the (overall) combined cycle.

Appendix E.1 - 15% COG/AA blend, operating pressure 8 atm.

Fuel Gas System:		
Fuel Flow Rate	0.0080	kmol/sec
Fuel Flow Rate	0.1273	kg/sec
HHV (fuel mix)	24,594.6	kJ/kg
LHV (fuel mix)	20,597.8	kJ/kg
Flue Gas:		
Outlet Temperature (1) small	393.0	K
Outlet Temperature (2) large	393.0	K
Turbine exhaust to recuperator	12.40	%
Steam System:		
Circulation Rate	0.4666	kg/sec
Air system:		
Total air	2.780	kg/sec
Secondary air	2.070	kg/sec
Primary air	0.710	kg/sec
Global Φ	0.307	
Percentage of air as secondary	74.4	%

Energy Flows:		
Fuel HHV Flow	3,130.49	kJ/sec
Fuel LHV Flow	2,621.76	kJ/sec
Boiler Duty	1,226.92	kJ/sec
Condenser Duty	853.81	kJ/sec
COG Compressor Power	8.99	kW
Air Compressor Power	736.62	kW
Condensate Pump Power	6.15	kW
Steam Turbine Power	367.59	kW
Gas Turbine Power	1,623.24	kW

Equipment Efficiencies:	Isentropic	Mechanical
COG Compressor	0.88	0.99
Air Compressor	0.88	0.99
Condensate Pump	0.80	0.95
Gas Turbine	0.90	0.99
Steam Turbine	0.75	0.97

Efficiency Values:	
GT Cycle (HHV Based)	67.23 %
GT Cycle (LHV Based)	80.27 %
(turbine exhaust heat incl.)	
Steam Cycle	29.46 %
Overall (HHV Based)	39.58 %
Overall (LHV Based)	47.26 %
Power Out - Power In	1,239.07 kW
Efficiency Brayton Cycle (LHV)	33.47 %
(no use of turbine exhaust)	

Appendix E.2 - 15% COG/AA blend, operating pressure 12 atm.

Fuel Gas System:		
Fuel Flow Rate	0.0080	kmol/sec
Fuel Flow Rate	0.1273	kg/sec
HHV (fuel mix)	24,594.6	kJ/kg
LHV (fuel mix)	20,597.8	kJ/kg
Flue Gas:		
Outlet Temperature (1) small	411.3	K
Outlet Temperature (2) large	411.3	K
Turbine exhaust to recuperator	10.20	%
Steam System:		
Circulation Rate	0.4026	kg/sec
Air system:		
Total air	2.975	kg/sec
Secondary air	2.265	kg/sec
Primary air	0.710	kg/sec
Global Φ	0.287	
Percentage of air as secondary	76.1	%

Energy Flows:		
Fuel HHV Flow	3,130.49	kJ/sec
Fuel LHV Flow	2,621.76	kJ/sec
Boiler Duty	1,058.82	kJ/sec
Condenser Duty	736.83	kJ/sec
COG Compressor Power	11.36	kW
Air Compressor Power	1,003.52	kW
Condensate Pump Power	5.31	kW
Steam Turbine Power	317.23	kW
Gas Turbine Power	1,971.25	kW

Equipment Efficiencies:	Isentropic	Mechanical
COG Compressor	0.88	0.99
Air Compressor	0.88	0.99
Condensate Pump	0.80	0.95
Gas Turbine	0.90	0.99
Steam Turbine	0.75	0.97

Efficiency Values:		
GT Cycle (HHV Based)	64.37	%
GT Cycle (LHV Based)	76.86	%
(turbine exhaust heat incl.)		
Steam Cycle	29.46	%
Overall (HHV Based)	40.51	%
Overall (LHV Based)	48.38	%
Power Out - Power In	1,268.29	kW
Efficiency Brayton Cycle (LHV)	36.48	%
(no use of turbine exhaust)		

Appendix E.3 - 15% COG/HA blend, operating pressure 8 atm.

Fuel Gas System:		
Fuel Flow Rate	0.0114	kmol/sec
Fuel Flow Rate	0.1847	kg/sec
HHV (fuel mix)	18,175.9	kJ/kg
LHV (fuel mix)	15,281.9	kJ/kg
Flue Gas:		
Outlet Temperature (1) small	393.0	K
Outlet Temperature (2) large	393.0	K
Turbine exhaust to recuperator	23.2	%
Steam System:		
Circulation Rate	0.4420	kg/sec
Air system:		
Total air	2.895	kg/sec
Secondary air	2.099	kg/sec
Primary air	0.796	kg/sec
Global Φ	0.316	
Percentage of air as secondary	72.5	%

Energy Flows:		
Fuel HHV Flow	3,357.08	kJ/sec
Fuel LHV Flow	2,822.55	kJ/sec
Boiler Duty	1,162.34	kJ/sec
Condenser Duty	808.87	kJ/sec
COG Compressor Power	12.84	kW
Air Compressor Power	767.09	kW
Condensate Pump Power	5.83	kW
Steam Turbine Power	348.24	kW
Gas Turbine Power	1,737.00	kW

Equipment Efficiencies:	Isentropic	Mechanical
COG Compressor	0.88	0.99
Air Compressor	0.88	0.99
Condensate Pump	0.80	0.95
Gas Turbine	0.90	0.99
Steam Turbine	0.75	0.97

Efficiency Values:		
GT Cycle (HHV Based)	63.13	%
GT Cycle (LHV Based)	75.09	%
(turbine exhaust heat incl.)		
Steam Cycle	29.46	%
Overall (HHV Based)	38.71	%
Overall (LHV Based)	46.04	%
Power Out - Power In	1,299.49	kW
Efficiency Brayton Cycle (LHV)	33.91	%
(no use of turbine exhaust)		

Appendix E.4 - 15% COG/HA blend, operating pressure 12 atm.

Fuel Gas System:		
Fuel Flow Rate	0.0114	kmol/sec
Fuel Flow Rate	0.1847	kg/sec
HHV (fuel mix)	18,175.9	kJ/kg
LHV (fuel mix)	15,281.9	kJ/kg
Flue Gas:		
Outlet Temperature (1) small	393.0	K
Outlet Temperature (2) large	393.0	K
Turbine exhaust to recuperator	21.6	%
Steam System:		
Circulation Rate	0.3984	kg/sec
Air system:		
Total air	3.090	kg/sec
Secondary air	2.294	kg/sec
Primary air	0.796	kg/sec
Global Φ	0.296	
Percentage of air as secondary	74.2	%

Energy Flows:		
Fuel HHV Flow	3,357.08	kJ/sec
Fuel LHV Flow	2,822.55	kJ/sec
Boiler Duty	1,047.77	kJ/sec
Condenser Duty	729.14	kJ/sec
COG Compressor Power	16.22	kW
Air Compressor Power	1,042.31	kW
Condensate Pump Power	5.25	kW
Steam Turbine Power	313.92	kW
Gas Turbine Power	2,101.91	kW

Equipment Efficiencies:	Isentropic	Mechanical
COG Compressor	0.88	0.99
Air Compressor	0.88	0.99
Condensate Pump	0.80	0.95
Gas Turbine	0.90	0.99
Steam Turbine	0.75	0.97

Efficiency Values:		
GT Cycle (HHV Based)	62.29	%
GT Cycle (LHV Based)	74.09	%
(turbine exhaust heat incl.)		
Steam Cycle	29.46	%
Overall (HHV Based)	40.27	%
Overall (LHV Based)	47.90	%
Power Out - Power In	1,352.04	kW
Efficiency Brayton Cycle (LHV)	36.97	%
(no use of turbine exhaust)		